

# UC Irvine

## UC Irvine Electronic Theses and Dissertations

### Title

Evolutionary and pharmacological modulation of voltage-gated proton channels

### Permalink

<https://escholarship.org/uc/item/0pw3j9wj>

### Author

Zhao, Chang

### Publication Date

2021

### Copyright Information

This work is made available under the terms of a Creative Commons Attribution-NonCommercial License, available at <https://creativecommons.org/licenses/by-nc/4.0/>

Peer reviewed|Thesis/dissertation

UNIVERSITY OF CALIFORNIA,  
IRVINE

Evolutionary and pharmacological modulation of voltage-gated proton channels

DISSERTATION

submitted in partial satisfaction of the requirements  
for the degree of

DOCTOR OF PHILOSOPHY

in Biomedical Sciences

by

Chang Zhao

Dissertation Committee:  
Professor Francesco Tombola, Chair  
Professor Todd C. Holmes  
Professor Geoffrey W. Abbott  
Professor Douglas J. Tobias  
Professor James E. Hall

2021



## DEDICATION

To

my doctoral advisor - Francesco Tombola

my parents - Kang Zhao and Zhaoxia Chang

my husband - Zebin Wang

# TABLE OF CONTENTS

|   |      |
|---|------|
| LIST OF FIGURES   | v    |
| LIST OF TABLES  | viii |
| ACKNOWLEDGEMENTS  | ix   |
| CURRICULUM VITAE  | x    |
| ABSTRACT OF THE DISSERTATION  | xiv  |
| Chapter 1: Introduction   | 1    |
| 1.1 Voltage-gated proton channel Hv1  | 1    |
| 1.2 Pathophysiological relevance of Hv1   | 12   |
| 1.3 Hv1 as a pharmacological target   | 19   |
| 1.4 References  | 23   |
| Chapter 2: Voltage-gated proton channels from fungi highlight role of peripheral regions<br>in channel activation | 28   |
| 2.1 Introduction  | 29   |
| 2.2 Materials and Methods   | 32   |
| 2.3 Results   | 37   |
| 2.4 Discussion  | 54   |
| 2.5 Supplementary Information   | 59   |
| 2.6 References  | 65   |
| Chapter 3: Voltage-gated proton channels in plants  | 70   |
| 3.1 Introduction  | 71   |
| 3.2 Materials and Methods   | 72   |
| 3.3 Results   | 76   |
| 3.4 Discussion  | 90   |
| 3.5 Supplementary Information   | 94   |
| 3.6 References  | 97   |
| Chapter 4: Development of HIFs: arginine-mimic inhibitors of Hv1 with improved VSD-<br>ligand interactions        | 99   |
| 4.1 Introduction  | 100  |
| 4.2 Materials and Methods   | 102  |
| 4.3 Results   | 107  |
| 4.4 Discussion  | 120  |
| 4.5 Supplementary Information   | 122  |
| 4.6 References  | 128  |

|   |     |
|---|-----|
| Chapter 5: Hv1 inhibition by HIF reveals a new druggable pocket in the voltage-sensing domain | 132 |
| 5.1 Introduction  | 133 |
| 5.2 Materials and Methods   | 134 |
| 5.3 Results   | 139 |
| 5.4 Discussion  | 155 |
| 5.5 Supplementary Information   | 160 |
| 5.6 References  | 169 |
| <br>  |     |
| Chapter 6: Overview and Future Directions   | 172 |
| 6.1 Overview  | 172 |
| 6.2 Future directions   | 174 |
| 6.3 References  | 186 |

## LIST OF FIGURES

|             |   |    |
|-------------|---|----|
| Figure 1.1  | Structural organization of voltage-gated ion channels and other proton channels   | 2  |
| Figure 1.2  | Schematic of human Hv1 transmembrane segments with relative positions of individual residues  | 4  |
| Figure 1.3  | Hv1 is a critical player in human physiology  | 13 |
| Figure 2.1  | Fungal Hv1s from species <i>S. luteus</i> and <i>A. oryzae</i> show distinct biophysical properties   | 39 |
| Figure 2.2  | Hv1s from <i>S. luteus</i> and <i>A. oryzae</i> are proton selective  | 42 |
| Figure 2.3  | Gating of fungal Hv1s is strongly $\Delta$ pH dependent   | 45 |
| Figure 2.4  | Pharmacological characteristics of Hv1s from <i>S. luteus</i> and <i>A. oryzae</i>  | 48 |
| Figure 2.5  | Swapping parts of SlHv1 with AoHv1 reveals regions with important role in channel activation  | 50 |
| Figure 2.6  | Activation properties of Sl/AoHv1 chimeric channel with combined swaps in S1-S2 and S3-S4 loops   | 53 |
| Figure S2.1 | Phylogenetic relationship between Hv1 channels from fungi and animals   | 59 |
| Figure S2.2 | Sequence alignment of proton channels from multiple fungal species  | 60 |
| Figure S2.3 | Voltage-dependent opening of fungal Hvs   | 61 |
| Figure S2.4 | Hv1s from <i>S. luteus</i> and <i>A. oryzae</i> are sensitive to mechanical stimulation   | 62 |
| Figure S2.5 | Alternative structural models for the VSD of SlHv1  | 63 |
| Figure S2.6 | Reduced pH sensitivity of the G-V relationship of chimera <i>ChL2-3</i> under symmetrical conditions  | 64 |
| Figure 3.1  | Hv1 from <i>Arabidopsis thaliana</i> localizes to the plasma membrane but displays no apparent proton current recorded with electrophysiology | 77 |
| Figure 3.2  | Angiosperm Hv1 channels behave differently than their counterparts from other plant species   | 79 |
| Figure 3.3  | Activation of AtHv1 and TcHv1 requires mechanical priming prior to membrane depolarization  | 82 |

|             |   |     |
|-------------|---|-----|
| Figure 3.4  | Hv1s from plant <i>P.sitchensis</i> , <i>A. thaliana</i> , and <i>S.moellendorffii</i> are proton selective                 | 84  |
| Figure 3.5  | Activation of plant Hvs are both $\Delta$ pH dependent and absolute pH dependent  | 88  |
| Figure 3.6  | Inhibition of Plant Hvs by 2GBI and ClGBI   | 89  |
| Figure S3.1 | Sequence alignment of Hvs from four plant species along with human Hv1  | 94  |
| Figure S3.2 | GFP-AtHv1 localized to the nuclear envelope or ER in elongated root cells when expressed in the <i>Arabidopsis thaliana</i> | 95  |
| Figure S3.3 | $V_{T, IV}$ derived from I-V relationships correlates with $V_{T, GV}$ acquired from G-V curves in PsHv1                    | 95  |
| Figure S3.4 | Shifts in voltage dependence subjecting to different pHs ( $\Delta$ pH = $\pm$ 1) from Hvs in three plant species and human | 96  |
| Figure 4.1  | Exploring how residue F150 influences Hv1 sensitivity to 2GBI   | 107 |
| Figure 4.2  | Aromatic interactions stabilizing ligand binding in Hv1 F150A   | 111 |
| Figure 4.3  | Simplified ligand for binding optimization  | 113 |
| Figure 4.4  | Impact of phenyl ring fluorination on ABI-mediated inhibition Hv1 WT and F150A  | 115 |
| Figure 4.5  | Hv1 inhibition by HIF compounds   | 116 |
| Figure S4.1 | Functional rescue of Hv1 F150* by suppressor tRNA.  | 122 |
| Figure S4.2 | HIF and 2GBI bound the Hv1 VSD  | 123 |
| Figure S4.3 | Hv1 inhibition by HIF <sub>EN</sub>   | 124 |
| Figure S4.4 | Predicted metabolism and toxicity of HIF compounds vs. 2GBI   | 125 |
| Figure 5.1  | Kinetics of Hv1 inhibition by HIF compounds compared to ABI and 2GBI  | 141 |
| Figure 5.2  | Four-state model replicates Hv1 inhibition by HIF   | 144 |
| Figure 5.3  | Structural determinants of HIF-mediated inhibition - open VSD   | 147 |
| Figure 5.4  | Structural determinants of HIF-mediated inhibition - closed VSD   | 150 |
| Figure 5.5  | HIF orientation within the closed Hv1 VSD   | 153 |
| Figure 5.6  | Proposed HIF binding site in the closed channel and trapping  |     |

|             |  |     |
|-------------|--|-----|
|             | mechanism  | 154 |
| Figure S5.1 | Effect of depolarization frequency on recovery from HIF-mediated inhibition  | 160 |
| Figure S5.2 | Kinetic modeling of HIF-mediated Hv1 inhibition  | 161 |
| Figure S5.3 | Comparisons between experimental and simulated data  | 162 |
| Figure S5.4 | Effects of voltage on HIF apparent binding to closed state   | 163 |
| Figure S5.5 | Effect of HIF on the conductance vs voltage relationship of Hv1 WT   | 164 |
| Figure S5.6 | Simulations of the time-course of HIF-mediated inhibition of Hv1 channels with destabilized B or T states                              | 165 |
| Figure S5.7 | Simulations of the time-course of HIF-mediated inhibition of Hv1 F150A   | 166 |
| Figure S5.8 | Extended model E compared to model S   | 167 |
| Figure S5.9 | Sequence alignment of S2 and S3 segments of representative human VSD-containing proteins   | 168 |
| Figure 6.1  | Chimera PsHv1-S4K displays mechanosensitivity similar to AtHv1, and requires mechanical priming prior to depolarization for activation | 178 |
| Figure 6.2  | PMA-induced ROS production in human neutrophils is potently inhibited by HIF   | 180 |
| Figure 6.3  | Selective HIF compounds slow down the proliferation and migration of the MDA-MB-231 breast cancer cells                                | 183 |
| Figure 6.4  | Relative wound density (%) over 48 hours post wound scratching from MDA-MB-231 breast cancer cells                                     | 184 |
| Figure 6.5  | Representative brightfield images of MDA-MB-231 breast cancer cells  | 185 |

## LIST OF TABLES

|   |     |
|---|-----|
| Table S3.1. Activation threshold potentials ( $V_{TS}$ ) from three plant Hv1 measured at various pH conditions from the inside-out patches | 96  |
| Table S4.1. Fit parameters for concentration dependences of Hv1 inhibitors  | 126 |

## ACKNOWLEDGEMENTS

I would like to express my deepest gratitude to my thesis advisor, Dr. Francesco Tombola, who kindly provided me with this precious opportunity in doctoral training. His tremendous support and persistent guidance throughout my graduate career have made a profound impact on both of my professional development as well as personal growth. I learnt to care for details that would determine the success vs. failure, and to appreciate figures that would speak for themselves. Most importantly, the wisdom I learnt from an intellect like him has influenced how I think in many aspects, which I'll carry with me for the rest of my career.

I would like to thank my committee members, Drs. Todd Holmes, Geoffrey Abbott, Douglas Tobias, and James Hall for their helpful advice on my thesis work and manuscript revision. I deeply appreciate the discussion with them and the insights they had provided.

I am grateful to all the current and former members from Tombola lab who had assisted me during my graduate work, especially Dr. Liang Hong for his patience and guidance in electrophysiology during my rotation, Dr. Medha Pathak, who introduced me to the ion channel world. In addition, I appreciate all the great efforts from the undergraduate research assistants who made contributions to the projects, especially Ethan Thuong and Johnny Han. It was both my honor to work with them and witnessed their growth over the years.

To my family and friends, I thank them for their love, support and understanding throughout my PhD journey, and this thesis would not have been completed without them. I thank my parents for their unconditional love, support, and trust for every decision I made since I came to the U.S. for undergraduate study. I am truly thankful to have Zebin, my husband, who has been standing behind me all the time, celebrating with me for my achievements and cheering me up during those challenging periods, including the COVID pandemic which started last year. To my friends, for all the food, beer, and wine that we shared, as well as hearing me out during some tough moments. The support from the peers was precious and incomparable.

Lastly, I would like to acknowledge my financial support provided by the National Institute of General Medical Sciences and the National Institute of Neurological Disorders and Stroke, through grant R01GM098973.

# CURRICULUM VITAE

## Chang Zhao

---

### Education

---

|  |                             |   |             |
|--|-----------------------------|---|-------------|
| <i>University of California, Irvine, Irvine, CA</i>            | <b>Doctor of Philosophy</b> | Biomedical Sciences- focus on Physiology & Biophysics | 2016 - 2021 |
| <i>University of California, Irvine, Irvine, CA</i>            | <b>Master of Science</b>    | Biotechnology   | 2014 - 2016 |
| <i>California State University, San Marcos, San Marcos, CA</i> | <b>Bachelor of Science</b>  | Molecular Biology                                     | 2010 - 2014 |
| <i>Xi'an University of Technology, China</i>                   | Transferred                 | Material Sciences & Engineering                       | 2008 - 2010 |

---

### Publications

---

**Zhao, C.**, Tombola, F. "Voltage-gated proton channels from fungi highlight role of peripheral regions in channel activation" *Communications Biology* 4:1-13.

**Zhao, C.**, Hong, L., Galpin, J., Riahi, S., Lim, V., Webster, P., Tobias, D., Ahern, A., Tombola, F. "Development of HIFs: arginine-mimic inhibitors of Hv1 with improved VSD-ligand interactions" (Manuscript under review).

**Zhao, C.**, Hong, L., Riahi, S., Lim, V., Tobias, D., Tombola, F. Hv1 inhibition by HIF reveals a new druggable pocket in the voltage-sensing domain" (Manuscript under review).

Liu, J., Liu, D., Liu, J. J., **Zhao, C.**, Yao, S., Hong, L. "Blocking the Nav1.5 channel using eicosapentaenoic acid reduces migration and proliferation of ovarian cancer cells" *International Journal of Oncology* 53.2 (2018): 855-865.

Panopoulos, A., D'Antonio, M., ... **Zhao, C.**, ... Frazer, K. (2017). "iPSCORE: A Resource of 222 iPSC Lines Enabling Functional Characterization of Genetic Variation across a Variety of Cell Types" *Stem Cell Reports* 8.4 (2017): 1086-1100.

Hu, L., **Zhao, C.**, Xu, L. (2011) "Fabrication and Properties of Porous HA Ceramics with Bionic Structure" *Orthopaedic Biomechanics Materials and Clinical Study*, 8(4): 4-7.

---

### Honors and Awards

---

- Recipient of School of Medicine Travel Award (2018, 2019 and 2020), UC Irvine
- Recipient of Poster presentation award, School of Medicine Grad Day, 2018 and 2019, UC Irvine
- Recipient of Departmental fellowship in 2015, Department of Molecular Biology and Biochemistry, UC Irvine (Master's degree)
- Recipient of CIRM Bridges Stipend, CSU San Marcos, 2013-2014
- Recipient of International student tuition fee waiver scholarships from CSU San Marcos, 2011 and 2012
- Dean's list in Fall 2010, Spring 2011, Spring 2012 and Fall 2012, CSU San Marcos
- Second place in the "English Public Speaking Competition" from Xi'an University of Technology (China), 2009
- Recipient of Scholarship from Xi'an University of Technology, China. 2009-2010
- Recipient of Research fellowship of Undergraduate Scientific and Technological Innovation Program, project "The Preparation of Biomimetic Materials", China

---

### Research Experience

---

**Graduate Student Researcher** September 2016 - June 2021  
 Department of Physiology and Biophysics, School of Medicine, University of California Irvine  
 (research advisor: Dr. Francesco Tombola)

- Develop and test rationally designed small-molecule inhibitors targeting voltage-gated proton channel Hv1 via patch clamp in *Xenopus* oocytes
- Characterize the binding sites of inhibitors in the voltage sensing domain through mutagenesis
- Biophysically characterize putative proton channels from plants and fungi
- Investigate and comparative analyze the structure function relationships in the proton channels from different species
- Extract human neutrophils and characterize Reactive Oxygen Species (ROS) inhibition in response to the novel Hv1 inhibitors
- Maintain breast cancer cell lines to generate RNAs for RNA-seq
- Conduct RNA-seq studies to identify differentially expressed genes from Hv1 KO breast cancer cells (MDA-MB-231) for understanding Hv1's potential role in breast cancer migration and metastasis

**Graduate Student Researcher** September 2015 - June 2016  
 Department of Physiology and Biophysics, School of Medicine, University of California Irvine  
 (research advisors: Dr. Lisa Flanagan, Dr. Medha Pathak and Dr. Francesco Tombola)

- Worked under the supervision of postdoctoral scholar Dr. Medha Pathak on the project aiming to generate Piezo1 knockout in the human foreskin fibroblasts and human neural stem cells via CRISPR/Cas9
- Performed routine maintenance of human fibroblasts and human iPS cells
- Designed and generated CRISPR/Cas9 plasmids
- Tested the efficiency of different guide RNAs through mismatch cleavage assay (T7E1) upon transfection
- Performed qRT-PCR to validate the modification at transcript level

**Research assistant, CIRM Bridges Intern**

August 2013 - August 2014

Institute of Genomic Medicine, University of California San Diego  
(research advisor: Dr. Kelly A. Frazer)

- Worked in a research team aiming to establish a high-throughput cardiac differentiation pipeline from iPSCs for related genetics studies from over 200 individuals
- Trained at Stem Cell Core facility at Salk institute for human stem cell and iPS culture
- Differentiated patient fibroblast derived iPS cells into cardiomyocytes plated in monolayers with small molecules
- Optimized and established a reliable staining protocol on cardiomyocytes for the downstream flow cytometry
- Validated the differentiation efficiency and characterized differentiated cell population using flow cytometry

**Undergraduate researcher**

January 2012 - July 2013

California State University San Marcos  
(research advisor: Dr. Betsy Read)

- Cultured and maintained marine algae *Emiliana huxleyi* in medium and agarose plates
- Experienced in cloning a novel construct using Gibson assembly method and identified a selectable marker that could be used for transformation
- Established a transformation system in *Emiliana huxleyi* using the Helium biolistic particle delivery platform aiming to facilitate

**Undergraduate volunteer**

July 2011 - September 2011

Salk Institute, gene expression lab  
(research advisor: Fred Gage)

- Worked under supervision of postdoctoral Dr. Wei Deng on the Studies of neuron response in hippocampus during information acquisition and retrieval
- Assisted in brain slice sectioning, mounting, confocal imaging and cell counting

**Undergraduate researcher**

September 2009 - May 2010

Xi'an University of Technology

- Developed protocols in clearing porous biological tissues including beef ribs in order to use them as natural molds
- Fabricated the porous HA ceramics using those prepared structures and facilitated the material characterization

---

**Conferences and Meeting Presentations**

---

- Poster presentation at the 64<sup>th</sup> Biophysical Society Meeting, San Diego, 2020
- Poster presentation at the 63<sup>rd</sup> Biophysical Society Meeting, Baltimore, 2019

- Platform Speaker at the 62<sup>nd</sup> Biophysical Society Meeting, San Francisco, 2018
- Poster presentation at Gordon Research Conference in Ion Channels, South Hadley, 2018
- Poster presentation at School of Medicine Grad Day, UC Irvine, 2018 and 2019
- “*Research in Progress*” seminars, Department of Physiology and Biophysics, UC Irvine, 2018-2020
- Poster presentation at International Society for Stem Cell Research Annual meeting, Vancouver, 2014
- Poster presentation at 2014 CIRM Bridges Trainee Meeting, San Francisco, 2014

---

### Pedagogical Experience

---

#### Graduate Teaching Assistant

September 2015 -December 2016

- Supervised and mentored laboratory courses consisting of 10-15 master students from the Biotechnology program along with fellow TAs
- Independently supervised laboratory courses consisting of 20-30 upper-level undergraduate students
- Held office hours and small teach sessions in the interim
- Generated weekly educational materials including quizzes, handouts and interactive classroom activities
- Prepared weekly lab reagents for the graduate level laboratory
- Proctored exams and graded assays, exams, and quizzes
- Courses taught: Nucleic Acids Biotechnology Laboratory, Protein Purification and Characterization Laboratory, Biotechnology Management Laboratory, The Physiology of Ion Channels

---

### Professional Membership

---

- Biophysical Society
- American Chemical Society

---

### Volunteer and Outreach

---

- STEM Outreach program in K-12 Education, San Marcos elementary school, 2011
- Volunteer at the San Diego Science Festival at CSU San Marcos Biotech booth, 2011
- Mentor to new students in the international friendship program - 2012, CSU San Marcos
- Student Assistant at the Language Learning Center, CSU San Marcos, 2011-2013
- Peer mentor to new international students in the School of Medicine, UC Irvine, 2017
- Mentor to Bio199 undergraduate students, 2016-2020
- Graduate coordinator for Research in Progress seminars, Department of Physiology & Biophysics, UC Irvine, 2018-2019
- Mentor to rotation graduate student, 2018

## ABSTRACT OF THE DISSERTATION

Evolutionary and pharmacological modulation of voltage-gated proton channels

By

Chang Zhao

Doctor of Philosophy in Biomedical Sciences

University of California, Irvine 2021

Professor Francesco Tombola, Chair

Voltage-gated proton channels (Hvs) are membrane proteins that belong to the superfamily of voltage-gated ion channels (VGICs). They are dimers consisting of two voltage sensing domains (VSDs), which resemble the ones from other VGICs, but lack the pore domain (PD) commonly found in other VGICs. They regulate cellular pH homeostasis and their activity is frequently coupled with reactive oxygen species (ROS) production by NADPH oxidase (NOX) enzymes, a critical process in the elimination of pathogens by phagocytes through the respiratory burst.

The structural determinants that set the voltage range of activation of Hv channels are poorly understood, and so is the mechanism underlying the dependence on co-stimuli, such as intracellular acidification and membrane stretch. Here, I exploited the functional diversity of Hv channels from distantly related organisms to identify protein regions responsible for the modulation of channel activation and to uncover new mechanisms of co-stimulation. By comparing Hv homologs from different species of fungi, I found that the distinctively negative voltage range of activation of some fungal Hv channels is controlled by their extracellular peripheral regions. By comparing Hv homologs from different species of plants, I identified Hv channels that require mechanical priming prior to voltage-dependent activation, a property most likely controlled by their S4 transmembrane segment, which is divergent between

angiosperm and gymnosperm plants. My findings suggest that evolution has tuned the biophysical properties of these channels to match the distinct physiological contexts in which they operate.

In human and other animals, the Hv1 channel is widely expressed in the immune system, including in B and T lymphocytes, macrophages, neutrophils, and basophils as well as in the microglia within the central nervous system (CNS). Previous studies have found that Hv1 activity plays a role in the progression of various types of cancers (e.g., B cell lymphoma, breast cancer, colorectal cancer), and impairs the recovery from CNS damage caused by ischemic stroke, traumatic brain injury, and spinal cord injury. Therefore, developing inhibitors targeting Hv1 could provide effective treatments for a variety of pathological conditions.

Based on our understanding of how a previous generation of guanidine mimics (e.g., 2GBI and ClGBI) inhibit Hv1, we rationally designed the next generation of compounds, named HIFs (Hv1 Inhibitor Flexible). I found that some HIF molecules inhibit Hv1 at lower concentrations compared to 2GBI, and possess desirable features for further drug development. I characterized the mechanism of HIF-mediated inhibition and found evidence of two distinct binding sites: one located deep into the intracellular vestibule of the channel and shared with 2GBI, and one located in a shallower part of the vestibule, closer to the inner mouth of the channel. The existence of the second binding site could explain some of the desirable pharmacological properties that distinguish HIFs from first-generation inhibitors.

## Chapter 1: Introduction

### 1.1 Voltage-gated proton channel Hv1

#### *Structural information of Hv1*

Though proton currents were firstly reported from snail neurons<sup>1</sup> and later from rat alveolar epithelial cells as well as other mammalian cells<sup>2</sup>, the voltage-gated proton channel Hv1 or VSOP (Voltage Sensor Only Protein) was not cloned and characterized until decades later<sup>3,4</sup>. Unlike voltage-gated sodium channels (Navs) and voltage-gated potassium channels (Kvs), where voltage changes detected by voltage-sensing domains (VSDs) are communicated to pore domains (PDs) to control ion permeation, Hv1 lacks a proper PD, and its VSDs both sense voltage changes and conduct protons (Figure 1.1). Hv1 is a homodimer<sup>5-7</sup> consisting of two VSDs that are coupled to a coiled-coil domain (CCD)<sup>8</sup>. Structural information about the human Hv1 channel is limited. The protein is only about 31kDa (based on its canonical sequence, other variants can be slightly shorter). The small size makes it unsuitable for structural determination by cryogenic electron microscopy. A crystal structure of a chimeric protein based on mouse Hv1 (mHv1cc, PDB 3WKV) was solved in 2014 to a 3.45-Å resolution<sup>9</sup>. In the chimera, the S2-S3 region of Hv1 is replaced by the corresponding part of the *Ciona Intestinalis* voltage-sensing phosphatase (Ci-VSP), and the CCD is replaced by a leucine-zipper motif from a *Saccharomyces cerevisiae* transcriptional activator GCN4. In addition, separate structures of isolated CCDs of human and mouse Hv1 were solved by a different group<sup>8,10</sup>. The mHv1cc provided limited information on the assumed closed state of the channel, and no information regarding the subunit interface. A solution NMR structure of human Hv1 in micelle was proposed to represent an intermediate state between activated states and the resting state<sup>11</sup>. Several models of human Hv1 in the open conformation have been generated by atomistic molecular dynamics (MD) simulations<sup>12-17</sup>,



represents side view and right panel shows top view. Na<sup>+</sup>, K<sup>+</sup> and H<sup>+</sup> ions are shown on top views to indicate the location of the conduction pathways. C) Topological arrangement of Otop proton channels (right). Segments 1-6 and 7-12 of N- and C-terminal domains are shown in pink and gray, respectively. Dimer of pseudo-dimer organization is shown on left. Red crosses in the center of the top views represent non-functional conduction pathways.

### ***Voltage and pH dependences of activation***

Like the other VGICs, activation of Hv1 is strongly voltage dependent. Though the location of the gate remains to be elucidated, three positively charged arginines (R205, R208 and R211) arranged periodically, interspaced by hydrophobic residues in S4 (figure 1.2) are thought to contribute significantly to voltage gating based on the similar role that homologous residues have on other VGICs. There has been a long-lasting interest in measuring the gating charge in Hv1, however several limitations have made this extremely difficult. Because the VSD in Hv1 both senses voltage changes and conducts protons, isolating the gating current from the ionic current has been challenging. Eliminating protons from the solution is not an option, as this would result in pH values that compromise the integrity of the protein. It is not until recent years that two separate studies showed some measurements of the gating charge of Hv1 in monomeric *Ciona* Hv1<sup>18</sup> or human Hv1<sup>19</sup>. Both studies took a strategy to eliminate the proton current by using a low-conducting mutant, combined with channel variants with facilitated activation. Carmona et al. chose the *Ciona* Hv1 monomer, which activates faster than the human Hv1. The ionic current was largely attenuated by introducing a low-conducting mutation (N264R, equivalent to N214 in human Hv1), and they estimated a gating charge of around 1.5e<sub>0</sub>. De La Rosa et al. used the same strategy (mutation N214R) to eliminate the ionic current in the human Hv1, but in combination with mutation W207A or R205A to speed up the activation. They performed measurements with both full-length dimer and C-terminal truncated monomeric channel (Hv1ΔC). The resulting gating charges measured from the monomer was around 1.5e<sub>0</sub>, consistent with the measurements for the dimer at around 3e<sub>0</sub>.

Under physiological pH conditions, Hv1 activates at considerably positive voltage ranges which

are not normally seen in other VGICs, and this is reflected by either the conductance-voltage relationship (G-Vs) or the voltage threshold of activation ( $V_T$ ), which is defined as voltage at which the proton current can be distinguished from the background noise (usually corresponding to ~1% of the maximal proton conductance). For example, under the symmetrical pH conditions, human Hv1 channel activates under strong depolarization with a half-maximal conductance ( $V_{1/2}$ ) at  $53 \pm 3 \text{ mV}$ <sup>5</sup>. Activation of Hv1 is also strongly dependent on  $\Delta\text{pH}$  ( $\text{pH}_o - \text{pH}_i$ ), and the current-voltage relationship (I-V) shifts around 40mV per unit of  $\Delta\text{pH}$ , known as the ‘rule of forty’<sup>20</sup>. The relationship summarized from over 15 mammalian cell types can be described by the equation  $V_T = 0.79E_H + 23 \text{ mV}$ . At symmetrical pH, the expected  $V_T$  is around 23mV, significantly greater than the Nernst potential for protons ( $E_H$ ).

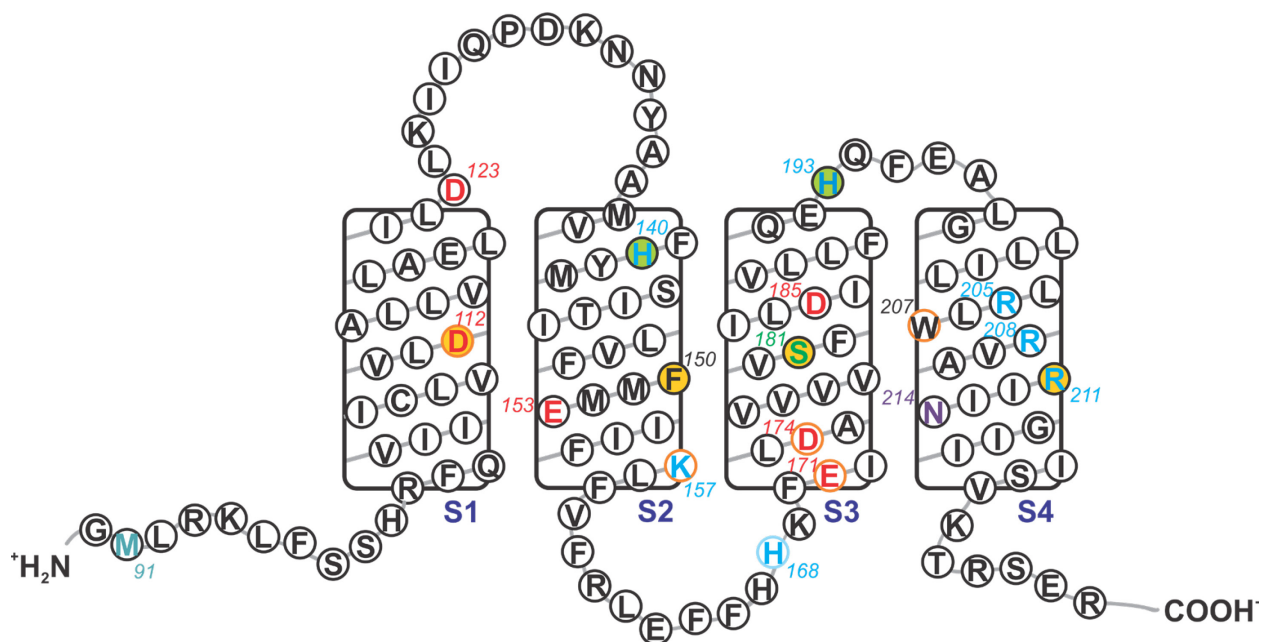


**Figure 1.1. Schematic of human Hv1 transmembrane segments with relative positions of individual residues displayed in bold (a.a 90-226).** Key acidic residues are in red and basic residues are in blue. Residues in circles highlighted in yellow form the 2GBI binding site, and residues in orange circles contribute to one of the HIF binding sites. The two extracellular histidines that contribute to  $\text{Zn}^{2+}$  binding are shown in circles highlighted in green.

While all proton channels allow  $\text{H}^+$  ions to move across the membrane following their electrochemical gradient, most Hv1s work as acid extruders (permitting only outward  $\text{H}^+$

movement). This is because strong depolarization is required for activation ( $V_T > E_H$ ). Under conditions in which higher concentration of protons on the extracellular side would favor inward proton conduction, the channel remains closed because its voltage dependence of activation is shifted to more positive potentials. Exception include Hv1s from dinoflagellate *Karlodinium Veneficum*<sup>21</sup> and fungi *Aspergillus oryzae*<sup>22</sup>, both activate at substantially negative voltages and conduct inward currents well below the Nernst potential for protons ( $V_T < E_H$ ).

Studies from several groups suggest the critical roles of transmembrane segments in the channel gating. Gonzalez et al. demonstrated neutralizing each of the three positively charged arginines in *Ciona* Hv1 reduces both effective gating charge and voltage dependent movement of S4, and results from cysteine accessibility (R1C) by MTS reagents suggest the middle of S4 moves across the electric field when channel transition from closed to open state<sup>23</sup>. Two subunits of the Hv1 dimer gate cooperatively<sup>5-7</sup>, and the second conformational change following the S4 movement was shown to be less voltage dependent, and mutations disrupt dimerization or at the inter-subunit interface affects the channel opening<sup>24</sup>. Based on results from cysteine accessibility scan to MTS reagents and voltage clamp fluorometry experiments done with the *Ciona* Hv1, Momy et al. proposed that in response to depolarization, the bottom of S1 undergoes outward motion following the upward and rotation of the S4, indicating a possible role of S1 of functioning as part of Hv1's gate<sup>25</sup>. This is also in agreement with their recent report that a great number of residues in S1 are part of the inter-subunit interface<sup>26</sup>.

While it is well established that the transmembrane region of the channel comprises the gating machinery, others identified possible roles of peripheral regions in channel activation. Fujiwara et al. reported that the cooperative gating in Hv1 is mediated by the coupling at C-terminus, which is directly influenced by the amino acid composition of the linker between S4 and CCD<sup>10</sup>. Interestingly, we recently discovered that the extracellular S1-S2 loop and S3-S4 loop are also

critical in modulating the voltage range of activation (see chapter 2).

Even though in all Hv1 channels studied so far, activation is greatly dependent on the pH gradient across the membrane ( $\Delta\text{pH}$ ), most of the channels are insensitive to absolute pHs, i.e., changing the  $\text{pH}_i$  and  $\text{pH}_o$  simultaneously while maintaining the same  $\Delta\text{pH}$  does not change the G-V or  $V_T$ .

Several studies report exceptions where Hv1 channels are sensitive to absolute pHs, indicating possible roles of intracellular domains in determining  $\Delta\text{pH}$  vs. absolute pH sensitivity. A human Hv1 isoform<sup>27</sup> with the first 68 amino acids missing from the N-terminus, found particularly in sperm, is sensitive to absolute pH changes unlike the full-length channel, which is only  $\Delta\text{pH}$  sensitive. This suggests a role for the N-terminus in switching between the two properties. The DeCoursey group reported Hv1 from snail *Helisoma trivolvis* (HtHv1)<sup>28</sup>, which is normal in sensing  $\text{pH}_o$  but only weakly sensitive to  $\text{pH}_i$ , and thus does not follow the ‘rule of forty’. The authors attribute this feature to a glutamine within the intracellular S2-S3 loop that in HtHv1. The homologous position in the human channel contains a histidine (H168). When that histidine was replaced with a glutamine, the  $\text{pH}_i$  sensitivity of the mutated human Hv1 was found to be significantly reduced<sup>29</sup>. Though it is possible that H168 itself acts as a  $\text{pH}_i$  sensor, the evidence is not conclusive: the sequences of the S2-S3 loop of HtHv1 and human Hv1 are quite divergent and differ not only at the H168 position. Furthermore, the reverse mutation, glutamine-to-histidine, in HtHv1 did not increase  $\text{pH}_i$  sensitivity. Nevertheless, the sequence diversity within the intracellular S2-S3 loop suggests that this part of the protein could contribute to  $\text{pH}_i$  sensitivity. Our recent characterization of Hv1s from fungal species also points to a role for the S2-S3 loop in modulating absolute pH sensitivity<sup>22</sup>. We first noticed a sequence of 7 amino acid from the S2-S3 loop from an absolute pH sensitive fungal channel SlHv1, which is not present in the AoHv1. When we remove this sequence in the mutant channel, the absolute pH sensitivity

was specifically attenuated (see supplementary fig.6 Chapter 2).

In sum, though it is unlikely that a single amino acid is fully responsible for intracellular pH sensing, intracellular domains are clearly critical in modulating this property, which might give rise to the adaptations organisms require for their proper functions under different pH conditions.

### ***Small single channel conductance and perfect proton selectivity***

In contrast to the non-conducting VSDs of Kvs and Navs, the VSD of Hv1 permeates protons<sup>20</sup> with a single channel conductance estimated in low femtosiemens at physiological pH<sup>30</sup>. This conductance is much smaller than the conductances of the pore domains of other VGICs. The near perfect proton selectivity is greatly associated with a negatively charged aspartate from S1 (D112 in hHv1) within the narrowest part of the inner vestibule, which is also known to be a critical component of the selectivity filter<sup>31</sup>. And this aspartate is conserved among all Hvs found in other species so far<sup>32</sup>. Neutralizing mutations at D112 either results in the channel becoming anion selective or non-conductive, and only one conservative mutation (D112E) retains proton selectivity and conduction. While it is well recognized that aspartate 112 has a unique role in conferring the proton selectivity, positively charged arginine residues from S4 are proposed to be part of the selectivity filter<sup>17,33,34</sup> as well. Particularly, when R211 (R3) is mutated to a serine, the mutant channel is no longer selective for protons and is able to conduct large organic molecule such as guanidium ( $\text{Gu}^+$ ), sharing the same conduction pathway with protons, as the  $\text{Gu}^+$  current could be almost completely inhibited by external  $\text{Zn}^{2+}$ <sup>33</sup>. Swapping the charges in D112 and R211 (in the double mutant D112R-R211D) retains proton selectivity. Based on these findings it has been proposed that R3 interacts with D112 to stabilize the activated state, forming the selectivity filter of Hv1.

### *Proton permeation and transport*

Besides Hv1 channels<sup>3,4</sup>, only two other types of proton channels have been identified in animals thus far. Otopetrins (Otops) are proteins known to be crucial for otoconia development<sup>35</sup>, and they have been shown to be proton channels<sup>36</sup>. Otop1 was found to be expressed in gustatory neurons where it functions as sour taste receptor<sup>36</sup>. HCN-like channels have been recently identified in the sperms of zebrafish and were found to possess proton conducting VSDs<sup>37</sup>. In contrast with Hvs which assemble as dimers<sup>5,6</sup> with each subunit containing a proton conduction pathway, both Otop1 and HCNL1 channels are multimers with four proton pores (also see figure 1.1B, C). Cryo-EM structures of otopetrin proteins<sup>38,39</sup> reveal a pseudo-tetrameric organization: a dimer with each subunit containing N- and C- pores. Structurally resembling the organization of “pacemaker” HCN channels, HCNL1 is also a tetramer activated by hyperpolarization, however with a non-functional PD, it carries proton currents through four VSDs. Interesting, both Otops and HCNL channels conduct inward rectifying proton currents, which makes the Hv1 channels the only proton channels that preferentially conduct outward proton currents. It is not yet clear how Otop1 and HCNL1 channels are gated. While the location of the selectivity filter of Otop channels is unknown, a methoine interspaced between the gating charges in S4 within the zebrafish HCNL1 is proposed to be the key residue that confers proton selectivity to this channel.

While it is well established that D112 is necessary for proton selectivity in Hv1, the mechanism of proton transfer and the role of D112 in this process are still under debate. Currently, there are three major competing hypotheses about how protons permeate the Hv1 VSD: 1) a mechanism that involves obligatory protonation and deprotonation of D112<sup>34</sup>; 2) a mechanism in which protons have to go through an energy barrier established by S4 arginines, which is lowered by the ionizable side chain of D112 only in the open conformation<sup>17</sup>; and 3) a

mechanism in which protons move by hopping through a water wire within the conduction pathway (or Grotthuss mechanism)<sup>12,40-43</sup>.

Though there is not yet a consensus on this topic, there is some experimental evidence supporting different perspectives. The DeCoursey group opposes the water wire theory and argue that it would not explain the anomalous guanidinium conductance under non-physiological high pH conditions (at pH 8.0, WThHv1 is not blocked by 100mM  $\text{Gu}^+$ )<sup>32</sup> or why large organic molecules like  $\text{Gu}^+$  could permeate but not other ions. DeCoursey proposed  $\text{Gu}^+$  conduction through Hv1 under such condition is due to denaturation of the protein caused by disrupting water structure (hydrogen bonds) and breaking the salt bridges between positively and negative charged residues<sup>44</sup>, experimental results from others suggest otherwise. Several studies reported blockade of Hv1 with guanidinium ions at mM ( $K_d = \sim 1\text{mM}$ ) concentrations<sup>5,33</sup> under physiological pH conditions. Guanidinium ions structurally resemble the side chain of arginine, consistent with the finding that N4R (N214R) mutation in Hv1 is known to lead to a channel with largely reduced conductance. On the other hand, there are several examples where proton or  $\text{Gu}^+$  conductance is observed in modified VSDs: in Shaker and Nav1.2 VSDs, mutating R1 to smaller amino acids such as serine and cysteine turns on the omega current (inward) under hyperpolarization<sup>45-47</sup>; mutating R3 to small amino acids such as serine also induces currents which could be carried by metal ions or guanidinium<sup>33</sup>, suggesting protons and guanidinium ions share the same conduction pathway.

MD simulations have also been used to gain insight into the mechanism of Hv1 permeation and gating, however there are frequently limitations. For example, Dudev et al. used a reduced quantum mechanical model only with the selectivity filter (D112-R208) and found that the introduction of  $\text{H}_3\text{O}^+$  breaks the hydrogen bond between the pair, and protonating the titratable side chain of the aspartate is sufficient to produce  $\text{H}^+$  conduction, without applying depolarizing

voltages to open the channel. Lee et al. used the chimeric structure mHv1cc as the template for the closed state, but used Kv1.2 as the template for the open conformation, and both S0 and S4 had to be manually modified as they were blocking the channel or partially disorganized since it is shorter than the S4 from Kv1.2. The most recent model from Geragotelis et al. 2020, revealed that though a depolarizing potential rearranges partners that form salt bridges within the VSD, the water wire remains largely stationary through the permeation pathway. This model provides valuable insights into voltage dependent proton conduction in Hv1. First, the template for the initial homology model was mHv1cc, second, it was based on all-atom simulations with a long-timescale (10 $\mu$ s) which included both hyperpolarization and depolarization phases. Membrane depolarization allowed the voltage sensor to move up without any initial assumptions on position. Lastly, the model agrees with the experimental result that proton conduction can be inhibited by an internal crosslink formed by Cd<sup>2+</sup> between V109C and F150C, indicating that V109 is in the vicinity of F150 under depolarizing potentials.

### ***Cooperative gating and inter-subunit interface***

The Hv1 channel is a dimeric complex comprising two VSDs which gate cooperatively<sup>5-7</sup>. While the CCD controls the dimerization process and mediates cooperativity, transmembrane helices that make up the inter-subunit interface remain elusive. Several groups proposed different dimer models with inter-subunit interface involving different transmembrane helices. While the Okamura group proposed a model with dimer interactions mainly between S4 transmembrane segments (S4-S4 model)<sup>48</sup> based on the crystal structures of mHv1cc<sup>9</sup> and isolated dimeric CCD<sup>10</sup>, Li et al. proposed hHv1 VSDs interact through both S1 and S4 transmembrane segments (S1-S4 model)<sup>49</sup>, supported by cross-linking data<sup>7</sup> indicating contacts between the outer ends of S1 of the two subunits, and a crystal structure of CiVSP dimer<sup>50</sup>. The Tombola group<sup>51</sup> probed the inter-subunit interface by investigating the strong allosteric binding of an open channel blocker

2-guanidinothiazole (GBTA), and concluded that the top of S1 from the two VSDs must be in close proximity in the open conformation to mediate the allosteric coupling. Their results are inconsistent with the model with extended S4-S4 interactions which places the outer ends of S1 too far apart. Recent work from the Isacoff group<sup>26</sup> examined the interface through a mutagenesis scan of S1 residues. Based on a comparative analysis between dimer and monomer, they interpret the results as evidence that the interface involves the entire S1, as well as interactions between S1 and S4, supporting the S1-S4 model.

### ***Mechanosensitivity***

Compared to specialized mechanically activated ion channels such as Piezo channels<sup>52</sup> and Msc channels<sup>53</sup>, the effect of mechanical stimulation on VGICs is usually overlooked as voltage activation is the primary mode of modulation. In fact, not only are many VGICs tuned by mechanical stimuli<sup>54-57</sup>, but the impact of mechanical stimulation has physiological relevance<sup>58</sup>, i.e., in the heart, myocardial cells, valve and papillary muscle surfaces continually experience blood flow generated shear forces, and VGICs including Kvs, Navs and HCN channels respond reversibly to such stimulation; in other disease conditions, such as ischemia-reperfusion injury and cardiac inflammation, voltage modulation might be irreversibly restructured, leading to the serious pathological consequences. Biophysical characterization of Nav1.5, which is abundant in heart, shows that both activation and inactivation are accelerated upon mechanical stimulation, also accompanied by a left shift in the channel's voltage dependence of activation.

As a member of the VGIC family, Hv1 is also sensitive to mechanical stimuli<sup>59</sup>, and this is relevant in the pathophysiological contexts, i.e., Hv1 is found in cellular locations experiencing frequent mechanical stresses such as airway epithelia<sup>60</sup> and sperm flagella<sup>61</sup>, and Hv1 could be potentiated by membrane swelling<sup>62</sup> and causes exacerbation of cerebral damage upon ischemic stroke<sup>63</sup>. Resembling the effect found in Nav1.5<sup>64</sup>, mechanical stretch accelerates Hv1

activation and this “facilitated” mode lasts for minutes before reverting back to the original state. Biophysical characterization of Hv1 expressed in *Xenopus* oocytes shows that membrane tension generated by high-speed pressure clamp (HSPC) produced  $-14.4 \pm 2.7$  mV left shift in GV<sup>59</sup>. The majority of the impact of mechanical stimulation was proposed to be mediated by subunit cooperative gating, as the GV shift was negligible in Hv1 monomers (monomer Hv1NCvsp was generated by replacing N- and C- terminus with corresponding components from CiVSP), though the activation could still be facilitated.

Chapters 2 and 3 of my thesis show our effort in understanding the mechanical modulation of Hv1 through orthologs from species within the fungi and plant kingdoms. Structure vs. function analysis among plant Hv1s reveals that the transmembrane segment S4 is a significant contributor to the strong mechanosensitivity seen in Hv1s of some plant species but not others.

## 1.2 Pathophysiological relevance of Hv1

### *Hv1 in immune system*

Hv1 is an ancient gene conserved across different kingdoms of life, from animals<sup>32</sup> to fungi<sup>22</sup> and even plants (see chapter 3). In the ocean, it plays an important role in the calcification process performed by several coccolithophore algae species<sup>65</sup>, a critical part of the carbon fixation cycle that influences the global climate<sup>66</sup>. It is also responsible for triggering bioluminescence in dinoflagellates upon mechanical stimulation<sup>21</sup>.

In human, Hv1 has important functions throughout the body, from the immune system<sup>67</sup> to the brain<sup>68</sup> and the male reproductive system<sup>69</sup>. Hv1 is expressed in a wide array of immune cells including granulocytes, macrophages, T cells and B cells<sup>70</sup>. The channel extrudes protons from the cell, counteracting cytoplasmic acidification and sustaining the generation of reactive

oxygen species (ROS) by NADPH oxidases (NOXs), which is known to be an electrogenic process (also see figure 1.3A). For example, in phagocytes Hv1 is required for ROS production to kill bacteria. In basophils, Hv1 activity promotes histamine release. In the airway epithelium, the channel contributes to pH homeostasis, and in B lymphocytes, it is known to interact directly with the B cell receptor to support B cell activation<sup>32</sup>.

In the brain, Hv1 is primarily found in the microglia, which serve as the resident immune cells of the central nervous system (CNS), supporting the proper function of the neuronal network by removing cell debris and damaged neurons upon injury. Similar to other types of immune cells, Hv1 supports ROS generation by NOX enzymes during the respiratory burst of microglia, and extrudes excessive acids. Under normal circumstances, microglial cells are required for pro-inflammatory responses and clearance of damaged tissues, however overactivation can induce further damages that prevent recovery.

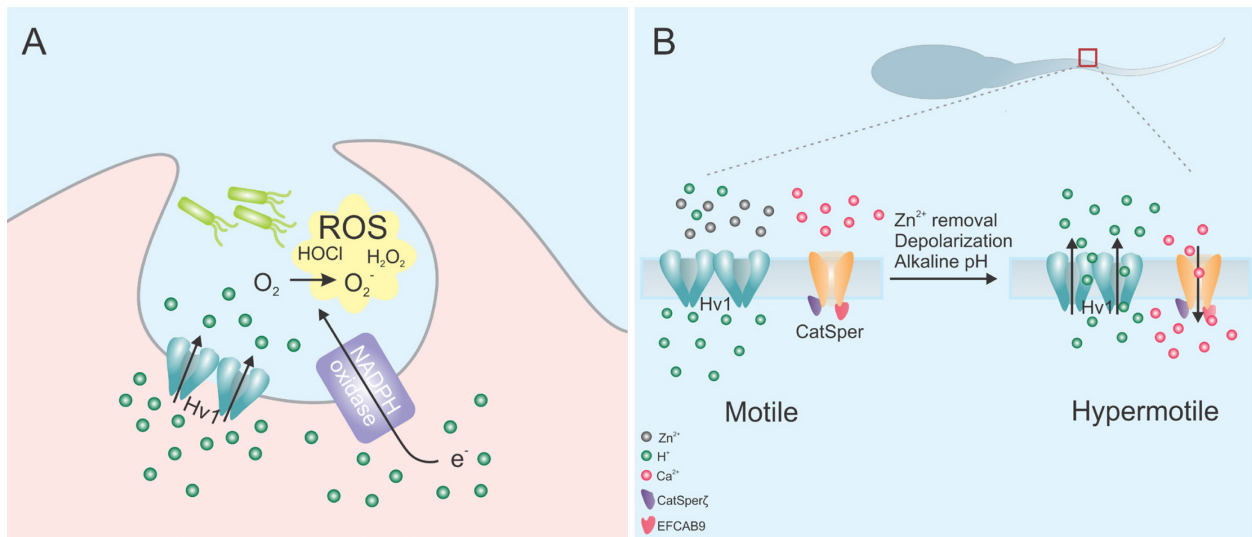


**Figure 1.2. Hv1 is a critical player in human physiology. A)** In phagocytes, proton extrusion by Hv1 sustains the ROS production by the NADPH oxidase to kill bacteria.  $H^+$  ions are shown as green spheres. They accumulate in the cytoplasm as a result of the reaction  $NADPH \rightarrow NADP^+ + 2e^- + H^+$ . **B)** In sperm, the removal of  $Zn^{2+}$ , membrane depolarization, together with extracellular alkaline pH activate the sperm to enter the hypermotile mode, and proton extrusion mediated by Hv1 and downstream events such as  $Ca^{2+}$  entry through CatSper channel are required for this process.

Prior to the identification of Hv1's role in microglia, several studies suggested that NOX activity is implicated in microglia-mediated cerebral damage in stroke<sup>71,72</sup>. The earliest study implicating Hv1's role in microglia was an animal experiment where ischemic stroke was induced with middle cerebral artery occlusion (MCAO) in mice. Hv1 knockout mice are protected from cerebral damage post ischemic stroke<sup>68</sup> compared to control mice, through a reduction in Hv1-dependent ROS. However, later studies suggested that the age of the organism<sup>73</sup> and the analyzed brain region<sup>74</sup> might affect the outcome of the experiment. While the aged Hv1 KO mice had significant decrease in neuronal damage and brain injury characterized by lowered infarct volume post ischemic stroke, no difference was found between younger Hv1 knockout and control mice<sup>73</sup>. A more recent study found that the age-dependent impact of Hv1 is more obvious in the cortex than in the striatum<sup>74</sup>.

In addition to ischemic stroke, multiple studies have shown that Hv1-related ROS production in microglia worsen the outcome of the CNS diseases such as traumatic brain injury (TBI)<sup>75</sup> and spinal cord injury (SCI)<sup>76</sup>. The optimal physiological pH in the brain is in the 7.0-7.4 range. Reduced blood flow and oxygen depletion at the lesion site post TBI cause anaerobic glycolysis and accumulation of lactic acid, carbon dioxide and protons, leading to cerebral acidosis. Cerebral acidosis is known to contribute to poor long-term recovery outcomes and neurological deficits. Reduced pH at the lesion site attracts microglia which further worsen the damage by increasing ROS production, inducing microglia proliferation, as well as causing membrane depolarization. Hv1 knockout mice also demonstrate improved motor recovery and significantly less secondary damage post SCI compared to the control mice<sup>76</sup>, through reducing microglia activation, production of ROS and IL-1 $\beta$ .

While it is clear that Hv1 is important for redox control and potentially can be targeted for treating ROS-related diseases in most cases, how it can be controlled for neuroprotective

treatment remains unclear, largely due to its differential expression and roles in the dynamic brain environment.

### ***Hv1 in sperm***

Alkalinization of the sperm cytoplasm and resulting  $\text{Ca}^{2+}$  entry from the plasma membrane regulate sperm chemotaxis, motility, capacitation, and the acrosome reaction<sup>61</sup>. In human, Hv1 and the pH sensitive CatSper (Cation channel of Sperm) channels co-localize to the principal piece of the sperm flagellum and mediate flagellar beating (figure 1.3B). While Hv1 regulates NOX activity in most immune cells, NOXs are not expressed in spermatozoa. Therefore Hv1's activity is not coupled to ROS production in this context. Patch clamp experiments showed that Hv1 is responsible for the outward proton current leading to sperm intracellular alkalinization<sup>61</sup>. Sperm Hv1 is activated by pH, membrane depolarization,  $\text{Zn}^{2+}$  removal as well as endogenous cannabinoid anandamide (AEA), an essential omega-6 fatty acid. Downstream events include the activation of CatSper channel, allowing for  $\text{Ca}^{2+}$  entry, eventually leading to the sperm hyperactivation in preparation for the acrosome reaction.

In addition to the full-length Hv1 isoform, Berger et al. reported a shorter isoform resulting from post-translational cleavage by a serine protease present in human sperm<sup>27</sup>. This shorter isoform, named as Hv1Sper, is 68 amino acids shorter from the N-terminus and forms heterodimers with the full-length protein. While the canonical Hv1 isoform is only sensitive to transmembrane  $\Delta\text{pH}$ , activation of Hv1Sper is also absolute pH dependent. The presence of the two isoforms in sperm suggests a specialized adaptation to fine tune intracellular pH. Interestingly, mouse sperm lacks Hv1 and intracellular alkalinization is achieved through  $\text{Na}^+$ -dependent  $\text{Cl}^-/\text{HCO}_3^-$  exchanger (NCB) and sperm specific  $\text{Na}^+/\text{H}^+$  exchanger (sNHE). NCB accumulates bicarbonate ions that activates bicarbonate-dependent atypical adenylyl cyclase

(ADCY10) dependent cAMP production, and cAMP binding to sNHE finally causes proton extrusion<sup>69</sup>. This intracellular pH elevation then further activates CatSper channel to trigger the Ca<sup>2+</sup> signaling cascade.

### ***Hv1 in other types of cells***

Besides the wide expression of Hv1 in immune and cancer cells, recent studies report the presence of Hv1 elsewhere including mesenchymal stem cells<sup>77</sup> and bone cells. Hv1-mediated proton currents measured in placenta/chorion-derived mesenchymal stem cells (cMSCs) show the same voltage and pH dependences as the currents measured in other cells. Block by ClGBI results in the decrease of cell migration and mineral matrix production as well as the induction of osteogenesis. Separate studies<sup>78-80</sup> also support the presence of proton channels in osteoclasts, the bone-resorbing cells which are critical for bone remodeling. Acidosis is a common stimulator that induces osteoclast generation from bone marrow precursors and osteoblasts. At the resorption pit, degradation of hydroxyapatite causes the increase in inorganic phosphate (Pi) concentration. Using a macrophage derived osteoclast cell line (RAW264), Li et al. found that extracellular Pi reversibly raised the current amplitude by shifting the voltage dependence to negative potentials and increasing the maximal conductance, accompanied by the robust production of ROS<sup>81</sup>. In summary, proton currents mediated by Hv1 are critical for bone physiology (i.e. bone matrix degradation, proliferation, and migration), and extracellular Pi might be a general modulator of Hv1 and ROS production in the osteoclasts.

### ***Hv1 in cancer***

While proper cellular expression of Hv1 is critical for redox balance, overexpression of Hv1 exacerbates various types of cancers including metastatic breast cancer<sup>63</sup>, colorectal cancer<sup>82</sup> and B-cell lymphoma<sup>83</sup>. Wang et al. first discovered high level of Hv1 expression in the patient-

derived metastatic breast cancer tissue, and then established a correlation between Hv1 expression and patients' survival: the ones with lower level of Hv1 expression had longer survival time compared to the ones with higher level. Similarly, overexpression of Hv1 in colorectal cancer is associated with tumor size, tumor classification, lymph node status, clinical stage, and p53 status, leading to overall poor prognosis and higher mortality<sup>82</sup>.

Cancer cells thrive in hypoxic conditions, frequently reprogram their energy metabolism to glycolysis even under aerobic conditions<sup>84-86</sup>, and are capable of remodeling extracellular matrix (ECM) to promote tissue invasion. Hv1 has been found to be a major pH regulator in breast cancer cells. By extruding excess acid, the channel supports cell survival and ECM degradation. *In vitro*, Hv1 knockdown (KD) by siRNA in MDA-MB-231 triple-negative breast cancer cells inhibits the extracellular proton secretion and intracellular pH recovery, decreases cell proliferation and migration, accompanied by reduced metalloproteinase expression, presumably critical for ECM degradation. *In vivo*, Hv1 KD MDA-MB-231 cells xenografted into nude mice also led to reduced tumor size compared to control. However, a more recent study in which Hv1 knockout (KO) cells were used in addition to KD cells casts doubts on the previous findings<sup>87</sup>. In the latest study, neither reduction of H<sub>2</sub>O<sub>2</sub> nor change in migration was observed with the Hv1 KO cells. Instead, elevated glycolytic rate and phospho-AKT activity were reported. Interestingly, the authors discovered that the adhesion molecule CD171/LCAM-1 is downregulated in KO cells, raising the possibility of using the molecule as a prognosis indicator. Though these findings might suggest that Hv1 KO and KD cells behave differently, there are non-negligible limitations with the strategy the authors used to generate the KO cells. WT Cas9 in combination with the single stranded guide RNA are efficient in editing the genome, but also create off-targets. In fact, the great variability between results from three KO clones in both of the *in vitro* cell assays and *in vivo* tumor xenograft experiments suggests there could be other confounding variables.

Hv1 is highly expressed in almost all types of immune cells and is particularly crucial for modulating the strength of B cell antigen receptor (BCR) signaling<sup>88</sup> and redox sensing. Hv1 was discovered to enhance BCR-dependent proliferation via modulation of ROS production, and to be co-internalized with the antigen-bound receptor prior to B cell activation. Hv1 deficient B cells from a gene trap mouse model produced less ROS and displayed attenuated BCR signaling with impaired tyrosine phosphatase SHP-1 oxidation. The consequences of weakened BCR signaling induced by Hv1 KO included reduced activation of Syk and Akt kinases, attenuated mitochondrial respiration and glycolysis and decreased antibody responses.

In B cells from 76 chronic lymphocytic leukemia (CLL) patients, a shorter variant of Hv1 lacking the first 20 amino acids of the canonical full-length protein was found to be the predominant channel isoform<sup>83</sup>. Co-internalization with the BCR was reduced in the shorter variant, leading to a greater membrane expression. Enrichment was not only found in B cells from CLL patients but also in several B-cell lymphoma cell lines. Overexpressing the shorter isoform but not the full-length protein in a B-cell lymphoma cell line resulted in an increase of cell proliferation and chemokine dependent migration, evidenced by the EdU incorporation and transwell assay of CXCL12. Interestingly, the shorter Hv1 variant behaves differently than the Hv1Sper variant found in sperm, which is also N-terminal truncated, but with 68 amino acids cleaved<sup>27</sup> post-translationally by a serine protease. In the variant found in B cells, the first 20 amino acids are missing because of alternative initiation of translation. The isoform displays a slower activation rate compared to full length Hv1 but responds more strongly to PKC-dependent phosphorylation (PMA stimulation).

A more recent genetic study<sup>89</sup> used whole-exome sequencing in an attempt to identify recurrent somatic mutations in follicular lymphoma (FL) patients. While most frequently mutated genes are found in the BCR and CXCR4 interconnected pathways (44.8% of the total patients), the

authors identified a number of novel genes with recurrent mutations including *HVCN1*, which might be useful in regard to prognosis and even target for treatment. The mutations in *HVCN1*, however, are quite heterogenous, including nonsense and splice-donor mutations predominantly causing frameshifts, which seems to be more diverse than what was reported from the CLL patients in the previous study<sup>83</sup>.

### 1.3 Hv1 as a pharmacological target

#### *Zn<sup>2+</sup> blockade*

Zinc is an essential trace element in human physiology, and zinc ion also binds the Hv1 channel from the extracellular side and inhibits proton currents<sup>3,4,90</sup>. In the male reproductive system where sperms are normally quiescent, Hv1 is inhibited by the high level of Zn<sup>2+</sup> found in the seminal fluid. When introduced to the female reproductive tract, low concentration of Zn<sup>2+</sup> leads to the activation of Hv1, allowing for alkalinization of sperm cytoplasm which is required for spermatozoa activation and flagellar beating<sup>61</sup>. Correspondingly, Zn<sup>2+</sup> was found to inhibit sperm capacitation<sup>91</sup>. Zn<sup>2+</sup> blocks animal Hv channels by stabilizing the closed state thus making them more difficult to open<sup>90</sup>. Two histidines (H140 at the top of S2 and H193 within the S3-S4 loop) are critical for coordinating Zn<sup>2+</sup> in human Hv1<sup>4,92,93</sup>, and mutating either one of them reduces the channel Zn<sup>2+</sup> sensitivity. As protons compete with Zn<sup>2+</sup> for the histidine sites, increasing the extracellular pH was found to enhance Zn<sup>2+</sup> binding<sup>90</sup>.

Interestingly, the inward-rectifying proton currents from the recently identified sour-tasting proton channel Otop1 can also be inhibited by extracellular Zn<sup>2+</sup><sup>36</sup>, though the mechanism remains unknown. Coincidentally, there are also histidines on the extracellular loops of Otop1, which might also contribute to its Zn<sup>2+</sup> sensitivity. Whether VSD-carrying current from HCNL1 channel can be blocked by Zn<sup>2+</sup> is yet to be explored. The presence of several histidines in the

the extracellular loops of HCNL1 from some species but not others suggests that the channel homologs might be differentially sensitive to  $Zn^{2+}$  block.

### ***Modified toxins and small peptides as Hv1 inhibitors***

Despite the pathological relevance of Hv1 and its potential as a drug target for treating a wide spectrum of diseases, few pharmacological developments have been made compared to other VGICs. There are plenty of examples of inhibitors that target VGICs by interacting with their PDs, but a limited number of toxins and small molecules inhibit the channels by interacting with their VSDs. A previous study showed Hv1 can be inhibited by high concentrations of tarantula hanatoxin<sup>94</sup>.

More recently, A small peptide named Corza6 (C6) was identified to be a potent Hv1 inhibitor<sup>95</sup>, from a phage-display screening platform with a library of ~1 million small peptides sharing the framework of the inhibitor cysteine knot. C6 preferentially binds to the extracellular S3-S4 loop, shifting the G-V curve to more positive potentials ( $\Delta V_{1/2}=+20mV$ ). Maximal inhibition of C6 is reached at 250nM with an IC50 around 30nM. Interestingly, maximizing the concentration of C6 could not block the Hv1 proton current completely, leaving ~50% of the current unblocked. Despite the incomplete inhibition and the room for further improvement, the authors demonstrated that inhibition of Hv1 by C6 leads to the block of acrosome reaction in human sperm, and is sufficient to inhibit ROS production in human white blood cells, making it a useful tool to study Hv1 in human physiology.

Another recent study raised the possibility of developing Hv1 inhibitors by modifying known toxins to other VGICs. AGAP, a scorpion toxin identified in a RP-HPLC screen, was shown to potently inhibit both Hv1 and a Nav channel<sup>96</sup>. Introducing the mutation W38F in AGAP strongly reduced binding to Nav1.2, while maintaining the ability to inhibit Hv1. AGAP/W38F has an IC50

of  $1.8 \pm 0.3 \mu\text{M}$ , and at  $10\mu\text{M}$  it inhibits the proton current completely. Similar to Corza6, AGAP/W38 inhibits Hv1 by stabilizing the closed state and making the channel more difficult to open ( $\Delta V_{1/2} \sim +20\text{mV}$ , tested under different  $\Delta\text{pH}$  conditions). Coincidentally, efficient binding of the AGAP/W38F also requires two extracellular histidines (H140 and H193), indicating it shares, at least partially, the binding pocket with  $\text{Zn}^{2+}$ . Results from Corza6 and AGAP/W38F suggest that both the S1-S2 and S3-S4 loops are potential hotspots for modulation of channel activation, and that blocking the proton currents completely might require interactions with both loops, not just one<sup>22</sup>.

### ***Small molecule inhibitors***

The Tombola group explored the pharmacology of Hv1 using a strategy based on small molecules, and identified a class of channel inhibitors that resemble arginine residues<sup>97</sup>. 2-guanidinobenzimidazole (2GBI), a guanidine derivative, binds to the inner vestibule of Hv1 only when it is activated<sup>97,98</sup>. In contrast to small peptides or modified toxins which bind to the extracellular side and make the channel more difficult to open, 2GBI is an open channel blocker and works by occluding the proton conduction pathway without causing shifts in GV, and it must leave the binding site located in the narrowest part of the inner vestibule before the gate can close. 2GBI inhibits WT human Hv1 in the micromolar range ( $\text{IC}_{50} = 38.3 \pm 0.7 \mu\text{M}$ ), making it a great tool to study Hv1. However, its micromolar working concentration and lack of capability of penetrating the membrane from the extracellular side makes it difficult to be applied as a drug *in vivo*.

Further studies<sup>51,98</sup> found that simply adding a chloro-substituent to the phenyl ring of 2GBI not only makes the derivative (ClGBI) a more potent inhibitor, but also strongly increase membrane permeability ( $\text{IC}_{50} = 26.3 \pm 2.2 \mu\text{M}$  when added extracellularly). This improvement makes the

applications *in vivo* possible, i.e., ClGBI is capable of inhibiting proton currents from the native Hv1 channels from the microglial BV-2 cells, and monocyte/macrophage cells RAW216.7 and THP-1 cells, evidenced by recordings from the whole-cell patch clamp. One caveat when using ClGBI is that under the physiological pH, blocking ~80% of the proton currents requires around 200  $\mu\text{M}$ , which indicates that a better inhibitor is needed.

Characterization of the binding site through mutant cycle analysis reveals 2GBI is coordinated by residues from all four transmembrane segments: D112, F150, S181 and R211<sup>51,98</sup>. An interesting finding from the mutagenesis screen was that 2GBI could inhibit the Hv1 F150A at nanomolar concentrations, more than two orders of magnitude better than the WT. We reasoned that understanding the interaction between the F150A mutant and 2GBI could provide insights into the development of more potent inhibitors. In chapter 4, I describe how we rationally designed the next generation of inhibitors named HIFs and in chapter 5, I provide the description of the mechanism of HIF-mediated channel inhibition.

## 1.4 References

1. Thomas, R.C. & Meech, R.W. Hydrogen ion currents and intracellular pH in depolarized voltage-clamped snail neurones. *Nature* **299**, 826-8 (1982).
2. DeCoursey, T.E. Hydrogen ion currents in rat alveolar epithelial cells. *Biophys. J.* **60**, 1243-53 (1991).
3. Sasaki, M., Takagi, M. & Okamura, Y. A voltage sensor-domain protein is a voltage-gated proton channel. *Science* **312**, 589-92 (2006).
4. Ramsey, I.S., Moran, M.M., Chong, J.A. & Clapham, D.E. A voltage-gated proton-selective channel lacking the pore domain. *Nature* **440**, 1213-6 (2006).
5. Tombola, F., Ulbrich, M.H. & Isacoff, E.Y. The voltage-gated proton channel Hv1 has two pores, each controlled by one voltage sensor. *Neuron* **58**, 546-56 (2008).
6. Koch, H.P. et al. Multimeric nature of voltage-gated proton channels. *Proc Natl Acad Sci U S A* **105**, 9111-6 (2008).
7. Lee, S.Y., Letts, J.A. & Mackinnon, R. Dimeric subunit stoichiometry of the human voltage-dependent proton channel Hv1. *Proc Natl Acad Sci U S A* **105**, 7692-5 (2008).
8. Li, S.J. et al. The role and structure of the carboxyl-terminal domain of the human voltage-gated proton channel Hv1. *J. Biol. Chem.* **285**, 12047-54 (2010).
9. Takeshita, K. et al. X-ray crystal structure of voltage-gated proton channel. *Nat. Struct. Mol. Biol.* **21**, 352-7 (2014).
10. Fujiwara, Y. et al. The cytoplasmic coiled-coil mediates cooperative gating temperature sensitivity in the voltage-gated H(+) channel Hv1. *Nature communications* **3**, 816 (2012).
11. Bayrhuber, M. et al. Nuclear Magnetic Resonance Solution Structure and Functional Behavior of the Human Proton Channel. *Biochemistry* **58**, 4017-4027 (2019).
12. Wood, M.L. et al. Water wires in atomistic models of the Hv1 proton channel. *Biochim. Biophys. Acta* **1818**, 286-93 (2012).
13. Morgan, D. et al. Peregrination of the selectivity filter delineates the pore of the human voltage-gated proton channel hHV1. *J. Gen. Physiol.* **142**, 625-40 (2013).
14. Chamberlin, A. et al. Hydrophobic plug functions as a gate in voltage-gated proton channels. *Proc Natl Acad Sci U S A* **111**, E273-82 (2014).
15. Gianti, E., Delemotte, L., Klein, M.L. & Carnevale, V. On the role of water density fluctuations in the inhibition of a proton channel. *Proc Natl Acad Sci U S A* **113**, E8359-E8368 (2016).
16. Randolph, A.L., Mokrab, Y., Bennett, A.L., Sansom, M.S. & Ramsey, I.S. Proton currents constrain structural models of voltage sensor activation. *Elife* **5**(2016).
17. Lee, M., Bai, C., Feliks, M., Alhadeff, R. & Warshel, A. On the control of the proton current in the voltage-gated proton channel Hv1. *Proc Natl Acad Sci U S A* **115**, 10321-10326 (2018).
18. Carmona, E.M. et al. Gating charge displacement in a monomeric voltage-gated proton (Hv1) channel. *Proc Natl Acad Sci U S A* **115**, 9240-9245 (2018).
19. De La Rosa, V. & Ramsey, I.S. Gating Currents in the Hv1 Proton Channel. *Biophys. J.* **114**, 2844-2854 (2018).
20. DeCoursey, T.E. Voltage-gated proton channels and other proton transfer pathways. *Physiol. Rev.* **83**, 475-579 (2003).
21. Smith, S.M. et al. Voltage-gated proton channel in a dinoflagellate. *Proc Natl Acad Sci U S A* **108**, 18162-7 (2011).
22. Zhao, C. & Tombola, F. Voltage-gated proton channels from fungi highlight role of

- peripheral regions in channel activation. *Commun Biol* **4**, 261 (2021).
23. Gonzalez, C., Rebolledo, S., Perez, M.E. & Larsson, H.P. Molecular mechanism of voltage sensing in voltage-gated proton channels. *J. Gen. Physiol.* **141**, 275-85 (2013).
  24. Gonzalez, C., Koch, H.P., Drum, B.M. & Larsson, H.P. Strong cooperativity between subunits in voltage-gated proton channels. *Nat. Struct. Mol. Biol.* **17**, 51-6 (2010).
  25. Mony, L., Berger, T.K. & Isacoff, E.Y. A specialized molecular motion opens the Hv1 voltage-gated proton channel. *Nat. Struct. Mol. Biol.* **22**, 283-290 (2015).
  26. Mony, L., Stroebel, D. & Isacoff, E.Y. Dimer interaction in the Hv1 proton channel. *Proc Natl Acad Sci U S A* **117**, 20898-20907 (2020).
  27. Berger, T.K. et al. Post-translational cleavage of Hv1 in human sperm tunes pH- and voltage-dependent gating. *J Physiol* **595**, 1533-1546 (2017).
  28. Thomas, S. et al. Exotic properties of a voltage-gated proton channel from the snail *Helisoma trivolvis*. *J. Gen. Physiol.* **150**, 835-850 (2018).
  29. Cherny, V.V., Morgan, D., Thomas, S., Smith, S.M.E. & DeCoursey, T.E. Histidine(168) is crucial for DeltapH-dependent gating of the human voltage-gated proton channel, hHV1. *J. Gen. Physiol.* **150**, 851-862 (2018).
  30. Cherny, V.V., Murphy, R., Sokolov, V., Levis, R.A. & DeCoursey, T.E. Properties of single voltage-gated proton channels in human eosinophils estimated by noise analysis and by direct measurement. *The Journal of general physiology* **121**, 615-628 (2003).
  31. Musset, B. et al. Aspartate 112 is the selectivity filter of the human voltage-gated proton channel. *Nature* **480**, 273-7 (2011).
  32. DeCoursey, T.E. Voltage-gated proton channels: molecular biology, physiology, and pathophysiology of the H(V) family. *Physiol. Rev.* **93**, 599-652 (2013).
  33. Berger, T.K. & Isacoff, E.Y. The pore of the voltage-gated proton channel. *Neuron* **72**, 991-1000 (2011).
  34. Dudev, T. et al. Selectivity Mechanism of the Voltage-gated Proton Channel, HV1. *Sci Rep* **5**, 10320 (2015).
  35. Hurle, B. et al. Non-syndromic vestibular disorder with otoconial agenesis in tilted/mergulhador mice caused by mutations in otopetrin 1. *Hum. Mol. Genet.* **12**, 777-89 (2003).
  36. Tu, Y.H. et al. An evolutionarily conserved gene family encodes proton-selective ion channels. *Science* **359**, 1047-1050 (2018).
  37. Wobig, L. et al. A family of hyperpolarization-activated channels selective for protons. *Proc Natl Acad Sci U S A* **117**, 13783-13791 (2020).
  38. Saotome, K. et al. Structures of the otopetrin proton channels Otop1 and Otop3. *Nat. Struct. Mol. Biol.* **26**, 518-525 (2019).
  39. Chen, Q., Zeng, W., She, J., Bai, X.C. & Jiang, Y. Structural and functional characterization of an otopetrin family proton channel. *Elife* **8**(2019).
  40. Ramsey, I.S. et al. An aqueous H<sup>+</sup> permeation pathway in the voltage-gated proton channel Hv1. *Nat. Struct. Mol. Biol.* **17**, 869-875 (2010).
  41. Pupo, A. & Gonzalez Leon, C. In pursuit of an inhibitory drug for the proton channel. *Proc Natl Acad Sci U S A* **111**, 9673-4 (2014).
  42. van Keulen, S.C. et al. Does Proton Conduction in the Voltage-Gated H(+) Channel hHV1 Involve Grothuss-Like Hopping via Acidic Residues? *J Phys Chem B* **121**, 3340-3351 (2017).
  43. Geragotelis, A.D. et al. Voltage-dependent structural models of the human Hv1 proton channel from long-timescale molecular dynamics simulations. *Proc Natl Acad Sci U S A* **117**, 13490-13498 (2020).
  44. DeCoursey, T.E. CrossTalk proposal: Proton permeation through H(V) 1 requires transient protonation of a conserved aspartate in the S1 transmembrane helix. *J*

- Physiol* **595**, 6793-6795 (2017).
45. Sokolov, S., Scheuer, T. & Catterall, W.A. Ion permeation through a voltage-sensitive gating pore in brain sodium channels having voltage sensor mutations. *Neuron* **47**, 183-9 (2005).
  46. Starace, D.M. & Bezanilla, F. A proton pore in a potassium channel voltage sensor reveals a focused electric field. *Nature* **427**, 548-53 (2004).
  47. Tombola, F., Pathak, M.M. & Isacoff, E.Y. Voltage-sensing arginines in a potassium channel permeate and occlude cation-selective pores. *Neuron* **45**, 379-88 (2005).
  48. Fujiwara, Y., Kurokawa, T. & Okamura, Y. Long alpha helices projecting from the membrane as the dimer interface in the voltage-gated H(+) channel. *J. Gen. Physiol.* **143**, 377-86 (2014).
  49. Li, Q. et al. Resting state of the human proton channel dimer in a lipid bilayer. *Proc Natl Acad Sci U S A* **112**, E5926-35 (2015).
  50. Li, Q. et al. Structural mechanism of voltage-dependent gating in an isolated voltage-sensing domain. *Nat. Struct. Mol. Biol.* **21**, 244-52 (2014).
  51. Hong, L., Singh, V., Wulff, H. & Tombola, F. Interrogation of the intersubunit interface of the open Hv1 proton channel with a probe of allosteric coupling. *Sci Rep* **5**, 14077 (2015).
  52. Kefauver, J.M., Ward, A.B. & Patapoutian, A. Discoveries in structure and physiology of mechanically activated ion channels. *Nature* **587**, 567-576 (2020).
  53. Booth, I.R. & Blount, P. The MscS and MscL families of mechanosensitive channels act as microbial emergency release valves. *J. Bacteriol.* **194**, 4802-9 (2012).
  54. Laitko, U., Juranka, P.F. & Morris, C.E. Membrane stretch slows the concerted step prior to opening in a Kv channel. *J. Gen. Physiol.* **127**, 687-701 (2006).
  55. Beyder, A. et al. Mechanosensitivity of Nav1.5, a voltage-sensitive sodium channel. *J Physiol* **588**, 4969-85 (2010).
  56. Schmidt, D., del Marmol, J. & MacKinnon, R. Mechanistic basis for low threshold mechanosensitivity in voltage-dependent K<sup>+</sup> channels. *Proc Natl Acad Sci U S A* **109**, 10352-7 (2012).
  57. Morris, C.E., Prikryl, E.A. & Joós, B. Mechanosensitive gating of Kv channels. *PLoS One* **10**, e0118335 (2015).
  58. Morris, C.E. Voltage-gated channel mechanosensitivity: fact or friction? *Frontiers in physiology* **2**, 25 (2011).
  59. Pathak, M.M. et al. The Hv1 proton channel responds to mechanical stimuli. *J. Gen. Physiol.* **148**, 405-418 (2016).
  60. Iovannisci, D., Illek, B. & Fischer, H. Function of the HVCN1 proton channel in airway epithelia and a naturally occurring mutation, M91T. *J. Gen. Physiol.* **136**, 35-46 (2010).
  61. Lishko, P.V., Botchkina, I.L., Fedorenko, A. & Kirichok, Y. Acid extrusion from human spermatozoa is mediated by flagellar voltage-gated proton channel. *Cell* **140**, 327-37 (2010).
  62. Morihata, H., Nakamura, F., Tsutada, T. & Kuno, M. Potentiation of a voltage-gated proton current in acidosis-induced swelling of rat microglia. *The Journal of neuroscience : the official journal of the Society for Neuroscience* **20**, 7220-7 (2000).
  63. Wang, Y., Li, S.J., Wu, X., Che, Y. & Li, Q. Clinicopathological and biological significance of human voltage-gated proton channel Hv1 protein overexpression in breast cancer. *J. Biol. Chem.* **287**, 13877-88 (2012).
  64. Morris, C.E. & Juranka, P.F. Nav channel mechanosensitivity: activation and inactivation accelerate reversibly with stretch. *Biophys. J.* **93**, 822-33 (2007).
  65. Taylor, A.R., Chrachri, A., Wheeler, G., Goddard, H. & Brownlee, C. A voltage-gated

- H<sup>+</sup> channel underlying pH homeostasis in calcifying coccolithophores. *PLoS Biol.* **9**, e1001085 (2011).
66. Paasche, E. A review of the coccolithophorid *Emiliania huxleyi* (Prymnesiophyceae), with particular reference to growth, coccolith formation, and calcification-photosynthesis interactions. *Phycologia* **40**, 503-529 (2001).
  67. Capasso, M., DeCoursey, T.E. & Dyer, M.J. pH regulation and beyond: unanticipated functions for the voltage-gated proton channel, HVCN1. *Trends Cell Biol.* **21**, 20-8 (2011).
  68. Wu, L.J. et al. The voltage-gated proton channel Hv1 enhances brain damage from ischemic stroke. *Nat. Neurosci.* **15**, 565-73 (2012).
  69. Lishko, P.V. & Kirichok, Y. The role of Hv1 and CatSper channels in sperm activation. *J Physiol* **588**, 4667-72 (2010).
  70. Fujiwara, Y., Takeshita, K., Nakagawa, A. & Okamura, Y. Structural characteristics of the redox-sensing coiled coil in the voltage-gated H<sup>+</sup> channel. *J. Biol. Chem.* **288**, 17968-75 (2013).
  71. Dringen, R. Oxidative and antioxidative potential of brain microglial cells. *Antioxid. Redox Signal.* **7**, 1223-33 (2005).
  72. Block, M.L., Zecca, L. & Hong, J.S. Microglia-mediated neurotoxicity: uncovering the molecular mechanisms. *Nat. Rev. Neurosci.* **8**, 57-69 (2007).
  73. Kawai, T. et al. Unconventional role of voltage-gated proton channels (VSOP/Hv1) in regulation of microglial ROS production. *J. Neurochem.* **142**, 686-699 (2017).
  74. Kawai, T. et al. Heterogeneity of microglial proton channel in different brain regions and its relationship with aging. *J. Neurochem.* (2021).
  75. Ritzel, R.M. et al. Proton extrusion during oxidative burst in microglia exacerbates pathological acidosis following traumatic brain injury. *Glia* **69**, 746-764 (2021).
  76. Murugan, M. et al. The voltage-gated proton channel Hv1 contributes to neuronal injury and motor deficits in a mouse model of spinal cord injury. *Molecular brain* **13**, 143 (2020).
  77. Meszaros, B. et al. The voltage-gated proton channel hHv1 is functionally expressed in human chorion-derived mesenchymal stem cells. *Sci Rep* **10**, 7100 (2020).
  78. Mori, H. et al. Regulatory mechanisms and physiological relevance of a voltage-gated H<sup>+</sup> channel in murine osteoclasts: phorbol myristate acetate induces cell acidosis and the channel activation. *J. Bone Miner. Res.* **18**, 2069-76 (2003).
  79. Nordström, T. et al. Regulation of cytoplasmic pH in osteoclasts. Contribution of proton pumps and a proton-selective conductance. *J. Biol. Chem.* **270**, 2203-12 (1995).
  80. Sakai, H. et al. Increases in intracellular pH facilitate endocytosis and decrease availability of voltage-gated proton channels in osteoclasts and microglia. *J Physiol* **591**, 5851-66 (2013).
  81. Li, G., Miura, K. & Kuno, M. Extracellular phosphates enhance activities of voltage-gated proton channels and production of reactive oxygen species in murine osteoclast-like cells. *Pflugers Arch* **469**, 279-292 (2017).
  82. Wang, Y., Wu, X., Li, Q., Zhang, S. & Li, S.J. Human voltage-gated proton channel hv1: a new potential biomarker for diagnosis and prognosis of colorectal cancer. *PLoS One* **8**, e70550 (2013).
  83. Hondares, E. et al. Enhanced activation of an amino-terminally truncated isoform of the voltage-gated proton channel HVCN1 enriched in malignant B cells. *Proc Natl Acad Sci U S A* **111**, 18078-83 (2014).
  84. Warburg, O., Wind, F. & Negelein, E. THE METABOLISM OF TUMORS IN THE BODY. *J. Gen. Physiol.* **8**, 519-30 (1927).

85. Warburg, O. On the origin of cancer cells. *Science* **123**, 309-14 (1956).
86. Warburg, O. On respiratory impairment in cancer cells. *Science* **124**, 269-70 (1956).
87. Bare, D.J., Cherny, V.V., DeCoursey, T.E., Abukhdeir, A.M. & Morgan, D. Expression and function of voltage gated proton channels (Hv1) in MDA-MB-231 cells. *PLoS One* **15**, e0227522 (2020).
88. Capasso, M. et al. HVCN1 modulates BCR signal strength via regulation of BCR-dependent generation of reactive oxygen species. *Nat. Immunol.* **11**, 265-72 (2010).
89. Krysiak, K. et al. Recurrent somatic mutations affecting B-cell receptor signaling pathway genes in follicular lymphoma. *Blood* **129**, 473-483 (2017).
90. Cherny, V.V. & DeCoursey, T.E. pH-dependent inhibition of voltage-gated H(+) currents in rat alveolar epithelial cells by Zn(2+) and other divalent cations. *J. Gen. Physiol.* **114**, 819-38 (1999).
91. Riffo, M., Leiva, S. & Astudillo, J. Effect of zinc on human sperm motility and the acrosome reaction. *International journal of andrology* **15**, 229-37 (1992).
92. Qiu, F. et al. Molecular mechanism of Zn<sup>2+</sup> inhibition of a voltage-gated proton channel. *Proc Natl Acad Sci U S A* **113**, E5962-E5971 (2016).
93. Jardin, C., Chaves, G. & Musset, B. Assessing Structural Determinants of Zn(2+) Binding to Human HV1 via Multiple MD Simulations. *Biophys. J.* **118**, 1221-1233 (2020).
94. Alabi, A.A., Bahamonde, M.I., Jung, H.J., Kim, J.I. & Swartz, K.J. Portability of paddle motif function and pharmacology in voltage sensors. *Nature* **450**, 370-5 (2007).
95. Zhao, R. et al. Role of human Hv1 channels in sperm capacitation and white blood cell respiratory burst established by a designed peptide inhibitor. *Proc Natl Acad Sci U S A* **115**, E11847-E11856 (2018).
96. Tang, D. et al. Scorpion toxin inhibits the voltage-gated proton channel using a Zn(2+)-like long-range conformational coupling mechanism. *Br. J. Pharmacol.* **177**, 2351-2364 (2020).
97. Hong, L., Pathak, M.M., Kim, I.H., Ta, D. & Tombola, F. Voltage-sensing domain of voltage-gated proton channel Hv1 shares mechanism of block with pore domains. *Neuron* **77**, 274-87 (2013).
98. Hong, L., Kim, I.H. & Tombola, F. Molecular determinants of Hv1 proton channel inhibition by guanidine derivatives. *Proc Natl Acad Sci U S A* **111**, 9971-6 (2014).

## Chapter 2: Voltage-gated proton channels from fungi highlight role of peripheral regions in channel activation

(Zhao & Tombola)

### Abstract

Here, we report the identification and characterization of the first proton channels from fungi. The fungal proteins are related to animal voltage-gated Hv channels and are conserved in both higher and lower fungi. Channels from *Basidiomycota* and *Ascomycota* appear to be evolutionally and functionally distinct. Representatives from the two phyla share several features with their animal counterparts, including structural organization and strong proton selectivity, but they differ from each other and from animal Hvs in terms of voltage range of activation, pharmacology, and pH sensitivity. The activation gate of Hv channels is believed to be contained within the transmembrane core of the protein and little is known about contributions of peripheral regions to the activation mechanism. Using a chimeragenesis approach, we find that intra- and extracellular peripheral regions are main determinants of the voltage range of activation in fungal channels, highlighting the role of these overlooked components in channel gating.

## 2.1 Introduction

Fungi and humans have a close, yet complicated, relationship: while many gill mushrooms are great resources of proteins and some filamentous fungi are widely exploited in the food industry, some are pathogenic to plants, humans and wildlife. Among at least 2.2 million fungal species<sup>95</sup>, over 8000 are known to infect plants and around 300 cause human diseases<sup>96</sup>. Fungi are capable of adapting to fluctuating, sometimes extreme, conditions. While most thrive in mildly acidic environment (e.g., growing on decaying or fermenting substrates), pathogenic fungi can survive in host organs with a wide range of pHs (pH 2-8)<sup>97</sup>. Different types of fungi actively modify the surrounding proton concentration by secreting organic acids<sup>98</sup> or ammonium<sup>99</sup>, promoting hyphae germination for host tissue invasion, meanwhile maintaining a relatively stable intracellular neutral pH<sup>100,101</sup>.

All living organisms use active and passive proton transport mechanisms to control intracellular pH and proton gradients across cell membranes. Passive mechanisms, mediated by ion channels, let protons flow along their electrochemical gradient in response to specific signals. In animal cells, two major classes of proton channels have been identified: voltage-gated Hv channels<sup>3,4</sup> (also known as VSOPs) and otopetrins<sup>31</sup>. In human, the Hv1 channel contributes to pH homeostasis in various cell types and has important functions in the immune, respiratory, and reproductive systems<sup>21</sup>, e.g., its activity is known to modulate the production of reactive oxygen species (ROS) by NADPH oxidase (NOX) enzymes<sup>25,102,103</sup>. Otopetrin 1 (Otop1) on the other hand, plays important roles in the sensory nervous system, acting as sour taste receptor<sup>31,104</sup> and supporting various aspects of vestibular function<sup>30,105</sup>.

Homologs of NOX enzymes have been identified in fungi as well and are known to be critical for filament growth and for infection and penetration of the host surface<sup>106</sup>. Moreover, pH sensing and signaling in fungi involving the PacC/Rim pathway have been particularly associated with fungal virulence<sup>97,107,108</sup>. It is reasonable to assume that fungi could use passive transport

mechanisms mediated by proton channels for pH regulation, in addition to the known active mechanisms mediated by the H<sup>+</sup>-ATPase (Pma1) on the plasma membrane<sup>101,109,110</sup> and the V-ATPase in intracellular vacuoles<sup>111,112</sup>.

In this study, we report the identification of members of the Hv channel family in both higher and lower fungi and the biophysical and pharmacological characterization of two of these channels: SlHv1 from *Suillus luteus*, a representative of the phylum *Basidiomycota*, and AoHv1 from *Aspergillus oryzae*, a representative of the phylum *Ascomycota*. We find that fungal Hvs share several features with their animal counterparts, including strong proton selectivity and gating modulation by transmembrane pH gradient ( $\Delta$ pH), but the channels differ from each other and from animal Hvs in terms of voltage range of activation, pharmacology, and pH sensitivity in the absence of transmembrane  $\Delta$ pH, which suggest functional adaptation to different environments.

Animal Hv proteins consist of an amphipathic helix S0 and four transmembrane helices S1 through S4 which form a voltage-sensing domain (VSD) structurally equivalent to the VSDs of voltage-gated Na<sup>+</sup>, K<sup>+</sup>, and Ca<sup>2+</sup> channels<sup>3,9,10</sup>. The VSD of Hv channels contains the H<sup>+</sup> conduction pathway, whereas a distinct pore domain, linked to the VSD, contains the ion conduction pathway in other channels<sup>5,6,113</sup>. Another structural feature typical of Hv proteins is a cytoplasmic coiled-coil domain (CCD) that mediates dimerization and is connected to the S4 helix of the VSD<sup>7,8,44</sup>.

Our current understanding of the mechanism of activation of Hv channels is based on studies focused on the S1-S4 transmembrane region, as the activation gate is thought to be located in this part of the protein<sup>13,15,38,93,114</sup>. Here, we find that SlHv1 and AoHv1 share the same structural elements found in animal Hvs. We then use a chimeragenesis approach to identify protein regions responsible for the strong difference in voltage-dependent activation between the two fungal channels. Our results point to previously unrecognized roles of peripheral regions –

defined as portions of the protein interacting with the membrane surface, including loops connecting the transmembrane helices – in the activation process.

## 2.2 Materials and Methods

### Protein sequence analysis

*Multiple sequence alignment and phylogenetic analysis* were performed using Clustal Omega from EMBL-EBI tools<sup>115</sup>. Phylogenetic tree and cladogram were constructed with iTOL 5.6.2<sup>116</sup>. Tree scale is at 0.1. Primary sequences for AoHv1 and SlHv1 were further analyzed with MPEX<sup>117</sup> and Coils - ExpASY<sup>118</sup>. The following protein sequences were used to construct the cladogram and the phylogenetic tree, and to search for potential fungal otopetrins:

### *Fungal Hvs in the cladogram*

*Hypsizygus marmoreus* (RDB21275.1, 215aa); *Amanita muscaria* (KIL69657.1, 218aa); *Psilocybe cyanescens* (PPQ83343.1, 214aa); *Suillus luteus* (KIK49332.1, 223aa); *Scleroderma citrinum* (KIM55885.1, 225aa); *Galerina marginata* (KDR81513.1, 217aa); *Mycena chlorophos* (GAT47218.1, 202aa); *Agaricus bisporus* (XP\_007326257.1, 183aa); *Piriformospora indica* (CCA68166.1, 210aa); *Fusarium oxysporum* (XP\_031056756.1, 230aa); *Sclerotinia sclerotiorum* (XP\_001595616.1, 226aa); *Cladophialophora immunda* (XP\_016251813.1, 259aa); *Talaromyces marneffeii* (EEA28233.1, 309aa); *Penicillium brasilianum* (CEJ60805.1, 205aa); *Aspergillus oryzae* (XP\_001825565.1, 211aa) and *Aspergillus flavus* (GenBank: XP\_002381556.1, 211aa).

### *Additional Hvs included in the phylogenetic tree*

*Rhodotorula toruloides* (EGU12623.1, 262aa); *Spizellomyces punctatus* (XP\_016610604.1, 227aa); *Lobosporangium transversal* (XP\_021881983.1, 208aa); *Mortierella elongate* (OAO32698.1, 206aa); *Basidiobolus meristosporus* (ORX99742.1, 207aa); *Rhizophagus clarus* (GBC03452.1, 235aa); *Bifiguratus adelaidae* (OZJ02879.1, 252aa); *Absidia repens* (ORZ16286.1, 220aa); *Rhizopus microspores* (CEI92734.1, 204aa); *Tieghemostelium lacteum* (KYQ94119.1, 262aa); *Polysphondylium violaceum* (KAF2071235.1, 331aa).

### ***Hvs listed as references from other organisms (cladogram and phylogenetic tree)***

*Nicoletia phytophila* (AMK01488.1, 239aa); *Octopus bimaculoides* (XP\_014789275.1, 348aa); *Ciona intestinalis* (NP\_001071937.1, 342aa); *Danio rerio* (NP\_001002346.1, 235aa); *Xenopus tropicalis* (NP\_001011262.1, 230aa); *Homo sapiens* (NP\_001035196.1, 273aa); *Mus musculus* (NP\_001035954.1, 269aa); *Gallus gallus* (NP\_001025834.1, 235aa); *Alligator sinensis* (XP\_006015244.1, 239aa).

### ***Search for otopetrin orthologs***

Otopetrin proteins from human (NP\_819056.1, NP\_835454.1, NP\_001258934.1, NP\_839947.1), zebrafish (NP\_942098.1), frog (XP\_012811170.1), fruitfly (NP\_001259255.1, NP\_722888.1 ) and nematode (XP\_001672406.1) were used in BLAST search for identification of possible homologues in fungi and returned with no hits.

### ***Channel expression in *Xenopus* oocytes***

DNA constructs encoding wild type SlHv1 and AoHv1 and chimeras ChL1-2 and ChCT3 were synthesized by GenScript after codon optimization for protein expression in animal cells. The construct containing the original cDNA sequence of human Hv1 was described in earlier work<sup>93</sup>. Chimeras ChL1-2a, ChL1-2b, ChL2-3, ChL3-4, ChCT1, and ChCT2 were prepared using the standard PCR technique. All constructs were generated by subcloning the sequences flanking BamHI/XbaI in the pGEMHE vector<sup>119</sup> and linearized with NheI or SphI restriction enzymes (New England Biolabs) before in vitro transcription. cRNAs were synthesized using T7 mMessage mMachine transcription kit (Ambion) or HiScribe™ T7 ARCA mRNA Kit (with tailing) (New England Biolabs). All constructs were confirmed by sequencing, and RNA quality was tested by agarose gel electrophoresis. *Xenopus* oocytes from Ecocyte Bioscience or *Xenopus* 1 were injected with mRNAs (50 nl per cell, 0.5-1.5 ng/nl) 1-3 days before the electrophysiological measurements.

Injections were performed with a Nanoject II (Drummond Scientific). Cells were kept at 18°C in ND96 medium containing 96 mM NaCl, 2 mM KCl, 1.8 mM CaCl<sub>2</sub>, 1 mM MgCl<sub>2</sub>, 10 mM HEPES, 5 mM pyruvate, 100 mg/ml gentamycin (pH 7.2).

### **Patch clamp measurements**

Voltage-clamp measurements were carried out either in inside-out patch or outside-out configurations, using an Axopatch 200B amplifier controlled by pClamp10 software through an Axon Digidata 1440A (Molecular Devices). The signal was lowpass filtered at 1 kHz (Bessel, -80 dB/decade) before digitalization (2 kHz sampling). Inside-out patch clamp experiments were performed under various pH conditions as specified in main text and figures. Bath or pipette recording solution at pH 6.0 contained 100 mM 2-(N-morpholino)ethanesulphonic acid (MES), 30mM tetraethylammonium (TEA) methanesulfonate, 5 mM TEA chloride, 5 mM ethylene glycol-bis(2-aminoethyl)-N,N,N',N'-tetra-acetic acid (EGTA), adjusted to pH 6.0 with TEA hydroxide. Recording solution at pH 5.5 contained 100 mM MES, 50 mM TEA methanesulfonate, 5 mM TEA chloride, adjusted with TEA hydroxide; solution at pH 6.5 contained 100 mM 1,4-piperazinediethanesulfonic acid, 5 mM TEA chloride, adjusted with TEA hydroxide. Outside-out measurements were performed in asymmetrical pH condition (pH<sub>i</sub> = 6.0, pH<sub>o</sub> = 7.0). Solution at pH 7.0 contained 100 mM 3-(N-morpholino)propanesulfonic acid, 40 mM TEA methanesulfonate, 5 mM TEA chloride with or without ZnCl<sub>2</sub> at final concentrations indicated in the text. All tested compounds were at the highest purity commercially available. Intracellular inhibitors 2-guanidinobenzimidazole (2GBI) and 5-chloro-2-guanidinobenzimidazole (ClGBI) were from Sigma-Aldrich. All measurements were carried out at 22 ± 1 °C. Pipettes had 1-3 MΩ access resistance. Unless otherwise specified, the holding potential was either -60 mV or -80 mV. Channel inhibition was determined by isochronal current measurements at the end of the depolarization pulses. For mechanical stimulation of membrane patches, a high-speed pressure

clamp (HSPC-1, ALA Scientific) controlled by pCLAMP 10.2 was used to apply negative pressure pulses through the patch pipette.

Gating charges were estimated using the limiting slope method as previously described<sup>120,121</sup>.

For SlHv1, voltage ramps from  $-80$  mV to  $-20$  mV with rates of  $0.2$  mV/s or  $0.5$  mV/s were used.

To accelerate channel activation,  $pH_i$  was  $5.5$  and  $pH_o$  was  $6.0$ . For AoHv1, voltage ramps from  $-80$  mV to  $-10$  mV with rates of  $0.5$  mV/s or  $1$  mV/s were used. The activation of this channel was fast enough to conduct the measurements at  $pH_i = pH_o = 6.0$ . No significant differences were observed between ramps at different rates for each channel. The voltage protocol included a pre-pulse sufficiently positive to reach maximal conductance. Pre-pulse voltage was  $30$  mV for SlHv1 (asymmetrical pH conditions) and  $60$  mV for AoHv1 (symmetrical pH conditions).

### **Homology modeling and similarity score mapping**

The homology model comprising the VSD and CCD of SlHv1 (Fig. 5a and Fig. S5 – Model 1) was generated using I-TASSER<sup>122</sup> and Swiss-pdb Viewer<sup>123</sup> based on the crystal structures of mHv1cc (PDB 3WKV), and the isolated CCD from mouse Hv1 (PDB 3VMX)<sup>9,44</sup>. The homology model of the SlHv1 VSD based on CiVSP (Fig. S5 – Model 2) was generated using the same approach and the crystal structure of the VSD of CiVSP (PDB 4G80)<sup>46</sup> as a template. The sequences of SlHv1 and AoHv1 covering the homology model structure (from S0 to the C-terminus) were aligned using Clustal Omega<sup>115</sup> with modifications aimed at preserving register of structural domains. Specifically, when shortening the SlHv1 CCD to match AoHv1, individual heptad repeats were removed keeping the register of the remaining repeats unaltered. The similarity scores were determined based on Blocks Substitution Matrix 62 (BLOSUM62) and affine gap penalties (opening: 8, extension: 1). The scores were then normalized and used to derive the scale indicating the deviation from average similarity. The scale (smoothed by adjacent averaging on a five-residue window and ranging from 0 to 1) was converted into a color gradient scale (blue

to red) and mapped on the SHV1 homology models in PyMOL (Schrödinger LLC). Predictions of CCD regions were performed with COILS ([https://embnet.vital-it.ch/software/COILS\\_form.html](https://embnet.vital-it.ch/software/COILS_form.html)), guided by structural information available for CCDs of animal Hvs.

### Data analysis

Current traces were analyzed using Clampfit10.2 (Molecular Devices) and Origin8.1 (OriginLab). Leak subtraction, rundown correction, and assessment of current inhibition were carried out as previously described<sup>93</sup>. Derivation of G-V relationships from I-V curves was performed using equation:

$$G(V) = I(V)/(V-V_{rev})$$

where  $V_{rev}$  is the reversal potential of the current. Due to the high  $H^+$  selectivity of Hv channels,  $V_{rev} \approx E_H$ . G(V) values were then divided by  $G_{max}$  for normalization. G-V relationships were also derived from tail currents, as described in earlier work<sup>124</sup>. Current rundown was corrected using a reference depolarization step preceding the test depolarization. G-V plots were fitted with the Boltzmann equation:

$$G/G_{max} = 1/(1+\exp(V_{1/2}-V)/s)$$

where  $V_{1/2}$  is the potential of half maximal activation, and  $s$  is the slope parameter.  $\tau_{on}(V)$  values were calculated by fitting currents traces in response to depolarizing voltage steps with the single-exponential equation:

$$I(V,t) = a \cdot \exp(-t/\tau_{on}(V)) + c$$

Half deactivation times ( $t_{1/2}(V)$ ) were measured by calculating the time the tail currents took

to decay to  $I_o(V)/2$ , where  $I_o(V)$  is the current at the beginning of the repolarization step. The effective gating charge ( $z_g$ ) associated with activation of SlHv1 and Ao Hv1 was estimated from the linear fit of the logarithm of the open probability [ $\ln(P_o)$ ] as a function of voltage under conditions in which  $P_o$  is very low (limiting slope method<sup>120,121</sup>).  $P_o$  was measured as  $G/G_{max}$  and  $z_g$  was derived from the *slope* of the liner fit through the equation:

$$z_g = (k_B T / e_o) \cdot \text{slope}$$

Where  $k_B$  is the Boltzmann constant,  $T$  is the absolute temperature, and  $e_o$  is the elementary charge.

### Statistics and reproducibility

All statistical analysis were performed using OrginLab 8.1. Data are represented as mean  $\pm$  SEM, unless otherwise indicated. Statistical analysis was performed in Origin (OriginLab). Datasets with two conditions were compared by applying a Welch's t-test. Datasets containing more than two conditions were compared using one-way ANOVA test with Tukey's post hoc correction.

## 2.3 Results

### *Identification of putative proton channels in Fungi*

The importance of pH regulation in fungi raised the question of whether these organisms possess proton channels similar to those found in the animal kingdom. Through BLAST search, we identified a group of putative Hv channels from the following organisms: *Hypsizygos marmoreus*, *Amanita muscaria*, *Psilocybe cyanescens*, *Suillus luteus*, *Scleroderma citrinum*, *Galerina marginata*, *Mycena chlorophos*, *Agaricus bisporus*, *Piriformospora indica*, *Fusarium oxysporum*, *Sclerotinia sclerotiorum*, *Cladophialophora immunda*, *Talaromyces marneffeii*, *Penicillium*

*brasilianum*, *Aspergillus oryzae*, and *Aspergillus flavus* (see Methods section for NCBI sequence IDs). We also searched for Otop orthologues in fungi but were unable to find any fungal protein related to this other type of proton channels (see Methods for details).

Overall, the putative fungal Hvs share 20-29% sequence identity with the human voltage-gated proton channel hHv1. Cladogram of proton channels from these species reveals that they are only distantly related to known Hvs, and there is a clear separation between *Fungi* and *Animalia* (Fig. 2.1A). Representatives from mammals, reptiles, amphibians, birds, fish, and ascidians were included in the cladogram, together with representatives from arthropods and molluscs (for a detailed comparison of animal Hvs, see ref. (19)). Phylogenetic analysis (Fig. S2.1) indicates the existence of Hv channels in all five major divisions of the *Fungi* kingdom and that Hvs from slime molds (protists) are more closely related to animal Hvs than their fungal counterparts. Hv representatives from gill mushrooms and molds seem to form two distinct groups. Therefore, we selected one candidate from each group for further investigation: Hv1 from *Suillus luteus* (SlHv1) and Hv1 from *Aspergillus oryzae* (AoHv1), which share 25.7 % sequence identity. Protein sequence analysis (see Methods) indicates a similar membrane topology and structural organization for SlHv1 and AoHv1 compared to animal Hvs (Fig. 2.1B). The S4 helix of the fungal channels carries positively charged residues typical of other voltage sensors. However, the S4 signature motif for mammalian Hvs is R·WR·R·N (where · is usually a hydrophobic residue), while the motifs for SlHv1 and AoHv1 are R·WR·K·G and R·WR·K·E, respectively. Additionally, the predicted CCD of AoHv1 is significantly shorter than the corresponding domain of SlHv1 and it is coupled directly to S4 without the linker region normally found in other Hvs (Fig. 2.1B, and Fig. S2.2).

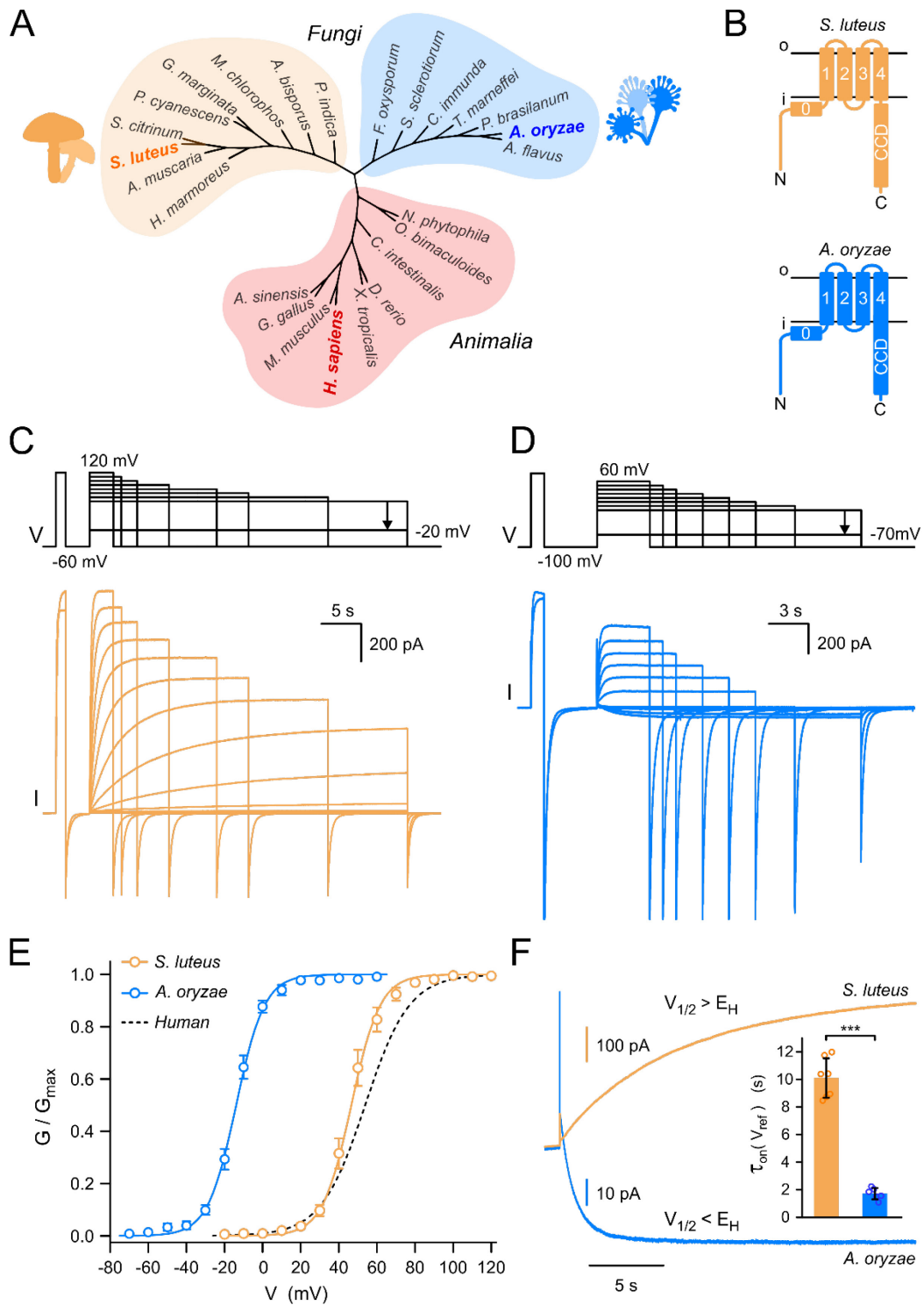


**Figure 2.1. Fungal Hv1s from species *S. luteus* and *A. oryzae* show distinct biophysical properties.** A) Unrooted cladogram places Hv1 channels of fungi into two large groups distinct from animal orthologs. B) Predicted topology of Hv1s from *S. luteus* and *A. oryzae* showing connections between C-terminal coiled-coil domains (CCD) and S4 transmembrane segment of different lengths. C-D) Representative proton currents from fungal Hv1s shown in (B) expressed in *Xenopus* oocytes and measured from inside-out patches ( $pH_i = pH_o = 6.0$ ). For clarity, only the first and last traces elicited by the depolarization pre-step are shown. E) Conductance versus voltage relationships ( $G$ -Vs) of SlHv1 and AoHv1 calculated from

current traces like those shown in (C-D). Curves are Boltzmann fits. For SlHv1,  $V_{1/2} = 46.5 \pm 2.3$  mV, slope =  $7.6 \pm 0.5$  mV; for AoHv1,  $V_{1/2} = -13.9 \pm 1.1$  mV, slope =  $7.4 \pm 0.9$  mV ( $n = 5$ ). Error bars are SEM. G-V for human Hv1 is shown as dashed line for reference ( $V_{1/2} = 53 \pm 3$  mV, slope =  $11.6 \pm 0.6$  mV, from Tombola et al. 2018). F) Representative activation currents of SlHv1 and AoHv1, each measured at a reference voltage ( $V_{ref}$ ) closest to their individual  $V_{1/2}$  ( $V_{ref} = 50$  mV for SlHv1 and  $-10$  mV for AoHv1).  $E_H$  indicates Nernst potential for protons, which in this case is 0 mV. Time constants of activation currents ( $\tau(V_{ref})$ ) are shown in inset as mean values  $\pm$  SEM ( $n = 7$  for SlHv1;  $n = 6$  for AoHv1). Welch's t-test was used for statistical analysis, \*\*\* $p < 0.001$ .

### ***Channel expression and voltage dependence of activation***

Having a structural organization similar to animal Hvs is not sufficient to predict proton channel activity, as previously shown with HVRP1/TMEM266, a membrane protein closely related to human Hv1 that does not function as a channel<sup>26,125,126</sup>. So, we expressed the fungal proteins in *Xenopus* oocyte and performed electrophysiological measurements in excised membrane patches (Fig. 2.1C-F). We were able to record robust voltage-dependent currents from both SlHv1 and AoHv1 using ionic conditions established for animal Hvs<sup>5</sup> with both intra- and extracellular media buffered at pH 6.0. Interestingly, the two proteins showed very different voltage ranges of activation and kinetic properties, with SlHv1 activating slowly, and at positive membrane potentials, and AoHv1 activating rapidly, and at negative membrane potentials (Fig. 2.1C-E). The conductance vs. voltage relationship (G-V) of SlHv1 was slightly left-shifted compared to the G-V of hHv1 (Fig. 2.1E,  $V_{1/2} = 46.5 \pm 2.3$  mV for SlHv1,  $V_{1/2} = 53 \pm 3$  mV for hHv1<sup>5</sup>), whereas the G-V of AoHv1 was strongly left-shifted (Fig. 2.1E,  $V_{1/2} = -13.9 \pm 1.1$  mV).

The two fungal channels also differed in their ability to conduct inward current, which depends on the relationship between the voltage range of activation and the Nernst potential for protons ( $E_H$ ). SlHv1 opens under electrochemical gradients that favor proton efflux, with  $V_{1/2} > E_H$  (Fig. 2.1F,  $I(V_{1/2}) > 0$ ), similar to what is observed with the large majority of Hvs from the animal kingdom<sup>21</sup>. AoHv1, on the other hand, opens when the electrochemical gradient favor proton influx, with  $V_{1/2} < E_H$  (Fig. 2.1F,  $I(V_{1/2}) < 0$ ). Besides being opposite in sign, the currents from SlHv1 and AoHv1 measured at a reference voltage  $V_{ref} \approx V_{1/2}$  reached steady-state level at

different rates. To quantify the difference, we fitted the currents with a single-exponential function. From the comparison of the relative time constants  $\tau_{\text{on}}(V_{\text{ref}})$ , we concluded that AoHv1 is ~6 fold faster than SlHv1 (Fig. 2.1F, bar graph). As previously observed with animal Hvs<sup>21</sup>, the time course of activation of SlHv1 and AoHv1 showed a time lag between the beginning of the depolarization and the rising phase of the current (Fig. S2.3A-B), suggesting that transitions between multiple closed states take place before the opening transition. The initial lag phase was more than one order of magnitude shorter than  $\tau_{\text{on}}$  and was excluded from our exponential fits of the currents (Fig S2.3A-B).

Animal Hvs are homodimers<sup>5-7</sup> in which the two subunits gate cooperatively<sup>44,124,127</sup>. Earlier studies found that the CCD plays a critical role in Hv dimerization<sup>5,6</sup> and that the lag phase in the time course of activation is a characteristic of the dimeric state as it disappears in monomerized channels<sup>128</sup>. The presence of the CCD in fungal Hvs and the lag phase in their currents suggest that these channels could be also made of multiple subunits. To further investigate this possibility, we estimated the gating charge associated with SlHv1 and AoHv1 activation ( $z_g$ ) using the limiting slope method<sup>120,121</sup>. We found that  $z_g$  was ~ 5 for both channels (Fig. S2.3C-E). Similar values were previously obtained for animal Hvs<sup>44,127</sup>. Based on the number of positively-charged residues located in the S4 helix of both animal and fungal Hvs, each subunit is expected to contribute up to 3 gating charges to the activation process. Hence, a  $z_g > 3$  indicates that more than one subunit is involved in cooperative activation.

### ***Proton selectivity of fungal Hvs***

It is well established that Hv channels from the animal kingdom have almost perfect proton selectivity<sup>3,4,21</sup>. So, we set out to determine whether SlHv1 and AoHv1 share the same characteristic. We measured the current reversal potential ( $V_{\text{rev}}$ ) under different transmembrane pH gradients ( $\Delta\text{pH} = \text{pH}_o - \text{pH}_i$ ), and compared it to the corresponding  $E_{\text{H}}$  (Fig

2.2). Currents were recorded from inside-out patches at different membrane potentials after a pre-depolarization step to 100 mV to open the channels (Fig. 2.2A, C). The intercept on the V axis was then plotted as a function of  $\Delta\text{pH}$  (Fig. 2.2B, D) and compared to the relationship  $E_H = -58.9\Delta\text{pH}$ , describing perfect proton selectivity (see Methods). Under the tested conditions, both SlHv1 and AoHv1 behaved similarly to animal Hvs suggesting that the mechanism of proton selection is conserved between animal and fungal Hvs. This finding is in agreement with the presence of a highly conserved aspartate at the center of the S1 helix in all fungal Hvs. That residue corresponds to D112 in hHv1 (Fig. S2.2A), which is known to be part of the proton selectivity filter<sup>26-29</sup>.

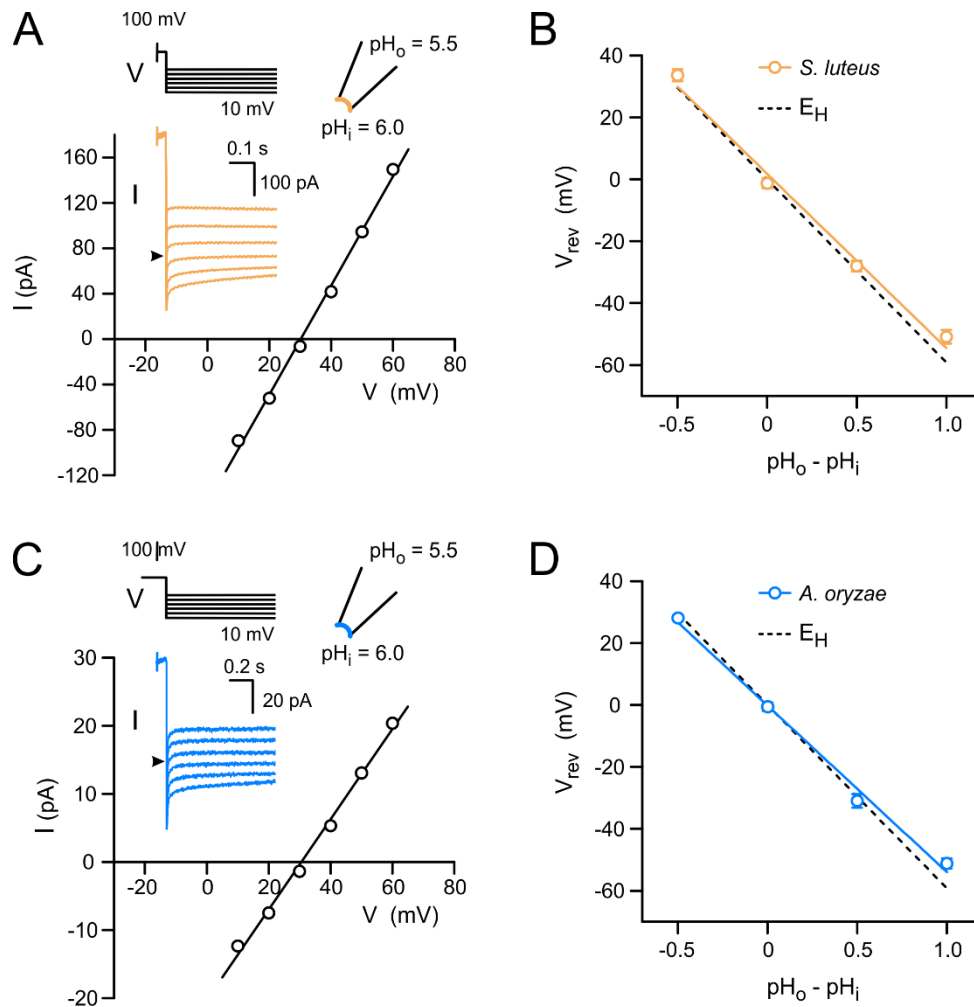


**Figure 2.2.** Hv1s from *S. luteus* and *A. oryzae* are proton selective. **A)** Example of measurement of reversal potentials ( $V_{\text{rev}}$ ) for SlHv1-mediated currents in the presence of a transmembrane pH gradient ( $\Delta\text{pH} = \text{pH}_o - \text{pH}_i$ ) of 0.5. Currents were measured at the indicated voltages after a depolarization step to

100 mV. Black arrowhead in inset indicates 0 pA. **B)**  $V_{rev}$  as a function of  $\Delta\text{pH}$ ; slope of liner fit:  $56 \pm 4$  mV/pH unit.  $E_H$ , displayed in dashed line, is the Nernst potential for protons and indicates perfect proton selectivity (slope: 59 mV/pH unit). **C)** Same as (A) but for AoHv1. **D)** Same as (B) but for AoHv1; slope of liner fit:  $54 \pm 3$  mV/pH unit.  $\Delta\text{pH}$  of -0.5, 0, 0.5, and 1, in (B) and (D) correspond to the following ( $\text{pH}_i$ ,  $\text{pH}_o$ ) pairs: (6.5, 6.0), (6.0, 6.0), (6.0, 6.5), and (5.5, 6.5), respectively. Each point in (B) and (D) represents the average of 3-4 independent measurements  $\pm$  SEM. Error bars are not shown where smaller than symbols.

### ***pH dependence of channel gating***

A ubiquitous feature of animal Hv channels is that their voltage dependence of activation shifts around 40 mV per unit of  $\Delta\text{pH}$ , known as the “rule of forty”<sup>21</sup>. This rule is often linked to the inability of most Hv channels to allow proton influx upon activation, because changing  $\Delta\text{pH}$  to values that would favor proton influx also shifts the voltage dependence of activation to more depolarized potentials, making the channel more difficult to open. Because AoHv1 was found to allow robust proton influx (Fig. 2.1D, F), we asked whether the fungal channels follow the rule of forty.

As commonly done with animal Hvs, we measured current vs. voltage (I-V) relationships under different  $\Delta\text{pH}$  conditions for SlHv1 (Fig. 2.3A-B) and AoHv1 (Fig. 2.3E-F). We changed  $\Delta\text{pH}$  by one positive or negative unit ( $\Delta\Delta\text{pH} = 1$  or  $-1$ , respectively), by perfusing intracellular solutions at different pH. We observed shifts in the threshold of activation that far exceeded the expected 40 mV per  $\Delta\text{pH}$  unit. The downward vertical arrows in Fig. 2.3A-B and Fig. 2.3E-F indicate the  $V_{\text{threshold}}$  (defined as the voltage at which proton current is first observed) that would be expected if the fungal channels followed the general relationship between  $V_{\text{threshold}}$  and  $\Delta\text{pH}$  previously derived from 15 different cell types expressing animal Hvs<sup>18</sup>. Both SlHv1 and AoHv1 deviate significantly from the rule of forty. But, SlHv1 carried outward currents under all tested conditions, whereas AoHv1 carried massive inward currents when  $\text{pH}_i$  was lower than  $\text{pH}_o$ . Its voltage dependence of activation was shifted to such hyperpolarized potentials that closing the channel completely became a challenge (Fig. 2.3E, gray trace).

To better quantify the shifts in voltage dependence of activation caused by changes in pH

gradient, normalized G-V curves were derived from I-V curves (see Methods) (Fig. 2.3C-D & G-H) and the relative shifts in  $V_{1/2}$  was plotted as a function of  $\Delta\Delta\text{pH}$  (Fig. 2.3I). The resulting  $\Delta V_{1/2}$  were in the order of 80-90 mV per  $\Delta\text{pH}$  unit. We also measured  $V_{1/2}$  as a function of pH under conditions in which  $\text{pH}_i = \text{pH}_o$  (Fig. 2.3J-K), expecting no change as long as  $\Delta\text{pH}$  remained constant, as previously observed with most animal Hvs<sup>21</sup>. AoHv1 did meet this expectation, with little change in  $V_{1/2}$  within the 5.5 - 6.5 pH range (Fig. 2.3K). However, SlHv1 showed a clear pH dependence within the same pH range (Fig. 2.3J), with a  $\Delta V_{1/2}$  of ~18 mV per pH unit.

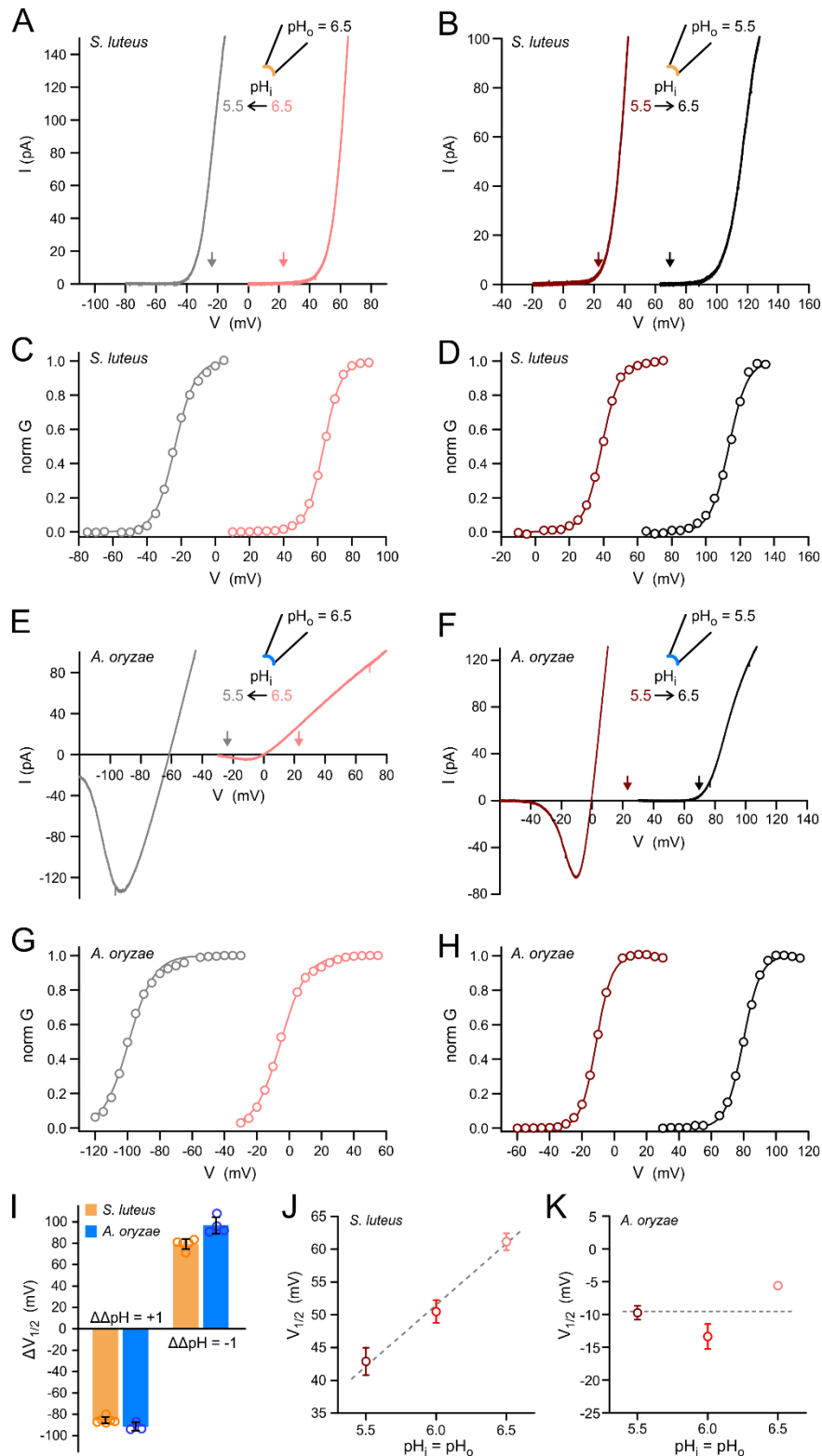


**Figure 2.3. Gating of fungal Hv1s is strongly  $\Delta pH$  dependent.** **A)** Change in I-V relationship for SIHv1 in response to change in  $\Delta pH$  from 0 to +1. **B)** Change in I-V relationship for SIHv1 in response to change in  $\Delta pH$  from 0 to -1. Currents in (A) and (B) were measured at the indicated  $\Delta pH$  in inside-out patches. Voltage was changed using ramp protocols described in Methods. Arrows represent the voltages at which

the SLHv1 should start conducting measurable current ( $V_{\text{threshold}}$ ) if the channel followed the general behavior of animal Hv1 channels (see main text), with shifts following the “rule of forty”. The colors of the arrows reflect the corresponding  $\Delta\text{pH}$  conditions. **C-D**) G-V relationships derived from I-V curves in (A) and (B), respectively (see Methods). **E-F**) same as (A) and (B) but for AoHv1. **G-H**) G-V relationships derived from I-V curves in (E) and (F), respectively. **I**) Average shifts in  $V_{1/2}$  as a function of change in  $\Delta\text{pH}$  ( $\Delta\Delta\text{pH}$ ) measured from G-Vs, like the ones shown in (C-D) and (G-H). Each bar represents the mean of 3 to 7 independent measurements  $\pm$  SEM. **J**)  $V_{1/2}$  of G-Vs from SLHv1 as a function of pH under symmetrical conditions ( $\Delta\text{pH} = 0$ ). Each point represents the mean of 5 to 6 independent measurements. Error bars are SEM. Dashed line is the linear fit of the data with slope =  $19 \pm 2$  mV/pH unit. **K**) Same as (J) but for AoHv1. Each point represents the mean of 3 to 4 independent measurements. Error bars (SEM) are not shown where smaller than symbols. Data are consistent with insensitivity to pH when  $\Delta\text{pH} = 0$ , shown as dashed line.

### ***Mechanosensitivity***

Mechanical stimulation has been shown to facilitate activation of human Hv1<sup>56</sup>. A rise in membrane tension increases both the amount of steady-state current generated by membrane depolarization (potentiation) and the rate of activation (acceleration). Once the channel has been mechanically stimulated it remains in a facilitated state for several minutes<sup>56</sup>. A simple two-pulse protocol can be used to assess both potentiation and acceleration. In this protocol, membrane tension is transiently increased between the two depolarization pulses by transient application of negative pressure to the patch pipette using a high-speed pressure clamp (HSPC). The current elicited by the depolarizing pulse that follows the mechanical stimulus can then be compared with the current elicited by the control pulse that precedes the increase in membrane tension (Fig. S2.4). We applied this protocol to both SLHv1 (Fig. S2.4A) and AoHv1 (Fig. S2.4B) and compared their behavior to hHv1. We found that potentiation was larger in SLHv1 compared to both AoHv1 and hHv1 (Fig. S2.4C), while acceleration was similar in the two fungal channels and smaller than the acceleration in hHv1 (Fig. S2.4C). Of the compared channels, AoHv1 was the least affected by the increase in membrane tension, which is in agreement with its voltage dependence and kinetics of activation. The channel opens readily even in the absence of the mechanical stimulus, making its activation more difficult to further facilitate.

## ***Pharmacology***

Human Hv1 is a potential pharmacological target for the treatment of a variety of diseases<sup>36,91-93,129</sup>. Several compounds that can inhibit the channel have been identified. These include guanidine derivatives 2GBI and ClGBI, which have an intracellular binding site<sup>94,130</sup>, and zinc ions, which bind the channel from the extracellular side<sup>3,4,86,88,89</sup>. We tested these inhibitors on fungal Hvs because they have a broad spectrum, i.e., they work on human Hv1 as well as on Hvs from other animal species. All compounds were delivered by perfusion of the bath solution during patch-clamp recordings (Fig. 2.4A). 2GBI and ClGBI were tested at concentrations of 200  $\mu\text{M}$  and 20  $\mu\text{M}$ , respectively, on inside-out patches with both intra- and extracellular pH at 6.0.  $\text{Zn}^{2+}$  was tested at a concentration of 100  $\mu\text{M}$  on outside-out patches. In this case, the extracellular pH was raised to 7.0 because less acidic conditions were previously shown to strengthen  $\text{Zn}^{2+}$  binding to animal Hvs<sup>86</sup>. At the concentrations tested, all inhibitors reduced the proton current from hHv1 of at least 80%.

Both fungal Hvs were substantially inhibited by 2GBI and ClGBI, but AoHv1 was inhibited more effectively by the two compounds (Fig. 2.4B). SlHv1 was inhibited less than hHv1, particularly by ClGBI (~50% vs. >90% inhibition, respectively). The effects of the inhibitors on AoHv1, on the other hand, were similar to those observed with hHv1 (Fig. 2.4B).  $\text{Zn}^{2+}$  inhibited both fungal channels very poorly (Fig. 2.4C-D). While the human channel was inhibited almost 100%, AoHv1 and SlHv1 were inhibited less than 60% and 20%, respectively (Fig. 2.4E). The  $\text{Zn}^{2+}$  concentration needed to be lowered to 0.5  $\mu\text{M}$  in order for the extent of inhibition of hHv1 to be comparable with the extent of inhibition of the fungal channels (Fig. 2.4D, lower traces, and Fig. 2.4E).

2GBI and ClGBI are known to inhibit hHv1 by binding the open channel and preventing proton flow<sup>93,94</sup>. Conversely,  $\text{Zn}^{2+}$  inhibits animal Hvs by binding preferentially the closed channel and making it more difficult to open<sup>86</sup>. As a result, the rate of channel opening is unaffected by

2GBI and ClGBI, but it is strongly reduced by  $Zn^{2+}$ . The slower opening of hHv1 in the presence of  $Zn^{2+}$  can be observed in the lower panel of Fig. 2.4D. To assess the effect of  $Zn^{2+}$  on the kinetics of channel opening in the fungal and human Hvs, the proton currents measured before (-) and after addition of the inhibitor (+) were fitted by single-exponential functions. The time constants from the fits were then used to determine the ratios  $\tau_{on(+)} / \tau_{on(-)}$  (Fig. 2.4F). Ratios higher than 1 indicate  $Zn^{2+}$ -induced deceleration of channel opening.

The deceleration was somewhat more pronounced in AoHv1 compared to SlHv1 (Fig. 2.4F). Fungal and human Hvs could not be compared at  $100 \mu M Zn^{2+}$  because the remaining currents for hHv1 at this concentration were too small to fit. Nonetheless, the deceleration observed with hHv1 at  $0.5 \mu M Zn^{2+}$  was an order of magnitude higher than the deceleration observed with AoHv1 at  $100 \mu M Zn^{2+}$ , (Fig. 2.4F). Considering that  $0.5 \mu M$  and  $100 \mu M Zn^{2+}$  produce similar levels of inhibition in hHv1 and AoHv1, respectively (Fig. 2.4E), the large difference in deceleration of the opening process suggests that  $Zn^{2+}$  interacts with fungal Hvs in a way that is distinct from the interaction with hHv1.

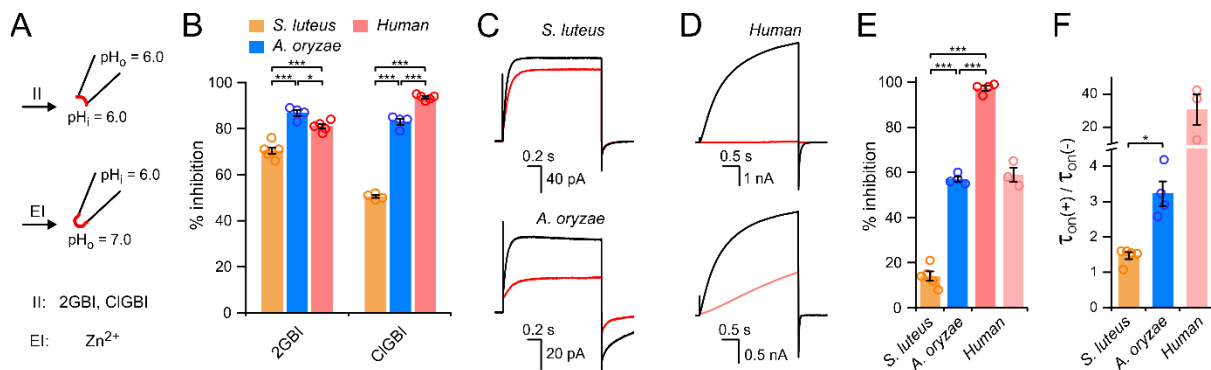


**Figure 2.4. Pharmacological characteristics of Hv1s from *S. luteus* and *A. oryzae*.** **A)** Schematics of conditions used to test intracellular and extracellular Hv1 inhibitors (II and EI, respectively) 2GBI and ClGBI were perfused on inside-out patches.  $Zn^{2+}$  was perfused on outside-out patches. **B)** Inhibition of AoHv1 and SlHv1 by  $200 \mu M$  2GBI and  $20 \mu M$  ClGBI. Currents were measured in response to depolarization steps to  $80 mV$ ,  $pH_i = pH_o = 6.0$  (see Methods). Each bar represents the average inhibition from at least 4 independent measurements  $\pm$  SEM. **C)** Representative current traces for SlHv1 (top) and AoHv1 (bottom) in response to voltage steps to  $60 mV$  in the absence (black) or presence (red) of  $100 \mu M ZnCl_2$  in the bath solution.  $pH_i = 6.0$ ,  $pH_o = 7.0$ . **D)** Representative current traces of hHv1 measured in response to voltage steps to  $60 mV$  in the absence (black) or presence of either  $100 \mu M ZnCl_2$  (red trace, top panel) or  $0.5 \mu M ZnCl_2$  (pale-red trace, bottom panel) in the bath solution.  $pH_i = 6.0$ ,  $pH_o = 7.0$ . **E)** Quantification

of the inhibition of the indicated channels by 100  $\mu\text{M}$   $\text{Zn}^{2+}$  (conditions as in C-D). Paler-red bar refers to the effect of 0.5  $\mu\text{M}$   $\text{Zn}^{2+}$  on hHv1. Each bar represents the average inhibition from 3 to 5 independent measurements  $\pm$  SEM. F) Changes in activation kinetics induced by  $\text{Zn}^{2+}$  for the indicated channels.  $\tau_{\text{on}}$  values were derived from single-exponential fits of current traces in the absence (-) and presence (+) of the inhibitor (conditions as in C-D). Each bar represents the average  $\tau_{\text{on}(+)}/\tau_{\text{on}(-)}$  ratio from at least 3 independent measurements  $\pm$  SEM. The data for SlHv1 and AoHv1 refer to 100  $\mu\text{M}$   $\text{Zn}^{2+}$ . The data for hHv1 refer to 0.5  $\mu\text{M}$   $\text{Zn}^{2+}$ . A one-way ANOVA with Tukey's post-hoc test was used for statistical analysis: \* $p < 0.05$ , \*\* $p < 0.01$ , \*\*\* $p < 0.001$ .

### ***Role of intra- and extracellular regions in gating modulation***

Surprised by the large difference in kinetics and voltage dependences of activation between the two fungal Hvs, we wondered whether amino acid sequence comparison, guided by structural information from homology modeling, could point to divergent regions in the two proteins responsible for the different functional properties. We constructed a homology model of SlHv1, based on the available crystal structures of mHv1cc<sup>9</sup>, a chimera between mouse Hv1 and the voltage-sensitive phosphatase CiVSP, and the isolated CCD from mouse Hv1<sup>44</sup>. Figure 2.5A shows the model representing one subunit of the homodimeric channel. From a sequence alignment of SlHv1 and AoHv1, we derived a scale of sequence divergence, defined as deviation from average similarity (see Methods), and converted it into a color gradient scale (blue to red), which we then mapped on the SlHv1 homology model. To assess the extent to which spatial patterns of high divergence on the map depends on the modeling template, we mapped the scale on an additional homology model based on the VSD structure of CiVSP<sup>46</sup>, Fig. S2.5.

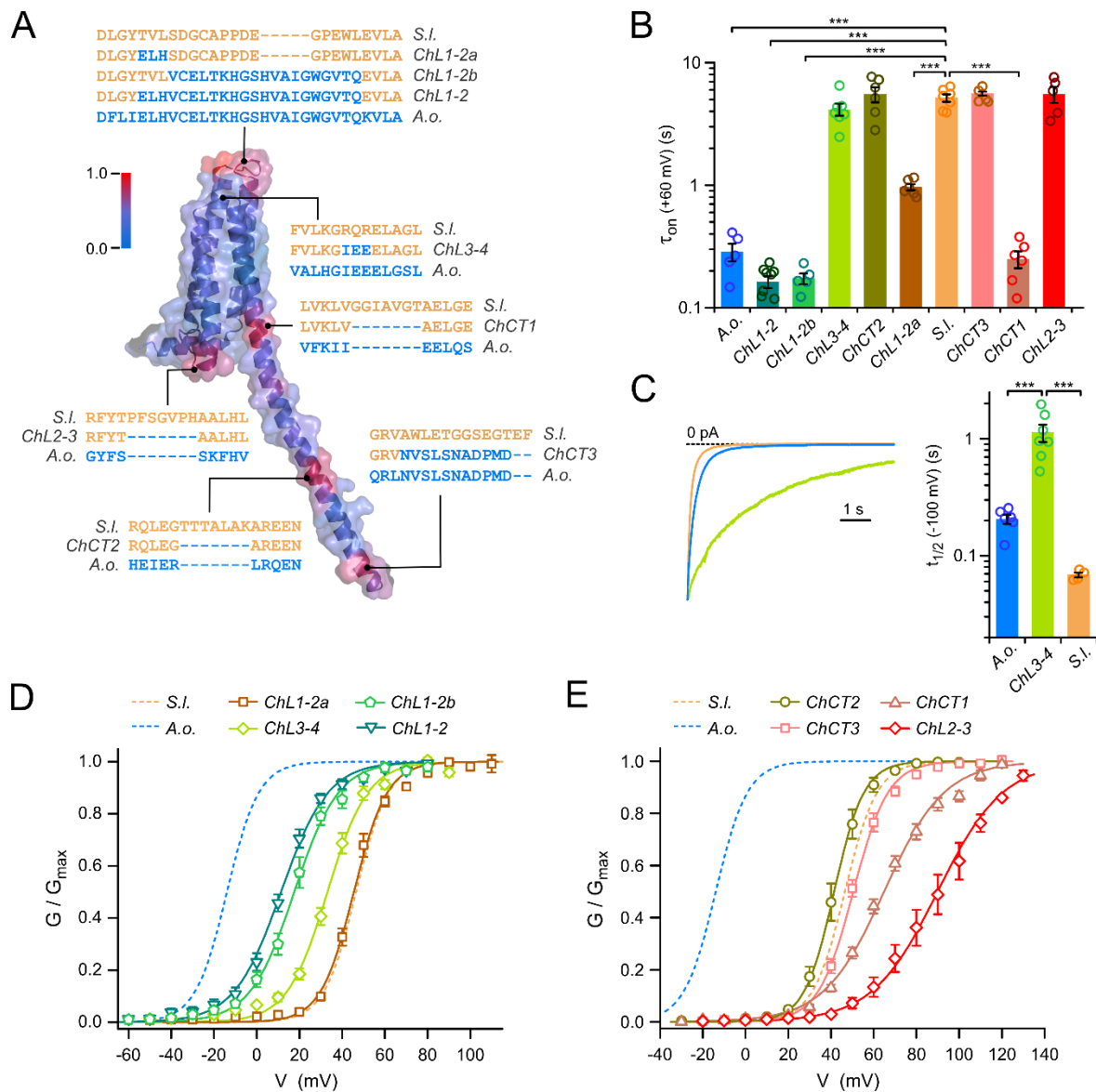


**Figure 2.5. Swapping parts of SIHv1 with AoHv1 reveals regions with important role in channel activation.** **A)** Structural model of SIHv1 (a.a. 25 - 221) based on crystal structures 3WKV and 3VMX. Color of surface and cartoon representations indicates divergence in sequence homology between SIHv1 and AoHv1. Gradient varies from minimal divergence (blue) to maximal divergence (red) (see methods for details). Swapped sequences in the eight SIHv1-AoHv1 chimeras: ChL1-2, ChL1-2a, ChL1-2b, ChL2-3, ChL3-4, ChCT1, ChCT2, ChCT3 are shown with their positions within the channel structure. **B)** Bar graph compares kinetics of activation of chimeric and wild type proteins. Proton currents from the indicated channels were measured in response to membrane depolarization to 60 mV and fitted with a single exponential function with time constant  $\tau_{on}$ . Bars are means  $\pm$  SEM ( $n = 5 - 9$ ). A one-way ANOVA with Tukey's post-hoc test was used for statistical analysis:  $***p < 0.001$ . Only comparison with SIHv1 are shown. **C)** Chimera ChL3-4 shows significant slowdown of deactivation compared to SIHv1 and AoHv1. Representative tail currents for ChL3-4, SIHv1, and AoHv1 measured at -100mV after channel activation. Bar graph quantifies half deactivation times ( $t_{1/2}$ ) for the three channels. A one-way ANOVA with Tukey's post-hoc test was used for statistical analysis:  $***p < 0.001$ . **D)** Voltage dependences of chimeras with swapped extracellular regions compared to references SIHv1 and AoHv1. Each  $G$ - $V$  relationship represents the mean of 5 to 9 independent measurements. Error bars are SEM. The following  $G$ - $V$  parameters were derived from Boltzmann fits of the data:  $V_{1/2} = 45.5 \pm 1.3$  mV, slope =  $7.8 \pm 0.3$  mV for Ch1-2a ( $n = 6$ ),

$V_{1/2} = 17.6 \pm 2.0$  mV, slope =  $10.3 \pm 0.7$  mV for ChL1-2b (n = 5),  $V_{1/2} = 11.4 \pm 1.4$  mV, slope =  $11.0 \pm 1.1$  mV for ChL1-2 (n = 9),  $V_{1/2} = 33.1 \pm 1.4$  mV, slope =  $9.4 \pm 0.6$  mV for ChL3-4 (n = 7). **E**) Voltage dependences of chimeras with swapped intracellular regions compared to reference SlHv1 and AoHv1. Each G-V relationship represents the mean of 5 to 6 independent measurements. Error bars are SEM. The following G-V parameters were derived from Boltzmann fits of the data:  $V_{1/2} = 64.9 \pm 1.7$  mV, slope =  $17.1 \pm 0.8$  mV for ChCT1 (n = 6),  $V_{1/2} = 41.5 \pm 2.1$  mV, slope =  $7.0 \pm 0.4$  mV for ChCT2 (n = 6),  $V_{1/2} = 50.5 \pm 1.2$  mV, slope =  $8.2 \pm 0.4$  mV for ChCT3 (n = 6),  $V_{1/2} = 90.0 \pm 3.9$  mV, slope =  $15.3 \pm 1.7$  mV for ChL2-3 (n = 5). All measurements were performed at  $\text{pH}_i = \text{pH}_o = 6.0$ .

The core of the channel, formed by transmembrane helices S1 through S4, was the most conserved part of the two proteins in both models. In contrast, multiple intracellular and extracellular peripheral regions showed hotspots of sequence divergence (Fig. 2.5A and Fig. S2.5), including the S1-S2, and S3-S4 extracellular loops, the S2-S3 intracellular loop, the terminal region of S4 connecting the VSD to the CCD, and the central and C-terminal parts of the CCD (the model based on CiVSP was limited to the VSD as the original protein does not contain a CCD). A comparison between the two homology models showed local differences in all the divergent regions and, in particular, in the region containing the S2-S3 loop (Fig. S2.5). However, the overall pattern of divergent regions was the same in the two models.

Since AoHv1 has functional properties that set it apart from other known Hvs, we tested whether replacing any individual divergent region of SlHv1 with the corresponding region of AoHv1 could transfer some of these unique properties to the resulting chimeric channel. We generated eight such chimeras, ChL1-2, ChL1-2a, ChL1-2b, ChL2-3, ChL3-4, ChCT1, ChCT2, ChCT3 (Fig. 2.5A) and compared the kinetic properties of their currents and voltage-dependence of activation (G-Vs) to those of the parent proteins AoHv1 and SlHv1.

We found that multiple chimeras had accelerated activation kinetics with  $\tau_{\text{on}}$  values similar to AoHv1 (Fig. 2.5B), these included the channels in which the swapped regions were in the S1-S2 loop (ChL1-2, ChL1-2a, ChL1-2b) or in the S4-CCD linker (ChCT1). On the other hand, none of the chimeras displayed slower activation compared to SlHv1 (Fig. 2.5B). Because the deactivation kinetics of Hv channels have more than one exponential component<sup>131</sup>, we measured the half deactivation time ( $t_{1/2}$ , see Methods) to simplify the comparison between

chimeras and parent proteins. For most chimeras,  $t_{1/2}$  values were either similar to SlHv1 or smaller (faster deactivation). A notable exception was ChL3-4, in which a swap within the S3-S4 loop produced a dramatic increase in  $t_{1/2}$ , indicating a deactivation much slower than the deactivation of both SlHv1 and AoHv1 (Fig. 2.5C).

Most of the channels with chimeric extracellular regions exhibited G-V curves shifted to more negative potentials compared to SlHv1 (Fig. 2.5D), whereas most channels with chimeric intracellular regions had G-V shifted to more positive potentials (Fig. 2.5E). The extracellular region between S1 and S2 was the most effective at transferring AoHv1 properties to SlHv1. The G-V curve of ChL1-2 was shifted -35 mV compared to SlHv1, bringing the voltage dependence of activation closer to AoHv1 than SlHv1 (Fig. 2.5D) mostly via a strong acceleration of channel opening (Fig. 2.5B). In ChL1-2, both the outermost part of the S1 helix and the S1-S2 loop are from AoHv1. To determine which of these two structural components was responsible for the AoHv1-like properties, we swapped them individually in chimeras ChL1-2a and ChL1-2b. ChL1-2a was accelerated compared to SlHv1 (Fig. 2.5B), but its voltage dependence of activation was the same as SlHv1 (Fig. 2.5D). ChL1-2b, on the other hand, was more accelerated (Fig. 2.5B) and its G-V curve was shifted -29 mV compared to SlHv1, pointing to the region containing the S1-S2 loop as the component with the largest contribution to the activation properties of the chimera. The G-V curve of the ChL3-4 chimera was also shifted to more negative potentials compared to SlHv1 (Fig. 2.5D,  $\Delta V_{1/2} = -13$  mV). But the shift was caused by a deceleration of channel closing rather than an acceleration of channel opening (Fig. 2.5B, C).

Because the opening and closing processes were differentially affected in ChL1-2b and ChL3-4, we tested whether the effects were additive by examining the chimera ChL1-2b+L3-4 in which both extracellular regions are swapped (Fig. 2.6A). The G-V curve of the combination chimera was shifted -34 mV compared to SlHv1, similar to the G-V shift observed with ChL1-2b alone,

indicating that the swap in the S1-S2 loop had a dominant effect. Consistent with this observation, the activation of ChL1-2b+L3-4 was accelerated compared to SlHv1 (Fig. 2.6B, left), and its deactivation was not slowed down (no increase in  $t_{1/2}$ , Fig. 2.6B, right). The G-V curve of ChL1-2b+L3-4 appeared to span a significantly wider voltage range than the G-V curves of the parent proteins AoHv1 and SlHv1. As a result, the chimeric channels started opening within the voltage range of activation of AoHv1 (Fig. 2.6A, blue-shadowed area), but maximal conductance was reached within the voltage range of activation SlHv1 (Fig. 2.6A, orange-shadowed area).

Of the chimeras with swapped C-terminal regions, the G-V curves of ChCT2 and ChCT3 were similar to the G-V curve of SlHv1 ( $\Delta V_{1/2}$  within  $\pm 5$  mV) with no significant changes in activation rates (Fig. 2.5B,E). However, the G-V curve of ChCT1 was shifted to more positive potentials compared to SlHv1 ( $\Delta V_{1/2} = 18$  mV) despite a strong acceleration of channel opening (Fig. 2.5B,E). Finally, the chimera with the swap within the intracellular S2-S3 loop, ChL2-3, exhibited a G-V curve with a large positive shift (Fig. 2.5E,  $\Delta V_{1/2} = 43$  mV) bringing the overall range of modulation of the SlHv1 voltage dependence of activation by peripheral regions to a remarkable 72 mV ( $\Delta V_{1/2}$  range between ChL1-2b and ChL2-3).

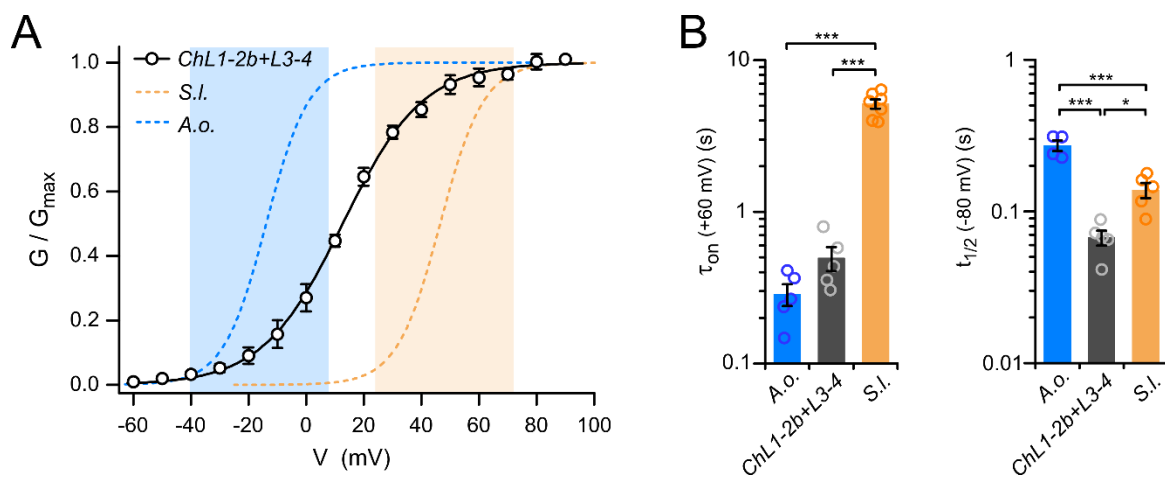


**Figure 2.6. Activation properties of Sl/AoHv1 chimeric channel with combined swaps in S1-S2 and S3-S4 loops.** A) G-V curve of ChL1-2b+L3-4 chimera compared to parent channels SlHv1 and AoHv1 ( $pH_i = pH_o = 6.0$ ). Conductance of chimera starts increasing within the voltage range of AoHv1 activation

(blue-shaded area) and reaches maximum within the voltage range of SlHv1 activation (orange-shaded area). G-V parameters derived from Boltzmann fit of the data are:  $V_{1/2} = 12.7 \pm 1.7$  mV, slope =  $13.9 \pm 1.3$  mV (n = 5). **B)** Time constant of activation ( $\tau_{on}$ ) and half-maximal deactivation time ( $t_{1/2}$ ) of ChL1-2b+3-4 compared to parent channels SlHv1 and AoHv1.  $\tau_{on}$  was measured at 60 mV and  $t_{1/2}$  was measured at -80 mV. Bars are mean values from 4-5 independent measurements  $\pm$  SEM. A one-way ANOVA multiple comparison test with Tukey's post-hoc correction was used for statistical analysis: \*p < 0.05, \*\*\*p < 0.001.

SlHv1 and AoHv1 differ in their pH dependence under symmetrical conditions. The G-V relationship for SlHv1 shifts approximately 18 mV per pH unit, whereas the G-V relationship for AoHv1 is insensitive to pH under the same conditions (Fig. 2.3J-K). Previous comparative studies on animal Hvs identified a potential pH<sub>i</sub> sensor located in the S2-S3 loop<sup>24</sup>. At the corresponding position, SlHv1 contains a 7-residue insertion which is missing in AoHv1 and in the ChL2-3 chimera (which is otherwise identical to SlHv1). Thus, we examined whether the G-V curve of the ChL2-3 channel was sensitive to pH under symmetrical conditions. Due to low expression, we were unable to perform the measurements at pH > 6.0, but we were able to compare pH 5.5 and 6.0 (Fig. S2.6). We found that, as observed with AoHv1, the G-V curve did not shift between pH 5.5 and 6.0 in the chimera, while it shifted ~7.6 mV in SlHv1, under the same conditions (Fig. 2.3J). These data suggest that the 7-residue insertion in the S2-S3 loop is responsible for the different pH sensitivity between SlHv1 and AoHv1 in the absence of a transmembrane pH gradient.

## 2.4 Discussion

Electricity is a key element for growth and development in various types of organisms including fungi. Action potential-like spikes, occurring spontaneously or triggered by cyanide, were first reported in the water mold *Neurospora crassa* in the '70s<sup>23,132</sup>. Similar electrical signals were subsequently recorded in other fungi species, from gill mushrooms to filamentous fungi<sup>133,134</sup>. Transcellular electric currents, ubiquitous among mycelial fungi, enter the tips of the hyphae

and exits their distal regions and are critical for hyphal polarization and branching<sup>135-137</sup>. They are also associated with material transfer and hydraulic pressure<sup>138</sup>. These currents have been shown to be carried primarily by protons in *N. crassa* and many other types of fungi<sup>137,139</sup>.

Proton transport is essential for fungi beyond the regulation of pH and membrane potential, yet only the H<sup>+</sup>-ATPase Pma1 from the plasma membrane is clearly described in this context, along with the PacC/Rim signaling transduction pathway<sup>140</sup>. The identification of members of the Hv channel family in all five major phyla of the fungi kingdom (*Ascomycota*, *Basidiomycota*, *Chytridiomycota*, *Zygomycota*, and *Glomeromycota*, Fig. S2.1) suggests that these proteins are ubiquitous components of proton transport mechanisms in fungi. The different biophysical characteristics of SlHv1 and AoHv1, and in particular the large difference in voltage range of activation, provide clues on possible physiological functions of these channels. SlHv1 opens only when the electrochemical gradient favors outward H<sup>+</sup> movement and so it is similar in behavior to the large majority of animal Hvs that act as proton extruders and counteract intracellular acidification and membrane depolarization caused by NOX enzymes<sup>25,102,103</sup>. Conversely, AoHv1 opens when the electrochemical gradient favors inward H<sup>+</sup> movement and so it can produce intracellular acidification and membrane depolarization. The only known Hv with a similar behavior is the channel from the dinoflagellate *Karlodinium veneficum* (kHv1)<sup>19</sup>. Dinoflagellates are well known for their ability to emit flashes of light thanks to cytoplasmic structure called scintillons. Hv channels like kHv1 are believed to be responsible for the initiation of the action potential that triggers the bioluminescent process within the scintillon<sup>141,142</sup>. Similarly, AoHv1 could provide the depolarizing current driving action potential-like spikes in molds<sup>132,133</sup>. However, the unprecedented range of modulation of voltage dependent activation by the transmembrane pH gradient observed in AoHv1 ( $\Delta V_{1/2} = \sim 90 \text{ mV}/\Delta\text{pH unit}$ , Fig. 2.3G-I) indicates that the channel can also work as a proton extruder under the appropriate conditions. As a result, some of AoHv1 functions could overlap with those of exclusive proton extruders like

SIHv1.

A large number of fungi are pathogenic to human, wildlife, or agricultural products. The phylogenetic tree of Fig. S2.1 includes representatives from *Rhodotorula spp.*, *Basidiobolus spp.*, *Sporothrix spp.*, *Fusarium spp.*, *Absidia spp.*, *Cladophialophora spp.*, *Talaromyces spp.* and *Thielavia spp.*, which can infect the human skin, respiratory and gastrointestinal tracts, bloodstream, eyes, and brain, as well as representatives from species like *Rhizopus*, *Sclerotinia*, and *Verticilium*, which are pathogenic to crops and cultivars such as maize, rice, sunflower, canola, and cruciferous vegetables. The ability of fungi to adapt to a wide range of pHs and to actively modify the pH in their surroundings makes them extremely difficult to eliminate. Drugs targeting fungal Hvs could provide new tools to study the functions of these channels *in vivo* and to fight mycotic infections.  $Zn^{2+}$  -mediated inhibition has an important role in the physiology of animal Hvs<sup>143</sup> and has been used as a pharmacological tool to study these channels<sup>144</sup>. In contrast, fungal Hvs are particularly resistant to this inhibitor (Fig. 2.4C-F). The lack of histidine residues corresponding to those proposed to coordinate  $Zn^{2+}$  in animal Hvs<sup>4,21</sup> (e.g., H140 and H193 in human Hv1, Fig. S2.2A) is likely to be responsible for the low  $Zn^{2+}$  sensitivity of fungal channels. On the other hand, guanidine derivatives, such as 2GBI and ClGBI, are more likely to be useful against fungal Hvs. These compounds were able to substantially inhibit SIHv1 and AoHv1 in the same concentration range used for hHv1 (Fig. 2.4A-B). The small but significant differences in inhibition observed between the fungal Hvs suggest that the compounds could be further optimized to enhance selectivity. Fungal Hvs are highly conserved between species of an individual genus. As a result, the pharmacological characteristics of AoHv1 described here are likely to be shared by Hvs from other *Aspergillus spp.*, including *Aspergillus flavus*, a well-known human pathogen (AfHv1 differs from AoHv1 only by one amino acid, Fig. S2.1).

Upon membrane depolarization, the VSD of Hv channels undergoes conformational changes that

result in gate opening and proton conduction<sup>38,48,145</sup>. Rearrangement in the S1 and S4 helices were shown to play critical roles in this process<sup>48,146</sup>. The activation gate is thought to be located within the transmembrane part of the VSD<sup>93</sup> and little is known about the participation of intra- and extracellular peripheral regions in channel gating. Earlier studies found that the CCD mediates cooperative activation of the two channel subunits<sup>5-7</sup>, while portions of the N-terminal region and loop connecting S2 and S3 contribute to intracellular pH sensitivity<sup>22,24</sup>. The N-terminal region of human Hv1 was shown to be differentially processed, leading to distinctive internalization between isoforms<sup>79</sup>, and to harbor a site for PKC phosphorylation that enhances channel gating<sup>147</sup>. In addition, the N-terminal region and part of S3 from the sea urchin Hv1 were found to accelerate channel activation when co-transplanted to slow-activating mouse Hv1<sup>148</sup>. In other voltage-gated ion channels, the extracellular loops of the VSDs are involved in interactions between channel-forming subunits and auxiliary/regulatory subunits<sup>149</sup> and in the Kv1.2 channel, the length and composition of the S3-S4 loop was shown to fine-tune voltage sensitivity<sup>150</sup>. These observations suggest that protein regions beyond the transmembrane portion of the VSD can provide important contributions to Hv channel function.

In this work, we found that intra- and extracellular peripheral regions of fungal Hvs are major determinants of their voltage dependence of activation, as swapping portions of these regions between AoHv1 and SlHv1 produced shifts in the G-V relationships of the chimeric channels of up to ~70 mV (Fig. 2.5D-E). In particular, the loop connecting S1 to S2 provided a dominant contribution to the difference in kinetics and voltage range of activation between AoHv1 and SlHv1 (Fig. 2.5D and Fig. S2.2A). The S3-S4 loop provided a smaller contribution, but as a result of a complementary mechanism. While swapping the S1-S2 loop mostly affected the rate of opening (Fig. 2.5B), swapping the S3-S4 loop mostly affected the rate of closing (Fig. 2.5C). Transplanting both extracellular loops of AoHv1 into SlHv1 resulted in a chimeric channel that starts opening within the voltage range of activation of AoHv1 and becomes fully open within

the voltage range of activation of SlHv1 (Fig. 2.6). Future studies should investigate whether small molecule compounds or proteins capable of binding the S1-S2 loop of fungal Hvs can shift their voltage range of activation leading to inhibition or enhancement of channel activity.

In animal Hvs, the S1 helix mediates intersubunit interactions that are important for cooperative gating<sup>7,48,130,145</sup>. A cysteine substitution introduced in the S1-S2 loop, close to the outer end of S1 (I127C in hHv1), was shown to form a spontaneous disulfide bond<sup>30</sup>, which enhanced allosteric coupling between subunits<sup>57</sup>. Fungal Hvs contain an endogenous cysteine either at, or in proximity of, the position homologous to I127 of hHv1 (Fig. S2.2A), suggesting that the intersubunit interface of these channels extends into the S1-S2 loop. We hypothesize that this interface could engage in intra- or intersubunit interactions with the S3-S4 loop and the S4 helix to set the range of voltage dependent activation. Future structural and site-directed mutagenesis studies will be needed to test this hypothesis and determine the mechanisms underlying gating modulation by peripheral regions in fungal Hv channels.

## 2.5 Supplementary Information

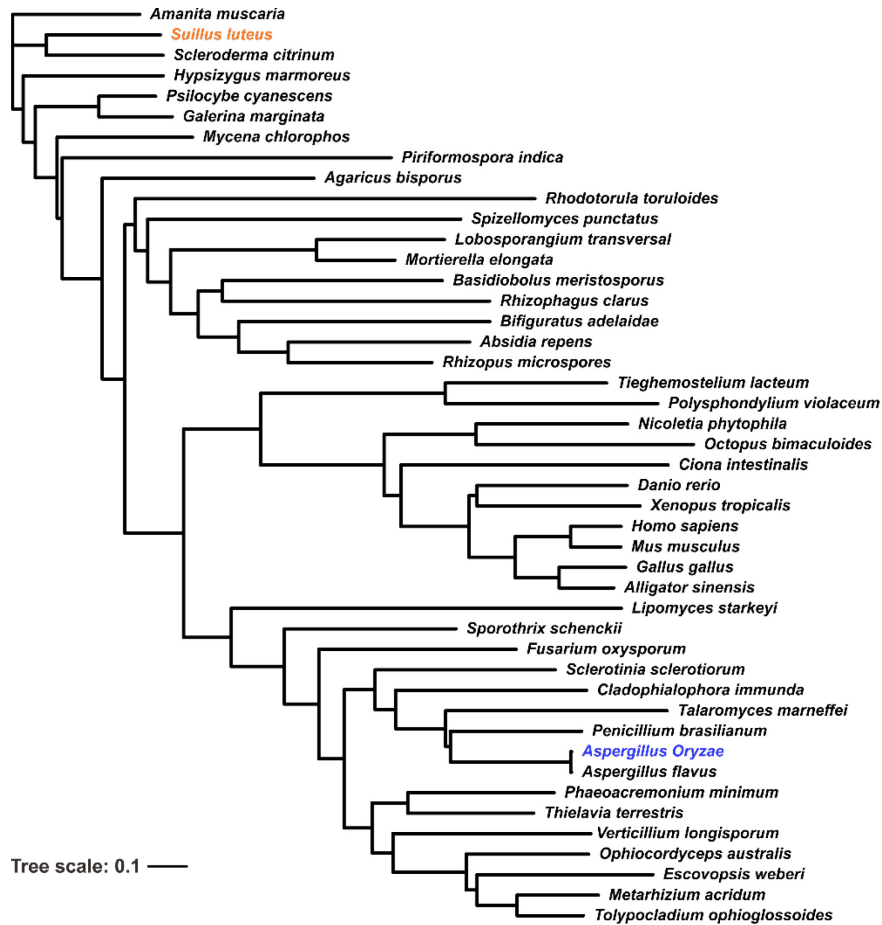


**Figure S2.1. Phylogenetic relationship between Hv1 channels from fungi and animals.** Organisms from the kingdom Fungi includes representatives from *Ascomycota*, *Basidiomycota*, *Chytridiomycota*, *Zygomycota* and *Glomeromycota* divisions (see methods section for sequence IDs and details). Tree scale 0.1 = 10 % difference between sequences. The same animal species from the cladogram of Fig. 1A were included in the phylogenetic tree. Representatives of slime molds (*Tieghemostelium*/*Dictyostelium* and *Polysphondylium* species) are also included here. These organisms used to be considered part of the *Fungi* kingdom, but they are now classified as protists.



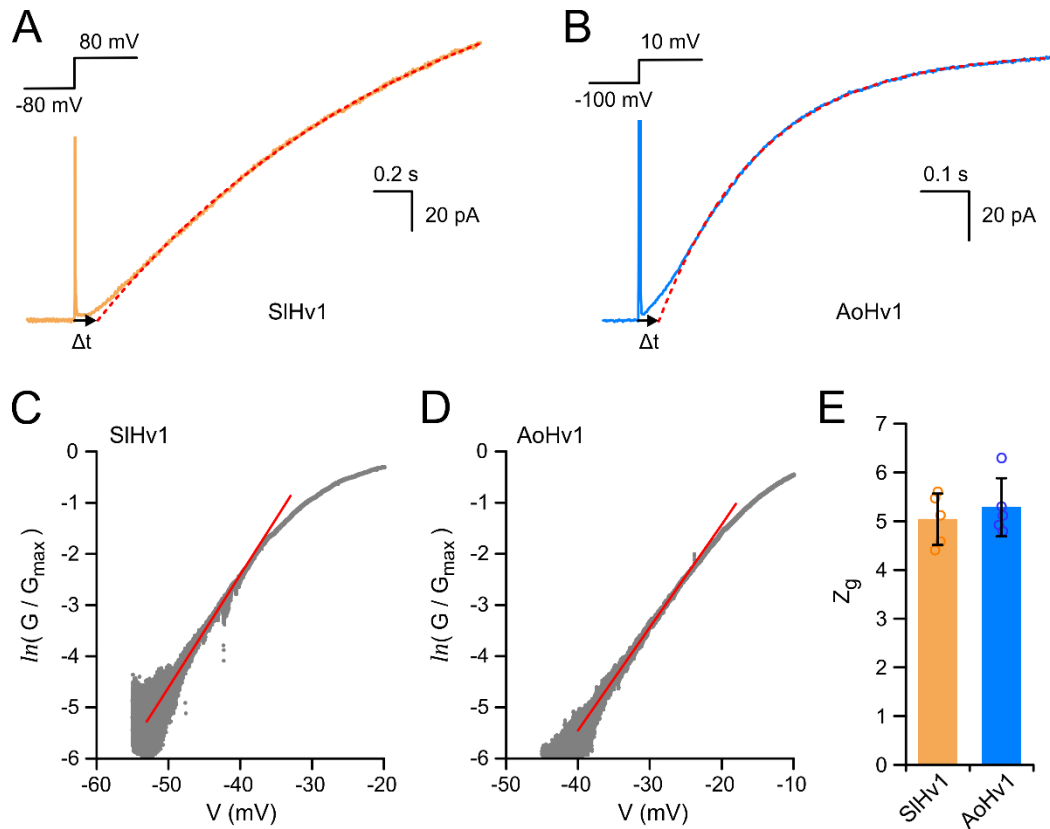


**Figure S2.3. Voltage-dependent opening of fungal Hvs.** A-B) Examples of the initial phase of the time-course of activation for SlHv1 (A) and AoHv1 (B) in response to the indicated voltage steps ( $pH_i = pH_o = 6.0$ ). Single exponential fits of the current traces, after the initial sigmoidal phase, are shown as red dotted lines. Black arrows indicate  $\Delta t = t_e - t_o$ , where  $t_e$  is the time at which the current extrapolated from the fit is zero, and  $t_o$  is the time of the transition in membrane potential. A  $\Delta t > 0$  indicates that the channel spends time transitioning through closed states before opening. In these examples,  $\Delta t$  was 123 ms for SlHv1, and 40 ms for AoHv1. C-D) Representative plots for the determination of the gating charge ( $z_g$ ) based on the limiting slope method.  $\ln(G/G_{max})$  was calculated as described in the methods section. The linear fit, showed as red line, was performed between the ordinate range -5 to -4. Measurements were carried out in inside-out patch configuration,  $pH_i = 5.5$ ,  $pH_o = 6.5$  for SlHv1;  $pH_i = pH_o = 6.0$  for AoHv1. E) Quantification of the gating charge ( $z_g$ ) associated with voltage-dependent activation of the indicated channels.  $z_g$  values were derived from the slope of linear fits like those shown in (C) and (D), see methods. Each bar represents a mean value from five independent measurements. Error bars are SD.

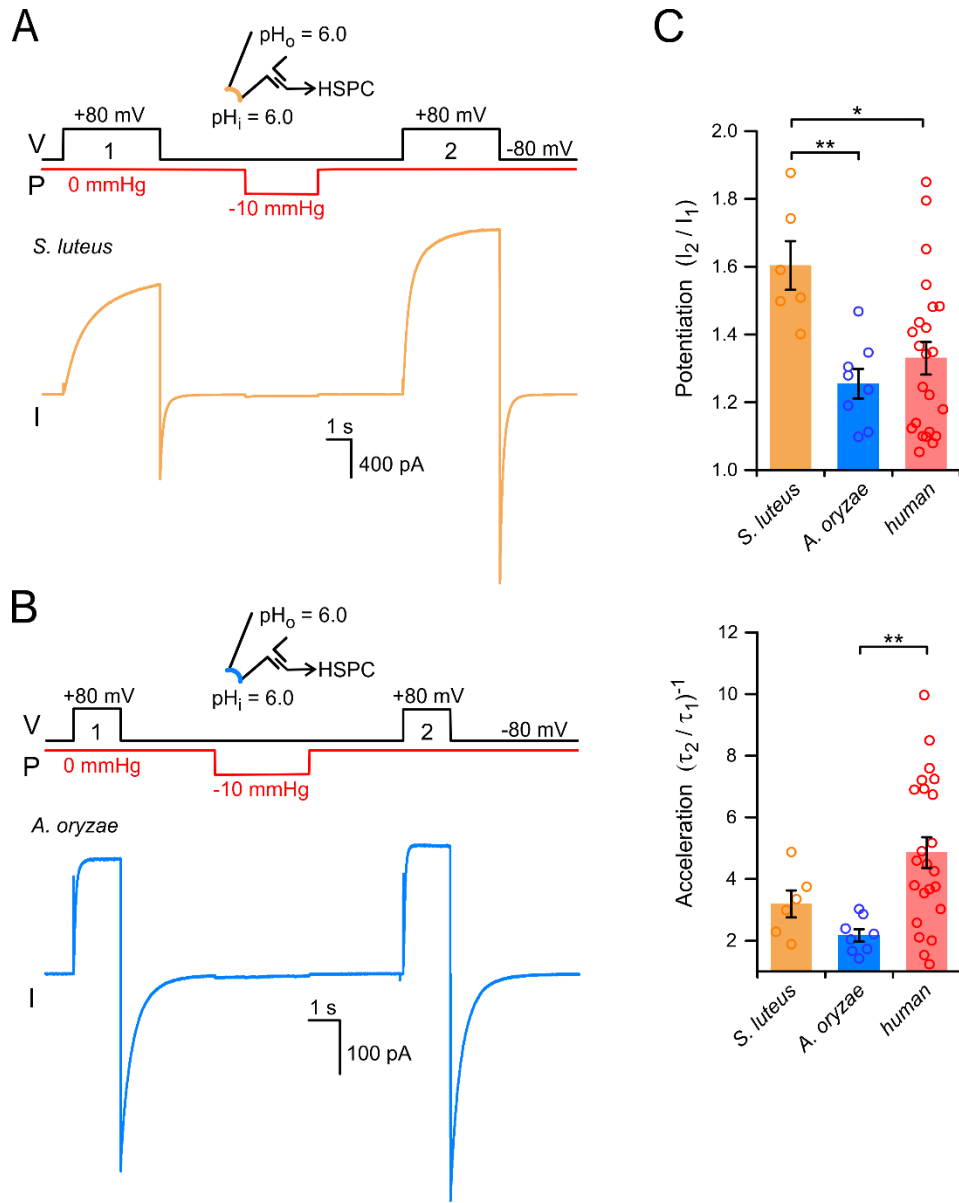


**Figure S2.4. Hv1s from *S. luteus* and *A. oryzae* are sensitive to mechanical stimulation. A-B)** Examples of proton currents elicited by membrane depolarization for SIHv1 (A) and AoHv1 (B) before (step 1) and after mechanical stimulus (step 2). Change in membrane tension was induced via negative pressure applied to the patch pipette. The mechanical stimulus was delivered at resting membrane potential to inside-out patches. **C)** Averaged increases in current (potentiation) and activation rate (acceleration) caused by the mechanical stimulus ( $\Delta P = -10$  mmHg) in fungal Hv1s compared to human channel. Current values  $I_1$  and  $I_2$  were measured at the end of depolarization steps 1 and 2, respectively. Time constants from mono-exponential fits of current traces were used to calculate acceleration in channel activation  $(\tau_1/\tau_2)^{-1}$ . Each bar represents the mean of at least 6 independent measurements  $\pm$  SEM. One-way ANOVA with Tukey's post-hoc tests were used for statistical analysis: \* $p < 0.05$ , \*\* $p < 0.01$ . Reference values for hHv1 are from Pathak et al. 2016.

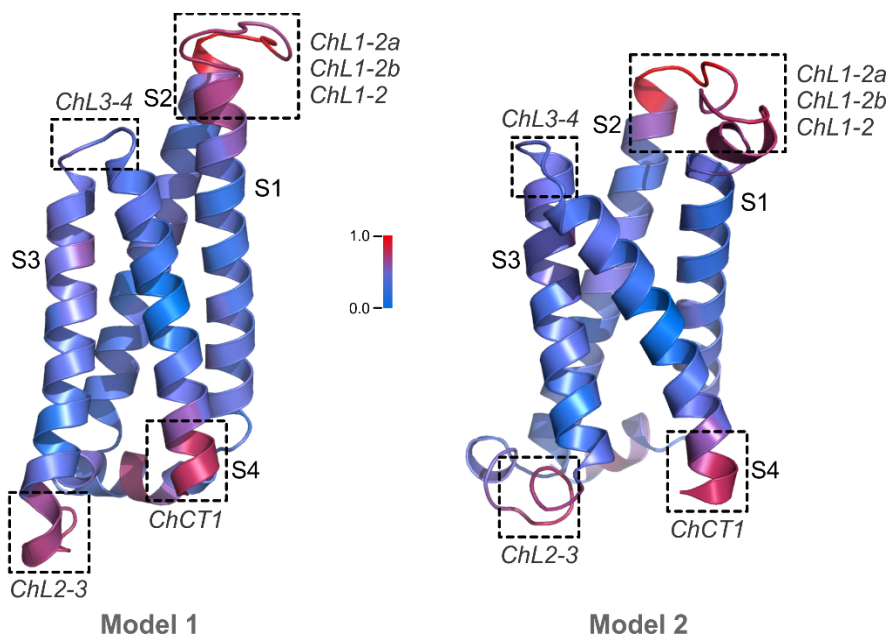


**Figure S2.5. Alternative structural models for the VSD of SlHv1.** Divergence in sequence homology between SlHv1 and AoHv1 mapped on two alternative models of the SlHv1 VSD. Model 1 is based on the structure of mHv1cc (3WKV:A). Model 2 is based on the structure of CiVSP-VSD (4G80:I). Color gradient varies from minimal divergence (blue) to maximal divergence (red) (same as Fig. 5a). Dashed boxes indicate regions with the largest sequence divergence which were targeted by chimeragenesis. In both models these regions include: the S1-S2 loop and the outermost portions of helices S1 and S2, the part of the S2-S3 loop closer to helix S3, the S3-S4 loop, and the innermost portion of helix S4. Local differences between the two models can be seen in all the divergent regions; the most noticeable involves the transition between the S2-S3 loop and helix S3 (region targeted in the ChL2-3 chimera).

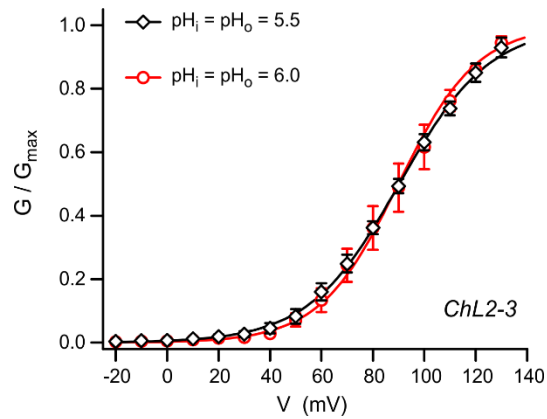


**Figure S2.6. Reduced pH sensitivity of the G-V relationship of chimera *ChL2-3* under symmetrical conditions ( $\Delta\text{pH} = 0$ ).** G-Vs under the indicated pH conditions represent the mean of 5 independent measurements. Error bars are SEM. The following G-V parameters were derived from Boltzmann fits of the data:  $V_{1/2} = 90.2 \pm 1.6$  mV, slope =  $17.7 \pm 1.8$  mV for  $\text{pH}_i = \text{pH}_o = 5.5$  ( $n = 5$ ), and  $V_{1/2} = 89.9 \pm 3.9$  mV, slope =  $15.3 \pm 1.7$  mV for  $\text{pH}_i = \text{pH}_o = 6.0$  ( $n = 5$ ). The negligible change in  $V_{1/2}$  is to be compared to the corresponding change observed with SlHv1 WT ( $\Delta V_{1/2} \sim 7.6$  mV) from Fig. 3J.

## 2.6 References

1. Hawksworth, D.L. & Lucking, R. Fungal Diversity Revisited: 2.2 to 3.8 Million Species. *Microbiol Spectr* **5**, 79--95 (2017).
2. Agrios, G. *Plant pathology*, (Academic Press, 2005).
3. Davis, D.A. How human pathogenic fungi sense and adapt to pH: the link to virulence. *Curr. Opin. Microbiol.* **12**, 365-70 (2009).
4. Vylkova, S. Environmental pH modulation by pathogenic fungi as a strategy to conquer the host. *PLoS Pathog* **13**, e1006149 (2017).
5. Vylkova, S. et al. The fungal pathogen *Candida albicans* autoinduces hyphal morphogenesis by raising extracellular pH. *mBio* **2**, e00055-11 (2011).
6. Hesse, S.J., Ruijter, G.J., Dijkema, C. & Visser, J. Intracellular pH homeostasis in the filamentous fungus *Aspergillus niger*. *Eur. J. Biochem.* **269**, 3485-94 (2002).
7. Kane, P.M. Proton Transport and pH Control in Fungi. *Adv. Exp. Med. Biol.* **892**, 33-68 (2016).
8. Sasaki, M., Takagi, M. & Okamura, Y. A voltage sensor-domain protein is a voltage-gated proton channel. *Science* **312**, 589-92 (2006).
9. Ramsey, I.S., Moran, M.M., Chong, J.A. & Clapham, D.E. A voltage-gated proton-selective channel lacking the pore domain. *Nature* **440**, 1213-6 (2006).
10. Tu, Y.H. et al. An evolutionarily conserved gene family encodes proton-selective ion channels. *Science* **359**, 1047-1050 (2018).
11. DeCoursey, T.E. Voltage-gated proton channels: molecular biology, physiology, and pathophysiology of the H(V) family. *Physiol. Rev.* **93**, 599-652 (2013).
12. DeCoursey, T.E., Morgan, D. & Cherny, V.V. The voltage dependence of NADPH oxidase reveals why phagocytes need proton channels. *Nature* **422**, 531-4 (2003).
13. Ramsey, I.S., Ruchti, E., Kaczmarek, J.S. & Clapham, D.E. Hv1 proton channels are required for high-level NADPH oxidase-dependent superoxide production during the phagocyte respiratory burst. *Proc Natl Acad Sci U S A* **106**, 7642-7 (2009).
14. El Chemaly, A. et al. VSOP/Hv1 proton channels sustain calcium entry, neutrophil migration, and superoxide production by limiting cell depolarization and acidification. *J. Exp. Med.* **207**, 129-39 (2010).
15. Zhang, J. et al. Sour Sensing from the Tongue to the Brain. *Cell* **179**, 392-402 e15 (2019).
16. Hurle, B. et al. Non-syndromic vestibular disorder with otoconial agenesis in tilted/mergulhador mice caused by mutations in otopetrin 1. *Hum. Mol. Genet.* **12**, 777-89 (2003).
17. Kim, E. et al. Regulation of cellular calcium in vestibular supporting cells by otopetrin 1. *J. Neurophysiol.* **104**, 3439-50 (2010).
18. Takemoto, D., Tanaka, A. & Scott, B. NADPH oxidases in fungi: diverse roles of reactive oxygen species in fungal cellular differentiation. *Fungal Genet. Biol.* **44**, 1065-76 (2007).
19. Davis, D. Adaptation to environmental pH in *Candida albicans* and its relation to pathogenesis. *Curr. Genet.* **44**, 1-7 (2003).
20. Penalva, M.A., Tilburn, J., Bignell, E. & Arst, H.N., Jr. Ambient pH gene regulation in fungi: making connections. *Trends Microbiol.* **16**, 291-300 (2008).
21. Serrano, R., Kielland-Brandt, M.C. & Fink, G.R. Yeast plasma membrane ATPase is essential for growth and has homology with (Na<sup>+</sup> + K<sup>+</sup>), K<sup>+</sup>- and Ca<sup>2+</sup>-ATPases. *Nature* **319**, 689-93 (1986).
22. Kuhlbrandt, W., Zeelen, J. & Dietrich, J. Structure, mechanism, and regulation of the *Neurospora* plasma membrane H<sup>+</sup>-ATPase. *Science* **297**, 1692-6 (2002).
23. Bowman, E.J. & Bowman, B.J. Identification and properties of an ATPase in vacuolar

- membranes of *Neurospora crassa*. *J. Bacteriol.* **151**, 1326-37 (1982).
24. Beyenbach, K.W. & Wiczczonek, H. The V-type H<sup>+</sup> ATPase: molecular structure and function, physiological roles and regulation. *J. Exp. Biol.* **209**, 577-89 (2006).
  25. Takeshita, K. et al. X-ray crystal structure of voltage-gated proton channel. *Nat. Struct. Mol. Biol.* **21**, 352-7 (2014).
  26. Bayrhuber, M. et al. Nuclear Magnetic Resonance Solution Structure and Functional Behavior of the Human Proton Channel. *Biochemistry* **58**, 4017-4027 (2019).
  27. Koch, H.P. et al. Multimeric nature of voltage-gated proton channels. *Proc Natl Acad Sci U S A* **105**, 9111-6 (2008).
  28. Tombola, F., Ulbrich, M.H. & Isacoff, E.Y. The voltage-gated proton channel Hv1 has two pores, each controlled by one voltage sensor. *Neuron* **58**, 546-56 (2008).
  29. Lee, S.Y., Letts, J.A. & MacKinnon, R. Functional reconstitution of purified human Hv1 H<sup>+</sup> channels. *J. Mol. Biol.* **387**, 1055-60 (2009).
  30. Lee, S.Y., Letts, J.A. & MacKinnon, R. Dimeric subunit stoichiometry of the human voltage-dependent proton channel Hv1. *Proc Natl Acad Sci U S A* **105**, 7692-5 (2008).
  31. Li, S.J. et al. The role and structure of the carboxyl-terminal domain of the human voltage-gated proton channel Hv1. *J. Biol. Chem.* **285**, 12047-54 (2010).
  32. Fujiwara, Y. et al. The cytoplasmic coiled-coil mediates cooperative gating temperature sensitivity in the voltage-gated H<sup>+</sup> channel Hv1. *Nat Commun* **3**, 816 (2012).
  33. Hong, L., Pathak, M.M., Kim, I.H., Ta, D. & Tombola, F. Voltage-sensing domain of voltage-gated proton channel Hv1 shares mechanism of block with pore domains. *Neuron* **77**, 274-87 (2013).
  34. Chamberlin, A. et al. Hydrophobic plug functions as a gate in voltage-gated proton channels. *Proc Natl Acad Sci U S A* **111**, E273-82 (2014).
  35. Randolph, A.L., Mokrab, Y., Bennett, A.L., Sansom, M.S. & Ramsey, I.S. Proton currents constrain structural models of voltage sensor activation. *Elife* **5**(2016).
  36. Banh, R. et al. Hydrophobic gasket mutation produces gating pore currents in closed human voltage-gated proton channels. *Proc Natl Acad Sci U S A* **116**, 18951-18961 (2019).
  37. Geragotelis, A.D. et al. Voltage-dependent structural models of the human Hv1 proton channel from long-timescale molecular dynamics simulations. *Proc Natl Acad Sci U S A* **117**, 13490-13498 (2020).
  38. Smith, S.M. et al. Voltage-gated proton channel in a dinoflagellate. *Proc Natl Acad Sci U S A* **108**, 18162-7 (2011).
  39. Kim, I.H. et al. Evidence for functional diversity between the voltage-gated proton channel Hv1 and its closest related protein HVRP1. *PLoS One* **9**, e105926 (2014).
  40. Musset, B. et al. Aspartate 112 is the selectivity filter of the human voltage-gated proton channel. *Nature* **480**, 273-7 (2011).
  41. Papp, F. et al. TMEM266 is a functional voltage sensor regulated by extracellular Zn(2). *Elife* **8**, e42372 (2019).
  42. Tombola, F., Ulbrich, M.H., Kohout, S.C. & Isacoff, E.Y. The opening of the two pores of the Hv1 voltage-gated proton channel is tuned by cooperativity. *Nat. Struct. Mol. Biol.* **17**, 44-50 (2010).
  43. Gonzalez, C., Koch, H.P., Drum, B.M. & Larsson, H.P. Strong cooperativity between subunits in voltage-gated proton channels. *Nat. Struct. Mol. Biol.* **17**, 51-6 (2010).
  44. Fujiwara, Y. et al. Gating of the designed trimeric/tetrameric voltage-gated H<sup>+</sup> channel. *J Physiol* **591**, 627-40 (2013).
  45. Almers, W. Gating currents and charge movements in excitable membranes. *Rev Physiol Biochem Pharmacol* **82**, 96-190 (1978).
  46. Sigg, D. & Bezanilla, F. Total charge movement per channel. The relation between gating charge displacement and the voltage sensitivity of activation. *J. Gen. Physiol.*

- 109, 27-39 (1997).
47. Berger, T.K. & Isacoff, E.Y. The pore of the voltage-gated proton channel. *Neuron* **72**, 991-1000 (2011).
  48. Dudev, T. et al. Selectivity Mechanism of the Voltage-gated Proton Channel, Hv1. *Sci Rep* **5**, 10320 (2015).
  49. Lee, M., Bai, C., Feliks, M., Alhadeff, R. & Warshel, A. On the control of the proton current in the voltage-gated proton channel Hv1. *Proc Natl Acad Sci U S A* **115**, 10321-10326 (2018).
  50. Decoursey, T.E. Voltage-gated proton channels and other proton transfer pathways. *Physiol. Rev.* **83**, 475-579 (2003).
  51. Pathak, M.M. et al. The Hv1 proton channel responds to mechanical stimuli. *J. Gen. Physiol.* **148**, 405-418 (2016).
  52. Seredenina, T., Demaurex, N. & Krause, K.H. Voltage-Gated Proton Channels as Novel Drug Targets: From NADPH Oxidase Regulation to Sperm Biology. *Antioxid. Redox Signal.* **23**, 490-513 (2015).
  53. Pupo, A. & Gonzalez Leon, C. In pursuit of an inhibitory drug for the proton channel. *Proc Natl Acad Sci U S A* **111**, 9673-4 (2014).
  54. Zhao, R. et al. Role of human Hv1 channels in sperm capacitation and white blood cell respiratory burst established by a designed peptide inhibitor. *Proc Natl Acad Sci U S A* **115**, E11847-E11856 (2018).
  55. Tang, D. et al. Scorpion toxin inhibits the voltage-gated proton channel using a Zn(2+) - like long-range conformational coupling mechanism. *Br. J. Pharmacol.* **177**, 2351-2364 (2020).
  56. Hong, L., Kim, I.H. & Tombola, F. Molecular determinants of Hv1 proton channel inhibition by guanidine derivatives. *Proc Natl Acad Sci U S A* **111**, 9971-6 (2014).
  57. Hong, L., Singh, V., Wulff, H. & Tombola, F. Interrogation of the intersubunit interface of the open Hv1 proton channel with a probe of allosteric coupling. *Sci Rep* **5**, 14077 (2015).
  58. Cherny, V.V. & DeCoursey, T.E. pH-dependent inhibition of voltage-gated H<sup>+</sup> currents in rat alveolar epithelial cells by Zn(2+) and other divalent cations. *J. Gen. Physiol.* **114**, 819-38 (1999).
  59. Qiu, F. et al. Molecular mechanism of Zn<sup>2+</sup> inhibition of a voltage-gated proton channel. *Proc Natl Acad Sci U S A* **113**, E5962-E5971 (2016).
  60. Jardin, C., Chaves, G. & Musset, B. Assessing Structural Determinants of Zn(2+) Binding to Human HV1 via Multiple MD Simulations. *Biophys. J.* **118**, 1221-1233 (2020).
  61. Li, Q. et al. Structural mechanism of voltage-dependent gating in an isolated voltage-sensing domain. *Nat. Struct. Mol. Biol.* **21**, 244-52 (2014).
  62. Villalba-Galea, C.A. Hv1 proton channel opening is preceded by a voltage-independent transition. *Biophys. J.* **107**, 1564-72 (2014).
  63. Cherny, V.V., Morgan, D., Thomas, S., Smith, S.M.E. & DeCoursey, T.E. Histidine(168) is crucial for DeltapH-dependent gating of the human voltage-gated proton channel, hHV1. *J. Gen. Physiol.* **150**, 851-862 (2018).
  64. Slayman, C.L., Scott Long, W. & Gradmann, D. "Action potentials" in NEUROSPORA CRASSA, a mycelial fungus. *Biochim. Biophys. Acta* **426**, 732-744 (1976).
  65. Thomas, S. et al. Exotic properties of a voltage-gated proton channel from the snail *Helisoma trivolvis*. *J. Gen. Physiol.* **150**, 835-850 (2018).
  66. Olsson, S. & Hansson, B.S. Action potential-like activity found in fungal mycelia is sensitive to stimulation. *Naturwissenschaften* **82**, 30-31 (1995).
  67. Adamatzky, A. On spiking behaviour of oyster fungi *Pleurotus djamor*. *Sci Rep* **8**, 7873 (2018).

68. Gow, N.A. Transhyphal electrical currents in fungi. *J Gen Microbiol* **130**, 3313-8 (1984).
69. McGillivray, A.M. & Gow, N.A.R. Applied Electrical Fields Polarize the Growth of Mycelial Fungi. *Microbiology* **132**, 2515-2525 (1986).
70. Harold, F.M., Kropf, D.L. & Caldwell, J.H. Why do fungi drive electric currents through themselves? *Experimental Mycology* **9**, 3-86 (1985).
71. Rayner, A.D.M. The Challenge of the Individualistic Mycelium. *Mycologia* (1991).
72. McGillivray, A.M. & Gow, N.A.R. The Transhyphal Electrical Current of *Neurospora crassa* is Carried Principally by Protons. *Microbiology* **133**, 2875-2881 (1987).
73. Cornet, M. & Gaillardin, C. pH signaling in human fungal pathogens: a new target for antifungal strategies. *Eukaryot. Cell* **13**, 342-52 (2014).
74. Eckert, R. II. Asynchronous Flash Initiation by a Propagated Triggering Potential. *Science* **147**, 1142-5 (1965).
75. Fogel, M. & Hastings, J.W. Bioluminescence: mechanism and mode of control of scintillon activity. *Proc Natl Acad Sci U S A* **69**, 690-3 (1972).
76. Lishko, P.V. et al. The control of male fertility by spermatozoan ion channels. *Annu. Rev. Physiol.* **74**, 453-75 (2012).
77. Noh, S. et al. The direct modulatory activity of zinc toward ion channels. *Integr Med Res* **4**, 142-146 (2015).
78. Qiu, F., Rebolledo, S., Gonzalez, C. & Larsson, H.P. Subunit interactions during cooperative opening of voltage-gated proton channels. *Neuron* **77**, 288-98 (2013).
79. Mony, L., Stroebel, D. & Isacoff, E.Y. Dimer interaction in the Hv1 proton channel. *Proc Natl Acad Sci U S A* **117**, 20898-20907 (2020).
80. Gonzalez, C., Rebolledo, S., Perez, M.E. & Larsson, H.P. Molecular mechanism of voltage sensing in voltage-gated proton channels. *J. Gen. Physiol.* **141**, 275-85 (2013).
81. Berger, T.K. et al. Post-translational cleavage of Hv1 in human sperm tunes pH- and voltage-dependent gating. *J Physiol* **595**, 1533-1546 (2017).
82. Hondares, E. et al. Enhanced activation of an amino-terminally truncated isoform of the voltage-gated proton channel HVCN1 enriched in malignant B cells. *Proc Natl Acad Sci U S A* **111**, 18078-83 (2014).
83. Musset, B. et al. Identification of Thr29 as a critical phosphorylation site that activates the human proton channel Hvcn1 in leukocytes. *J. Biol. Chem.* **285**, 5117-21 (2010).
84. Sakata, S. et al. Comparison between mouse and sea urchin orthologs of voltage-gated proton channel suggests role of S3 segment in activation gating. *Biochim. Biophys. Acta* **1858**, 2972-2983 (2016).
85. Isom, L.L., De Jongh, K.S. & Catterall, W.A. Auxiliary subunits of voltage-gated ion channels. *Neuron* **12**, 1183-94 (1994).
86. Sand, R., Sharmin, N., Morgan, C. & Gallin, W.J. Fine-tuning of voltage sensitivity of the Kv1.2 potassium channel by interhelix loop dynamics. *J. Biol. Chem.* **288**, 9686-95 (2013).
87. Madeira, F. et al. The EMBL-EBI search and sequence analysis tools APIs in 2019. *Nucleic Acids Res.* **47**, W636-W641 (2019).
88. Letunic, I. & Bork, P. Interactive Tree Of Life (iTOL) v4: recent updates and new developments. *Nucleic Acids Res.* **47**, W256-W259 (2019).
89. Snider, C., Jayasinghe, S., Hristova, K. & White, S.H. MPEX: a tool for exploring membrane proteins. *Protein Sci.* **18**, 2624-8 (2009).
90. Lupas, A., Van Dyke, M. & Stock, J. Predicting coiled coils from protein sequences. *Science* **252**, 1162-4 (1991).
91. Liman, E.R., Tytgat, J. & Hess, P. Subunit stoichiometry of a mammalian K<sup>+</sup> channel determined by construction of multimeric cDNAs. *Neuron* **9**, 861-71 (1992).
92. Roy, A., Kucukural, A. & Zhang, Y. I-TASSER: a unified platform for automated protein

- structure and function prediction. *Nat Protoc* **5**, 725-38 (2010).
93. Guex, N. & Peitsch, M.C. SWISS-MODEL and the Swiss-PdbViewer: an environment for comparative protein modeling. *Electrophoresis* **18**, 2714-23 (1997).

### Chapter 3: Voltage-gated proton channels in plants

(Zhao, De Angeli, Tombola)

#### Abstract

pH homeostasis is crucial for almost all living organisms, from animals, fungi, bacteria to plants, and many take advantages of both active and passive proton transport. The family of voltage-gated proton channels (Hvs), were previously identified from animals and fungi. In other organisms, Hv channels allows passive proton transport following their electrochemical gradient, and most of the time they function as acid extruders to protect the intracellular compartments. pH regulation is essential for plant growth and development, as well as shaping the tissue under abiotic stress. Yet the players within the pH regulation networks and their roles in plants remain to be fully elucidated. Other equivalents of the players found in other organisms including the H<sup>+</sup>-ATPases and NOX enzymes were identified in plants but not Hv proteins. Here we show the presence of Hv homologues from several plant species, members of angiosperm, gymnosperm, as well as primitive vascular plants. We confirmed that these channels are proton selective and activate in response to voltages. Strikingly, we found the Hv proteins from angiosperm but not other plant species respond to electrical stimulus similarly to their animal counterparts only if the channels have been pre-exposed to mechanical stimulus. Therefore, we defined these angiosperm Hv channels are “mechanically-primed”, which behave differently from mechanically gated ion channels. We expect our findings would lay the groundwork for the beginning of understanding these proton channels’ roles in plant physiology, providing the possibility that this unique feature might be the consequence of environmental adaptations such as responding to turgor pressure and abiotic stress.

### 3.1 Introduction

The voltage-gated proton channels (Hvs)<sup>1,2</sup> belong to the superfamily of voltage-gated ion channels (VGICs). VGICs are critical in communicating both electrical and chemical signals, generating action potentials and maintaining the resting membrane potential. In other channels from the family, such as voltage-gated Na<sup>+</sup>, K<sup>+</sup> and Ca<sup>2+</sup> channels, ions permeate through the pore domains (PDs), which are controlled by the voltage-sensing domains (VSDs). Distinct from other members of the family, Hv channels are dimers consisting of two individual VSDs<sup>3-5</sup>, and each of the VSDs senses both changes in membrane potential and conducts protons upon activation. Resemble VSDs from voltage-gated Na<sup>+</sup>, K<sup>+</sup>, Ca<sup>2+</sup> channels, VSDs from Hv proteins also consist of S1-S4 transmembrane segments, with S4 carrying periodically arranged positively charged residues separated by hydrophobic residues (In human Hv1, the signature motif in S4 is R·R·R·N, however it can be R·R·K·E or R·R·K·G in fungi).

Hv proteins have been previously identified from animals<sup>6</sup>, protists<sup>7,8</sup> as well as fungi<sup>9</sup>. It is well expected to find proton channels in these organisms, given the universal requirement of proton transport in maintaining the pH homeostasis. In human, Hv1 is expressed in a wide variety of immune cells including B and T lymphocytes, macrophages and granulocytes such as basophils and neutrophils<sup>6</sup>. It is critical for respiratory burst, and almost exclusively works as an acid extruder to sustain the Reactive Oxygen Species (ROS) production by NADPH oxidases (NOXs), which is known to be an electrogenic process<sup>6</sup>. In some fungi such as *Aspergillus*, Hv1 activates at ultra-negative voltage ranges that is well below the Nernst potential for protons, allowing inward proton currents in most conditions. This suggests Hvs might function differently in those organisms, likely due to evolutionary adaptation<sup>9</sup>.

So far, no proton channels have been characterized from the plants, despite Hv1 homolog has been identified in *P.patens* through BLAST search<sup>7</sup>. Though other commonly shared players

within the pH regulation network were previously identified in plants, including H<sup>+</sup>-ATPase<sup>10</sup> and Ca<sup>2+</sup>/H<sup>+</sup> antiporters<sup>11</sup> at the apoplast, it is unclear whether and how these predicted Hv1 proteins could function as proton channels. Here, we report the identification and characterization of Hv1 homologs from several plant species, including members of angiosperms, gymnosperms, and more primitive vascular plants. The signature motif in S4 from angiosperms is different from the ones in gymnosperms and other vascular species.

Different from Hv1 channels from other plant species, we showed that angiosperm Hv1 channels, from *Arabidopsis thaliana* (AtHv1) and *Theobroma cacao* (TcHv1) particularly, activate in response to membrane depolarization only if the channels have been pre-exposed to the mechanical stimuli. To be distinguished from mechanically gated ion channels, we defined this exclusive requirement for mechanical stimulus from voltage-gated ion channels as “mechanical priming”. Coinciding with the discovery that AtHv1 localizes to root cells where mechanoreception is critical for growth and organ morphogenesis, this intrinsic feature of the channel protein could be the consequence of environmental adaptations such as turgor pressure and abiotic stress.

### **3.2 Materials and Methods**

#### ***Cladogram and phylogeny***

Multiple sequence alignment and phylogenetic analysis were performed using Clustal Omega from EMBL-EBI tools<sup>12</sup>. Phylogenetic tree and cladogram were constructed with iTOL 5.6.2<sup>13</sup>. Tree scale is at 0.1. Following protein sequences were used to construct the cladogram and the phylogenetic tree.

#### ***Plant Hvs used for biophysical characterization***

*Picea sitchensis* (ABR16431.1, 260aa); *Selaginella moellendorffii* (EFJ10096.1 242aa); *Arabidopsis thaliana* (NP\_001321473.1, 236 aa) and *Theobroma cacao* (XP\_017974731.1 234aa).

#### **Other plant Hvs from the phylogenetic tree and cladogram**

*Klebsormidium nitens* (GAQ80331.1, 289aa); *Marchantia polymorpha* (PTQ41489.1, 261aa); *Physcomitrella patens* (XP\_024364004.1, 285aa); *Nymphaea colorata* (XP\_031481790.1, 236 aa); *Nelumbo nucifera*(XP\_010244071.1, 240aa); *Populus trichocarpa* (XP\_006375506.1 253aa); *Prosopis alba* (XP\_028759754.1 246aa); *Arachis hypogaea* (QH009623.1 234aa); *Lupinus albus* (KAE9604961.1 239aa); *Citrus clementina* (XP\_006436991.1, 250aa); *Nicotiana tabacum* (XP\_016501726.1, 237aa); *Solanum demissum* (ANJ02807.1, 232aa); *Gossypium hirsutum* (XP\_016748187.1, 248aa); *Vitis vinifera* (XP\_002265639.1, 239aa); *Cannabis sativa* (XP\_030507068.1, 278aa); *Prunus persica* (XP\_007225522.1, 265aa); *Camellia sinensis* (XP\_028062609.1, 229aa)

#### **Gymnosperms found from Gymno PLAZA 1.0**

(<https://bioinformatics.psb.ugent.be/plaza/versions/gymno-plaza/>) with the following sequence IDs:

*Ginkgo Biloba* (GBI00022260, 261aa); *Pseudotsuga menziesii* (PME00027381, 261aa) and *Pinus Sylvestris* (PSY00020417, 259aa).

#### **Hvs listed as references from other organisms**

*Hypsizygus marmoreus* (RDB21275.1, 215aa); *Amanita muscaria* (KIL69657.1, 218aa); *Suillus luteus* (KIK49332.1, 223aa); *Galerina marginata* (KDR81513.1, 217aa); *Mycena chlorophos* (GAT47218.1, 202aa); *Agaricus bisporus* (XP\_007326257.1, 183aa); *Fusarium oxysporum* (XP\_031056756.1, 230aa); *Cladophialophora immunda* (XP\_016251813.1, 259aa); *Talaromyces*

*marneffe* (EEA28233.1, 309aa); *Penicillium brasilianum* (CEJ60805.1, 205aa) and *Aspergillus oryzae* (XP\_001825565.1, 211aa).

*Nicoletia phytophila* (AMK01488.1, 239aa); *Octopus bimaculoides* (XP\_014789275.1, 348aa); *Ciona intestinalis* (NP\_001071937.1, 342aa); *Danio rerio* (NP\_001002346.1, 235aa); *Xenopus tropicalis* (NP\_001011262.1, 230aa); *Homo sapiens* (NP\_001035196.1, 273aa); *Mus musculus* (NP\_001035954.1, 269aa); *Gallus gallus* (NP\_001025834.1, 235aa); *Alligator sinensis* (XP\_006015244.1, 239aa).

### ***Channel expression in Xenopus Oocytes***

Constructs containing the sequence of the human HVCN1 channel were generated from cDNA kindly provided by David Clapham and from IMAGE clone 5577070 (Open Biosystems).

Mutagenesis was performed as previously described. All constructs were subcloned in the pGEMHE vector and linearized with NheI or SphI restriction enzymes (New England Biolabs) before in vitro transcription. cRNAs were synthesized using T7 mMessage mMachine transcription kit (Ambion). *Xenopus* oocytes from Ecocyte Bioscience or *Xenopus 1* were injected with cRNAs (50 nl per cell, 0.5-1.5 ng/nl) 1-3 days before the electrophysiological measurements. Injections were performed with a Nanoject II (Drummond Scientific). Cells were kept at 18°C in ND96 medium containing 96 mM NaCl, 2 mM KCl, 1.8 mM CaCl<sub>2</sub>, 1 mM MgCl<sub>2</sub>, 10 mM HEPES, 5 mM pyruvate, 100 mg/ml gentamycin (pH 7.2).

### ***Patch clamp measurements***

Voltage-clamp measurements were either performed in inside-out patch or outside-out configurations, using an Axopatch 200B amplifier controlled by pClamp10 software through an Axon Digidata 1440A (Molecular Devices). The signal was lowpass filtered at 1 kHz (Bessel, -80 dB/decade) before digitalization (2 kHz sampling).

All patch clamp experiments with inside-out configuration were performed under symmetrical pH6.0 conditions unless otherwise specified. For solution at pH6.0, bath and pipette solutions contained 100 mM 2-(N-morpholino)ethanesulphonic acid (MES), 30mM tetraethylammonium (TEA) methanesulfonate, 5 mM TEA chloride, 5 mM ethylene glycol-bis(2-aminoethyl)-N,N,N',N'-tetra-acetic acid (EGTA), adjusted to pH 6.0 with TEA hydroxide. For pipette solutions used in the selectivity measurements, solution at pH 5.5 contained 100mM MES, 50mM tetraethylammonium (TEA) methanesulfonate, 5 mM TEA chloride, adjusted with TEA hydroxide; solution at pH 6.5 contained 100mM 1,4-Piperazinediethanesulfonic acid, 5 mM TEA chloride, adjusted with TEA hydroxide; solution at pH 7.0 solution contained 100mM 3-(N-Morpholino)propanesulfonic acid, 40mM tetraethylammonium (TEA) methanesulfonate, 5mM TEA chloride. Outside-out measurements were performed in asymmetrical pH condition ( $pH_i=6.0$ ,  $pH_o=7.0$ ). Same solution at pH 7.0 was used for outside-out configuration with addition of  $ZnCl_2$  at desired concentrations.

All measurements were performed at  $22 \pm 1$  °C. Pipettes had 1-3 M $\Omega$  access resistance. Unless otherwise specified, the holding potential was either -60 mV or -80mV and the depolarization potential +80 mV. Channel inhibition was determined by isochronal current measurements at the end of the depolarization pulses.

### ***Mechanical stimulation of membrane patches***

High-speed pressure clamp (HSPC-1, ALA Scientific) was used in the mechanosensitivity experiments to apply negative suction pulses through the patch pipette, controlled by pCLAMP 10.2. For AtHv1 and TcHv1, the pressure pulse at -10mmHg

### ***Data analysis***

Current traces were analyzed using Clampfit10.2 (Molecular Devices) and Origin8.1 (OriginLab). Leak subtraction, run-down correction, and the derivation of concentration

dependence curves were performed as previously described. G-V measurements were carried out as the previously described. Tail currents were measured at -60mV after depolarization steps from -20mV to +120mV for SlHv1, or measured at -100mV after depolarization steps from -70mV to +60mV for AoHv1. Current rundown was corrected using a reference depolarization step preceding the test depolarization. G-V plots were fitted with the Boltzmann equation:

$$G/G_{max} = 1/(1 + e^{(V_{1/2}-V)/s})$$

where  $V_{1/2}$  is the potential of half maximal activation, and  $s$  is the slope, all in mV.  $V_{ref}$  of each fungal Hvs are chosen as the voltage that is the closest to the  $V_{1/2}$ , respectively. Unless otherwise specified, data are reported as averages from at least four independent measurements, and error bars are standard error of the mean (SEM). All tested compounds were at the highest purity commercially available. Intracellular inhibitors 2-guanidinobenzimidazole (2GBI) and 5-chloro-2-guanidinobenzimidazole (Cl-GBI) were from Sigma-Aldrich.

### 3.3 Results

#### *Identification of Hvs from plants*

We initially identified a homolog of human Hv1 in plant species *Arabidopsis thaliana* (AtHv1) through BLAST search (see Methods for sequence ID), which shares 14.5% sequence identity with human Hv1. AtHv1 appears to have similar transmembrane topological organization as other voltage-gated proton channels, with positive charged residues found in S4 (Fig. 3.1A inset and Fig. S3.1), though the signature motif from S4 is presented as S·WR·R·E (· as a hydrophobic residue). We expressed AtHv1 in *Xenopus* oocytes and attempted to record currents from inside-out patches under symmetrical pH 6.0 using a regular depolarizing protocol established for

human Hv1<sup>5</sup>, however failed to observe apparent current (Fig. 3.1A) under reasonable incubation time period (currents were either minimal or could not be differentiated from leak). Suspecting insufficient expression level limited by the excised patches, we also recorded from the entire oocyte using Two-electrode Voltage Clamp (TEVC), yet still no obvious current was detected. Though *Xenopus* oocytes are preferred heterologous expression systems for plant ion channels and transporters, mistargeting can still happen. Uncertain about whether the issue is caused by disorganized protein assembly or aberrant translocation to plasma membrane, we expressed a construct with GFP-tagged AtHv1 in the *Arabidopsis thaliana* following the p35S promoter (Fig. 3.1B top right). While majority of the GFP-AtHv1 localized to the plasma membrane of the root hair cells, root tip cells, as well as elongated root cells (Fig. 3.1B), there was also GFP signal detected at the intracellular organelles such as ER (Fig. S3.2B).

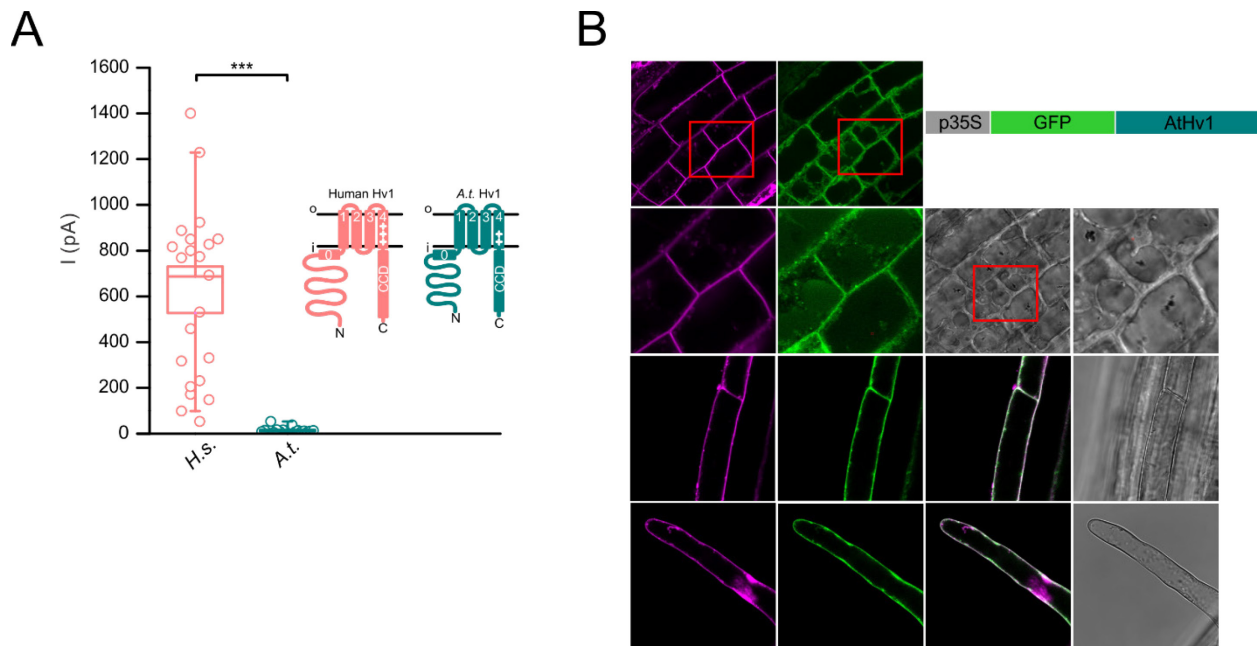


**Figure 3.1. Hv1 from *Arabidopsis thaliana* localizes to the plasma membrane but displays no apparent proton current recorded with electrophysiology. A)** No apparent currents were detected from excised membrane patches from *Xenopus* oocytes expressing the AtHv1, compared to human Hv1 within the same time frame (inset shows AtHv1 has similar membrane organization as human Hv1 though S4 carries less positively charged residues). **B)** Construct expressing GFP-AtHv1 localized to the plasma membrane of root cells. Magenta: plasma membrane marker FM64. Green: GFP. Grey and white: TEM images. Top two panels: root tip cells. 3<sup>rd</sup> panel: elongated root cells. Bottom: root hair cells.

To exclude the possibility that AtHv1 is a special case, we broadened the BLAST search and identified a group of putative proton channels from a variety of plant species (see Methods for details) for further investigation. These putative plant Hvs share only 14-17% sequence identity with human voltage-gated proton channel Hv1. Cladogram based on proton channels (Fig. 3.2A) reveal these plant Hv1s are only distantly related to known Hvs from kingdoms of *Animalia* and *Fungi*. In addition, two distinctive clusters form within the *Plantae* kingdom, with one mainly composed of angiosperms, and the other consisting of gymnosperms along with more ancient ancestors. While protein sequence analysis indicates these plant proton channels have similar structural organization and the S4 transmembrane segment also carries positively charged residues that are typically found in other voltage sensors, the signature motif from gymnosperms and more primitive species is often presented as N·WR·R·H, rather than S·WR·R·E seen in AtHv1 and other angiosperms. Therefore, we selected two candidates from the non-angiosperm group for further investigation: Hv1 from Sitka spruce *Picea sitchensis* (PsHv1), a gymnosperm; and Hv1 from spikemoss *Selaginella moellendorffii* (SmHv1), which is even more primitive than gymnosperm. We also chose another angiosperm, chocolate plant *Theobroma Cacao* (TcHv1), to confirm whether it shares similar electrophysiological properties as AtHv1.

Interestingly, when we expressed these proteins in *Xenopus* oocytes, we could detect robust current from all plant species except TcHv1 and AtHv1 (Fig. 3.2B), suggesting what happened to AtHv1 is unlikely to be a protein assembly or transport issue, but something unique with the angiosperm. We measured the voltage dependence of activation (G-Vs) in PsHv1 (Fig. 3.3A), using a similar protocol as we established for human Hv1<sup>5</sup>. G-V curve of PsHv1 resembles the one from human Hv1, only with a slight left shift ( $V_{1/2} = 40.7\text{mV} \pm 1.03$ ) and a slightly steeper slope ( $15.3\text{mV} \pm 0.51$ ) compared to human Hv1.

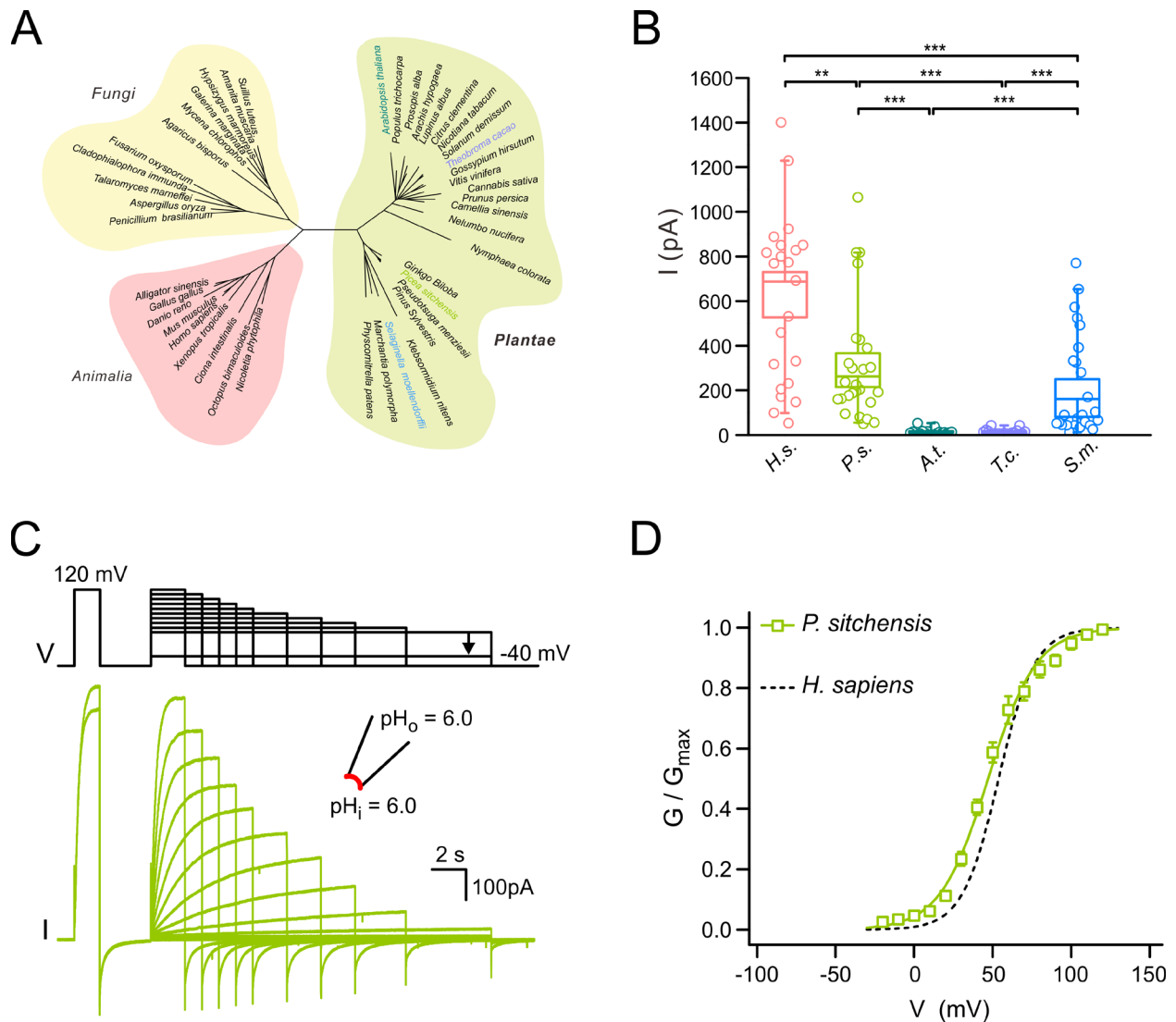


**Figure 3.2. Angiosperm Hv1 channels behave differently than their counterparts from other plant species.** **A)** Unrooted cladogram of Hv1s reveal proton channels from plant are distantly related to animal and fungal orthologs, and two distinctively clusters are formed between angiosperms and gymnosperms along with more primitive ancestors. **B)** Apparent currents were detected in membrane patches of *Xenopus* oocytes expressing proton channels, buffered at symmetrical pH 6.0, from plant species of sitka spruce (*P.s.*) and spikemoss (*S.m.*), but not from two other angiosperms (*A.t.* and *T.c.*). N is between 18-26 for five plant species. Two-sample t-tests were used for statistical analysis between every two species. \*\* $p < 0.01$ , \*\*\* $p < 0.001$ . Selected statistics are omitted for conciseness: *P.s* and *T.c.*: \*\*\*; *T.c.* and *S.m.*: \*\*\*; no statistical significance found between *A.t.* and *T.c.*, *P.s.* and *S.m.* **C)** Representative current traces for G-V measurement of *P.s* and the corresponding voltage protocol. Voltage steps from 120mV to -40mV at increment of -10mV were used. A pre-pulse at 120mV is included at the beginning of the protocol for normalizing the current rundown. **D)** G-V relationship of PsHv1 calculated from current traces like those shown in (C). Curves are Boltzmann fits. For PsHv1 shown in green,  $V_{1/2} = 40.7 \pm 1.03$  mV, slope =  $15.3 \pm 0.51$ . G-V for human Hv1 is shown as reference in dashed line ( $V_{1/2} = 53 \pm 3$  mV, slope =  $11.6 \pm 0.6$  mV, from Tombola et al. 2018). Error bars on the squares are SEM.

### ***Hvs from angiosperm require mechanical priming prior to voltage stimulation for activation***

Given the minimal current detected in the inside-out patches as well as whole cells expressing those angiosperm Hvs even under protocols with seconds-long depolarization steps, we thought about the possibility that those Hvs are in fact functional at the plasma membrane but remain quiescent under conditions that were used for recording other proton channels. Therefore, we sought for other stimuli that could possibly potentiate the channels, which were documented to facilitate the activation of other VGICs as well as human Hv1. Mechanical stretch was found to potentiate other VGICs including Navs and shifts the G-V curve to negative potentials<sup>14</sup>. Our previous work also demonstrated that mechanical stretch could facilitate the activation of human Hv1 and increase the channel conductance<sup>15</sup>.

If lacking apparent macroscopic current in AtHv1 and TcHv1 is due to the undetectably slow activation, mechanical stimuli could make the current detectable by facilitating the activation. We applied protocols including a -10mmHg pressure step lasted a few seconds (2 or 3s depending on the channels) during the resting states prior to the depolarization step, through the high-speed pressure clamp (HSPC) to the excised patches buffered in pH6.0 (Fig. 3.3A-B top panel). Exceeded our expectation, mechanical priming ahead of but not during the depolarization step led to a dramatic increase of current amplitude in AtHv1 as well as TcHv1 (Fig. 3.3B), in addition to greatly facilitated activation kinetics. Other Hvs from gymnosperm or primitive ancestor including Pshv1 and SmHv1 are also mechanosensitive, however displayed much less increase in macroscopic current and activation kinetics upon mechanical priming, even under the negative pressure that lasts 3s than 2s (Fig. 3.3A). We quantified the increase in channel conductance by measuring the peak currents before (pulse A) and after the stretch (pulse B), and reported the ratios ( $G_B/G_A$ ) as an indicator for their differential levels of mechanosensitivity (Fig. 3.3C). The dramatic changes in channel conductance that

are elicited by mechanical stimuli in these plant Hvs, especially AtHv1 and TcHv1, might suggest their intrinsic requirement to sense and function with the presence of membrane tension under physiological conditions, which is distinctively different from any other Hv1 that has been previously reported. Interestingly, voltage gating is secondary in AtHv1 and TcHv1, and those channels robustly respond to voltage only after they have been mechanically primed, rather than requiring sustained mechanical stimulation. We suspect that this mechanoreception is likely an intrinsic property that originated from part of the AtHv1 and TcHv1 channel proteins.

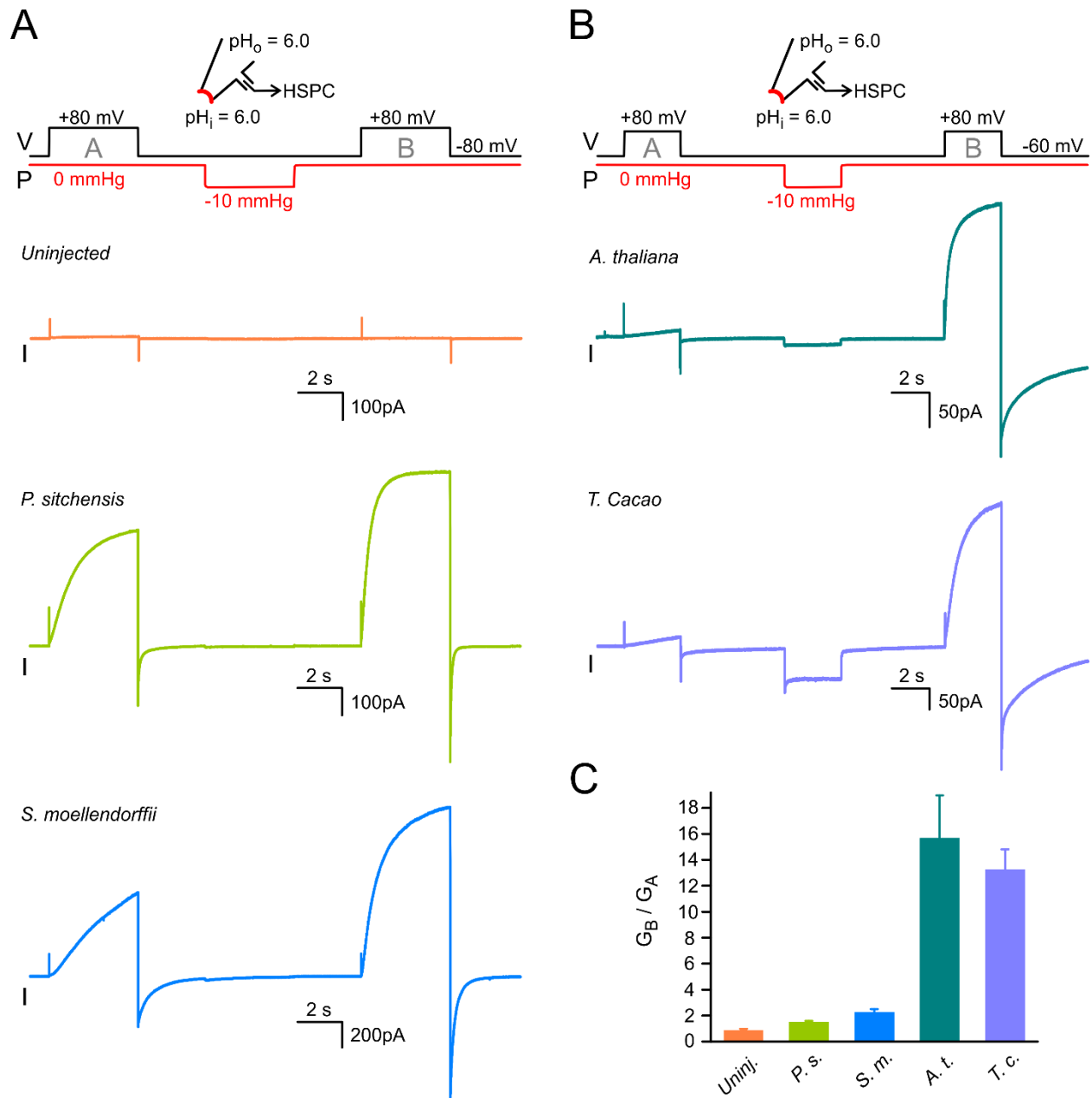


**Figure 3.3. Activation of AtHv1 and TcHv1 requires mechanical priming prior to membrane depolarization.** **A)** Representative current traces from *P. sitchensis* (green) and *S. moellendorffii* (blue) showing currents before and after the pressure pulse. Corresponding voltage and pressure protocols used are aligned at the top panel. Negative pressure at -10 mmHg lasted 3 seconds between two depolarizing pulses (pulse A and pulse B) is provided by the HSPC. Representative current traces from uninjected control undergone the same protocol is in orange. **B)** Representative current traces from *A. thaliana* (teal) and *T. cacao* (purple) showing currents before and after the pressure pulse. Shorter depolarization steps and mechanical pulse (2s for both) were used for both angiosperm Hvs. **C)** Fold increase of channel conductance from five plant Hv1s resulted from mechanical stimulation. The ratio of conductance ( $G_B/G_A$ ) is calculated from using the peak currents from Pulse B and A. N is from 4-6. Error bars are SEM.

### Plant Hvs are proton selective

An indispensable property of a voltage-gated proton channel is its superior proton selectivity. For proton channels like PsHv1 which presents sufficient current without mechanical stimulation, we could use regular protocols to measure the reversal potentials from the tail currents and compare to the Nernst potential for protons ( $E_H$ ). For PsHv1, we examined its selectivity for protons by measuring reversal potentials under different  $\Delta pH$ s across the cell membrane in the inside-out patches. Figure 3.4A shows an example where we applied repolarization steps that cover the  $E_H$ , following a depolarization step at +120mV, at  $\Delta pH$  ( $pH_o - pH_i$ ) of -0.5, and found the reversal potential is around 30mV, as is expected for perfect proton selectivity. PsHv1 is selective for protons at all tested  $\Delta pH$  (-0.5 to 1.0) conditions (Fig. 3.4B). For AtHv1 and SmHv1, measuring reversal potential without mechanical stimulation is particularly challenging due to their slow activation in nature. To speed up the channel activation and make the measurements more feasible within reasonable time scale, we delivered the negative pressure (-10mmHg pulse lasting 2 or 3 seconds) through HSPC to the membrane patches and then estimated the reversal potentials using ramps that follow the depolarization step (e.g. -40mV to 40mV at  $\Delta pH$  of 0, as shown in the inset of Fig. 3.4C and D). Both AtHv1 (Fig. 3.4C) and SmHv1 (Fig. 3.4D) demonstrate superior proton selectivity under tested  $\Delta pH$ s (-1, 0 and 1). Despite the limited sequence homology between these plant Hvs and their mammalian counterparts, an aspartate (D112 in human Hv1) from S1 and the third arginine from S4 (R211 in human Hv1) are absolutely conserved (Fig. S3.1), which were shown to be the main contributors of the selectivity filter<sup>16,17</sup> in animal Hv1s, coincide with the findings that these plant Hvs are also strictly proton selective.

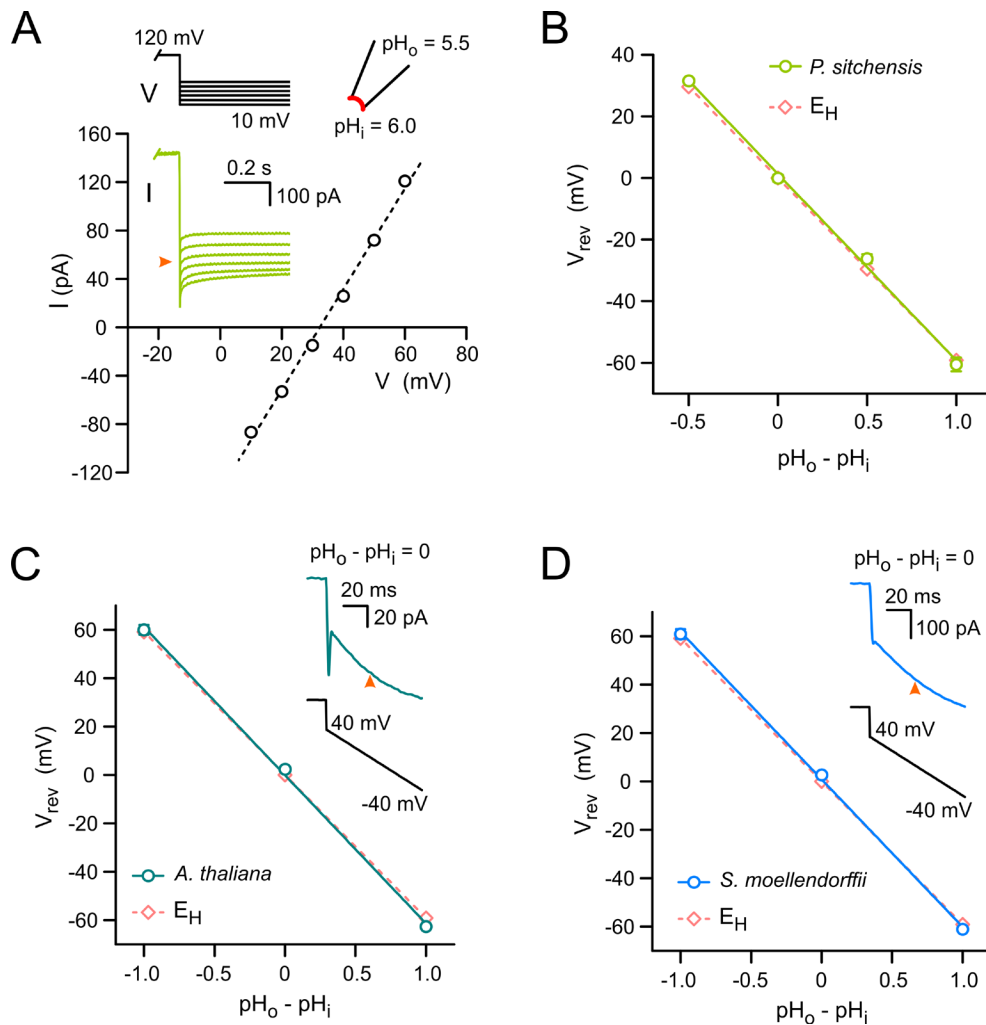


**Figure 3.4.** Hv1s from plant *P.sitchensis*, *A. thaliana*, and *S.moellendorffii* are proton selective. **A)** Representative measurement of reversal potential at  $\Delta\text{pH}=-0.5$  ( $\text{pH}_i=6.0$ ,  $\text{pH}_o=5.5$ ). Inset shows the representative tail currents and the corresponding voltage steps that cover the expected the reversal potential (orange arrow indicates current trace at 0pA). **B)** Reversal potentials of PsHv1 (green) measured at  $\Delta\text{pHs}$  (from 0.5 to 1.0) demonstrate its almost perfect proton selectivity, referenced to Nernst potential for protons ( $E_H$  in pink dashed line).  $N=4-6$  at each pH condition. Error bars are SEM. **C- D)** Reversal potentials of (C) AtHv1 (teal) and (D) SmHv1 (blue) measured at various  $\Delta\text{pHs}$  (-1.0, 0 and 1.0), referenced to  $E_H$  in pink. Inset shows the voltage protocol and the corresponding representative current trace at  $\Delta\text{pH}$  of 0.

### **Absolute pH and $\Delta\text{pH}$ dependences of voltage gating**

A common property of known Hvs is their activation is dependent on pH gradient ( $\Delta\text{pH}$ ) across membrane, and the G-V shifts around 40mV per unit of  $\Delta\text{pH}$  change<sup>6</sup>. Exceptions to this rule are Hvs from snail *Helisoma trivolvis* (HtHv1)<sup>18</sup>, and fungal Hv1s from *Aspergillus oryzae*

(AoHv1) and *Suillus luteus* (SlHv1)<sup>9</sup>. We had previously demonstrated that these greater shifts per unit of  $\Delta\text{pH}$  in fungal Hvs are likely due to their differential sensitivities to absolute pHs. While there is strong correlation between its voltage dependence and the absolute pH in SlHv1 ( $\sim 20\text{mV}/\text{pH}$  unit), AoHv1 has different sensitivities across the pH range (5.5-6.5) without obvious pattern (also see Chapter 2 Fig.2.3).

While plant Hv1s exhibit great diversity in terms of biophysical properties explored so far, we wondered whether they are also  $\Delta\text{pH}$  or absolute pH gated. Different from PsHv1, mechanical stimulation by HSPC was necessary to achieve sufficient current in reasonable time scale for the measurements in AtHv1 and SmHv1. And since measuring G-Vs with a regular step protocol within extended time period could not be easily achieved upon mechanical stimulation, especially for AtHv1 and SmHv1, we instead thought of acquiring I-V curves with voltage ramps after the initial pressure step. Other than reporting the voltage at half-maximal conductance ( $V_{1/2}$ ) derived from the Boltzmann fit of the G-V relationship, another possible indication of voltage dependence is the threshold potential ( $V_T$ ), which is the voltage at which current is firstly detected, acquired from extrapolating the maximal slope of the I-V curve (Fig. S3.3 A-B). To validate  $V_T$ s acquired from either I-Vs and G-Vs are interchangeable, we took PsHv1 as an example, and compared  $V_T$  acquired from G-Vs converted from the I-Vs ( $V_{T,IV}$ ) measured using the ramp protocol, to  $V_T$  obtained from G-Vs ( $V_{T,GV}$ ), measured using a regular step protocol, and found they are perfectly correlated under various tested pH conditions (Fig. S3.3C).

$V_T$  is particularly useful especially in cases where maximal conductance is not reached, but is  $V_T$  a good representation as  $V_{1/2}$ ? To confirm that we could reliably use  $V_T$  as an indicator for voltage dependence under different pH conditions, we demonstrated in PsHv1 that the shifts in  $V_{1/2}$  ( $\Delta V_{1/2}$ ) and shifts in  $V_T$  ( $\Delta V_T$ ) are highly consistent with each other in all tested  $\Delta\text{pH}$  conditions (Fig. S3.3D). The only limitation of using  $V_T$  derived from I-V curve is in situations

where the it comes too close to the reversal potential ( $V_{rev}$ ), therefore one can only measure  $V_T$  or  $V_{1/2}$  from the G-V curve in those cases. Taken together,  $V_T$  acquired from the I-V curve is also a reliable representation of voltage dependence of activation, similar to  $V_{1/2}$ , under most conditions.

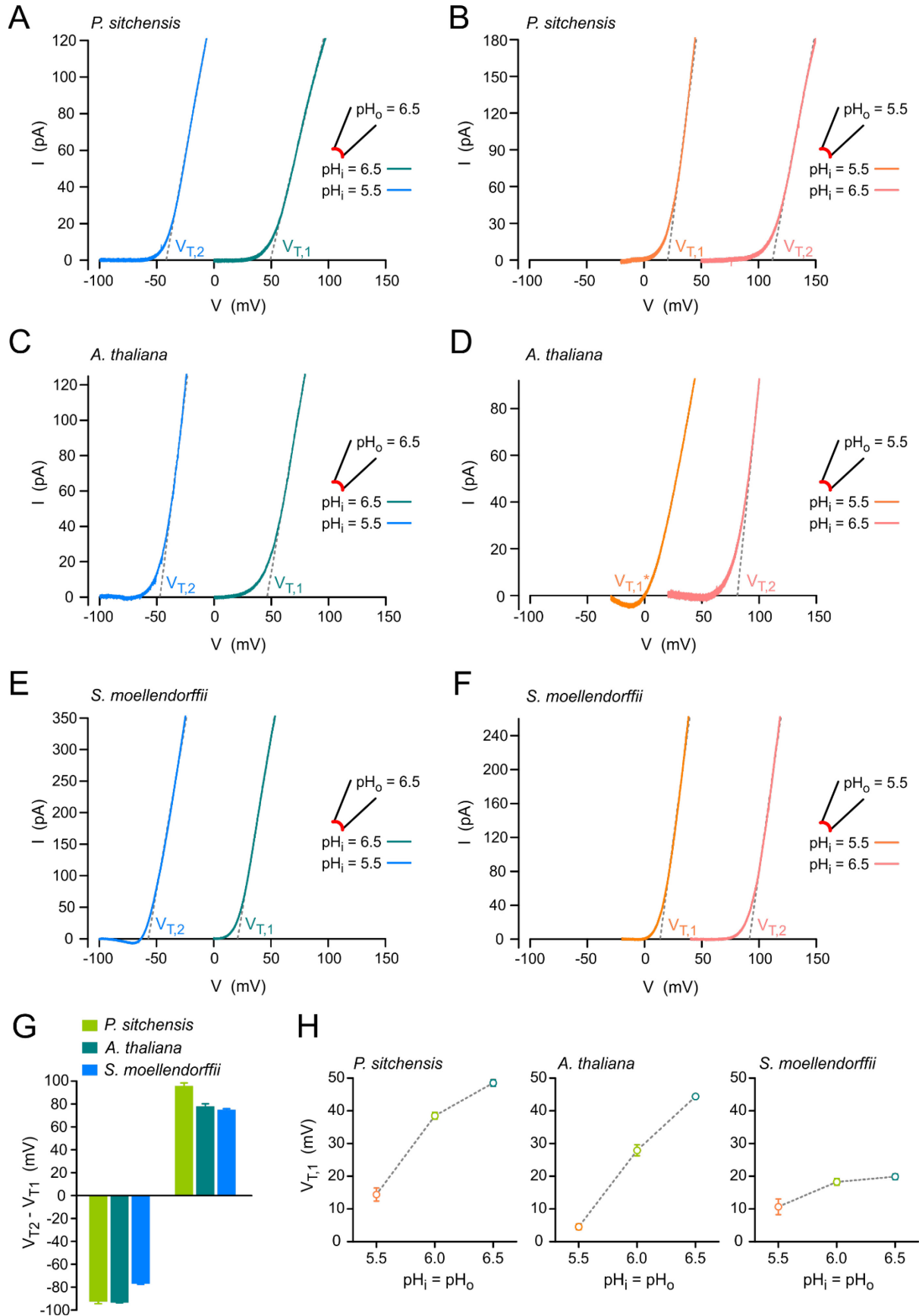


**Figure 3.5. Activation of plant Hvs are both  $\Delta\text{pH}$  dependent and absolute pH dependent.** A) I-V curve of PsHv1 in symmetric pH 6.5 (teal,  $\Delta\text{pH} = 0$ ) left shifts around 90mV ( $V_{T2} - V_{T1}$ ) when intracellular  $\text{pH}_i$  is switched to 5.5 (blue,  $\Delta\text{pH} = +1$ ). B) I-V curve of PsHv1 in symmetric pH 5.5 (orange,  $\Delta\text{pH} = 0$ ) right shifts around 90mV ( $V_{T2} - V_{T1}$ ) when intracellular  $\text{pH}_i$  is switched to 6.5 (pink,  $\Delta\text{pH} = -1$ ). C) I-V curve of AtHv1 in symmetric pH 6.5 (teal,  $\Delta\text{pH} = 0$ ) left shifts around 100mV ( $V_{T2} - V_{T1}$ ) when intracellular  $\text{pH}_i$  is switched to 5.5 (blue,  $\Delta\text{pH} = +1$ ). D) I-V curve of AtHv1 in symmetric pH 5.5 (orange,  $\Delta\text{pH} = 0$ ) right shifts around 70mV ( $V_{T2} - V_{T1}$ ) when intracellular  $\text{pH}_i$  is switched to 6.5 (pink,  $\Delta\text{pH} = -1$ ). E) I-V curve of SmHv1 in symmetric pH 6.5 (teal,  $\Delta\text{pH} = 0$ ) left shifts around 70mV ( $V_{T2} - V_{T1}$ ) when intracellular  $\text{pH}_i$  is switched to 5.5 (blue,  $\Delta\text{pH} = +1$ ). F) I-V curve of SmHv1 in symmetric pH 5.5 (orange,  $\Delta\text{pH} = 0$ ) shifts around 70mV ( $V_{T2} - V_{T1}$ ) when intracellular  $\text{pH}_i$  is switched to 6.5 (pink,  $\Delta\text{pH} = -1$ ). G) Shifts of  $V_T$  ( $V_{T2} - V_{T1}$ ) under each paired conditions from (A-F) present in bar graph. Errors are SEM. H)  $V_{T,1s}$  from Hv1s from three plant species under various symmetric pH conditions show their differential sensitivities across the pH range 5.5-6.5.

We measured the I-V curves in the following experimental setups with inside-out patches expressing PsHv1 (Fig. 3.5A-B), AtHv1 (Fig. 3.5C-D) as well as SmHv1 (Fig. 3.5E-F): 1) Record I-V curve at symmetrical pH 6.5 ( $\Delta\text{pH} = 0$ ) then measure again after switching intracellular solution to pH 5.5 ( $\Delta\text{pH} = \text{pH}_o - \text{pH}_i = 1$ ) through perfusion. 2) Record I-V curve at symmetrical pH 5.5 ( $\Delta\text{pH} = 0$ ) then measure again after switching to intracellular pH 6.5 ( $\Delta\text{pH} = \text{pH}_o - \text{pH}_i = -1$ ) through perfusion.

Interestingly, the shifts from all three plant Hvs were all more than expected 40mV with each unit of  $\Delta\text{pH}$  change, with the largest shift seen in PsHv1 (Fig. 3.5G, also see table S3.1 for values from all pH conditions). We found in PsHv1,  $V_T$  shifts around 100mV/unit of  $\Delta\text{pH}$  symmetrically ( $-92.4 \pm 2.06$  mV when  $\Delta\text{pH} = +1$ ,  $95.5 \pm 2.87$ mV when  $\Delta\text{pH} = -1$ ). In SmHv1, the shifts are less however still symmetric ( $-76.9 \pm 0.63$  mV when  $\Delta\text{pH} = +1$ ,  $74.8 \pm 1.09$  mV when  $\Delta\text{pH} = -1$ ). Whereas the shifts are asymmetric in AtHv1 ( $-93.4 \pm 0.34$  mV at  $\Delta\text{pH} = +1$ ,  $77.7 \pm 2.46$  mV at  $\Delta\text{pH} = -1$ ) and SmHv1 ( $-76.9 \pm 0.63$  mV at  $\Delta\text{pH} = +1$ ,  $74.8 \pm 1.09$  mV at  $\Delta\text{pH} = -1$ ). In addition, all three plant Hv1s demonstrate differential sensitivities across symmetrical pH conditions (Fig. 3.5H). In contrast to SmHv1, which is only weakly sensitive to absolute pH (less than 10mV/pH unit), PsHv1 and AtHv1 are much more sensitive to absolute pH changes, showing 40mV/pH unit or more, respectively.

## Pharmacology

Previous studies from our lab demonstrated that human Hv1 can be inhibited by guanidine derivatives such as 2GBI and Cl-GBI<sup>19</sup>, and residues from all four transmembrane segments (D112, F150, S181, and R211) located in the deepest region of vestibule consist the binding site. While the aspartate (D112 in hHv1) and the arginine (R211 in hHv1) are conserved across the plant Hv1s (also see Fig. S1), both the phenylalanine (F150 in hHv1) and the serine (S181 in human Hv1) are not present (F is replaced with L and S is replaced with A in all tested plant Hv1s), therefore we predict these plant Hv1s should be substantially less sensitive to 2GBI or ClGBI.

We obtained the concentration dependences of inhibition to 2GBI (Fig. 3.6A) and Cl-GBI (Fig. 3.6B) in PsHv1, in the inside-out patches with inhibitors delivered through perfusion. PsHv1 appears to be less sensitive to both inhibitors than human Hv1 (black dashed line). We also tested AtHv1 and SmHv1's sensitivities to both inhibitors at concentrations that are close to IC50s found in PsHv1, and discovered SmHv1 is similarly sensitive to both inhibitors, whereas AtHv1 is slightly more sensitive (Fig. 3.6C).

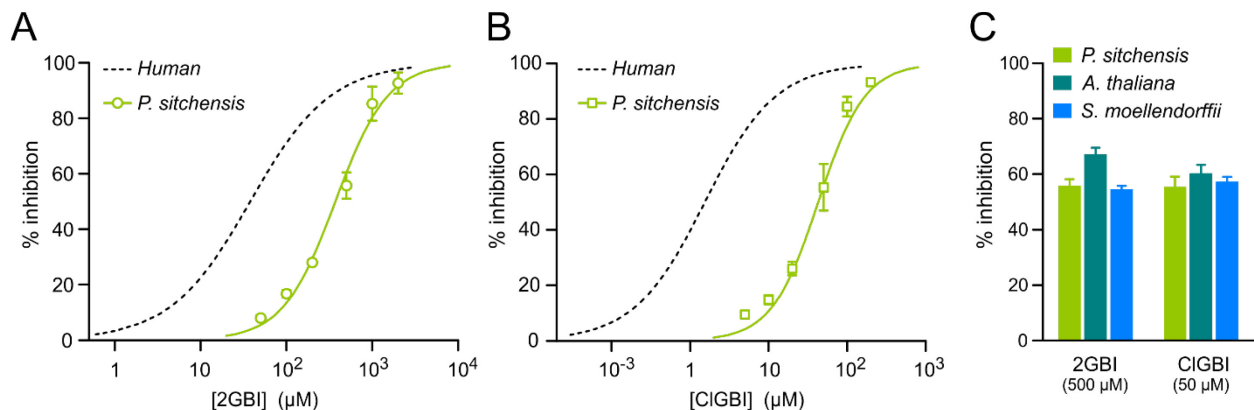


**Figure 3.6. Inhibition of Plant Hvs by 2GBI and ClGBI.** **A)** Concentration dependence of 2GBI inhibition in PsHv1 (green). Human Hv1 as reference is shown in black dashed line. **B)** Concentration dependence of ClGBI inhibition in PsHv1. Human Hv1 as reference is shown in black dashed line. **C)** Hv1s from *S. moellendorffii* and *A. thaliana* display similar levels of inhibition when subjected to 500uM 2GBI and 50uM ClGBI.

### 3.4 Discussion

We here identified and characterized the voltage-gated proton channels from plant species *Arabidopsis thaliana*, *Theobroma cacao*, *Picea sitchensis*, and *Selaginella moellendorffii*, which are members of angiosperm, gymnosperm and primitive vascular plants, respectively. All Hvs from these plant species proved to be *bonafide* proton channels with perfect proton selectivity under all tested pH conditions. Aspartate 112 from human, known to be part of the selectivity filter<sup>16</sup>, is absolutely conserved among all plant Hvs. These plant Hvs demonstrate similar structural organization as known Hvs, with VSDs consist of S1-S4 transmembrane segments, however their signature motifs in S4 are distinct and display divergence between groups: while it is S·R·R·E in angiosperm, N·R·R·H is found to be common among gymnosperm and those more primitive vascular plants.

While PsHv1 activates around the similar voltage range as human Hv1 ( $V_{1/2} = 40.7 \pm 1.03$  mV), other plant Hvs seem difficult to activate in similar depolarization voltages or even more positive voltages. Our previous work demonstrated human Hv1 are mechanosensitive and its activation can be greatly facilitated by mechanical stimulation at the membrane<sup>15</sup>. In addition, we also discovered among Hvs from two fungi species, the one that activates faster at substantially lower voltage range responds much less to the mechanical stimulation than the one that activates slower at higher voltage range<sup>9</sup>. These discoveries are in line with our hypothesis that Hv1 that responds poorly to the voltage stimulation alone could be more sensitive towards other stimuli.

We subjected SmHv1, AtHv1 and TcHv1 to mechanical stimuli and hoping it could facilitate the channel activation to some extent. Strikingly, two angiosperm Hv1 channels (AtHv1 and TcHv1, Fig. 3.3B) appeared to be the most mechanosensitive to mechanical stretch: both channels are dramatically potentiated, from almost no current detected to comparable

amplitude of currents as other species upon mechanical stimulation, using protocols at similar depolarization steps and timescale, for instance, human Hv1 and PsHv1. In these cases, membrane depolarization is effective only if the channels were pre-exposed to the mechanical stimuli, and we therefore defined this feature as requirement of “mechanical priming” before voltage activation. This unique property is distinguishable from mechanically gated ion channels, and is the first report showing members of the VGIC family respond to electrical stimulus the way they usually do only upon a one-time mechanical stimulus.

These channels bear ‘memory’ from the past mechanical stimulation: once AtHv1 or TcHv1 is mechanically primed, it remains activated for minutes, where one can easily apply depolarization steps at similar or less positive voltages to activate the channel. This also leaves us the question whether there are other stimuli that could potentiate these Hv1 channels by overcoming the energy barrier during initial priming, similar to the effects we saw from mechanical stimuli.

In mammalian Hvs, the voltage and pH dependences are coupled, and their relationship obeys the ‘rule of forty’<sup>6</sup>: their voltage dependences shift around 40mV per unit of  $\Delta$ pH change. We discovered all plant Hvs tested are outliers to this rule, but similar to previously reported fungal Hvs<sup>9</sup> and dinoflagellate Hv1<sup>8</sup>. These shifts are all significantly greater than 40mV, ranging from 60mV to 100mV (Fig.3.5). A great portion of these shifts detected in plant Hvs can be explained by their superior sensitivities to absolute pHs (20-30mV/pH unit in PsHv1 and AtHv1, <10mV/pH in SmHv1), and this suggest even different plant species might have different requirement for sensing absolute pHs (no gradient across membranes).

pH regulation by active and passive transport is universally exploited by different organisms, from animals<sup>6</sup>, fungi<sup>9</sup>, to protists<sup>7,8</sup>. pH regulation is also critical to plants: other players from the pH regulation network including H<sup>+</sup>-ATPases<sup>10</sup>, non-selective proton permeable channels, as well as antiporters (Ca<sup>2+</sup>/H<sup>+</sup> exchangers)<sup>20</sup> have been associated with plants oscillatory

growth. Interestingly, there has been speculation in the past whether there are physiological needs for plants to have proton channels<sup>21</sup>: Apoplast has a pH around 5-6, and cytoplasm is usually maintained at pH 7.2-7.5, so H<sup>+</sup>-ATPase at apoplast actively pump out protons to establish the pH gradient, it would be energetically wasteful for proton channels to leak proton back to the cytoplasm. However, we reason that at such condition where  $\Delta\text{pH}$  is always negative ( $\Delta\text{pH}=\text{pH}_{\text{Apo}}-\text{pH}_{\text{Cyt}}$ ) and the reversal potential of protons is always positive, the plant proton channel would not be activated to allow protons to flow into the cytoplasm. Given the possibility that the plant proton channel could remain quiescent from substantial voltage changes under such pH environment, our unexpected findings support the idea that other stimuli that are relevant to plant physiology such as mechanical stimulation (turgor pressure in plant), might be one of the primary modalities for activation. Mechanoreception as part of these channels' intrinsic property might be the consequence of long-term environmental adaptation.

In human immune system where Hv1 is mostly expressed, its activity is usually coupled with ROS production by the NOX enzymes, and extruding excess protons are necessary to sustain this electrogenic process. Plants do not share NOX enzymes as human, but possess respiratory burst oxidative homologs (RBOHs)<sup>22,23</sup>. For example, *Arabidopsis thaliana* has 10 RBOH genes that serve different purposes<sup>24</sup>. Since there are Ca<sup>2+</sup>-binding EF-hand and phosphorylation sites from the N-terminus of RBOH, ROS production is dependent on intracellular Ca<sup>2+</sup> and regulated by phosphorylation, ROS in turn could control the phosphorylation of many proteins<sup>23</sup>.

A common feature that is shared between human and plants is that ROS production by NOX or RBOH is essential for innate immunity upon infection<sup>23</sup>. In plant, it could be the microbial infection (bacteria and fungi) or damages caused by herbivores. In those situations, ROS signaling regulates turgor pressure of the guard cells through ion channels, receptors and

other transmembrane proteins, eventually leading to stomatal closure that gives plants protection.

ROS production can also be triggered by mechanical stimuli exogenously or endogenously, which is also involved in organ morphogenesis in plants<sup>25</sup>. For example, ROS regulates the expansion of polarized cells in root hairs and pollen tube growth<sup>20</sup>, as well as facilitating the seeds germination and ripening<sup>26</sup>. Crosstalks between second messengers such Ca<sup>2+</sup> and ROS, together with pH changes (intracellular acidification and apoplastic alkalization) in response to mechanical stimuli trigger downstream events that eventually shape the plant organs (e.g. bending of shoot and slippage of root in response to wind and obstacles in the soil, respectively)<sup>27</sup>. Our findings about AtHv1 localized to root tissues where mechanoreception is critical for plant growth and development support the notion that the proton channel itself could be mechanosensitive, highlighting its possible role in greater contexts.

### 3.5 Supplementary Information

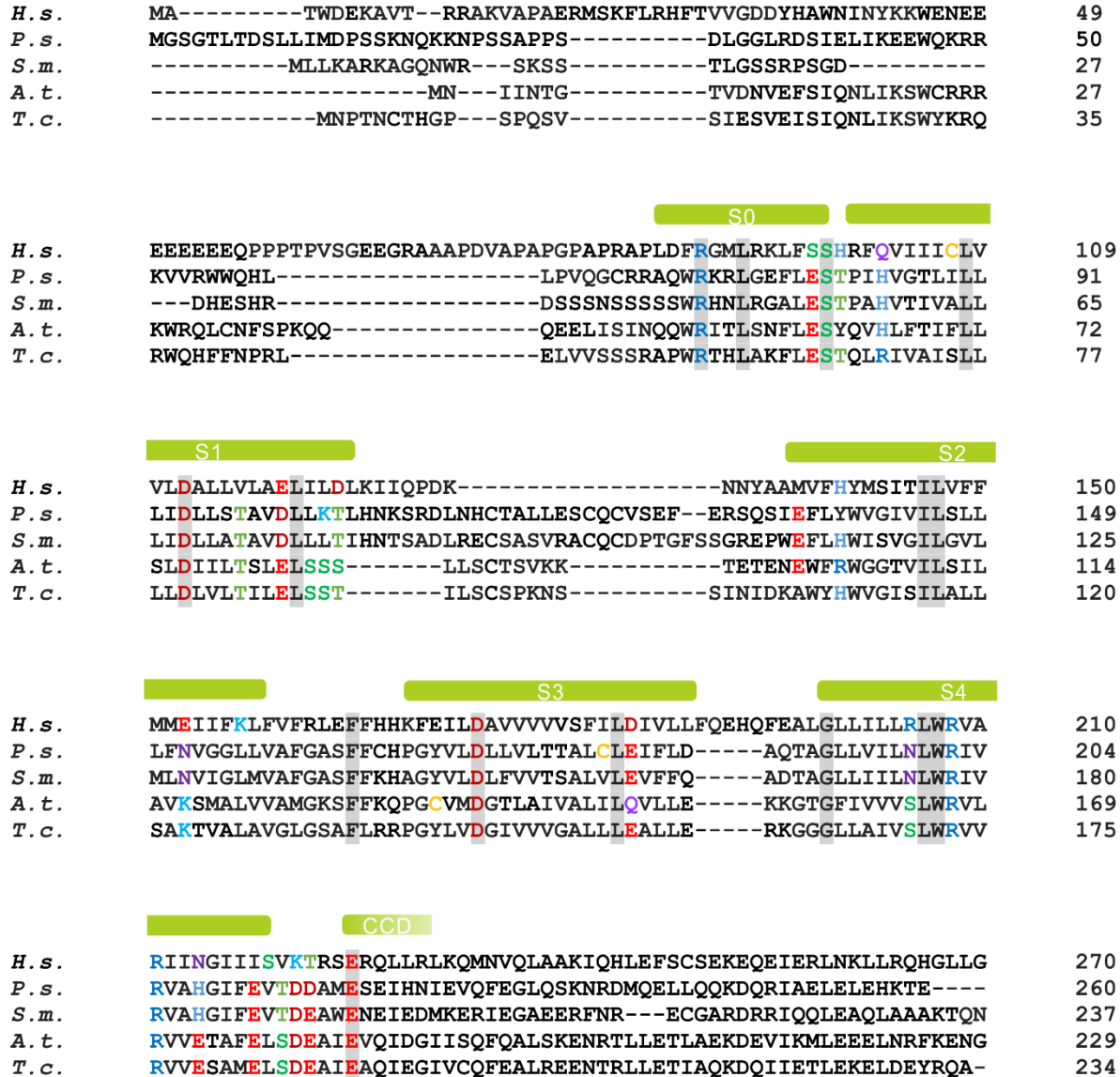
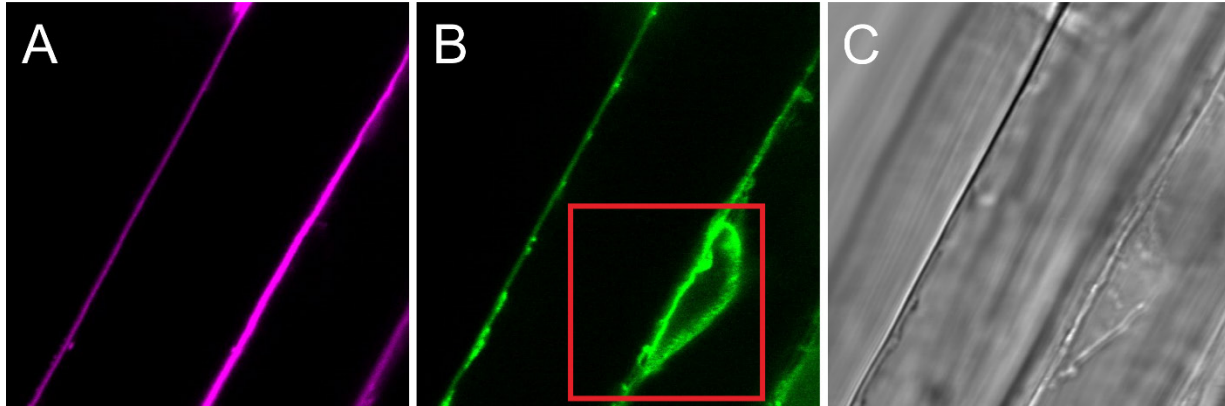
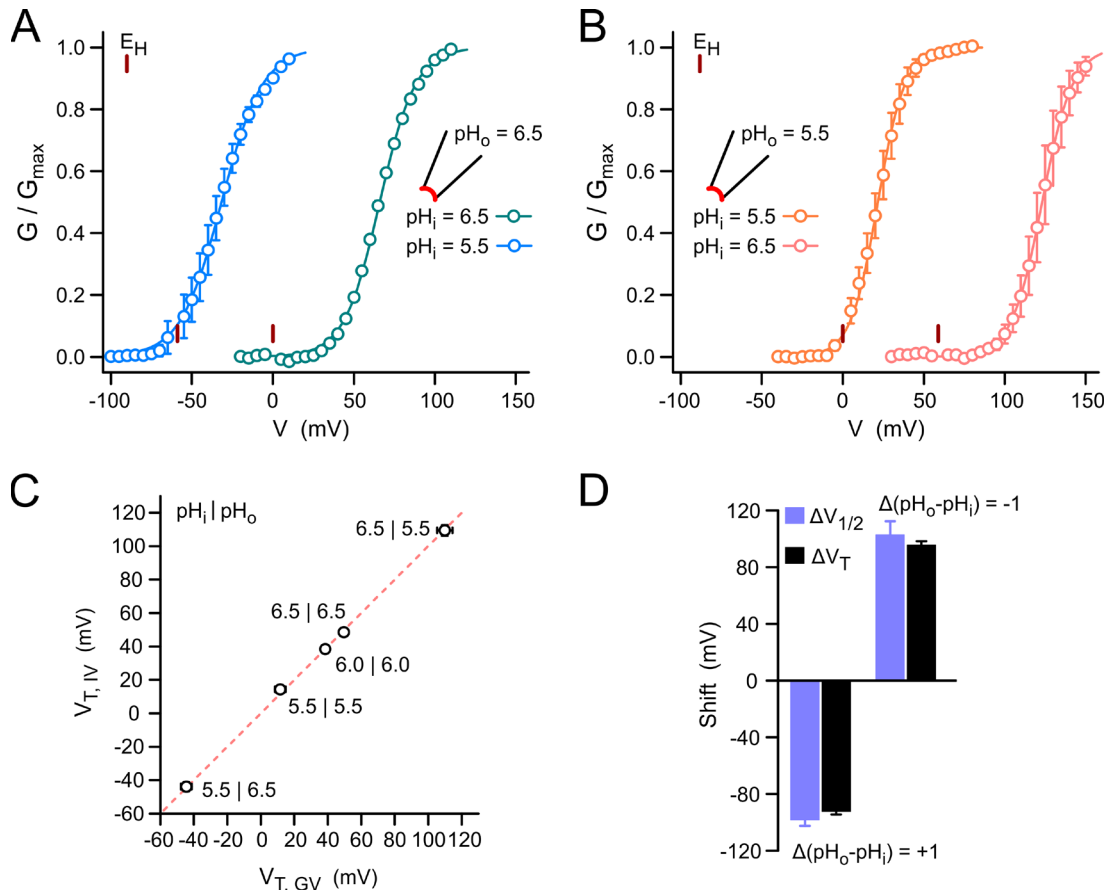


Figure S3.1. Sequence alignment of Hvs from four plant species along with human Hv1.



**Figure S3.2.** GFP-AtHv1 localized to the nuclear envelope or ER in elongated root cells when expressed in the *Arabidopsis thaliana*. **A)** Plasma membrane of elongated root cells labeled by marker FM64 in magenta. **B)** GFP-AtHv1 signal localized to the plasma membrane as well as intracellular compartments (red box), likely to be nuclear envelope or ER. **C)** TEM image of the same specimen.



**Figure S3.3.**  $V_{T,IV}$  derived from I-V relationships correlates with  $V_{T,GV}$  acquired from G-V curves in PsHv1. **A-B)** Normalized G-V relationships derived from the I-V measurements with symmetric pH conditions (pH 6.5 or 5.5), and asymmetric pH conditions ( $pH_o/pH_i = 6.5/5.5$  or  $5.5/6.5$ ). Nernst potentials

for proton are indicated as red bars for reference. **C)** Threshold potentials ( $V_T$ s) from I-V and G-V measurements demonstrate perfect correlation in all pH conditions. **D)** Shifts of voltage dependence in response to pH changes ( $\Delta\text{pH} = \pm 1$ ) are consistent between  $\Delta V_{1/2}$  and  $\Delta V_T$ .

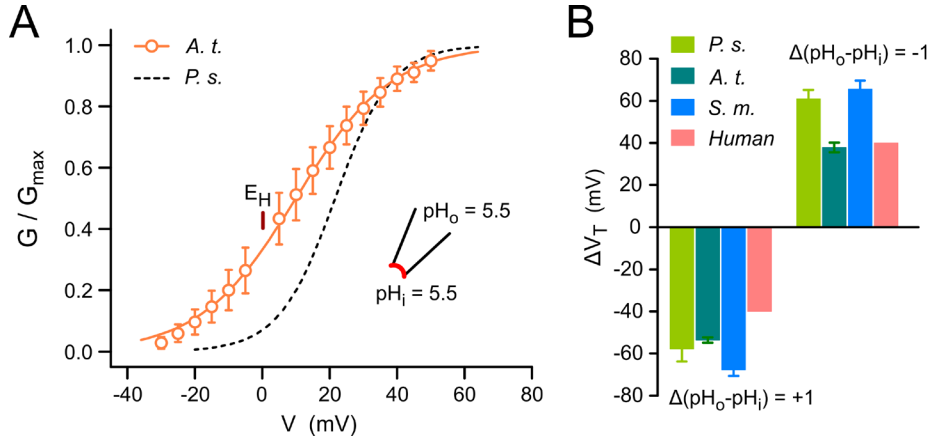


**Figure S3.4. Shifts in voltage dependence subjected to different pHs ( $\Delta\text{pH} = \pm 1$ ) from Hvs in three plant species and human. A)** AtHv1 displays left shifted and less steep G-V relationship compared to PsHv1. **B)** Shifts in  $\Delta V_T$  subjected to different pHs ( $\Delta\text{pH} = \pm 1$ ) from Hvs in three plant species. Human Hv1 is included for reference. It has around 40mV shifts per  $\Delta\text{pH}$  change as previously demonstrated by other groups.

|                 |                 | <i>P.s.</i> |           | <i>A.t.</i>  |             | <i>S.m.</i> |            |
|-----------------|-----------------|-------------|-----------|--------------|-------------|-------------|------------|
| pH <sub>o</sub> | pH <sub>i</sub> | 5.5         | 6.5       | 5.5          | 6.5         | 5.5         | 6.5        |
|                 |                 | 5.5         | 13.9±3.56 | 109.4±3.25   | 4.5± 0.84   | 82.2 ± 1.61 | 10.6 ±2.40 |
|                 | 6.5             | -43.9±2.37  | 48.5±0.97 | -49.1 ± 0.40 | 44.4 ± 0.64 | -57.0 ±0.51 | 19.9 ±0.83 |

**Table S3.1. Activation threshold potentials ( $V_T$ s) from three plant Hv1 measured at various pH conditions from the inside-out patches.**

### 3.6 References

1. Ramsey, I.S., Moran, M.M., Chong, J.A. & Clapham, D.E. A voltage-gated proton-selective channel lacking the pore domain. *Nature* **440**, 1213-6 (2006).
2. Sasaki, M., Takagi, M. & Okamura, Y. A voltage sensor-domain protein is a voltage-gated proton channel. *Science* **312**, 589-92 (2006).
3. Koch, H.P. et al. Multimeric nature of voltage-gated proton channels. *Proc Natl Acad Sci U S A* **105**, 9111-6 (2008).
4. Lee, S.Y., Letts, J.A. & Mackinnon, R. Dimeric subunit stoichiometry of the human voltage-dependent proton channel Hv1. *Proc Natl Acad Sci U S A* **105**, 7692-5 (2008).
5. Tombola, F., Ulbrich, M.H. & Isacoff, E.Y. The voltage-gated proton channel Hv1 has two pores, each controlled by one voltage sensor. *Neuron* **58**, 546-56 (2008).
6. DeCoursey, T.E. Voltage-gated proton channels: molecular biology, physiology, and pathophysiology of the H(V) family. *Physiol. Rev.* **93**, 599-652 (2013).
7. Taylor, A.R., Chrachri, A., Wheeler, G., Goddard, H. & Brownlee, C. A voltage-gated H<sup>+</sup> channel underlying pH homeostasis in calcifying coccolithophores. *PLoS Biol.* **9**, e1001085 (2011).
8. Smith, S.M. et al. Voltage-gated proton channel in a dinoflagellate. *Proc Natl Acad Sci U S A* **108**, 18162-7 (2011).
9. Zhao, C. & Tombola, F. Voltage-gated proton channels from fungi highlight role of peripheral regions in channel activation. *Commun Biol* **4**, 261 (2021).
10. Falhof, J., Pedersen, J.T., Fuglsang, A.T. & Palmgren, M. Plasma Membrane H<sup>(+)</sup>-ATPase Regulation in the Center of Plant Physiology. *Molecular plant* **9**, 323-337 (2016).
11. Pittman, J.K. & Hirschi, K.D. CAX-ing a wide net: Cation/H<sup>(+)</sup> transporters in metal remediation and abiotic stress signalling. *Plant biology (Stuttgart, Germany)* **18**, 741-9 (2016).
12. Madeira, F. et al. The EMBL-EBI search and sequence analysis tools APIs in 2019. *Nucleic Acids Res.* **47**, W636-W641 (2019).
13. Letunic, I. & Bork, P. Interactive Tree Of Life (iTOL) v4: recent updates and new developments. *Nucleic Acids Res.* **47**, W256-W259 (2019).
14. Morris, C.E. Voltage-gated channel mechanosensitivity: fact or friction? *Frontiers in physiology* **2**, 25 (2011).
15. Pathak, M.M. et al. The Hv1 proton channel responds to mechanical stimuli. *J. Gen. Physiol.* **148**, 405-418 (2016).
16. Musset, B. et al. Aspartate 112 is the selectivity filter of the human voltage-gated proton channel. *Nature* **480**, 273-7 (2011).
17. Berger, T.K. & Isacoff, E.Y. The pore of the voltage-gated proton channel. *Neuron* **72**, 991-1000 (2011).
18. Thomas, S. et al. Exotic properties of a voltage-gated proton channel from the snail *Helisoma trivolvis*. *J. Gen. Physiol.* **150**, 835-850 (2018).
19. Hong, L., Kim, I.H. & Tombola, F. Molecular determinants of Hv1 proton channel inhibition by guanidine derivatives. *Proc Natl Acad Sci U S A* **111**, 9971-6 (2014).
20. Mangano, S., Juárez, S.P. & Estevez, J.M. ROS Regulation of Polar Growth in Plant Cells. *Plant Physiol.* **171**, 1593-605 (2016).
21. Felle, H.H. pH: Signal and Messenger in Plant Cells. *Plant Biol.* **3**, 577-591 (2001).
22. Inupakutika, M.A., Sengupta, S., Devireddy, A.R., Azad, R.K. & Mittler, R. The evolution of reactive oxygen species metabolism. *J. Exp. Bot.* **67**, 5933-5943 (2016).
23. Segal, A.W. NADPH oxidases as electrochemical generators to produce ion fluxes and

- turgor in fungi, plants and humans. *Open biology* **6**(2016).
24. Orman-Ligeza, B. et al. RBOH-mediated ROS production facilitates lateral root emergence in *Arabidopsis*. *Development* **143**, 3328-39 (2016).
  25. Huang, H., Ullah, F., Zhou, D.X., Yi, M. & Zhao, Y. Mechanisms of ROS Regulation of Plant Development and Stress Responses. *Frontiers in plant science* **10**, 800 (2019).
  26. El-Maarouf-Bouteau, H. & Bailly, C. Oxidative signaling in seed germination and dormancy. *Plant signaling & behavior* **3**, 175-82 (2008).
  27. Monshausen, G.B., Bibikova, T.N., Weisenseel, M.H. & Gilroy, S. Ca<sup>2+</sup> regulates reactive oxygen species production and pH during mechanosensing in *Arabidopsis* roots. *Plant Cell* **21**, 2341-56 (2009).

## Chapter 4: Development of HIFs: arginine-mimic inhibitors of Hv1 with improved VSD-ligand interactions

(Zhao, Hong, Galpin, Riahi, Lim, Webster, Tobias, Ahern, Tombola)

### Abstract

The human voltage-gated proton channel Hv1 is a drug target for cancer, ischemic stroke, and neuroinflammation. It resides on the plasma membrane and endocytic compartments of a variety of cell types where it mediates outward proton movement and regulates the activity of NOX enzymes. Its voltage-sensing domain (VSD) contains a gated and proton-selective conduction pathway, which can be blocked by aromatic guanidine derivatives such as 2-guanidinobenzimidazole (2GBI). Mutation of Hv1 residue F150 to alanine was previously found to increase 2GBI apparent binding affinity more than two orders of magnitude. Here, we explore the contribution of aromatic interactions between the inhibitor and the channel in the presence and absence of the F150A mutation, using a combination of electrophysiological recordings, classic mutagenesis, and site-specific incorporation of fluorinated phenylalanines via nonsense suppression methodology. Our data suggest that the increase in apparent binding affinity is due to a rearrangement of the binding site allowed by the smaller residue at position 150. We then use this information to design new arginine mimics with improved affinity for the non-rearranged binding site of the wild type channel. The new compounds, named “Hv1 Inhibitor Flexible” (HIFs), consist of two “prongs”, an aminoimidazole ring and an aromatic group connected by extended flexible linkers. Some HIF compounds display inhibitory properties that are superior to those of 2GBI, thus providing a promising scaffold for further development of high-affinity Hv1 inhibitors.

## 4.1 Introduction

The Hv1 protein (also known as HVCN1 or VSOP) consists of four transmembrane helices, S1 through S4, forming a proton-conducting VSD<sup>1,2</sup> and lacks the pore domain typical of other voltage-gated ion channels<sup>3,4</sup>. Hv1 regulates cellular pH homeostasis and the production of reactive oxygen species by NOX enzymes<sup>5-7</sup>. Its activity has been reported to increase tumor metastatic potential in different types of cancer<sup>8-10</sup>, and to worsen brain damage after ischemic stroke<sup>11,12</sup> in an age-dependent manner<sup>13</sup>, motivating the development of Hv1 inhibitors as potential anticancer drugs and neuroprotective agents. The role of microglial Hv1 in exacerbating inflammation in traumatic brain injury<sup>14</sup> and its contribution to motor deficits after spinal cord injury<sup>15</sup> point to further useful applications of Hv1 inhibitors. Furthermore, Hv1 activity has been found to promote human sperm cell capacitation and motility<sup>16,17</sup>, suggesting that Hv1 antagonists could be used to aid male contraceptive treatments<sup>18</sup>.

Two major strategies have proved successful in developing ligands targeting the Hv1 VSD: one focused on the use of peptide toxins binding the channel extracellular side<sup>19-21</sup>, the other focused on small organic molecules targeting the channel intracellular side<sup>22-25</sup>. Some of these ligands have found applications as pharmacological tools to study the channel gating and permeation mechanisms of proton-conducting VSDs<sup>26-30</sup>, and the role of Hv1-mediated proton currents in cellular physiology<sup>20,31-33</sup>. Drug screening approaches on native proton currents, or on other ion channels, have led to the identification of additional potential ligands<sup>34-37</sup>. However, the mechanism of action of these compounds has yet to be determined.

Like the VSDs of other voltage-gated channels, the Hv1 VSD changes conformation in response to membrane depolarization as its S4 helix transitions from a down state to an up state<sup>38-41</sup>. The change in conformation also opens the conduction pathway, allowing protons to reach the selectivity filter located deep in the core of the VSD<sup>42,43</sup>. The arginine-mimic 2-guanidinobenzimidazole (2GBI) inhibits the human Hv1 channel by binding to the intracellular

vestibule of the open VSD in the proximity of the selectivity filter<sup>23,26,29,41</sup>. Among the residues involved in 2GBI binding, phenylalanine 150, located in the S2 helix, was found to play a particularly important role<sup>22</sup>. The wild-type channel (WT) is inhibited by 2GBI in the micromolar concentration range<sup>23,44</sup>. However, when F150 is mutated to alanine, inhibition occurs in the nanomolar range<sup>23</sup> (Fig. 4.1A-B,  $IC_{50,WT} = 38 \pm 2 \mu M$ ,  $IC_{50,150A} = 118 \pm 7 nM$ ). Understanding the molecular mechanism underlying this difference can lead to the design of new arginine mimics with higher binding affinity for the non-mutated channel.

Here, we explore the effect of the F150A mutation on 2GBI-mediated inhibition using both standard mutagenesis and unnatural amino acid substitutions and find evidence of a local rearrangement in the binding site that leads to the increase in affinity. We then use this information to design more potent inhibitors for the wild type channel. We investigate the effect of fluorination on aromatic rings involved in ligand-channel interactions and find that modifications of the six-membered ring of the inhibitor can negatively affect binding of the condensed five-membered ring. In the new HIF inhibitors, the two rings are separated by an extended linker. We show that the separation improves the apparent binding to the WT channel over the F150A mutant and allows the fluorination of the six-membered ring to be fully effective at strengthening ligand-channel interactions.

## 4.2 Materials and Methods

### *DNA constructs and channel expression*

Constructs containing the sequence of the human HVCN1 channel were generated from cDNA kindly provided by David Clapham<sup>1</sup> and from IMAGE clone 5577070 (Open Biosystems). Mutagenesis was performed as in<sup>23,45</sup>. The monomeric version of Hv1 (Hv1NC<sub>VSP</sub>) was previously described<sup>27</sup>. All constructs were subcloned in the pGEMHE vector<sup>46</sup> and linearized with NheI or SphI restriction enzymes (New England Biolabs) before *in vitro* transcription. cRNAs were synthesized using T7 mMessage mMachine transcription kit (Ambion). *Xenopus* oocytes from Ecocyte Bioscience or *Xenopus* 1 were injected with cRNAs (50 nl per cell, 0.5-1.5 ng/nl) 1-3 days before the electrophysiological measurements. Injections were performed with a Nanoject II (Drummond Scientific). Cells were kept at 18 °C in ND96 medium containing 96 mM NaCl, 2 mM KCl, 1.8 mM CaCl<sub>2</sub>, 1 mM MgCl<sub>2</sub>, 10 mM HEPES, 5 mM pyruvate, 100 mg/ml gentamycin (pH 7.2).

### *Unnatural amino acid substitutions*

Amber (UAG) stop codons were introduced at specific positions of HVCN1 constructs using site directed mutagenesis. To ensure proper termination of translation, the native UAG stop codon was replaced by a UAA stop codon. Preparation of synthetic aminoacyl-tRNAs was performed as previously described<sup>47</sup>. In brief, N-Boc protected amino acids were activated as cyanomethyl esters for subsequent coupling to the hybrid dinucleotide phospho-deoxycytidine-phospho-adenosine (pdCpA). Modified tRNA from *Tetrahymena thermophila* (THG73) containing the CUA anticodon was generated *in vitro* and ligated to pdCpA carrying the amino acid at the 3'-end. Deprotected aminoacyl-tRNAs were kept at -80 °C until use. Right before injection, frozen tRNA aliquots were resuspended in ice-cold RNAase-free water. After centrifugation at 4 °C for 25 minutes at 9600 g, the solutions were transferred in prechilled tubes containing cRNAs with

amber stop codons at positions F150 or F182. The resulting mixtures had cRNA:tRNA ratios of 1:1 (w/w). 50 nl of mixture were injected per cell. Injection of constructs with amber stop codons in the absence of tRNA, or in the presence of non-acylated tRNA did not produce measurable currents. Acylated tRNA carried either non-substituted phenylalanine (Phe) or one of the following fluorinated amino acids: 4-fluoroPhe (PheF), 3,4-difluoroPhe (Phe2F), or 3,4,5-trifluoroPhe (Phe3F).

### ***Patch clamp measurements***

Voltage-clamp measurements were performed in inside-out patch configuration, using an Axopatch 200B amplifier controlled by pClamp10 software through an Axon Digidata 1440A (Molecular Devices). The signal was lowpass filtered at 1 kHz (Bessel, -80 dB/decade) before digitalization (2 kHz sampling). For display purposes, it was further filtered offline at 200 or 150 Hz (Bessel, -80 dB/decade). Bath and pipette solutions contained 100 mM 2-(N-morpholino) ethanesulphonic acid (MES), 30 mM tetraethylammonium (TEA) methanesulfonate, 5 mM TEA chloride, 5 mM ethylene glycol-bis(2-aminoethyl)-N,N,N',N'-tetra-acetic acid (EGTA), adjusted to pH 6.0 with TEA hydroxide. All measurements were performed at  $22 \pm 1$  °C. Pipettes had 1-3 M $\Omega$  access resistance. Unless otherwise specified, the holding potential was -40 mV and the depolarization potential +120 mV. Channel inhibition was determined by isochronal current measurements at the end of the depolarization pulses. Hv1 inhibitors were introduced in the bath using a computer-controlled gravity-fed multi-valve perfusion system (Warner Instruments).

### ***Tested Hv1 ligands***

All tested compounds were at the highest purity commercially available. 2-aminobenzimidazole (ABI), 2-guanidinobenzimidazole (2GBI), 2-aminobenzothiazole (ABTA), and 2-guanidino-

benzothiazole (GBTA) were from Sigma-Aldrich. 6-fluoro-1H-1,3-benzodiazol-2-amine (ABIF<sub>β</sub>), 5,6-difluoro-1H-1,3-benzodiazol-2-amine (ABIF<sub>2</sub>), and 4,5,6-trifluoro-1H-1,3-benzodiazol-2-amine (ABIF<sub>3</sub>) were from Enamine. 4-fluoro-1H-1,3-benzodiazol-2-amine (ABIF<sub>α</sub>) was from Combi-Blocks. HIF, HIF<sub>NF</sub>, HIF<sub>NH</sub>, HIF<sub>OH</sub>, and HIF<sub>EN</sub> were custom synthesized by Enamine at a minimum purity of 95% (LCMS). See Supplementary Methods for characterization.

### Data analysis

Current traces were analyzed using Clampfit10.2 (Molecular Devices) and Origin8.1 (OriginLab). Leak subtraction, run-down correction, and the derivation of concentration dependence curves were performed as in <sup>23</sup>. Concentration dependences were fitted with the Hill equation (1):

$$\%i = \%i_{max}[ligand]^h / ([ligand]^h + IC_{50}^h)$$

where %<sub>i</sub> is the percentage of inhibition at the ligand concentration [*ligand*], %<sub>i,max</sub> is (1)

the percent of maximal inhibition (assumed to be 100%) <sup>22,23</sup>, IC<sub>50</sub> is the half maximal

inhibitory concentration, and *h* is the Hill coefficient. The Hill coefficients for all the measured concentration dependences were in the range 0.83 - 1.28 (see Table S4.1 for details) in

agreement with earlier findings <sup>22,27</sup>. ΔG<sub>i</sub> free energies were estimated using the relationship:

ΔG<sub>i</sub> = RTlnIC<sub>50</sub>, where R is the gas constant and T the absolute temperature.

G-V curves were derived from tail currents as previously described <sup>23,48</sup>. Current rundown was

corrected using a reference depolarization step preceding the test depolarization. Conductance

was determined from  $G(V_{test}) = (I_{test} - I_{tail}) / (V_{test} - V_{tail})$ , where *I*<sub>tail</sub> and *V*<sub>tail</sub> are the tail current and

voltage (-40 mV) following the depolarization step at *V*<sub>test</sub> (ranging from -30 mV to +120 mV),

and *I*<sub>test</sub> is the current measured at the end of the depolarization step. *G*<sub>max</sub> was determined

from maximal *I*<sub>tail</sub> (and corresponding *I*<sub>test</sub>) in the *V*<sub>test</sub> region in which the tail current (2)

saturated. G-V plots were fitted with the Boltzmann equation (2):

$$G/G_{max} = 1 / (1 + e^{(V_{1/2} - V)/s})$$

where  $V_{1/2}$  is the potential of half maximal activation, and  $s$  is the slope, all in mV. Unless otherwise specified, data are reported as averages from at least four independent measurements, and error bars are standard error of the mean (SEM). Fitting parameters are shown with standard error (SE). Each average comes from measurements performed on at least two distinct batches of cells. A Welch's t-test was used for statistical analysis of datasets for two compared conditions. A one-way ANOVA test with Tukey's post hoc correction was used for multiple comparison analysis. No randomization or blinding was applied to this study.

### ***Docking calculations and molecular dynamics simulations***

HIF was parameterized using CGenFF version 2b4<sup>49,50</sup>. MD simulations of HIF-bound Hv1 VSD embedded in a solvated POPC lipid bilayer were performed using NAMD 2.13<sup>51</sup>. The CHARMM36 force field<sup>52,53</sup> was used for both protein and lipid, and the TIP3P model was used for water<sup>54</sup>. The model of the human Hv1 VSD in the up state was from<sup>41</sup>. The final structure of a 25 ns-long trajectory of the Hv1 VSD + 2GBI was used as the initial structure of the Hv1 VSD + HIF system, where 2GBI was substituted by a HIF molecule (aligned and superimposed on to the 2GBI structure). Subsequently, 50 steps of geometry optimization and 1 ns of equilibration under NVT conditions were performed followed by a 25 ns of isothermal-isobaric ensemble simulation. Langevin MD<sup>55</sup> with  $1 \text{ ps}^{-1}$  frictional coefficient and Nose-Hoover barostat<sup>56</sup> were used to maintain the temperature and pressure at 300 K and 1 atm, respectively. MD trajectories were obtained with the time step of 2 fs while all bonds involving H atoms were constrained using the SHAKE algorithm<sup>57</sup>. The system composed of 10784, 175, 33, and 38 water, lipid, Na, and Cl molecules, respectively, inside an orthorhombic box unit cell ( $82.0 \times 82.0 \times 83.6 \text{ \AA}^3$ ) under periodic boundary conditions. The short ranged nonbonded interactions were included at the 12 Å cutoff distance and the long-range electrostatic interactions were incorporated using the Particle Mesh Ewald (PME) algorithm<sup>58</sup>. The system was simulated under

0 mV membrane potential.

### ***In silico ADMET predictions***

Absorption, Distribution, Metabolism, and Excretion - Toxicity (ADMET) properties of 2GBI and HIF compounds were predicted using online tools available at SwissADME (<http://www.swissadme.ch>), XenoSite (<https://swami.wustl.edu/xenosite>), and MetaTox ([www.way2drug.com/mg2](http://www.way2drug.com/mg2)).

SwissADME<sup>59</sup> provides predictions on pharmacokinetics, drug-likeness and medicinal chemistry friendliness. Through its BOILED-Egg model, it predicts gastrointestinal absorption and brain penetration of small molecules<sup>60</sup>. XenoSite uses a robust neural-network model to predict the atomic sites at which xenobiotics will undergo metabolic modification by Cytochrome P450 enzymes<sup>61</sup>, whereas MetaTox utilized the GUSAR algorithm<sup>62</sup> to estimate the integrated toxicity of xenobiotics and their predicted metabolites expressed as LD<sub>50</sub> for rats with intravenous type of administration<sup>63</sup>.

### 4.3 Results

#### *Mutation F150A induces a local rearrangement in the 2GBI binding site*

An earlier mutant cycle analysis of 2GBI binding uncovered an interaction between the condensed phenyl ring of the inhibitor and the aromatic ring of F150<sup>22</sup> but the mechanism of this interaction remained unexplored. If either direct steric hindrance or aromatic interactions between rings had a dominant effect on binding, a tryptophan substitution at position 150 would be expected to substantially affect the overall ligand-channel interaction. To test this possibility, we replaced F150 with tryptophan by standard site-directed mutagenesis, expressed the mutant channel in *Xenopus* oocytes and measured the inhibition curve (concentration dependence of inhibition) of the resulting proton currents in excised membrane patches (Fig. 4.1B). The amino acid substitution produced only a minor change in the inhibition curve ( $IC_{50,150W} = 52 \pm 2 \mu\text{M}$ ), suggesting that the effect of mutation F150A involves a more complex mechanism.

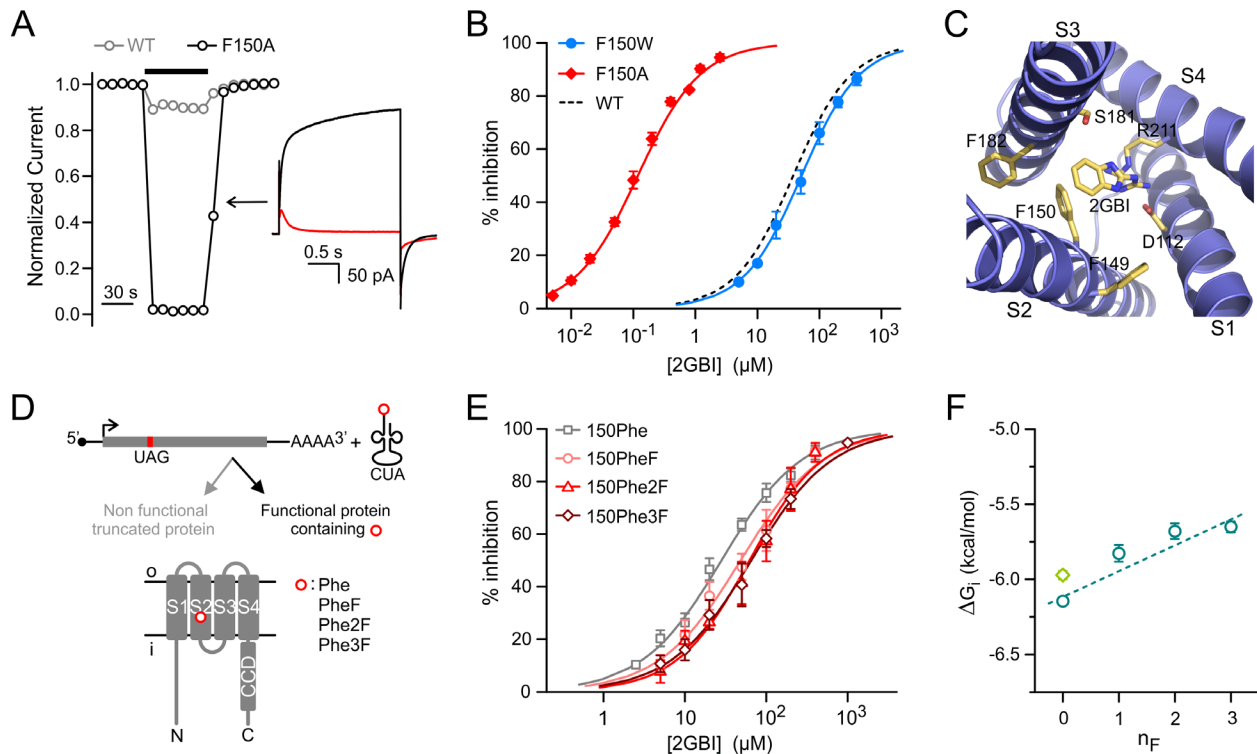


**Figure 4.1. Exploring how residue F150 influences Hv1 sensitivity to 2GBI. A)** Drop in normalized current produced by  $2\mu\text{M}$  2GBI in Hv1 WT and F150A. Black bar indicates the presence of the inhibitor in

the bath solution. Representative traces from Hv1 F150A before (black) and after (red) addition of 2 $\mu$ M 2GBI (inset). Measurements were performed in inside-out patch configuration. Currents were assessed at the end of a depolarization step to +120 mV from a holding potential of -40 mV, pH<sub>i</sub> = pH<sub>o</sub> = 6.0. **B**) Concentration dependence of 2GBI-mediated inhibition of Hv1 mutants F150A and F150W compared to WT. Data points are averages of at least 6 independent measurements. Error bars are SD. **C**) Structural model of the VSD of the human Hv1 in the open state from Geragotelis et al., 2020, showing the positions of F149 and F182 relative to F150 and other residues in the binding site (residue-ligand centroid distances in Å: 5.2 for F150, 8.5 for F149, and 9.1 for F182). **D**) Schematics of unnatural amino acid substitution approach. **E**) Concentration dependences of 2GBI-mediated inhibition of Hv1 constructs in which F150 is substituted with the indicated amino acids using the approach shown in (D). Data points are averages from 3-7 independent measurements  $\pm$  SD. Curved lines in (B) and (E) represent fits of the data using Eq. 1. See Table S4.1 for fit parameters. **F**)  $\Delta G_i$ s measured from IC<sub>50</sub>s from (E) as a function of the number of fluoro substituents in the phenylalanine ring. Light-green diamond is the value for Hv1 WT. Error bars are SE. Dashed line is the linear fit of the data points in teal.

Compared to phenylalanine, tryptophan is larger in size and can engage in stronger cation- $\Pi$  or  $\Pi$ -stacking interactions with positively charged or aromatic ligands, respectively. Thus, the F150W substitution may have a mixed effect on 2GBI binding, with a destabilizing component caused by an increase in steric hindrance and a stabilizing component caused by strengthened aromatic interactions. To dissect interactions with opposing effects, we manipulated the  $\Pi$  electron-density of F150 by unnatural amino acid substitutions (UAS) via codon-suppression technology<sup>64-66</sup> (Fig. 4.1D). Due to their high electronegativity and compact size, fluoro-substituents are particularly suitable for altering the  $\Pi$  electron-density of aromatic rings without causing large steric perturbations. Fluoro-substitutions affect both cation- $\Pi$  and  $\Pi$ -stacking interactions and have been previously used to uncover the role of aromatic residues in the stabilization of protein conformations and ligand binding<sup>67,68</sup>.

We first verified that introducing phenylalanine with no substituents at position 150 using the codon-suppression method produced channels with the same properties of wild-type Hv1 (Fig. S4.1). We then replaced the ring of F150 with rings containing one, two, or three fluoro-substituents and measured 2GBI inhibition curves for each modified channel (Fig. 4.1E). We calculated apparent binding free energy ( $\Delta G_i$ ) values from IC<sub>50</sub>s and plotted them as a function of the number of fluoro-substituents ( $n_F$ ) in F150 (Fig. 4.1F). We observed a positive correlation between  $\Delta G_i$  and  $n_F$ , suggesting a destabilization of 2GBI apparent binding ( $\Delta G_i$

becomes less negative) with the reduction of the  $\Pi$ -electron density at F150. This result is consistent with the existence of a cation- $\Pi$  interaction between 2GBI and F150. However, the stabilizing contribution of the interaction appears to be modest, as indicated by the shallow slope of the linear fit in Fig. 4.1F ( $\Delta G_i/\Delta n_F = 0.17 \pm 0.03$  kcal/mol).

The weakly stabilizing interaction between 2GBI and F150 in Hv1 WT must be replaced by stronger interactions between the ligand and the binding site in Hv1 F150A to account for the lower  $IC_{50}$  of the mutant channel. We considered the possibility that the replacement of the aromatic ring of F150 with the small methyl group of alanine could cause rearrangements in the side-chains of neighboring residues, resulting in new stabilizing interactions with the inhibitor molecule. We searched for candidate side chains in a structural model of the human Hv1 VSD in the open conformation, built using the 3WKV crystal structure<sup>41</sup> as initial template (Fig. 4.1C). We noticed that F150 is in proximity to other two aromatic residues: F149 and F182 and hypothesized that one of these residues could be closer to the inhibitor in the F150A mutant producing a stabilization of 2GBI binding.

Stabilizing aromatic interactions between 2GBI and a phenylalanine in the binding site are expected to be abolished by an alanine substitution at the phenylalanine position, leading to a shift of the inhibition curve to higher inhibitor concentrations (right shift). Conversely, the same interactions are expected to be strengthened by a tryptophan substitution, leading to a shift of the inhibition curve to lower inhibitor concentrations (left shift). Hence, to determine whether F149 or F182 participate in 2GBI binding in Hv1 F150A, we measured inhibition curves for channels in which F149 or F182 were replaced by either an alanine or a tryptophan, in the presence and absence of the additional mutation F150A.

When F150 was not mutated, alanine or tryptophan substitutions at F149 or F182 produced negligible changes in the inhibition curve (Fig. 4.2A, C), confirming our previous finding that

these phenylalanines are not involved in 2GBI binding in wild type Hv1<sup>22</sup>. In the presence of F150A however, the same substitutions perturbed 2GBI-mediated inhibition in different ways (Fig. 4.2B, D). The inhibition curve was shifted to lower concentrations by the F149A mutation and was unaffected by the F149W mutation (Fig. 4.2B,  $IC_{50,150A,149A} = 14 \pm 2$  nM,  $IC_{50,150A,149W} = 123 \pm 6$  nM). On the other hand, the inhibition curve was shifted to higher concentrations by the F182A mutation and to lower concentrations by the F182W mutation (Fig. 4.2D,  $IC_{50,150A,182A} = 826 \pm 22$  nM,  $IC_{50,150A,182W} = 33 \pm 1$  nM).

The changes in  $IC_{50}$  caused by mutations F182A and F182W in the presence of F150A are consistent with a stabilizing interaction between 2GBI and F182 via aromatic interactions. In contrast, the shift of the inhibition curve to lower concentrations observed with the F149A substitution (Fig. 4.2B) suggests that additional rearrangements of the binding site are responsible for binding stabilization in the F149A-F150A channel. Furthermore, replacing F149 with leucine, rather than alanine, produced only a negligible shift in the inhibition curve (F149L, Fig. 4.2B), indicating that the effect of the F149A mutation is most likely due to the reduction in the size of the side-chain rather than the loss of the aromatic ring.

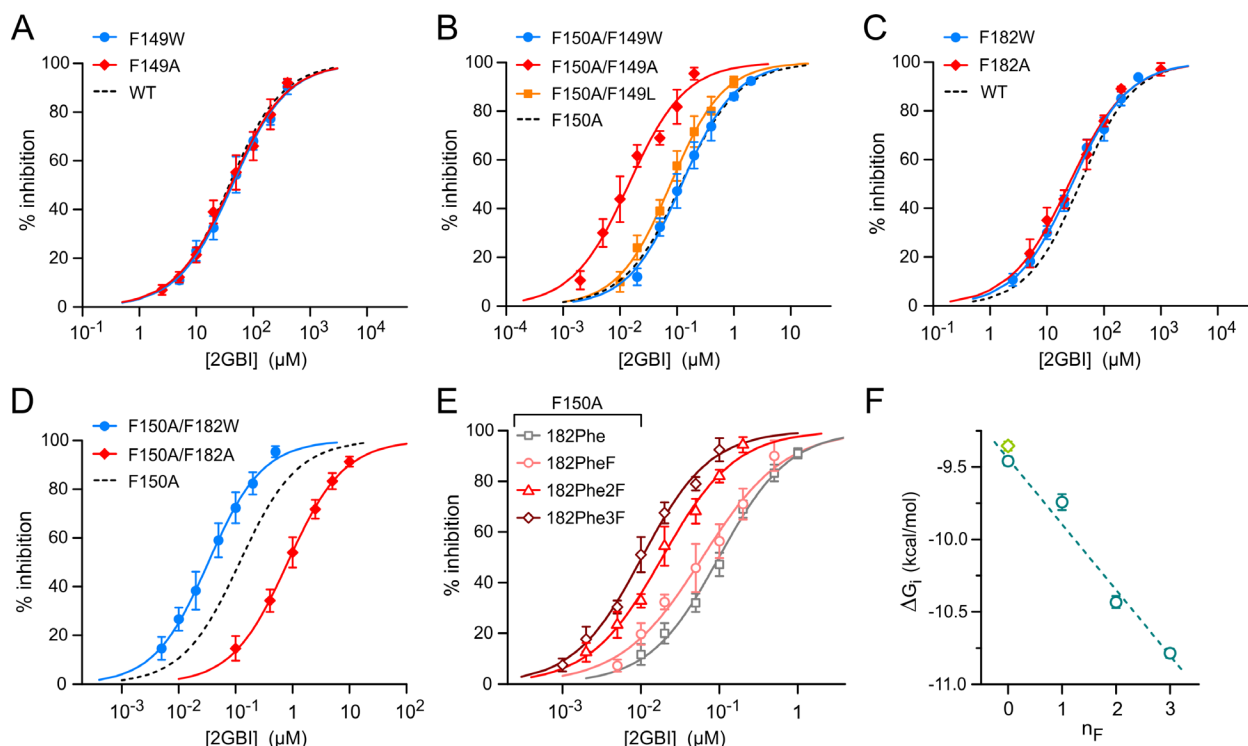


**Figure 4.2. Aromatic interactions stabilizing ligand binding in Hv1 F150A.** A-B) Concentration dependences of 2GBI-mediated inhibition of Hv1 WT (A) and F150A (B) with and without the indicated substitutions at position F149. C-D) Concentration dependences of 2GBI-mediated inhibition of Hv1 WT (C) and F150A (D) with and without the indicated substitutions at position F182. Each data point in (A-D) is an average from 3 to 9 independent measurements. Error bars are SD. E) Concentration-dependences of 2GBI-mediated inhibition of Hv1 F150A in which F182 is substituted with the indicated amino acids introduced via UAG suppressor tRNA. Each data point is an average from 3 to 8 independent measurements. Curved lines represent fits of the data using Eq. 1. See Table S4.1 for fit parameters. F)  $\Delta G_{i,s}$  measured from  $IC_{50}$ s from (E) as a function of the number of fluoro substituents in the phenylalanine ring. Light-green diamond is the value for Hv1 WT. Error bars are SE. Dashed line is the linear fit of the data points in teal.

### **Evidence for $\pi$ -stacking interactions between 2GBI and F182 in Hv1 F150A**

To better understand how F182 stabilizes 2GBI apparent binding in the context of the F150A mutation, we introduced fluoro-substituted phenylalanines at position 182 and measured how the resulting modification in  $\pi$ -electron-density affected the inhibition curve (Fig. 4.2E). We first verified that the introduction of non-substituted phenylalanine at position F182 using the codon-suppression method did not significantly alter 2GBI-mediated inhibition in the F150A background (Fig. 4.2F, points at  $n_F=0$ ). We then replaced F182 with phenylalanines containing rings with one, two, or three fluoro-substituents and measured 2GBI inhibition curves for each

modified F150A channel (Fig. 4.2E). We calculated  $\Delta G_i$  values from  $IC_{50}$ s and plotted them as a function of  $n_F$  (Fig. 4.2F). We observed a negative correlation between  $\Delta G_i$  and  $n_F$ , suggesting a stabilization of 2GBI apparent binding ( $\Delta G_i$  becomes more negative) with the reduction of the  $\Pi$ -electron density in the F182 ring.

Fluorination of an aromatic sidechain can alter protein-ligand interactions in different ways, depending on the orientation of the ligand relative to the sidechain, the charge of the ligand, and the polarity of the binding environment. For example, a face-to-face  $\Pi$ -stacking interaction with an electron-rich aromatic ligand in a hydrophobic environment is expected to be strengthened by fluoro-substituents in the aromatic sidechain<sup>69</sup>. While our findings are consistent with a  $\Pi$ -stacking interaction between 2GBI and F182 in Hv1 F150A, we cannot rule out the existence of other stabilizing interactions of electrostatic or steric nature. In any case, the interaction seems to provide a stronger contribution to 2GBI-mediated inhibition than the interaction with F150 assessed in Hv1 WT, as indicated by the steeper slope of the linear fit in Fig. 4.2F ( $\Delta G_i/\Delta n_F = -0.45 \pm 0.04$  kcal/mol).

***ABI: a simplified 2GBI analog suitable for investigating binding to the F150A mutant***

Because addition of fluoro-substituents to the phenyl ring of F182 decreased the  $IC_{50}$  of 2GBI-mediated inhibition of Hv1 F150A, we wondered whether we could create compounds that bind the channel with higher affinity by adding fluoro-substituents to the condensed phenyl ring of the ligand (Fig. 4.3A, yellow shade). To investigate this point, we focused on a simplified version of the inhibitor in which the guanidino group linked to the benzimidazole unit is replaced by an amino group. This compound, 2-aminobenzimidazole (ABI) (Fig. 4.3A), was identified as a 2GBI analog with reduced potency in earlier inhibition assays of Hv1 WT<sup>23</sup>.

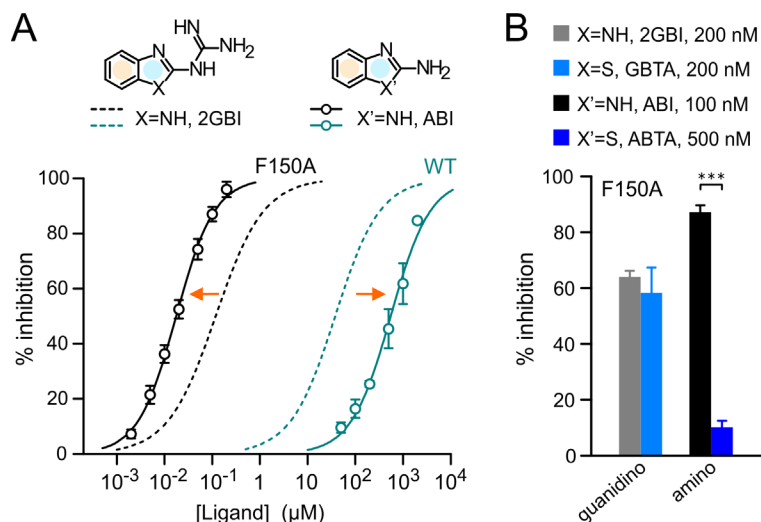


**Figure 4.3. Simplified ligand for binding optimization.** **A)** Concentration dependences of inhibition of Hv1 WT and F150A by 2GBI and ABI. Data points are averages from 3 to 5 independent measurements  $\pm$  SD. Curved lines represent fits of the data using Eq. 1. See Table S4.1 for fit parameters. Orange arrows indicate that Hv1 F150A is more sensitive to ABI than 2GBI, while the situation is reversed for WT. Condensed phenyl and 2-substituted imidazole rings are highlighted in yellow and pale blue, respectively. **B)** Percentages of inhibition of Hv1 F150A by guanidino- and amino-derivatives of benzimidazole and benzothiazole at the indicated concentrations. GBTA and 2GBI showed similar potency, so they could be compared at the same concentration. This was not the case for ABTA and ABI. The minimal concentration at which ABTA-mediated inhibition could be accurately measured was 500 nM, but at that concentration ABI-mediated inhibition was saturated. Despite lowering ABI concentration to 100 nM, this inhibitor still produced a much larger inhibition than ABTA. Error bars are SD ( $n = 3-9$ ). Welch's t-test was used for statistical analysis, \*\*\* $p < 0.001$ .

We confirmed that the apparent binding affinity of Hv1 WT for ABI is lower than the apparent binding affinity for 2GBI ( $IC_{50} = 553 \pm 43 \mu\text{M}$  for ABI,  $IC_{50} = 38 \pm 2 \mu\text{M}$  for 2GBI, Fig. 4.3A); but we found that the situation is reversed for Hv1 F150A. In this case, ABI has the higher apparent binding affinity ( $IC_{50} = 18 \pm 1 \text{ nM}$  for ABI,  $IC_{50} = 118 \pm 7 \text{ nM}$  for 2GBI, Fig. 4.3A).

We also found that the inhibition of Hv1 F150A by ABI is more sensitive to modifications of the benzimidazole unit than the inhibition by 2GBI. Replacing the NH group of 2GBI with a sulfur substituent (Fig. 4.3B, GBTA) resulted in only a negligible change in inhibitor potency (Fig. 4.3B, guanidino). However, when the analogous NH group of ABI was replaced by the same substituent (Fig. 4.3B, ABTA), the effect on potency was much larger (Fig. 4.3B, amino). We reasoned that the ability of ABI to inhibit Hv1 F150A with high affinity and in a way that is highly sensitive to modifications of the benzimidazole unit would make this ligand a good model to study how

fluoro-substituents affect binding.

### ***Fluoro-substituted ABIs reveal limitation of ligands with condensed rings***

We measured the inhibition of Hv1 WT and F150A by ABI derivatives containing one, two, or three fluoro-substitutions in the condensed phenyl-ring of the benzimidazole unit (Fig. 4.4A, yellow shade). We found that the addition of one or two substituents produced only small changes in the inhibition curve ( $IC_{50,ABIF\beta} = 312 \pm 17 \mu\text{M}$ ,  $IC_{50,ABIF2} = 244 \pm 19 \mu\text{M}$  for WT;  $IC_{50,ABIF\beta} = 13 \pm 1 \text{ nM}$ ,  $IC_{50,ABIF2} = 12 \pm 1 \text{ nM}$  for F150A), while the addition of the third substituent significantly shifted the  $IC_{50}$  to higher concentrations ( $IC_{50,ABIF3} = 699 \pm 45 \mu\text{M}$  for WT;  $IC_{50,ABIF3} = 93 \pm 6 \text{ nM}$  for F150A) (Fig. 4.4B,D). The trend was the same in Hv1 WT and F150A, but the shift in  $IC_{50}$  with the trifluorinated ligand was more pronounced in Hv1 F150A.

Ligand fluorination was expected to strengthen  $\Pi$ -stacking interaction with aromatic residues like F182 in the F150A channel. So, why did the  $IC_{50}$  shift to higher concentrations with the addition of the third fluorine? We suspected that, as the fluoro-substituents withdraw  $\Pi$  electrons from the ligand condensed phenyl ring, they may also perturb the charge distribution in the adjacent five-membered ring (Fig. 4.4A, pale-blue shade) destabilizing its interactions with other parts of the binding site. In this case, a substituent positioned closer to the five-membered ring (Fig. 4.4A,  $ABIF_{\alpha}$ ) should have a stronger destabilizing effect than a substituent positioned farther from that ring ( $ABIF_{\beta}$ ). To test this hypothesis by comparing the concentration dependences of  $ABIF_{\alpha}$  and  $ABIF_{\beta}$  inhibition (Fig. 4.4C,E). Indeed, we found that while the substitution at the beta position caused a small increase in apparent affinity, the substitution at the alpha position caused a decrease. Again, the destabilizing effect was more pronounced in Hv1 F150A ( $IC_{50,ABIF_{\alpha}} = 729 \pm 56 \mu\text{M}$ ,  $IC_{50,ABIF_{\beta}} = 312 \pm 17 \mu\text{M}$  for WT;  $IC_{50,ABIF_{\alpha}} = 40 \pm 1 \text{ nM}$ ,  $IC_{50,ABIF_{\beta}} = 13 \pm 1 \text{ nM}$  for F150A).

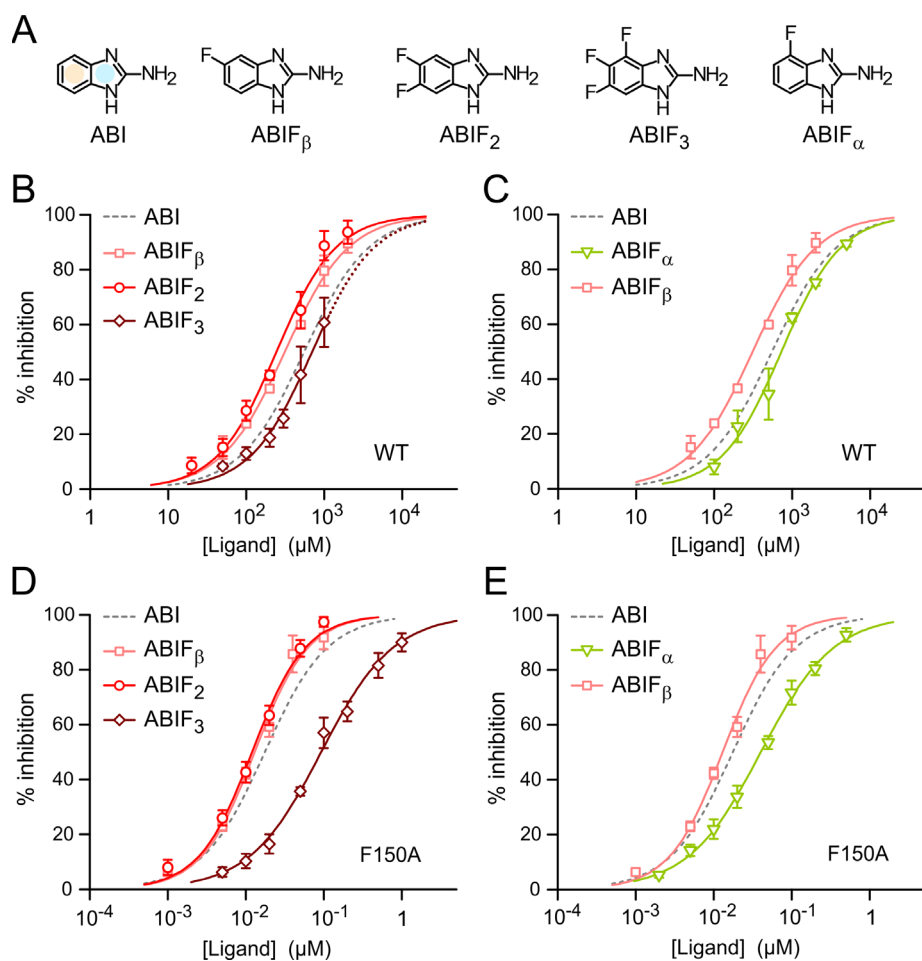


**Figure 4.4. Impact of phenyl ring fluorination on ABI-mediated inhibition Hv1 WT and F150A.** A) Structures of tested ABIs showing positions of fluoro substituents in condensed phenyl ring (yellow shade). B-E) Concentration-dependences of inhibition of Hv1 WT (B-C) and F150A (D-E) by the indicated compounds. Each data point is the average value from 3-8 independent measurements. Error bars are SD. Curved lines represent fits of the data using Eq. 1. See Table S4.1 for fit parameters. Dotted line in (B) indicates extrapolation of the inhibition curve for ABIF<sub>3</sub> to concentrations higher than 1 mM (the compound was not soluble at higher concentrations under tested conditions).

### ***Design of HIFs: two-pronged arginine mimics with non-condensed rings***

We reasoned that the presence of two condensed aromatic rings in ABI and 2GBI presents a potential vulnerability for the development of analogs with increased binding affinity because substituents intended to stabilize the interaction between one ring and the binding site can interfere with interactions mediated by the other ring. To prevent this interference, we designed a new class of Hv1 inhibitors related to ABI in which the phenyl ring and the 2-aminoimidazole ring are separated by a flexible linker and named them HIFs (Hv1 Inhibitor

Flexible) (Fig. 4.5A).

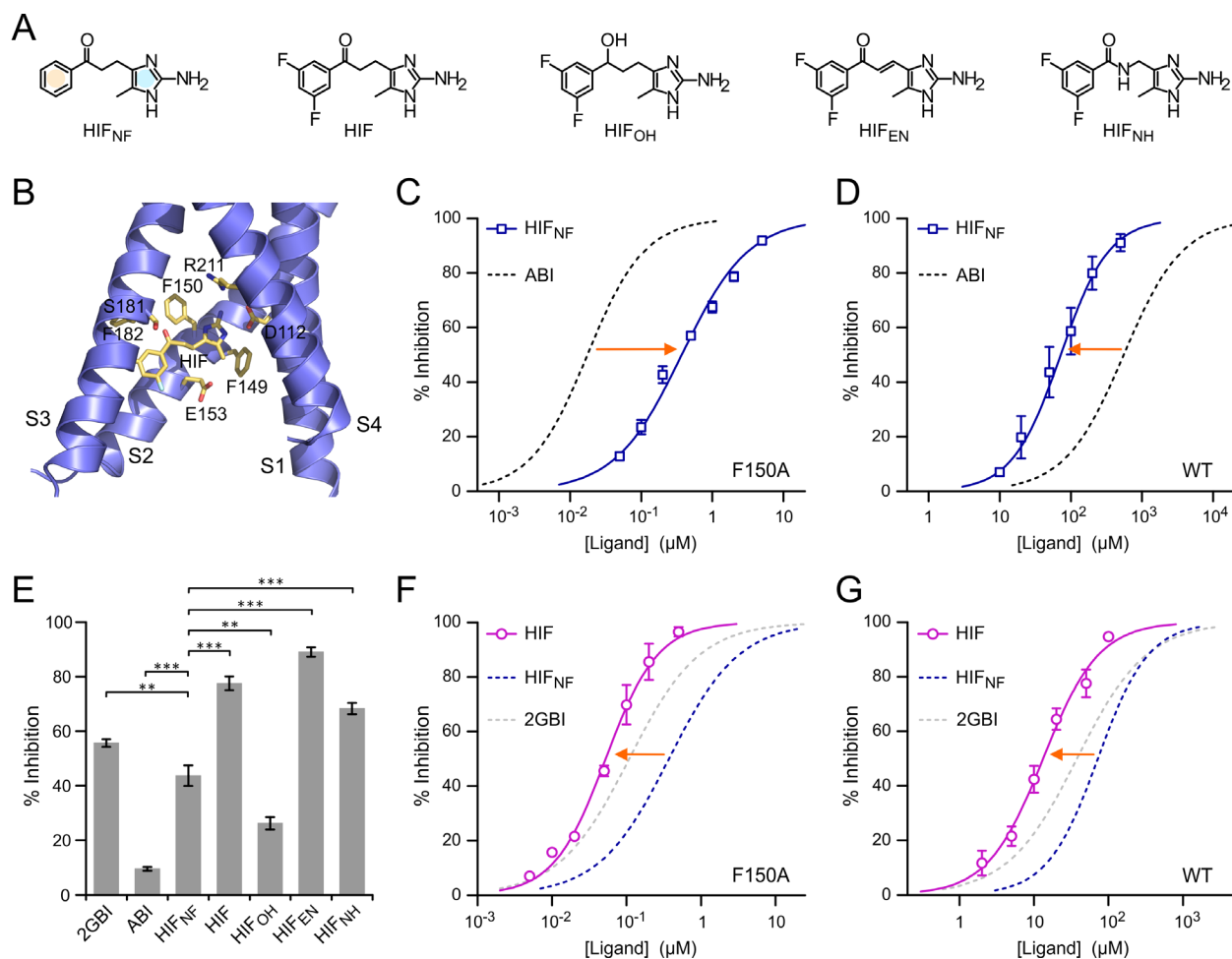


**Figure 4.5. Hv1 inhibition by HIF compounds.** **A)** Structures of HIF and related compounds. In HIF<sub>NF</sub>, the separate phenyl and 2-aminoimidazole rings are highlighted in yellow and blue, respectively. **B)** Structural model of the VSD of human Hv1 in the activated conformation (from Geragotelis et al. 2020) interacting with HIF at the end of the MD simulation described in the Methods section and showing residues in the vicinity of the ligand. **C-D)** Concentration dependences of HIF<sub>NF</sub>-mediated inhibition of Hv1 F150A (C) and Hv1 WT (D) compared to ABI. Each data point represents the mean of 3 to 7 independent measurements  $\pm$  SD. Curved lines represent fits of the data using Eq. 1. See Table S4.1 for fit parameters. Orange arrows indicate that HIF<sub>NF</sub> is more effective than ABI at inhibiting Hv1 WT, whereas the situation is reversed for Hv1 F150A. **E)** Inhibition of Hv1 WT by the indicated compounds tested at a concentration of 50  $\mu$ M. Each bar is the mean of 4 to 9 independent measurements. Error bars are SEM. A one-way ANOVA with Tukey's post-hoc test was used for statistical analysis. Comparisons between all pairs of inhibitors were statically significant ( $p < 0.05$ ), except for HIF/HIF<sub>NH</sub> ( $p > 0.05$ ). For clarity, only comparisons with HIF<sub>NF</sub> are shown. \*\* $p < 0.01$ , \*\*\* $p < 0.001$ . **F-G)** Concentration dependences of HIF-mediated inhibition of Hv1 F150A (F) and Hv1 WT (G) compared to HIF<sub>NF</sub>. Each data point represents the mean of 3 to 5 independent measurements  $\pm$  SD. Curved lines represent fits of the data using Eq. 1. See Table S4.1 for fit parameters. Orange arrows indicate that fluorination of the phenyl ring increases the ligand apparent binding affinity to both Hv1 WT and F150A.

The 2-aminoimidazole moiety was previously identified as an arginine-mimic pharmacophore

for Hv1<sup>22,23</sup>. As a result, this part of the ligand was preserved in HIF compounds. We tested three different ways to connect the phenyl ring to the 2-aminoimidazole moiety. The different connecting linkers were designed to allow the phenyl ring to explore the binding site for potential stabilizing interactions while minimizing the increase in overall hydrophobicity. The carbonyl group connected to the phenyl ring in HIF<sub>NF</sub> and HIF is replaced by a hydroxyl group in HIF<sub>OH</sub>, or by an amide group in HIF<sub>NH</sub>. A double bond in the *E*-configuration is present in the linker of HIF<sub>EN</sub>. The unsaturated linker is expected to reduce flexibility and extend the delocalization of  $\Pi$ -electrons.

HIF shares the same core structure of HIF<sub>NF</sub>, but its phenyl ring is fluorinated. These two compounds were chosen to investigate how ring separation affects the modulation of binding interactions by substituents in the phenyl ring. At pH 6.0, all HIF compounds have predicted LogD values (logarithm of distribution coefficients) lower than 1 (LogD (HIF) = 0.37, LogD (HIF<sub>EN</sub>) = 0.83, LogD (HIF<sub>OH</sub>) = 0.28, LogD (HIF<sub>NF</sub>) = 0.09, LogD (HIF<sub>NH</sub>) = -0.45) and, for the most part, in the range of LogDs of fluorinated ABIs calculated at the same pH (-0.1 – 0.5, ChemAxon LogD Predictor).

We verified that the new inhibitor core structure is compatible with the 2GBI binding site<sup>22</sup> by docking HIF within the structural model of the Hv1 VSD in the up state that was previously used for the characterization of 2GBI binding<sup>41,70</sup>. We set the initial position of HIF so that its 2-aminoimidazole ring and the two carbon atoms at positions 4 and 5 would overlap with the corresponding moiety of bound 2GBI. We then run an unrestrained all-atom molecular dynamics simulation and followed the movement of the inhibitor for 25 ns. The position of the inhibitor at the end of the simulation is shown in Fig. 4.5B. A comparison between HIF and 2GBI bound to the same location within the Hv1 VSD is reported in Fig. S4.2.

### ***Hv1 inhibition by HIF compounds compared to inhibition by ABI and 2GBI***

We tested HIF<sub>NF</sub> at different concentrations on proton currents measured in inside-out patches from oocytes expressing Hv1 F150A and Hv1 WT. From the resulting concentration curves (Fig. 4.5C-D) we found that, HIF<sub>NF</sub> is less potent on Hv1 F150A compared to ABI, ( $IC_{50,ABI} / IC_{50,HIFNF} \sim 0.05$ ), but it is more potent on the wild type channel ( $IC_{50,ABI} / IC_{50,HIFNF} \sim 7.7$ ). All HIF compounds were more potent than ABI at inhibiting Hv1 WT, and some of them were even more potent than 2GBI (Fig. 4.5E). The different potencies observed with HIF compounds containing different linkers indicate that the connection between the 2-aminoimidazole ring and the phenyl ring affects how the ligands interact with the channel. In particular, HIF<sub>OH</sub> was less effective at reducing the proton current than HIF, HIF<sub>NH</sub>, and HIF<sub>EN</sub> (Fig. 4.5E) pointing to an important role for the carbonyl group in the linker.

We compared inhibition curves of HIF<sub>NF</sub> and its fluorinated analog, HIF, and found that fluorination of the phenyl ring produced significant increases in potency. The  $IC_{50, HIFNF} / IC_{50,HIF}$  was  $\sim 7.0$  for Hv1 F150A and  $\sim 5.4$  for Hv1 WT (Fig. 4.5F-G). These increases were much larger than those observed with similar fluorination of the condensed phenyl ring of ABI (Fig. 4.4B-E). Despite lacking the guanidino group of 2GBI, HIF was able to inhibit Hv1 WT with a lower  $IC_{50}$  (Fig. 4.5G,  $IC_{50,HIF} = 13 \pm 1 \mu M$ ,  $IC_{50,2GBI} = 38 \pm 2 \mu M$ ). HIF<sub>NH</sub> and HIF<sub>EN</sub> had similar or larger potency than HIF (Fig. 4.5E). Taken together, these findings indicate that the scaffold of HIF compounds interacts more favorably with the wild type channel than the ABI/2GBI scaffold, making HIFs promising lead candidates for the development of high-affinity Hv1 inhibitors.

While at 50  $\mu M$ , HIF<sub>EN</sub> is more potent than HIF, this is not the case at all concentrations (Fig. S4.3A) due to the steeper concentration dependence of HIF<sub>EN</sub>, which has a Hill coefficient significantly larger than 1 (Fig. S4.3B, inset). In an earlier study<sup>27</sup>, we found that the Hill coefficient for the 2GBI analog GBTA was larger than 1 for dimeric Hv1, but not for the monomeric version of the channel. So, we determined the concentration dependence of HIF<sub>EN</sub> also for monomeric Hv1 (Fig. S4.3B), but found that, in this case, monomerization does not

cause significant changes in the Hill coefficient. The potential implications of this result are addressed in Zhao et al., 2021b.

#### 4.4 Discussion

We investigated the molecular mechanism underlying the increased binding affinity of Hv1 for 2GBI in the presence of the F150A mutation and found evidence of a local rearrangement of the binding site in the mutant channel. As a result of this rearrangement, a stabilizing interaction between F150 and 2GBI is replaced by stronger interactions. We propose that the mutation causes the aromatic side chain of phenylalanine 182 to move closer to the phenyl ring of 2GBI allowing for a stabilizing  $\Pi$ -stacking interaction, which replaces a weaker cation- $\Pi$  interaction between F150 and the ligand. We found that introducing fluoro substituents in the phenyl ring of F182 via unnatural amino acid substitutions further stabilized 2GBI apparent binding, suggesting that a similar effect could be observed by fluorinating the phenyl ring of the ligand. Testing this hypothesis on fluorinated ABIs revealed a potential liability of Hv1 inhibitors with two conjugated rings, as substituents introduced in one ring to optimize channel-ligand interactions can destabilize binding by perturbing interactions mediated by the other ring. The separation of the two rings in HIF compounds by an extended linker prevented this liability and allowed the inhibitor to adopt binding poses with higher affinity within the intracellular vestibule of the WT channel.

We interpret the stronger potency of HIF compared to HIF<sub>NF</sub> (Fig. 4.5F-G) as an indication that fluorination of the phenyl ring stabilizes binding without destabilizing electrostatic interactions mediated by the positively-charged protonated 2-aminoimidazole group. The finding opens the possibility of further exploiting the derivatization at the phenyl ring to strengthen binding of the HIF scaffold. Changes in the linker could offer another avenue for binding optimization. Our binding model (Fig. 4.5B) shows that the methyl group connected to the five membered ring points toward a relatively wide region within the channel intracellular vestibule, suggesting that the moiety could be expanded to increase ligand-protein contacts.

HIF inhibitors are predicted to have ADMET properties superior to 2GBI and its analogs. When compared with in silico tools available in SwissADME<sup>59,60</sup> and XenoSite<sup>61</sup>, both 2GBI and HIF compounds showed good solubility, high GI absorption, and favorable P450-mediated metabolism (Fig. S4.4A). However, 2GBI and derivatives are predicted to be unable to cross the blood-brain barrier, limiting their utilization as neuroprotective agents in models of stroke and inflammation following CNS injury. A similar problem affects inhibitor peptides, such as C6<sup>20</sup> and AGAP/W38F<sup>21</sup>. HIF and HIF<sub>EN</sub>, on the other hand, are predicted to cross the blood-brain barrier, offering opportunities for the development of drugs capable of targeting microglial Hv1 in vivo. When potential toxicity was examined with MetaTox<sup>63</sup>, HIF and HIF<sub>EN</sub> were predicted to have LD<sub>50</sub> values similar to 2GBI, whereas HIF<sub>NH</sub> was predicted to have lower toxicity (Fig. S4.4B). While these predictions will need to be tested in animal models, they all point to more favorable features of the HIF scaffold compared to 2GBI.

2GBI has been shown to inhibit Hv1 through an open-channel block mechanism<sup>23</sup>. Besides F150, other residues were found to interact with the ligand, including D112, S181, and R211 from the S1, S3, and S4 helices, respectively<sup>22,26,29,70</sup>. In order to develop high affinity inhibitors based on the HIF scaffold, it is important to establish whether the same residues involved in 2GBI binding interact with HIF or whether there are different/additional molecular determinants. This point is investigated in the accompanying article<sup>71</sup>, which explores the mechanism of HIF-mediated inhibition and the ability of the Hv1 VSD to trap the ligand in the down state.

## 4.5 Supplementary Information

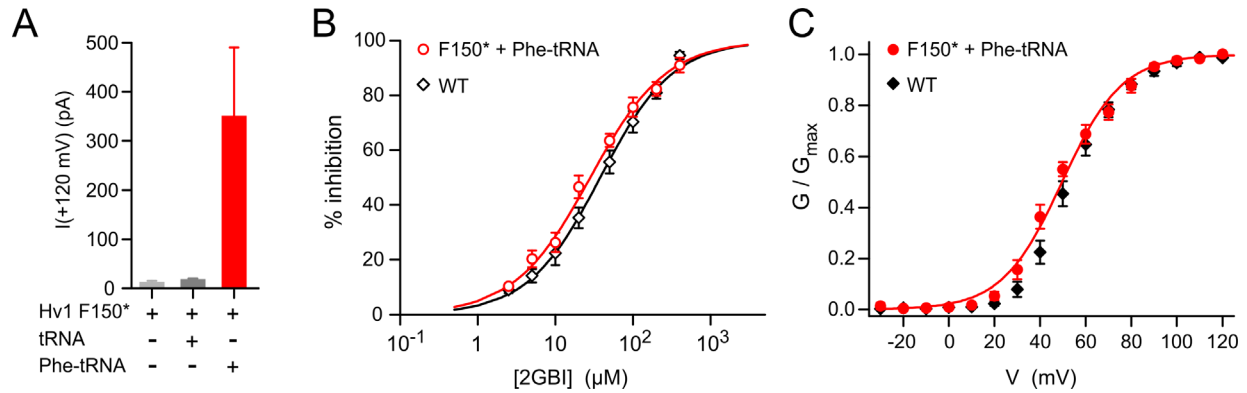


**Figure S4.1. Functional rescue of Hv1 F150\* by suppressor tRNA.** Suppressor Phe-tRNA rescues function of Hv1 mRNA containing UAG codon at position F150 (F150\*). **A)** Average currents measured from oocytes injected with the indicated combinations of F150\* cRNA and tRNAs. Measurements were performed at +120 mV in inside-out patch configuration on 7-10 cells per condition, at  $pH_i = pH_o = 6.0$ . Error bars are SEM. **B)** Concentration dependences of 2GBI-mediated inhibition of proton currents from the indicated channels. Points are averages from at least 3 independent measurements  $\pm$  SD. Curved lines represent fits of the data using Eq. 1. ( $IC_{50} = 28 \pm 2 \mu M$  for F150\* cRNA + Phe-tRNA,  $IC_{50} = 38 \pm 2 \mu M$  for Hv1 WT). **C)** G-V relationships of proton currents from F150\* cRNA + Phe-tRNA and Hv1 WT. Points are averages from at least 4 independent measurements  $\pm$  SEM. Data were fitted with Eq. 2. Fit is shown as curved line for F150\* cRNA + Phe-tRNA. ( $V_{1/2} = 50 \pm 3$  mV, slope =  $13 \pm 1$  mV for F150\* cRNA + Phe-tRNA;  $V_{1/2} = 53 \pm 3$  mV, slope =  $11 \pm 1$  for Hv1 WT).

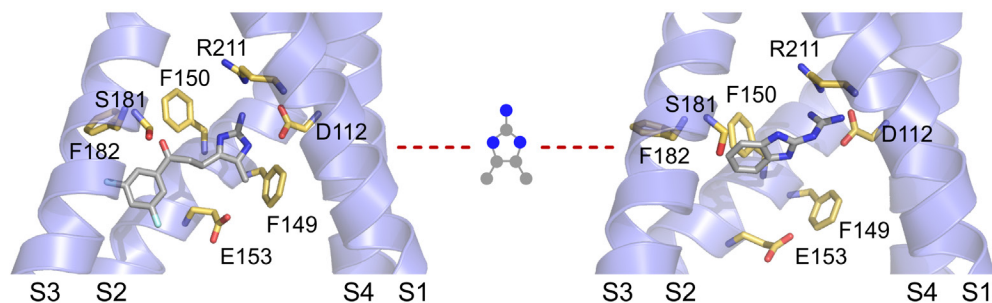


**Figure S4.2.** HIF and 2GBI bound the Hv1 VSD. Comparison of HIF and 2GBI poses within the Hv1 intracellular vestibule in the up state. The 2GBI pose is from Geragotelis et al., 2020. The drawing in the center represents the moiety used to align the two inhibitors at the beginning of the HIF simulation. Left panel shows the HIF pose at the end of the simulation.

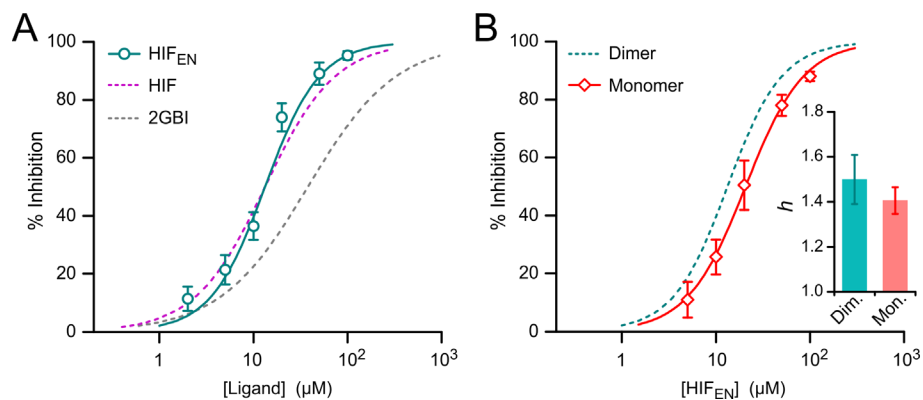


**Figure S4.3. Hv1 inhibition by HIF<sub>EN</sub>.** **A)** Concentration dependence of inhibition of Hv1 WT by HIF<sub>EN</sub> (teal) compared to HIF (purple) and 2GBI (gray). Each data point represents the mean of 5 to 6 independent measurements; error bars are SD. **B)** Concentration dependence of HIF<sub>EN</sub>-mediated inhibition of monomeric Hv1 (red diamonds) compared to dimeric Hv1 (teal dashed line). Monomeric Hv1 was Hv1NC<sub>VSP</sub> as in Hong et al., 2015. Each data point represents the mean of 4 to 5 independent measurements; error bars are SD. Data points in (A) and (B) were fitted with Eq. 1. The resulting Hill coefficients (*h*) are compared in the bar graph. Error bars are SE. IC<sub>50</sub> values are reported in Table S4.1.

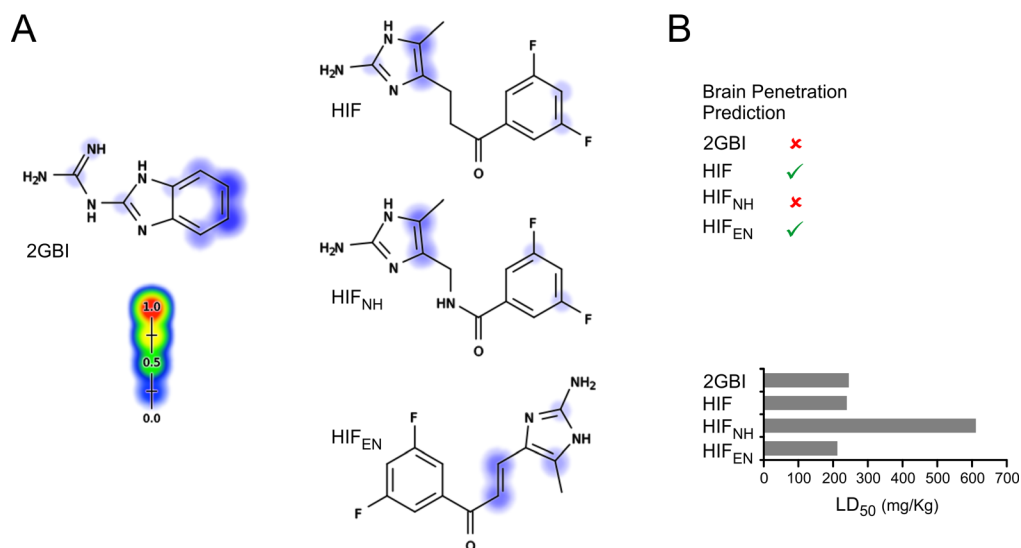


**Figure S4.4. Predicted metabolism and toxicity of HIF compounds vs. 2GBI.** **A)** Sites of cytochrome P450-mediated metabolism for 2GBI, HIF, HIF<sub>NH</sub>, and HIF<sub>EN</sub> predicted by XenoSite (<https://swami.wustl.edu/xenosite>). Scale goes from 0% (blue) to 100% (red) probability of metabolism. **B) Upper panel:** Ability to permeate the blood-brain barrier for the indicated compounds predicted using BOILED-Egg (<http://www.swissadme.ch>). **Lower panel:** Prediction of integrated toxicity of the indicated compounds from MetaTox ([www.way2drug.com/mg2](http://www.way2drug.com/mg2)). Values take into account effects of all first and second-level metabolites and effect of parent compound on integrated toxicity.

| Hv1                  | Inhibitor         | IC <sub>50</sub> ± SE (μM) | h ± SE      |
|----------------------|-------------------|----------------------------|-------------|
| WT                   | 2GBI              | 37.8 ± 1.8                 | 0.93 ± 0.04 |
|                      | ABI               | 553 ± 43                   | 1.05 ± 0.09 |
|                      | ABIF <sub>α</sub> | 729 ± 56                   | 1.13 ± 0.10 |
|                      | ABIF <sub>β</sub> | 312 ± 17                   | 1.06 ± 0.06 |
|                      | ABIF <sub>2</sub> | 244 ± 19                   | 1.13 ± 0.09 |
|                      | ABIF <sub>3</sub> | 699 ± 45                   | 1.09 ± 0.08 |
|                      | HIF <sub>NF</sub> | 72.1 ± 3.7                 | 1.28 ± 0.04 |
|                      | HIF               | 13.3 ± 1.0                 | 1.16 ± 0.10 |
|                      | HIF <sub>EN</sub> | 13.3 ± 1.3                 | 1.50 ± 0.11 |
| Hv1NC <sub>VSP</sub> | HIF <sub>EN</sub> | 20.6 ± 0.7                 | 1.41 ± 0.06 |
| F150A                | 2GBI              | 0.118 ± 0.007              | 0.86 ± 0.03 |
|                      | ABI               | 0.018 ± 0.001              | 1.08 ± 0.04 |
|                      | ABIF <sub>α</sub> | 0.040 ± 0.001              | 0.93 ± 0.03 |
|                      | ABIF <sub>β</sub> | 0.013 ± 0.001              | 1.27 ± 0.12 |
|                      | ABIF <sub>2</sub> | 0.012 ± 0.001              | 1.27 ± 0.10 |
|                      | ABIF <sub>3</sub> | 0.093 ± 0.006              | 0.94 ± 0.05 |
|                      | HIF <sub>NF</sub> | 0.37 ± 0.03                | 0.92 ± 0.03 |
|                      | HIF               | 0.053 ± 0.003              | 1.24 ± 0.08 |
| F150W                |                   | 51.6 ± 1.6                 | 0.92 ± 0.03 |
| F150Phe              |                   | 28.2 ± 1.3                 | 0.88 ± 0.02 |
| F150PheF             | 2GBI              | 48.4 ± 4.5                 | 0.86 ± 0.07 |
| F150Phe2F            |                   | 62 ± 6                     | 0.96 ± 0.08 |
| F150Phe3F            |                   | 66 ± 5                     | 0.88 ± 0.05 |
| F149A                | 2GBI              | 40.2 ± 2.5                 | 0.89 ± 0.05 |
| F149W                |                   | 43.2 ± 2.0                 | 0.90 ± 0.04 |
| F182A                | 2GBI              | 24.4 ± 1.6                 | 0.84 ± 0.05 |
| F182W                |                   | 27.5 ± 1.2                 | 0.88 ± 0.03 |
| F149A/F150A          |                   | 0.014 ± 0.002              | 0.87 ± 0.09 |
| F149L/F150A          | 2GBI              | 0.077 ± 0.004              | 0.94 ± 0.04 |
| F149W/F150A          |                   | 0.123 ± 0.006              | 0.92 ± 0.05 |
| F150A/F182A          | 2GBI              | 0.826 ± 0.022              | 0.88 ± 0.02 |
| F150A/F182W          |                   | 0.033 ± 0.001              | 0.91 ± 0.03 |
| F150A/F182Phe        |                   | 0.099 ± 0.005              | 0.97 ± 0.05 |
| F150A/F182PheF       | 2GBI              | 0.061 ± 0.006              | 0.83 ± 0.07 |
| F150A/F182Phe2F      |                   | 0.019 ± 0.001              | 0.93 ± 0.06 |
| F150A/F182Phe3F      |                   | 0.010 ± 0.001              | 1.00 ± 0.05 |

**Table S4.1.** Fit parameters for concentration dependences of Hv1 inhibitors.

## Supplementary Methods

The following compounds were custom synthesized by Enamine at a minimum purity of 95% (LCMS):

**HIF:** 3-(2-amino-5-methyl-1H-imidazol-4-yl)-1-(3,5-difluorophenyl)propan-1-one hydrochloride ( $C_{13}H_{14}ClF_2N_3O$ )  $^1H$ -NMR (400 MHz,  $D_2O$ )  $\delta$ : 1.89 (s, 3H), 2.76 (t,  $J$  = 6.7 Hz, 2H), 3.20 (t,  $J$  = 6.8 Hz, 2H), 7.14 (t,  $J$  = 8.9 Hz, 1H), 7.42 (m, 2H), 8.34 (s, 1H).  $^{13}C$ -NMR (126 MHz, MeOD)  $\delta$ : 7.29, 17.22, 37.22, 107.89, 110.51, 110.72, 118.01, 120.32, 139.75, 146.37, 162.13, 164.11, 196.47. HRMS (ESI):  $m/z$  calc. for  $[M+H]^+$ : 266.1105, found: 266.1113.

**HIF<sub>NF</sub>:** 3-(2-amino-5-methyl-1H-imidazol-4-yl)-1-phenylpropan-1-one hydrochloride ( $C_{13}H_{16}ClN_3O$ )  $^1H$ -NMR (400 MHz, Methanol- $d_4$ )  $\delta$ : 2.07 (s, 3H), 2.85 (t, 2H), 3.33 (t, 2H), 7.49 (m, 2H), 7.60 (m, 1H), 7.98 (m, 2H).  $^{13}C$ -NMR (101 MHz, MeOD)  $\delta$ : 7.28, 17.27, 37.01, 117.97, 120.64, 127.71, 128.41, 133.12, 136.49, 146.19, 199.19. HRMS (ESI):  $m/z$  calc. for  $[M+H]^+$ : 230.1293, found: 230.1287.

**HIF<sub>NH</sub>:** N-[(2-amino-5-methyl-1H-imidazol-4-yl)methyl]-3,5-difluorobenzamide ( $C_{12}H_{12}F_2N_4O$ )  $^1H$ -NMR (400 MHz, MeOD)  $\delta$ : 2.07 (s, 3H), 4.28 (s, 2H), 7.10 (t, 1H), 7.42 (m, 2H).  $^{13}C$ -NMR (101 MHz, MeOD)  $\delta$ : 8.78, 34.85, 105.85, 106.11, 106.37, 110.16, 122.34, 122.67, 137.93, 148.63, 161.64, 164.17, 165.70. HRMS (ESI):  $m/z$  calc. for  $[M+H]^+$ : 267.1057, found: 267.1065.

**HIF<sub>OH</sub>:** 3-(2-amino-5-methyl-1H-imidazol-4-yl)-1-(3,5-difluorophenyl)propan-1-ol hydrochloride ( $C_{13}H_{16}ClF_2N_3O$ )  $^1H$ -NMR (500 MHz, Methanol- $d_4$ )  $\delta$ : 1.90 (m, 2H), 2.05 (s, 3H), 2.57 (t, 2H), 4.64 (m, 1H), 6.80 (m, 1H), 6.97 (m, 2H).  $^{13}C$ -NMR (126 MHz, Methanol- $d_4$ )  $\delta$ : 7.29, 19.11, 37.32, 71.21, 101.43, 101.63, 101.84, 108.12, 108.17, 108.28, 108.32, 117.62, 120.93, 146.11, 149.87, 149.94, 150.00, 162.03, 162.13, 163.99, 164.09. HRMS (ESI):  $m/z$  calc. for  $[M+H]^+$ : 268.1261, found: 268.1250.

**HIF<sub>EN</sub>:** (2E)-3-(2-amino-5-methyl-1H-imidazol-4-yl)-1-(3,5-difluorophenyl)prop-2-en-1-one hydrochloride ( $C_{13}H_{12}ClF_2N_3O$ )  $^1H$ -NMR (400 MHz, DMSO- $d_6$ )  $\delta$ : 2.21 (s, 3H), 7.20 (br.s, 2H), 7.26 (d,  $J$  = 14.4 Hz, 1H), 7.47 (d,  $J$  = 14.8 Hz, 1H), 7.52 (t,  $J$  = 8.9 Hz, 1H), 7.60 (m, 2H).  $^{13}C$ -NMR (126 MHz, DMSO)  $\delta$ : 11.65, 108.14, 111.15, 111.36, 112.41, 121.53, 130.20, 142.43, 151.65, 162.08, 163.54, 164.05, 185.15. HRMS (ESI):  $m/z$  calc. for  $[M+H]^+$ : 264.0948, found: 264.0943.

## 4.6 References

1. Ramsey, I.S., Moran, M.M., Chong, J.A. & Clapham, D.E. A voltage-gated proton-selective channel lacking the pore domain. *Nature* **440**, 1213-6 (2006).
2. Sasaki, M., Takagi, M. & Okamura, Y. A voltage sensor-domain protein is a voltage-gated proton channel. *Science* **312**, 589-92 (2006).
3. Bayrhuber, M. et al. Nuclear Magnetic Resonance Solution Structure and Functional Behavior of the Human Proton Channel. *Biochemistry* **58**, 4017-4027 (2019).
4. Takeshita, K. et al. X-ray crystal structure of voltage-gated proton channel. *Nat Struct Mol Biol* **21**, 352-7 (2014).
5. Ramsey, I.S., Ruchti, E., Kaczmarek, J.S. & Clapham, D.E. Hv1 proton channels are required for high-level NADPH oxidase-dependent superoxide production during the phagocyte respiratory burst. *Proc Natl Acad Sci U S A* **106**, 7642-7 (2009).
6. El Chemaly, A. et al. VSOP/Hv1 proton channels sustain calcium entry, neutrophil migration, and superoxide production by limiting cell depolarization and acidification. *J Exp Med* **207**, 129-39, S1-2 (2010).
7. DeCoursey, T.E. Voltage-gated proton channels: molecular biology, physiology, and pathophysiology of the H(V) family. *Physiol Rev* **93**, 599-652 (2013).
8. Wang, Y., Li, S.J., Wu, X., Che, Y. & Li, Q. Clinicopathological and biological significance of human voltage-gated proton channel Hv1 protein overexpression in breast cancer. *J Biol Chem* **287**, 13877-88 (2012).
9. Wang, Y., Wu, X., Li, Q., Zhang, S. & Li, S.J. Human voltage-gated proton channel hv1: a new potential biomarker for diagnosis and prognosis of colorectal cancer. *PLoS One* **8**, e70550 (2013).
10. Hondares, E. et al. Enhanced activation of an amino-terminally truncated isoform of the voltage-gated proton channel HVCN1 enriched in malignant B cells. *Proc Natl Acad Sci U S A* **111**, 18078-83 (2014).
11. Wu, L.J. et al. The voltage-gated proton channel Hv1 enhances brain damage from ischemic stroke. *Nat Neurosci* **15**, 565-73 (2012).
12. Li, W., Ward, R., Dong, G., Ergul, A. & O'Connor, P. Neurovascular protection in voltage-gated proton channel Hv1 knock-out rats after ischemic stroke: interaction with Na(+)/H(+) exchanger-1 antagonism. *Physiol Rep* **7**, e14142 (2019).
13. Kawai, T. et al. Unconventional role of voltage-gated proton channels (VSOP/Hv1) in regulation of microglial ROS production. *J Neurochem* **142**, 686-699 (2017).
14. Ritzel, R.M. et al. Proton extrusion during oxidative burst in microglia exacerbates pathological acidosis following traumatic brain injury. *Glia* **69**, 746-764 (2021).
15. Murugan, M. et al. The voltage-gated proton channel Hv1 contributes to neuronal injury and motor deficits in a mouse model of spinal cord injury. *Mol Brain* **13**, 143 (2020).
16. Lishko, P.V., Botchkina, I.L., Fedorenko, A. & Kirichok, Y. Acid extrusion from human spermatozoa is mediated by flagellar voltage-gated proton channel. *Cell* **140**, 327-37 (2010).
17. Musset, B. et al. NOX5 in human spermatozoa: expression, function, and regulation. *J Biol Chem* **287**, 9376-88 (2012).
18. Lishko, P.V. Contraception: Search for an Ideal Unisex Mechanism by Targeting Ion Channels. *Trends Biochem Sci* **41**, 816-818 (2016).
19. Alabi, A.A., Bahamonde, M.I., Jung, H.J., Kim, J.I. & Swartz, K.J. Portability of paddle motif function and pharmacology in voltage sensors. *Nature* **450**, 370-5 (2007).
20. Zhao, R. et al. Role of human Hv1 channels in sperm capacitation and white blood cell

- respiratory burst established by a designed peptide inhibitor. *Proc Natl Acad Sci U S A* **115**, E11847-E11856 (2018).
21. Tang, D. et al. Scorpion toxin inhibits the voltage-gated proton channel using a Zn(2+) -like long-range conformational coupling mechanism. *Br J Pharmacol* (2020).
  22. Hong, L., Kim, I.H. & Tombola, F. Molecular determinants of Hv1 proton channel inhibition by guanidine derivatives. *Proc Natl Acad Sci U S A* **111**, 9971-6 (2014).
  23. Hong, L., Pathak, M.M., Kim, I.H., Ta, D. & Tombola, F. Voltage-sensing domain of voltage-gated proton channel Hv1 shares mechanism of block with pore domains. *Neuron* **77**, 274-87 (2013).
  24. Kalia, J. & Swartz, K.J. Common principles of voltage-dependent gating for Hv and Kv channels. *Neuron* **77**, 214-6 (2013).
  25. Pupo, A. & Gonzalez Leon, C. In pursuit of an inhibitory drug for the proton channel. *Proc Natl Acad Sci U S A* **111**, 9673-4 (2014).
  26. Chamberlin, A. et al. Hydrophobic plug functions as a gate in voltage-gated proton channels. *Proc Natl Acad Sci U S A* **111**, E273-82 (2014).
  27. Hong, L., Singh, V., Wulff, H. & Tombola, F. Interrogation of the intersubunit interface of the open Hv1 proton channel with a probe of allosteric coupling. *Sci Rep* **5**, 14077 (2015).
  28. Qiu, F., Rebolledo, S., Gonzalez, C. & Larsson, H.P. Subunit interactions during cooperative opening of voltage-gated proton channels. *Neuron* **77**, 288-98 (2013).
  29. Gianti, E., Delemotte, L., Klein, M.L. & Carnevale, V. On the role of water density fluctuations in the inhibition of a proton channel. *Proc Natl Acad Sci U S A* **113**, E8359-E8368 (2016).
  30. Wobig, L. et al. A family of hyperpolarization-activated channels selective for protons. *Proc Natl Acad Sci U S A* **117**, 13783-13791 (2020).
  31. Rennhack, A., Grahn, E., Kaupp, U.B. & Berger, T.K. Photocontrol of the Hv1 Proton Channel. *ACS Chem Biol* **12**, 2952-2957 (2017).
  32. Asuaje, A. et al. The inhibition of voltage-gated H(+) channel (HVCN1) induces acidification of leukemic Jurkat T cells promoting cell death by apoptosis. *Pflugers Arch* **469**, 251-261 (2017).
  33. Meszaros, B. et al. The voltage-gated proton channel hHv1 is functionally expressed in human chorion-derived mesenchymal stem cells. *Sci Rep* **10**, 7100 (2020).
  34. Shin, H. & Song, J.H. Antipsychotics, chlorpromazine and haloperidol inhibit voltage-gated proton currents in BV2 microglial cells. *Eur J Pharmacol* **738**, 256-62 (2014).
  35. Song, J.H., Marszalec, W., Kai, L., Yeh, J.Z. & Narahashi, T. Antidepressants inhibit proton currents and tumor necrosis factor-alpha production in BV2 microglial cells. *Brain Res* **1435**, 15-23 (2012).
  36. Shin, H., Kim, J. & Song, J.H. Clozapine and olanzapine inhibit proton currents in BV2 microglial cells. *Eur J Pharmacol* **755**, 74-9 (2015).
  37. Kornilov, P. et al. Promiscuous gating modifiers target the voltage sensor of K(v)7.2, TRPV1, and H(v)1 cation channels. *FASEB J* **28**, 2591-602 (2014).
  38. Chamberlin, A., Qiu, F., Wang, Y., Noskov, S.Y. & Larsson, H.P. Mapping the gating and permeation pathways in the voltage-gated proton channel Hv1. *J Mol Biol* **427**, 131-45 (2015).
  39. Gonzalez, C., Rebolledo, S., Perez, M.E. & Larsson, H.P. Molecular mechanism of voltage sensing in voltage-gated proton channels. *J Gen Physiol* **141**, 275-85 (2013).
  40. Okamura, Y., Fujiwara, Y. & Sakata, S. Gating mechanisms of voltage-gated proton channels. *Annu Rev Biochem* **84**, 685-709 (2015).
  41. Geragotelis, A.D. et al. Voltage-dependent structural models of the human Hv1 proton channel from long-timescale molecular dynamics simulations. *Proc Natl Acad Sci U S A*

- 117, 13490-13498 (2020).
42. Berger, T.K. & Isacoff, E.Y. The pore of the voltage-gated proton channel. *Neuron* **72**, 991-1000 (2011).
  43. Musset, B. et al. Aspartate 112 is the selectivity filter of the human voltage-gated proton channel. *Nature* **480**, 273-7 (2011).
  44. Gerdes, B. et al. Quantification of Hv1-induced proton translocation by a lipid-coupled Oregon Green 488-based assay. *Anal Bioanal Chem* **410**, 6497-6505 (2018).
  45. Tombola, F., Ulbrich, M.H. & Isacoff, E.Y. The voltage-gated proton channel Hv1 has two pores, each controlled by one voltage sensor. *Neuron* **58**, 546-56 (2008).
  46. Liman, E.R., Tytgat, J. & Hess, P. Subunit stoichiometry of a mammalian K<sup>+</sup> channel determined by construction of multimeric cDNAs. *Neuron* **9**, 861-71 (1992).
  47. Infield, D.T. et al. Replacing voltage sensor arginines with citrulline provides mechanistic insight into charge versus shape. *J Gen Physiol* **150**, 1017-1024 (2018).
  48. Tombola, F., Ulbrich, M.H., Kohout, S.C. & Isacoff, E.Y. The opening of the two pores of the Hv1 voltage-gated proton channel is tuned by cooperativity. *Nat Struct Mol Biol* **17**, 44-50 (2010).
  49. Vanommeslaeghe, K. & MacKerell, A.D., Jr. Automation of the CHARMM General Force Field (CGenFF) I: bond perception and atom typing. *J Chem Inf Model* **52**, 3144-54 (2012).
  50. Vanommeslaeghe, K., Raman, E.P. & MacKerell, A.D., Jr. Automation of the CHARMM General Force Field (CGenFF) II: assignment of bonded parameters and partial atomic charges. *J Chem Inf Model* **52**, 3155-68 (2012).
  51. Phillips, J.C. et al. Scalable molecular dynamics with NAMD. *J Comput Chem* **26**, 1781-802 (2005).
  52. Klauda, J.B. et al. Update of the CHARMM all-atom additive force field for lipids: validation on six lipid types. *Journal of Physical Chemistry B* **114**, 7830-7843 (2010).
  53. MacKerell, A.D. et al. All-atom empirical potential for molecular modeling and dynamics studies of proteins. *Journal of Physical Chemistry B* **102**, 3586-3616 (1998).
  54. Jorgensen, W.L., Chandrasekhar, J., Madura, J.D., Impey, R.W. & Klein, M.L. Comparison of Simple Potential Functions for Simulating Liquid Water. *Journal of Chemical Physics* **79**, 926-935 (1983).
  55. Tuckerman, M.E. & Berne, B.J. Molecular-Dynamics in Systems with Multiple Time Scales - Systems with Stiff and Soft Degrees of Freedom and with Short and Long-Range Forces. *Journal of Chemical Physics* **95**, 8362-8364 (1991).
  56. Martyna, G.J., Tobias, D.J. & Klein, M.L. Constant-Pressure Molecular-Dynamics Algorithms. *Journal of Chemical Physics* **101**, 4177-4189 (1994).
  57. van Gunsteren, W.F. & Berendsen, H.J.C. Algorithms for macromolecular dynamics and constraint dynamics. *Molecular Physics* **34**, 1311-1327 (1977).
  58. Darden, T., York, D. & Pedersen, L. Particle Mesh Ewald - an N.Log(N) Method for Ewald Sums in Large Systems. *Journal of Chemical Physics* **98**, 10089-10092 (1993).
  59. Daina, A., Michielin, O. & Zoete, V. SwissADME: a free web tool to evaluate pharmacokinetics, drug-likeness and medicinal chemistry friendliness of small molecules. *Sci Rep* **7**, 42717 (2017).
  60. Daina, A. & Zoete, V. A BOILED-Egg To Predict Gastrointestinal Absorption and Brain Penetration of Small Molecules. *ChemMedChem* **11**, 1117-21 (2016).
  61. Zaretski, J., Matlock, M. & Swamidass, S.J. XenoSite: accurately predicting CYP-mediated sites of metabolism with neural networks. *J Chem Inf Model* **53**, 3373-83 (2013).
  62. Zakharov, A.V. et al. QSAR Modeling and Prediction of Drug-Drug Interactions. *Mol Pharm* **13**, 545-56 (2016).

63. Rudik, A.V. et al. MetaTox: Web Application for Predicting Structure and Toxicity of Xenobiotics' Metabolites. *J Chem Inf Model* **57**, 638-642 (2017).
64. Rodriguez, E.A., Lester, H.A. & Dougherty, D.A. Improved amber and opal suppressor tRNAs for incorporation of unnatural amino acids in vivo. Part 1: minimizing misacylation. *RNA* **13**, 1703-14 (2007).
65. Rodriguez, E.A., Lester, H.A. & Dougherty, D.A. Improved amber and opal suppressor tRNAs for incorporation of unnatural amino acids in vivo. Part 2: evaluating suppression efficiency. *RNA* **13**, 1715-22 (2007).
66. Infield, D.T. et al. Main-chain mutagenesis reveals intrahelical coupling in an ion channel voltage-sensor. *Nat Commun* **9**, 5055 (2018).
67. Pless, S.A. & Ahern, C.A. Unnatural amino acids as probes of ligand-receptor interactions and their conformational consequences. *Annu Rev Pharmacol Toxicol* **53**, 211-29 (2013).
68. Van Arnam, E.B. & Dougherty, D.A. Functional probes of drug-receptor interactions implicated by structural studies: Cys-loop receptors provide a fertile testing ground. *J Med Chem* **57**, 6289-300 (2014).
69. Cockroft, S.L., Hunter, C.A., Lawson, K.R., Perkins, J. & Urch, C.J. Electrostatic control of aromatic stacking interactions. *J Am Chem Soc* **127**, 8594-5 (2005).
70. Lim, V.T. et al. Insights on small molecule binding to the Hv1 proton channel from free energy calculations with molecular dynamics simulations. *Sci Rep* **10**, 13587 (2020).
71. Zhao, C. et al. Hv1 inhibition by HIF reveals a new druggable pocket in the voltage-sensing domain. *Co-submitted to J. Gen. Physiol.* (2021b).

## Chapter 5: Hv1 inhibition by HIF reveals a new druggable pocket in the voltage-sensing domain

(Zhao, Hong, Riahi, Lim, Tobias, Tombola)

### Abstract

Voltage-gated sodium, potassium, and calcium channels consist of four voltage-sensing domains (VSDs) that surround a central pore domain and transition from a down state to an up state in response to membrane depolarization. While many types of drugs bind pore domains, the number of organic molecules known to bind VSDs is limited. The Hv1 voltage-gated proton channel is made of two VSDs and does not contain a pore domain, providing a simplified model for studying how small ligands interact with VSDs. Here, we describe a ligand, named HIF, that interacts with the Hv1 VSD at two sites with different accessibilities in the up and down states. We find that HIF rapidly inhibits proton conduction in the up state by blocking the open channel, as previously described for 2-guanidinobenzimidazole and its derivatives. HIF, however, interacts with an additional site slowly accessible in the down state. Functional studies and MD simulations suggest that this interaction traps the compound in a narrow pocket lined with charged residues within the VSD intracellular vestibule, which results in slow recovery from inhibition. Our findings point to a “wrench in gears” mechanism of trapping whereby side chains within the binding pocket act as teeth of interlocking gears. We propose that the use of screening strategies designed to target binding sites with slow accessibility similar to the one identified here could lead to the discovery of new ligands capable of interacting with VSDs of other voltage-gated ion channels in the down state.

## 5.1 Introduction

The voltage-gated proton channel Hv1 plays important roles in numerous biological processes including pH homeostasis, the immune response, and sperm cell function<sup>1,2</sup>. It belongs to the large family of proteins containing VSDs, which also includes Nav, Kv, and Cav channels, and voltage sensitive phosphatases<sup>3,4</sup>. The channel consists of two identical subunits<sup>5-7</sup> that gate cooperatively<sup>8-10</sup>. Each subunit contains four transmembrane helices, S1 through S4, which form a VSD<sup>11,12</sup>.

Hv1 is an emerging pharmacological target due to its role in a variety of diseases, such as ischemic stroke and cancer<sup>13,14</sup>. Because of its simplified structural organization, it is also a good model for studying how small molecules interact with VSDs. Proton conduction in Hv1 does not occur through a pore domain, as in other voltage-gated channels, it occurs through the VSD itself. Accordingly, ligand binding can be monitored via its direct effect on the VSD-mediated current rather than its indirect effects on the pore domain, as first shown with the prototypical Hv1 inhibitor Zn<sup>2+</sup><sup>3,4,15,16</sup>.

VSDs change conformation in response to membrane depolarization as their S4 helix transitions from a down state to an up state<sup>17</sup>. In the Hv1 VSD, the proton conduction pathway is closed in the down state and open in the up state. The arginine-mimic 2-guanidinobenzimidazole (2GBI) was previously shown to inhibit the human Hv1 channel by binding to the intracellular side of the VSD in the open conformation (up state)<sup>18-21</sup>. Both the imidazole ring and the condensed phenyl ring of the compound were found to interact with the channel<sup>22</sup>. In order to improve such interactions, a new class of inhibitors was generated in which the two rings were separated by flexible linkers<sup>23</sup>. These compounds, named HIFs, were also compared to 2-aminobenzimidazole (ABI) derivatives to assess the effect of fluorination on the ligand apparent binding affinity. The compound HIF, which contains a difluorophenyl ring, was found to be

superior to both ABI and 2GBI at inhibiting Hv1, and its binding site within the VSD in the open conformation was proposed to overlap with the 2GBI binding site<sup>23</sup>.

Here, we investigate HIF interactions with the Hv1 VSD in more detail and find that, in addition to the binding site responsible for open channel block (binding to the up state), HIF interacts with a second site which is accessible in the down state and is responsible for key features of HIF-mediated inhibition, such as the slow component of current decay and the slow recovery from inhibition. We use mutagenesis-based perturbation analysis, molecular docking, and atomistic simulations to identify the location of this additional site. Its amino acid composition and structural features suggest that similar interaction sites could exist in the VSDs of other voltage-gated ion channels.

## 5.2 Materials and Methods

### *DNA constructs and chemical reagents*

Mutagenesis was performed as previously described<sup>21</sup>. mRNAs were synthesized using T7 mMessage mMachine transcription kit (Ambion) or HiScribe T7 ARCA mRNA kit (with tailing) (New England Biolabs) from linearized DNA constructs described in Zhao et al., 2020a. All chemical reagents were at the highest purity commercially available. 2-aminobenzimidazole (ABI), and 2-guanidinobenzimidazole (2GBI) were from Sigma-Aldrich. 3-(2-amino-5-methyl-1H-imidazol-4-yl)-1-(3,5-difluorophenyl)propan-1-one (HIF), 3-(2-amino-5-methyl-1H-imidazol-4-yl)-1-phenyl-propan-1-one (HIF<sub>NF</sub>), N-[(2-amino-5-methyl-1H-imidazol-4-yl)methyl]-3,5-difluorobenzamide (HIF<sub>NH</sub>), 3-(2-amino-5-methyl-1H-imidazol-4-yl)-1-(3,5-difluorophenyl)propan-1-ol (HIF<sub>OH</sub>), and (2E)-3-(2-amino-5-methyl-1H-imidazol-4-yl)-1-(3,5-difluorophenyl)prop-2-en-1-one (HIF<sub>EN</sub>) were custom synthesized by Enamine (see Zhao et al., 2020a). With the exception of HIF<sub>NH</sub>, all HIF compounds were in the form of hydrochloride salt. Stock solutions of Hv1 inhibitors in DMSO or methanol were diluted in the bath medium at the

desired final concentration before each experimental session.

### ***Electrophysiology***

Xenopus oocytes were from Ecocyte Bioscience or Xenopus 1. 1-3 days before the electrophysiological measurements, cells were injected with mRNAs (50 nl per cell, 0.5-1.5 ng/nl) using a Nanoject II (Drummond Scientific). Cells were kept at 18°C in ND96 medium containing 96 mM NaCl, 2 mM KCl, 1.8 mM CaCl<sub>2</sub>, 1 mM MgCl<sub>2</sub>, 10 mM HEPES, 5 mM pyruvate, 100 mg/ml gentamycin (pH 7.2). Voltage-clamp measurements were performed in inside-out patch configuration, using an Axopatch 200B amplifier controlled by pClamp10 software through an Axon Digidata 1440A (Molecular Devices). The signal current was lowpass filtered online at 1 kHz, before digitalization (2 kHz sampling), and then further filtered offline at 150 Hz (Bessel, -80 dB/decade). All measurements were performed at 22 ± 1 °C. Pipettes had 1-3 MΩ access resistance. Bath and pipette solutions contained 100 mM 2-(N-morpholino) ethanesulphonic acid (MES), 30 mM tetraethylammonium (TEA) methanesulfonate, 5 mM TEA chloride, 5 mM ethylene glycol-bis(2-aminoethyl)-N,N,N',N'-tetra-acetic acid (EGTA), adjusted to pH 6.0 with TEA hydroxide. Unless otherwise specified, the holding potential was -40 mV and the depolarization potential +120 mV.

Channel inhibition was determined by isochronal current measurements at the end of the depolarization pulses. To test whether the time course of HIF-mediated Hv1 inhibition was state dependent, voltage protocols with variable relative depolarization time<sup>24</sup> were used. RDT is defined as  $t_d/(t_r + t_d)$ , where  $t_d$  is the time spent at +120 mV and  $t_r$  is the time at -40 mV between consecutive depolarizations. The  $t_d/(t_r + t_d)$  values were 0.1 (2s/20s), 0.2 (3s/15s), 0.3 (3s/10s), and 0.5 (3s/6s). Comparisons between HIF and its analogues, and between Hv1 mutants and WT, were performed at RDT = 0.2, with the exception of F150A and D112E. To properly track the fast kinetic of inhibition of Hv1 F150A, the RDT was increased to 0.3.

Conversely, to properly track the slow kinetic of inhibition of Hv1 D112E, the RDT was decreased to 0.1. Matched RDTs were used for comparisons with WT. Hv1 inhibitors were introduced in the bath using a computer-controlled gravity-fed multi-valve perfusion system (Warner Instruments). Fast perfusion experiments were carried out with a multi-barrel perfusion pencil (Automate Scientific) mounting a delivery tip 360  $\mu\text{m}$  in diameter positioned in front of the patch pipette.

### **Data analysis**

Clampfit10.2 (Molecular Devices) and Origin8.1 (OriginLab) were used for data analysis. Leak subtraction and run-down correction of current traces were performed as previously described<sup>21</sup>.

Time-courses of Hv1 inhibition were fitted with the double-exponential function (1):

$$I(t)/I_o = c_{\infty} + c_{fast}e^{(t_o-t)/\tau_{fast}} + c_{slow}e^{(t_o-t)/\tau_{slow}} \quad (1)$$

where  $(I(t)/I_o)$  is the normalized current decay in the presence of the inhibitor, and  $\tau_{fast}$  and  $\tau_{slow}$  are the time constants for the fast and slow components of the decay with weights  $c_{fast}$  and  $c_{slow}$ , respectively.  $t_o$  indicates the start of the decay when the perfusion of the inhibitor begins.  $c_{\infty}$  is the fraction of the remaining current when inhibition reaches steady state. For the recovery from inhibition, the fitting was performed with the single-exponential function (2):

$$I(t)/I_o = 1 - c_{off}e^{(t_o-t)/\tau_{off}} \quad (2)$$

where  $\tau_{off}$  is the time constant of the recovery, while  $c_{off}$  quantifies the amplitude of the recovery.  $t_o$  indicates the time at which the inhibitor is removed from the bath compartment by perfusion of recording solution.

G-V measurements were carried out as the previously described<sup>7</sup>. Tail currents were measured at -40 mV after depolarization steps from -20mV to +120mV. Current rundown was corrected using a reference depolarization step preceding the test depolarization. G-V plots were fitted

with the Boltzmann equation (3):

$$G/G_{max} = 1/(1 + e^{(V_{1/2}-V)/s}) \quad (3)$$

where  $V_{1/2}$  is the potential of half maximal activation, and  $s$  is the slope, all in mV. Unless otherwise specified, data are reported as averages from at least four independent measurements, and error bars are standard error of the mean (SEM). Fitting parameters are shown with standard error (SE). Each average comes from measurements performed on at least two distinct batches of cells.

### ***State model of HIF block***

The process of HIF-mediated Hv1 inhibition was simulated with Berkeley Madonna 9.1<sup>25</sup> using the four-state model shown in Figure 2A (model S), or the 5-state model shown in Figure S8 (model E). C and O are the fractions of unbound channels in the closed and open states, respectively. Both models assume that the inhibitor interacts differently with the channel in the closed and open states. B and T (model S) or  $B_1$ ,  $I_2$ , and  $T_2$  (model E) are the fractions of channels interacting with the inhibitor in the modalities described in the Results section. The total number of channels ( $N = N_C + N_O + N_B + N_T$  for model S, or  $N = N_C + N_O + N_{B1} + N_{I2} + N_{T2}$  for model E) was set to remain constant during the simulation ( $dN/dt = 0$ ). Assuming that the rate constants under the simulated conditions remain the same at equilibrium, detailed balance principle was applied to satisfy the following relationships:  $(k_{CO} \cdot k_{OB} \cdot k_{BT} \cdot k_{TC}) / (k_{OC} \cdot k_{BO} \cdot k_{TB} \cdot k_{CT}) = 1$  for model S, or  $(k_{CO} \cdot k_{OI2} \cdot k_{I2T2} \cdot k_{T2C}) / (k_{OC} \cdot k_{I2O} \cdot k_{T2I2} \cdot k_{CT2}) = 1$  and  $(k_{OB1} \cdot k_{B1I2} \cdot k_{I2O}) / (k_{B1O} \cdot k_{I2B1} \cdot k_{OI2}) = 1$  for model E. A common feature of the two models is that the  $T \leftrightarrow B$  and  $T_2 \leftrightarrow I_2$  transitions are significantly slower than the  $C \leftrightarrow O$  transition. For simplicity, the deceleration was applied uniformly at all voltages by multiplying the voltage-dependent rate constants  $k_{CO}$  and  $k_{OC}$  by non-voltage-dependent parameters ( $f_s$ ), so that  $k_{TB} = f_{TB} \cdot k_{CO}$ ,  $k_{BT} = f_{BT} \cdot k_{OC}$ ,  $k_{T2I2} = f_{T2I2} \cdot k_{CO}$ , and  $k_{B2T2} = f_{B2T2} \cdot k_{OC}$ . The integration method was Runge-Kutta 4 with step size of either 0.01 or 0.02

s. The models calculated the proton current as a function of applied membrane potential ( $V_m$  in mV) through the equation  $I = G_{\max} \cdot O \cdot V_m$ , where  $O = N_o/N$ , and  $G_{\max}$  is the maximal conductance in nS (the reversal potential was assumed to be 0 mV to match experimental conditions). Simulation parameters for HIF-mediated inhibition of Hv1 WT are reported in Fig. S2 for model S, and Fig. S8 for model E. Simulation parameters for HIF-mediated inhibition of Hv1 F150A with model S are reported in Fig. S7. The shift in the Hv1 voltage dependence of activation caused by HIF (Fig. S5A) means that the simulation conditions described here should be utilized only when strong membrane depolarizations ( $V_m > 100$  mV) are applied to monitor channel inhibition. If lower membrane potentials are used, the additional reduction in current produced by the G-V shift needs to be considered (see Discussion).

### ***Docking calculations and molecular dynamics simulations***

HIF was docked into a previously described closed-state model of the human Hv1 VSD<sup>19</sup> using AutoDock Vina<sup>26</sup>. Docking was performed using 100 protein configurations extracted from the last part (~3  $\mu$ s) of a 8-microsecond simulation at 0 mV<sup>19</sup>. The membrane and all water molecules were removed during docking. The search space included the entire intracellular vestibule up to D112 (total volume search space: 33 Å × 33 Å × 24 Å). The starting pose for MD simulations was chosen from visual evaluation of the ligand's proximity to putative binding site residues based on experimental data (proximity of the five-membered ring to D174 and proximity of fluorinated ring to W207). HIF was parameterized as described in Zhao et al., 2020a. MD simulations of HIF-bound Hv1 VSD embedded in a solvated POPC lipid bilayer were performed using NAMD 2.13<sup>27</sup>. The CHARMM36 force field<sup>28,29</sup> was used for both protein and lipid, and the TIP3P model was used for water<sup>30</sup>. The system was first energy-minimized using the conjugate gradient algorithm then equilibrated for 8 ns in the canonical (NVT) ensemble at a temperature of 300 K maintained by the Langevin thermostat with a damping constant of 1

ps<sup>-1</sup>. All simulations were run with a 2-femtosecond (fs) time step, with constrained bonds to hydrogen atoms using the SHAKE algorithm, and with periodic boundary conditions applied in all directions. Bonded interactions and short-range forces were calculated every 2 fs, and long-range forces were calculated every 4 fs. Long-range electrostatic interactions were treated using the Particle Mesh Ewald (PME) algorithm<sup>31</sup>, while short-range Lennard-Jones and Coulombic interactions were calculated with a cutoff of 12 Å and a switching function applied beyond 10 Å. The system was simulated under 0 mV membrane potential. Following NVT equilibration, dynamics were run for 120 ns in the isothermal-isobaric (NPT) ensemble at a pressure of 1 atm applying the Langevin piston method<sup>32,33</sup> with an oscillation period of 200 fs and a damping time of 100 fs. All other simulation settings were maintained as described for the NVT stage.

### 5.3 Results

#### *HIF-mediated inhibition of Hv1 has two kinetically distinct components*

In Hv1 WT, the processes of 2GBI binding and unbinding are faster than the process of channel opening<sup>21</sup> (timescale of seconds). Accordingly, Hv1 proton currents measured from inside-out patches were rapidly reduced to a stable inhibited level (close to 50% of the original current) upon perfusion of 50 μM 2GBI in the intracellular compartment, and they returned to their original level in few seconds upon 2GBI wash out (Fig. 1A). When tested at the same concentration, ABI inhibited the proton current to a smaller extent but with similar kinetics (Fig. 1A). In contrast, the time course of Hv1 inhibition by 50 μM HIF displayed an initial fast decrease in proton current followed by a further decrease on a much longer time scale (Fig. 1B). The kinetics of inhibition could be best fitted by a two-exponential decay (eq. 1) with time constants  $\tau_{\text{fast}} < 5$  s and  $\tau_{\text{slow}} > 40$  s (Fig. 1C). After removal of the inhibitor, the current recovered

only slowly (Fig. 1B). The time course of recovery was fitted with a single exponential function (eq. 2) which produced a time constant  $\tau_{\text{off}} \geq 80$  s (Fig. 1C). To check whether the time course of inhibition depended on the relative time spent in the open state during HIF application, we performed measurements in which the relative depolarization time (RDT, see Methods) was varied from 0.1 (1 tenth of the time in the open state) to 0.5 (half of the time in the open state). Membrane patches were not as long-lasting at high depolarization frequencies as they were at low depolarization frequencies. As a result, it was not possible to follow the time course of inhibition for high RDTs as long as for low RDTs. Nevertheless, the data could be well fitted by a double exponential function in all cases, providing fast and slow time constants.

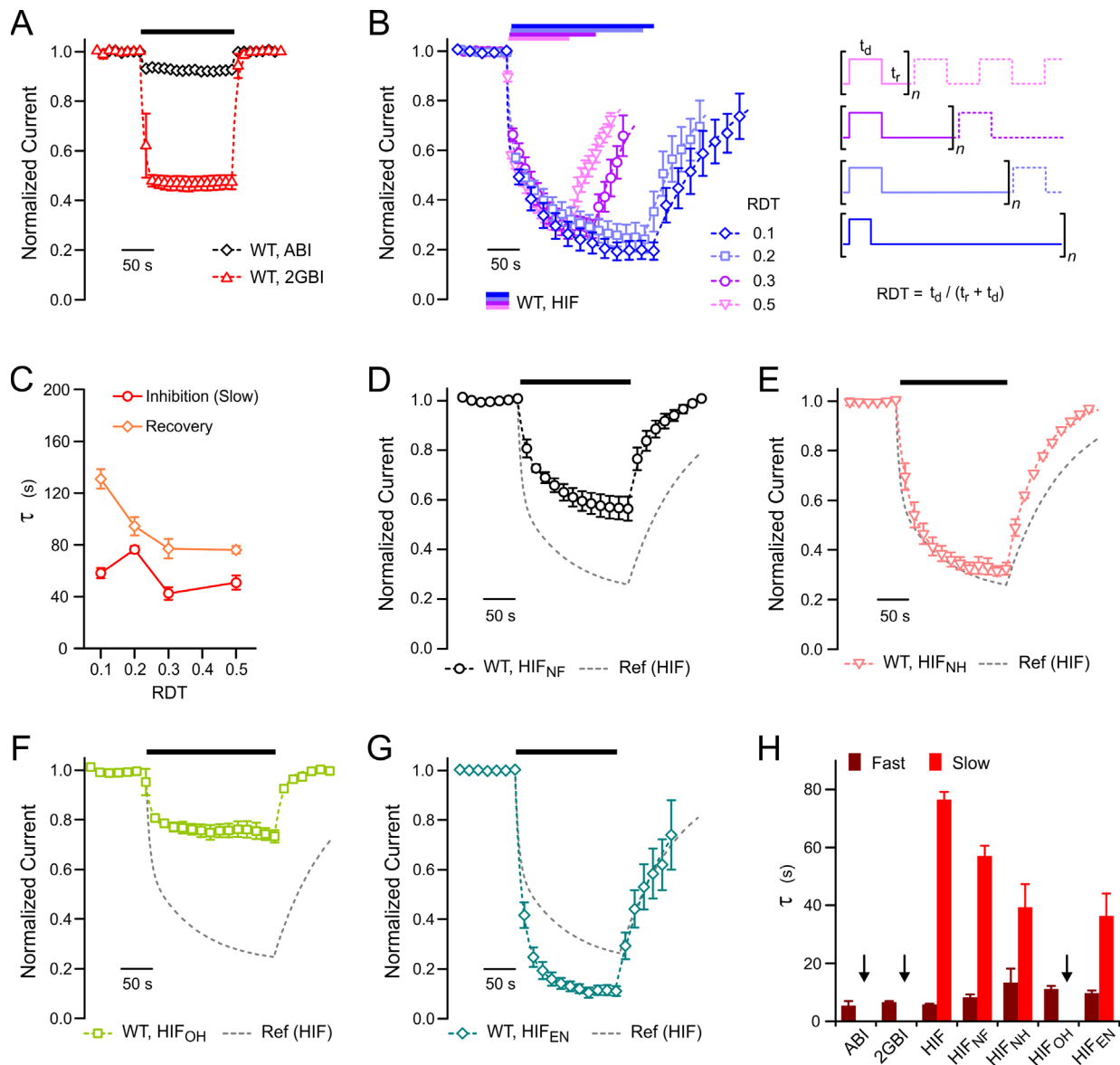


**Figure 5.1. Kinetics of Hv1 inhibition by HIF compounds compared to ABI and 2GBI.** **A)** Time courses of channel inhibition by 50  $\mu\text{M}$  ABI or 2GBI. Black bar indicates the presence of the inhibitor in the bath solution. Currents were measured in inside-out patches from oocytes expressing Hv1 WT. Membrane was depolarized to +120 mV from a holding potential of -40 mV,  $\text{pH}_i = \text{pH}_o = 6.0$ . Data points are averages from 3 independent measurements for each inhibitor  $\pm$  SEM. **B)** Time courses of channel inhibition by 50  $\mu\text{M}$  HIF under different RDT conditions. Horizontal bars indicate the presence of the inhibitor in the bath solution. Currents were measured as in (A) following voltage protocols with variable RDT. Data points are averages from  $n$  independent measurements for each RDT condition  $\pm$  SEM ( $n = 7, 7, 5, 8$  for RDT = 0.1, 0.2, 0.3, 0.5, respectively). Fitting curves are shown as dashed lines (see Methods). **C)** Time constants of HIF-mediated inhibition of Hv1 WT (slow component, red) and recovery (orange) as a function of RDT from fits of data points in (B). Error bars are SE. **D-G)** Time courses of inhibition of Hv1 WT by the indicated compounds compared to HIF (gray dash line). All compounds were tested using a voltage protocol with RDT = 0.2. Black bars indicate the presence of 50  $\mu\text{M}$  inhibitor in the bath solution. Data points are averages from  $n$  independent measurements for each inhibitor ( $n = 5, 4, 4, 5$  for HIF<sub>NF</sub>, HIF<sub>NH</sub>, HIF<sub>OH</sub>, HIF<sub>EN</sub>, respectively). Error bars are SEM. **H)** Time constants  $\tau_{\text{fast}}$  and  $\tau_{\text{slow}}$  from fitting of time courses of inhibition reported in (A-B) and (D-G). Error bars are SE. Black arrows indicate lack of the slow

component of channel inhibition.

We found that the time course of inhibition, and  $\tau_{\text{slow}}$  in particular, did not show a clear dependence on RDT (Fig. 1B-C). However, the recovery from inhibition upon washout became faster ( $\tau_{\text{off}}$  decreased) as RDT increased (Fig. 1C). To confirm that the recovery from inhibition is a function of the relative depolarization time during wash out ( $\text{RDT}_{\text{off}}$ ), we used a protocol with  $\text{RDT}_{\text{on}} = 0.2$  to monitor the current decay induced by 100  $\mu\text{M}$  HIF. Once the inhibition reached  $\sim 90\%$ , we removed the inhibitor while simultaneously switching to a different recording protocol with  $\text{RDT}_{\text{off}}$  values of either 0.1 or 0.5 (Fig. S1, blue and pink traces, respectively). We fitted each recovery of inhibition with a single exponential function and confirmed that the time constant  $\tau_{\text{off}}$  decreased as  $\text{RDT}_{\text{off}}$  increased (Fig. S1, bar graph), suggesting that more frequent channel openings allow for faster HIF unbinding.

We then measured the time courses of channel inhibition by 50  $\mu\text{M}$  of HIF analogs  $\text{HIF}_{\text{NF}}$ ,  $\text{HIF}_{\text{NH}}$ ,  $\text{HIF}_{\text{OH}}$ , and  $\text{HIF}_{\text{EN}}$ , which differ from HIF in the way the phenyl ring is substituted or connected to the common 2-aminoimidazole moiety (Zhao et al., 2020). The inhibition kinetics for  $\text{HIF}_{\text{NF}}$ ,  $\text{HIF}_{\text{NH}}$ , and  $\text{HIF}_{\text{EN}}$  resembled the one for HIF, with fast and slow components (Fig. 1D,E,G), and could be fitted with a double-exponential decay (Fig. 1H). On the other hand, the inhibition kinetics for  $\text{HIF}_{\text{OH}}$  did not have a significant slow component (Fig. 1F) and could be fitted by a single exponential decay with a time constant similar to  $\tau_{\text{fast}}$  of HIF (Fig. 1H). These findings indicate that: 1) HIF compounds interact with Hv1 via two processes that are kinetically distinct, and 2) the hydroxyl group in  $\text{HIF}_{\text{OH}}$  strongly reduces the slow inhibitory process that distinguish HIF compounds from 2GBI and ABI.

### ***Mechanism of Hv1 inhibition by HIF: a kinetic model***

The simplest kinetic scheme that can describe Hv1 inhibition by 2GBI and ABI involves three

states: closed (C), open (O), and blocked (B) with S4 down in the C state and up in the O and B states (Fig. 2A-B). The kinetic properties of the inhibition process and the position of the binding site within the VSD are consistent with a mechanism in which the channel can bind the inhibitor only in the open state and cannot close until the binding site is vacated<sup>18-21</sup>. Hv1 inhibition by HIF and its analogs occurs in at least two steps with distinct kinetic components. As a result, a model with more than three states is required for its description. We found that the addition of a fourth state connected to the B and C states and with S4 down (Fig. 2A-B) was sufficient to explain the main properties of the HIF-mediated inhibition (see Methods and Figs. S2-S3 for details). We refer to the additional state as "trapped" (T) because the kinetic rates associated with the B ↔ T and C ↔ T transitions are much slower than channel activation at the tested voltage and the process of open-channel block (C ↔ O and O ↔ B transitions) (Fig. S2 and Fig. 2B). The four-transition scheme shown in Fig. 2A (hereafter referred to as model S) successfully reproduced the experimental time course of channel inhibition, with its two components, and the slow recovery after HIF removal (Fig. 2C). Changing RDT<sub>on</sub> from 0.5 to 0.1 produced only minor changes in  $\tau_{\text{slow}}$  in the simulated inhibition in agreement with the experimental observation (Fig. S3A-B). In addition, the model replicated the dependence of the recovery from inhibition on RDT<sub>off</sub> (Fig. S3C), and the overall concentration dependence of inhibition (Fig. S3D).

The proposed mechanism of HIF inhibition implies that the compound can bind the VSD in the closed state. To confirm this point, we assessed channel inhibition under pulsed application of the inhibitor (100  $\mu\text{M}$  for 3 s, Fig. 2D). The membrane was kept at -40 mV during each application, and the effect on the proton current was measured after each pulse with a depolarization step at +120 mV (Fig. 2E). Control pulses of 100  $\mu\text{M}$  2GBI were applied first to verify that the inhibitor could be completely removed from the intracellular solution between consecutive depolarizations (Fig. 2E-F). The time course of inhibition under pulsed conditions

is shown in Fig. 2F (teal squares). The current slowly decayed following a single exponential function with  $\tau = 46 \pm 4$  s, which is in good qualitative agreement with the kinetics of inhibition predicted by model S (black circles). The current decay predicted by a four-state model similar to model S but lacking the  $C \leftrightarrow T$  transition is also shown (Fig. 2F, pink circles).

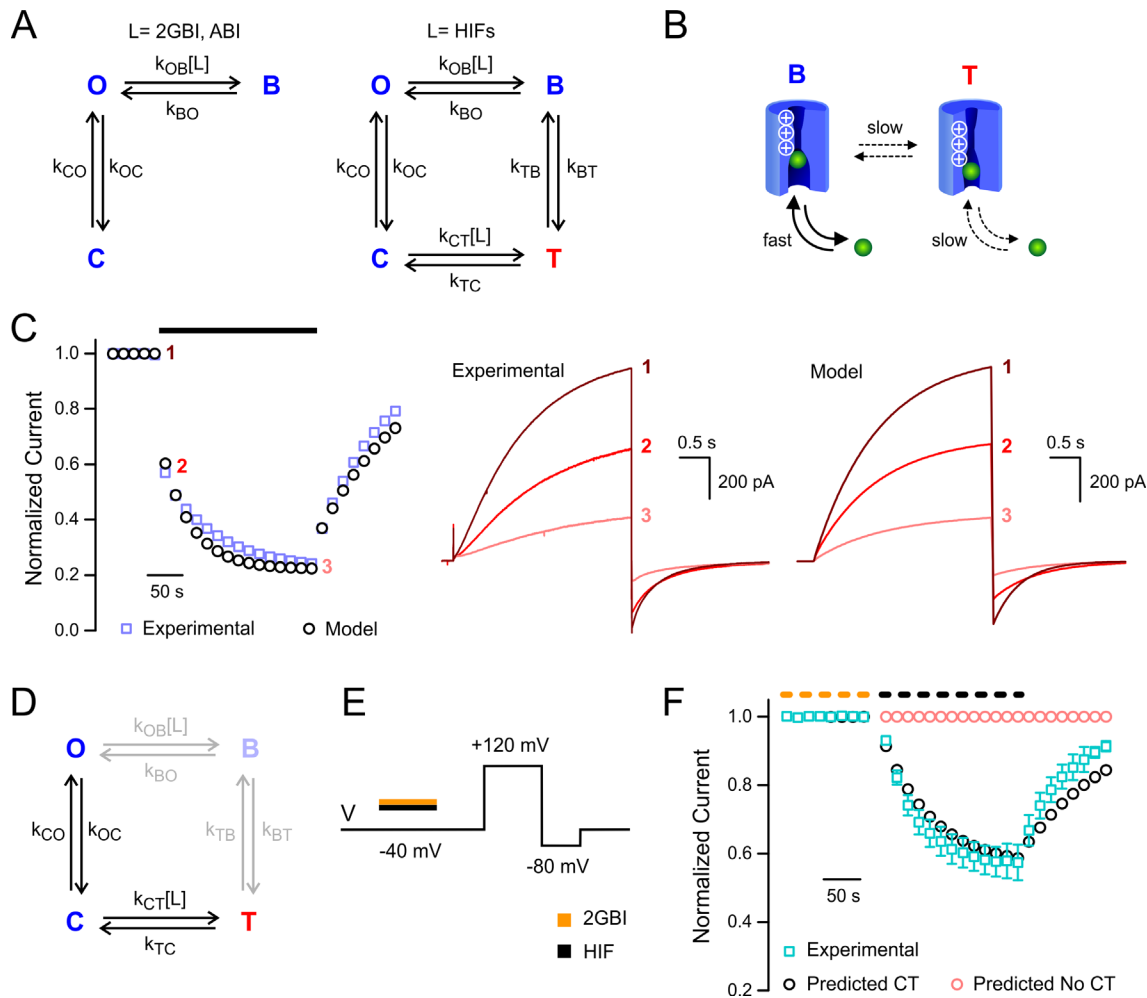


**Figure 5.2. Four-state model replicates Hv1 inhibition by HIF.** **A)** Kinetic schemes for modeling Hv1 inhibition by the indicated compounds. For ABI and 2GBI, the scheme involves three states: O (open), B (blocked), and C (closed). For HIFs, an additional state (T) is required (model S). **B)** Correspondence between B and T states with open and closed VSD configurations. The inhibitor can quickly bind and unbind from the open VSD (S4 in the activated position). The inhibitor can slowly bind and unbind from the closed VSD (S4 not activated). White positive charges represent S4 arginines. **C)** Simulated time course of HIF-mediated Hv1 inhibition and recovery using model S compared to experimental data from Fig. 1B. For modeling parameters, see Fig. S2A. Black bar indicates the presence of 50  $\mu$ M HIF in the bath compartment. Current traces generated by the model at time points 1, 2, and 3 are compared to the current traces measured experimentally at the corresponding time points. **D)** Kinetic scheme in effect when the channel is exposed to HIF in the closed state only (minimized fraction of channels in the B state). **E)** Protocol used to expose the channel to HIF selectively in the closed state. Yellow and black bars indicate the presence of 100  $\mu$ M 2GBI or HIF in the bath compartment, respectively (each sweep was

15s-long with depolarization step lasting 3 s, see also Fig. S2B). F) Time course of channel inhibition and recovery under protocol (E) - teal squares. Yellow and black dashed lines indicate recurring transient exposure to 2GBI or HIF, respectively. Data points are averages from 7 independent measurements  $\pm$  SEM. Black and light-red circles indicate normalized current predicted by the four-state model in the presence and absence of the C  $\leftrightarrow$  T transition, respectively. For modeling parameters, see Fig. S2B.

We then tested whether the resting membrane potential used to keep the channel closed affected the inhibition under pulsed conditions. We performed measurements at -80 mV (Fig. S4, blue circles), a voltage at which the closed state is much more stable than the open state, and at 0 mV (Fig. S4, green circles), a voltage near the opening threshold (foot of the G-V curve). We found that HIF inhibited the channel to a greater extent at 0 mV (more efficient trapping) compared to -80 mV ( $55 \pm 3\%$  at 0 mV,  $33 \pm 4\%$  at -80 mV). Hv1 is known to transition through multiple closed states before opening<sup>8,10,34-36</sup>. The dependency of channel inhibition on resting membrane potential might reflect different populations of closed channels with different affinities for HIF. Additionally, the processes of HIF binding and unbinding could be intrinsically voltage dependent.

Another implication of the proposed mechanism of HIF inhibition is that the closed VSD could be stabilized by the bound inhibitor making the channel more difficult to open. We verified whether this stabilization affected the channel voltage dependence of activation by comparing the G-V curve measured in the presence of 50  $\mu$ M HIF to the G-V curve measured in the absence of inhibitor (Fig. S5A). We did observe a  $\sim$ 15 mV shift to more positive potentials in the  $V_{1/2}$  of activation, consistent with a stabilization of the closed VSD induced by HIF. This finding contrasts with the lack of G-V shift observed with 2GBI under equivalent conditions (Fig. S5B), which is expected, as 2GBI is an open channel blocker unable to stabilize the closed state<sup>21</sup>.

### ***Structural determinants of Hv1 inhibition by HIF***

The requirement for two distinct inhibitor-bound states (B and T) in the kinetic model of HIF inhibition could be easily explained by assuming that HIF binds the VSD in two different

modalities or binding sites, which we refer to as site 1 and 2. Under this assumption, HIF interaction with site 1 would be responsible for the fast component of the time course of inhibition (transition to state B), the interaction with site 2 would be responsible for the slow component (transition to state T), and the inability of 2GBI to interact with site 2 would provide a simple justification for the lack of a slow component in its time course of inhibition. Accordingly, model S predicts that a destabilization of state T (interaction with site 2) will eliminate or strongly reduce the slow component of channel inhibition (Fig. S6A), whereas the destabilization of state B (interaction with site 1) will eliminate or strongly reduce the fast component of channel inhibition (Fig. S6B).

To test these possibilities and gain insight into the nature of the two sites within the channel protein, we compared the time course of inhibition of various Hv1 mutants to Hv1 WT ([HIF] = 50  $\mu$ M) and assessed the effect of each mutation on the fast and slow components of the current decay. First, we measured the effect of HIF on the proton current of a monomeric version of Hv1, a chimeric channel in which the N- and C- termini are replaced with the corresponding parts of the voltage-sensitive phosphatase CiVSP<sup>7,37</sup> (Fig. 3A). We found that the kinetics of inhibition was perturbed compared to WT. The time constants for the two components ( $\tau_{fast}$  and  $\tau_{slow}$ ) were too close to each other to be reliably resolved by a double-exponential fit. As a result, the time course of inhibition was fitted with a single-exponential function. Despite the differences in kinetics, the extent of inhibition in the chimeric channel was not reduced (Fig. 3A), indicating that a functional intersubunit interface is not required for HIF binding.

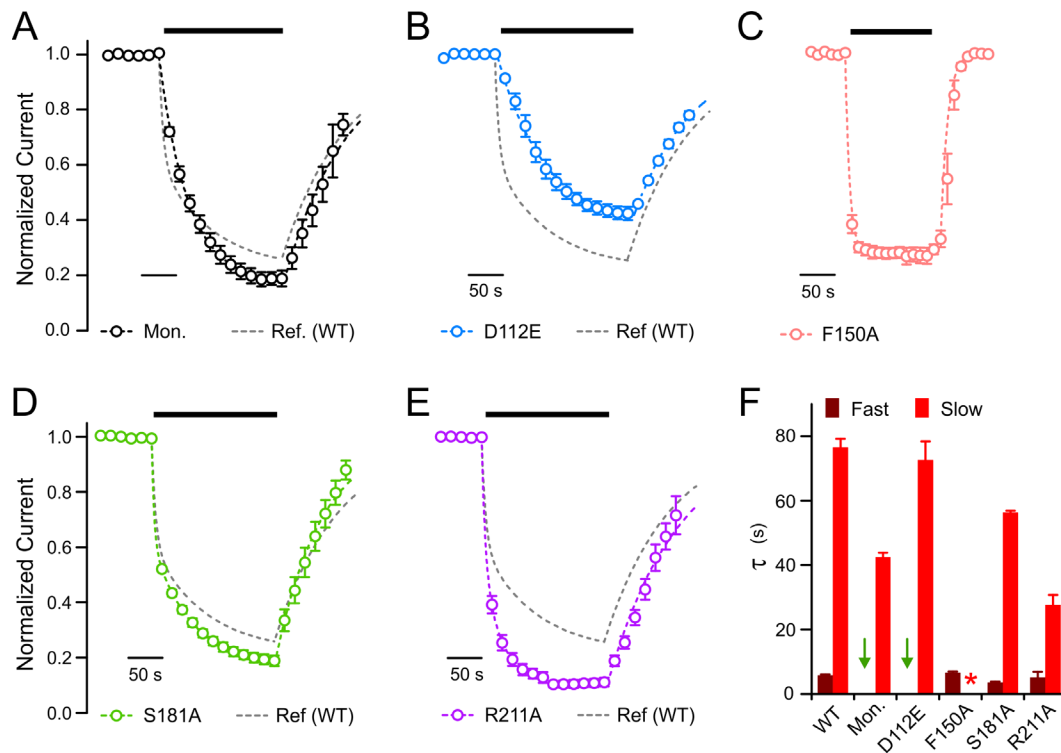


**Figure 5.3. Structural determinants of HIF-mediated inhibition - open VSD.** **A)** Time course of inhibition of monomeric Hv1 by 50  $\mu$ M HIF compared to WT (dimeric) channel. The fast component is slowed down and cannot be resolved from the slow component. **B)** Time course of inhibition of Hv1 D112E by 50  $\mu$ M HIF shows lack of fast component. **C)** Time courses of inhibition of Hv1 F150A by 100 nM HIF displays enhanced fast component. **D)** Time courses of inhibition of Hv1 S181A by 50  $\mu$ M HIF shows only minor deviations from WT. **E)** Time courses of inhibition of Hv1 R211A by 50  $\mu$ M HIF displays accelerated slow component and increased steady-state inhibition. Data points in (A-E) are averages from  $n$  independent measurements  $\pm$  SEM ( $n = 7, 4, 5, 5, 9$  for mon., D112E, F150A, S181A, R211A, respectively). Black bars indicate the presence of the inhibitor in the bath compartment. Fitting curves are shown as dashed lines with colors matching the corresponding symbols. Gray dash lines represent current decay and recovery of Hv1 WT. **F)** Time constants  $\tau_{\text{fast}}$  and  $\tau_{\text{slow}}$  from fitting of time courses of channel inhibition reported in (A-E). Error bars are SE. Green arrows indicate either non-resolved (mon.) or missing (D112E) fast component. Red asterisk indicates lack of slow component.

Hv1 residues at positions 112, 150, 181, and 211 were previously shown to participate in 2GBI binding when the channel is in the open conformation<sup>22</sup>. We assumed that some of these residues could interact with HIF as well. We measured the time courses of HIF-mediated inhibition of mutants D112E, F150A, S181A, and R211A and compared them to the time course of inhibition of WT (Fig. 3B-F). We found that the fast component of the inhibition process was eliminated by mutation D112E, while the slow component was unaffected (Fig. 3B). The fast component was strongly enhanced by mutation F150A to the point that the concentration of

HIF had to be reduced from 50  $\mu\text{M}$  to 100 nM to maintain an inhibition level comparable to WT (Fig. 3C). The effects of mutations D112E and F150A closely resembled those previously observed with 2GBI-mediated inhibition<sup>21,22</sup>, indicating that both HIF and 2GBI interact with a site comprising D112 and F150.

The R211A mutation accelerated the slow component of HIF-mediated inhibition (64% reduction in  $\tau_{\text{slow}}$ ) and decreased steady state remaining current (15% higher inhibition) (Fig. 3E, F). S181A had an impact similar to R211A but smaller in magnitude (26% reduction in  $\tau_{\text{slow}}$ , 7% higher inhibition, Fig. 3D, F). The fast component of inhibition was not significantly altered by the two mutations, suggesting that HIF and 2GBI may differ in the way they interact with R211 and S181.

D112 is located in the narrowest part of the Hv1 proton conduction pathway, approximately half way across the membrane where it serves as selectivity filter<sup>12,38,39</sup>. Earlier work showed that the residue is accessible to arginine mimics from the intracellular side of the membrane only when the channel is open<sup>19,21,22</sup>. The selective effect of mutation D112E on the fast component of HIF-mediated inhibition resembles what is predicted by model S when the B state is destabilized (Fig. S6A) and suggests that HIF interaction with D112 occurs in the open state at a location consistent with site 1. The effect of mutation F150A is predicted by model S when binding to site 1 is strongly stabilized and the gating process is accelerated compared to Hv1 WT (Fig. S7A). The biphasic shape of the current traces (increase followed by a decrease) in the presence of HIF indicates that the inhibitor must wait for the channel to open in order to interact with site 1 (Fig. S7B). This behavior was described earlier for 2GBI and its analogs {Hong, 2013; Hong, 2015}.

The finding that HIF interaction with site 1 in the open state involves D112 and F150 raises the question of how the positively charged inhibitor interacts with the closed state (site 2). Besides D112, Hv1 contains four other acidic residues in the transmembrane region at position 153, 171,

174, and 185. We tested for potential roles of these residues in HIF binding by measuring the time course of inhibition of channels mutated at each of the four positions. In the mutant selection process, we first tried conservative charge-neutralizing substitutions E/Q or D/N or alanine substitutions. However, we found that mutations at position 174 other than the charge-preserving D/E substitution resulted in proton currents too small to be reliably measured in inside-out patch configuration. In addition, mutation E153C resulted in better expression than the more conservative substitution E153Q. As a result, we tested HIF inhibition on channels carrying mutations E153C, E171Q, D174E, or D185A (Fig. 4).

The total extent of inhibition did not decrease in the E153C mutant, but the relative contribution of the slow component, measured as  $c_{slow}/(c_{fast} + c_{slow})$  (from Eq. 1), increased from 0.51 of the WT to 0.80 at the expense of the fast component (Fig. 4A). In addition, we observed a significant slowdown in the recovery from inhibition (Fig. 4A, black arrow,  $\tau_{off}$  (WT) =  $94 \pm 7$  s,  $\tau_{off}$  (E153C) =  $294 \pm 57$  s). These findings point to a reduced ability of Hv1 E153C to release HIF from its binding site and suggest a relative stabilization of the T state over the B state caused by the mutation.

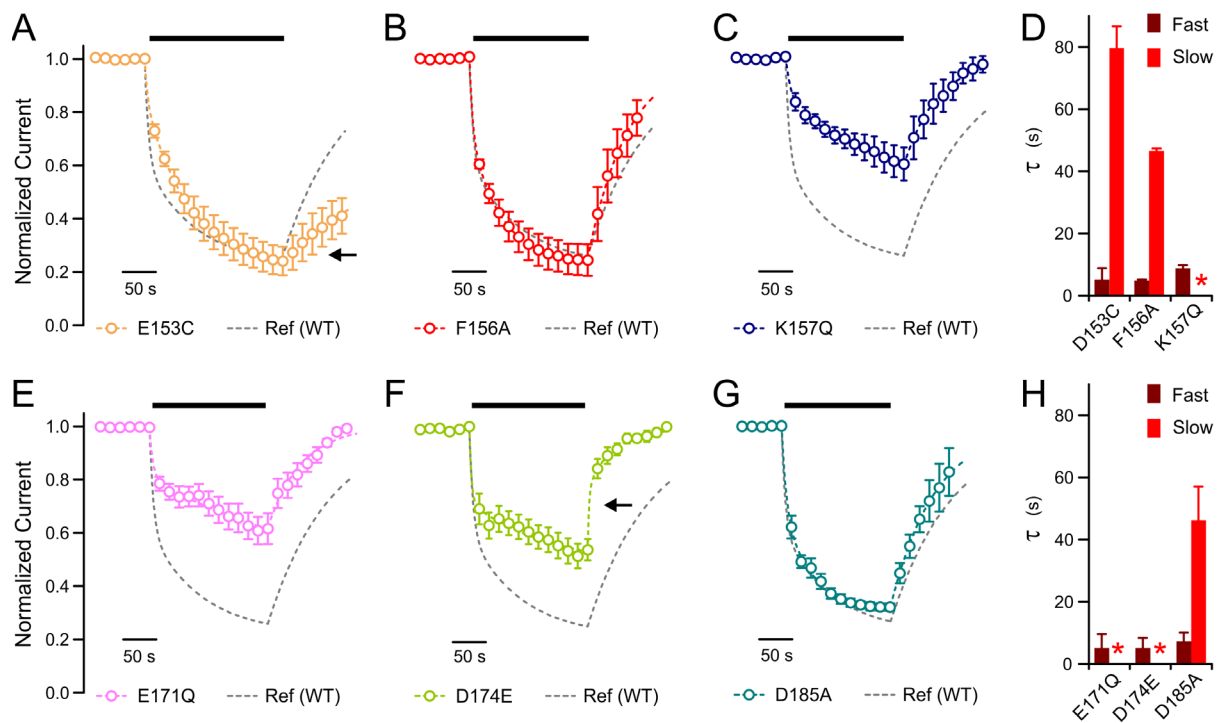


**Figure 5.4. Structural determinants of HIF-mediated inhibition - closed VSD.** A-C) Time courses of inhibition of Hv1 E153C, F156A, and K157Q by 50  $\mu$ M HIF. Black bars indicate the presence of the inhibitor in the bath compartment. Data point are averages from  $n$  independent measurements  $\pm$  SEM ( $n = 6, 7, 5$  for E153C, F156A, K157Q, respectively). K157Q reduces the extent of inhibition and decelerates current decay. E153C affects primarily the rate of recovery from inhibition (black arrow in (A)). F156A has negligible effects. D) Time constants  $\tau_{fast}$  and  $\tau_{slow}$  from fitting of time courses of channel inhibition reported in (A-C). Error bars are SE. E-G) Time courses of inhibition of Hv1 E171Q, D174E, and D185A by 50  $\mu$ M HIF. Black bars indicate the presence of the inhibitor in the bath compartment. Data point are averages from  $n$  independent measurements  $\pm$  SEM ( $n = 7, 8, 6$  for E171Q, D174E, D185A, respectively). E171Q and D174E perturbs the time course of channel inhibition significantly. In addition, D174E strongly accelerates recovery from inhibition (black arrow in (F)). D185A has negligible effects. H) Time constants  $\tau_{fast}$  and  $\tau_{slow}$  from fitting of time courses of channel inhibition reported in (E-G). Error bars are SE. Red asterisks in (D) and (H) indicate  $\tau_{slow} > 200$  s (too slow to be accurately quantified).

In the E171Q and D174E channels, the extent of HIF inhibition was reduced (46% and 35% reduction, respectively; Fig. 4E-F) and  $\tau_{slow}$  increased to such an extent ( $> 200$  s) that an accurate value could no longer be determined by double exponential fit. Furthermore, mutation D174E caused a marked acceleration of the recovery from inhibition ( $\tau_{off}$  (WT) =  $94 \pm 7$  s,  $\tau_{off}$  (D174E) =  $37 \pm 6$  s; Fig. 4F, black arrow). Mutation D185A, on the other hand, did not appreciably affect the extent or time course of HIF-mediated inhibition (Fig. 4G). The effect of mutation D174E and, to a smaller extent, the effect of D171Q resemble what is predicted by model S

when the T state is destabilized (Fig. S6B) consistent with the involvement of D174 and E171 in the process of HIF trapping in the closed VSD (interaction with site 2).

D174 is part of a network of charged residues forming electrostatic interactions in the intracellular vestibule of the channel<sup>12,18,40,41</sup> and it is located in the proximity of E171 and K157. The perturbation of HIF-mediated inhibition by neutralization of E171 suggested that a similar perturbation could be induced by neutralization of K157. We measured proton currents from Hv1 K157Q in the presence of 50  $\mu$ M HIF and found that the time course of inhibition resembled the one from the E171Q mutant, with a very low transition rate to the trapped state ( $\tau_{\text{slow}} > 200$  s) and reduced extent of inhibition (46% reduction, Fig. 4C). In contrast, mutation of residue F156, next to K157, did not result in any significant change in HIF inhibition (F156A, Fig. 4B). Based on these findings, we propose that the neutralization of E171 or K157 affects the electrostatic network that includes D174 and destabilizes the VSD-HIF interactions in the trapped state.

### ***Separating protein movements from ligand rearrangement***

In model S, S4 moves from the “down” conformation of the T state to the “up” conformation of the B state upon membrane depolarization, while the inhibitor concurrently moves from site 2 to site 1. So, the T  $\leftrightarrow$  B transition is a combination of two processes, one involving the protein and one involving the ligand. To emphasize the latter, the T and B states can be renamed as T<sub>2</sub> and B<sub>1</sub>, respectively (Fig S8A). Merging the two processes in one transition simplifies the description of HIF-mediated inhibition, but it is not a necessary condition. In the alternative model shown in Fig. S8A (model E) for example, the movement of S4 is separated from the movement of the ligand. Upon depolarization, T<sub>2</sub> leads to an intermediate state I<sub>2</sub> in which S4 is in the “up” conformation but the ligand is still interacting with site 2 (Fig. S8B). The ligand can then move to site 1 from I<sub>2</sub> to form B<sub>1</sub>. This model also implies the presence of a transition

$O \leftrightarrow I_2$  in which the ligand binds site 2 in the VSD open conformation. We found that model E can replicate the predictions of model S when the  $T_2 \leftrightarrow I_2$  transition (protein conformational change) is much slower than the  $I_2 \leftrightarrow B_1$  transition (rearrangement of the ligand). For the purpose of this work, model E did not offer significant advantages over model S. However, model E can be further implemented to explain aspects of Hv1 inhibition by HIF, and potentially other compounds that bind site 2, which have not been investigated here (see Discussion).

### ***HIF interactions with site 2***

To better understand the interactions between HIF with the closed VSD at site 2, we utilized a computational approach based on the structural model of the Hv1 VSD in the closed conformation generated from the 3WKV crystal structure<sup>12,19</sup> and equilibrated in a solvated POPC lipid membrane at 0 mV (see Methods). We first used the program AutoDock Vina<sup>26</sup> to search for potential binding sites within the VSD intracellular vestibule. We set the search space to include the entire vestibule and assigned to HIF a positive charge by protonating its five-membered ring. In 7 out of 9 most stable binding poses, HIF fluorinated phenyl ring was inserted in the narrowest part of the vestibule and pointed toward S4 residues W207 and R208; whereas the protonated 2-aminoimidazole ring was located in the wider part of the vestibule and interacted with the electrostatic network in the proximity of D174. An example of such poses is shown in Fig. 5A. We verified whether perturbation at positions 207 and 208 affected HIF-mediated inhibition by testing conservative mutations W207Y and R208K and found that Hv1 W207Y was inhibited to a smaller extent compared to Hv1 WT (38 % reduction, Fig. 5B), mostly due to a strong decrease in the transition rate to the trapped state ( $\tau_{\text{slow}} > 200$  s, Fig. 5D). R208K, on the other hand, had more subtle effects; the extent of inhibition was slightly increased compared to WT, but the fast kinetic component could no longer be resolved from the slow component (Fig. 5C, D). We were unable to measure proton currents from Hv1 channels

bearing less-conservative mutations at position R208. Overall, these results agree with the docking poses placing HIF fluorinated ring in the proximity of W207.

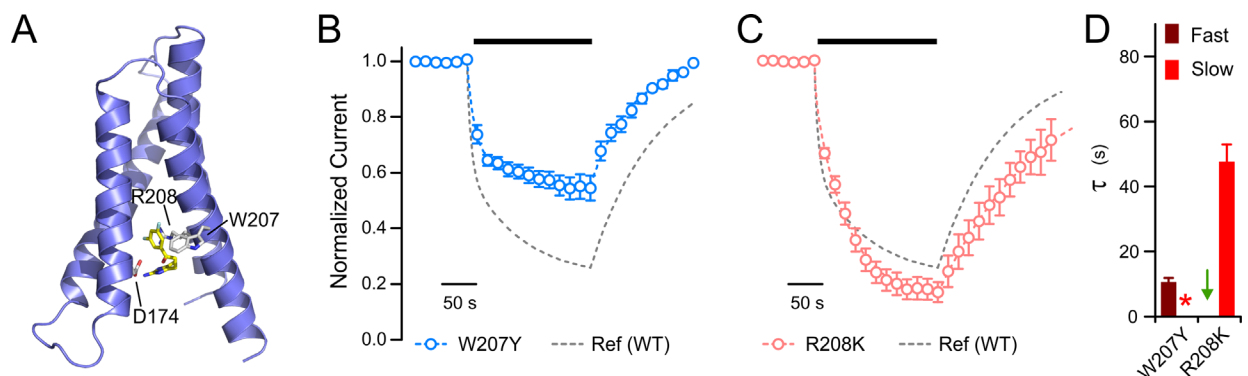


**Figure 5.5. HIF orientation within the closed Hv1 VSD. A)** Example of one of the highest scored binding poses predicted by AutoDock Vina for HIF showing the proximity of the ligand fluorinated phenyl ring to W207 and R208, and the proximity of the ligand 2-aminoimidazole ring to D174. **B)** Time courses of HIF-mediated inhibition for Hv1 W207Y. Black bar indicates the presence of 50  $\mu\text{M}$  HIF in the bath compartment. A reduced slow component in the current decay results in a decreased extent of inhibition compared to WT. **C)** Time courses of HIF-mediated inhibition for Hv1 R208K. Black bar indicates the presence of 50  $\mu\text{M}$  HIF in the bath compartment. The extent of the perturbation is significantly smaller than for W207Y. Data points in (B) and (C) represent averages from  $n$  independent measurements  $\pm$  SEM ( $n = 7$  for W207Y,  $n = 8$  for R208K). **D)** Time constants  $\tau_{\text{fast}}$  and  $\tau_{\text{slow}}$  from fitting of time courses of channel inhibition reported in (B) and (C). Error bars are SE. Asterisk in red indicates  $\tau_{\text{slow}} > 200$ . Green arrow indicates lack of resolvable fast component.

We then let the HIF molecule explore the Hv1 intracellular vestibule using unrestrained all-atom molecular dynamics simulations and the same structural model of the closed VSD<sup>19</sup> (Fig. 6). We used the data from molecular docking calculations and the data from mutagenesis experiments to set up the initial pose of HIF within the vestibule (see Methods section). The movement of the inhibitor within the putative binding site was then followed for 120 ns. As shown in Fig. 6A, the ligand center of mass (CM) did not move extensively in the  $z$  direction orthogonal to the membrane plane.

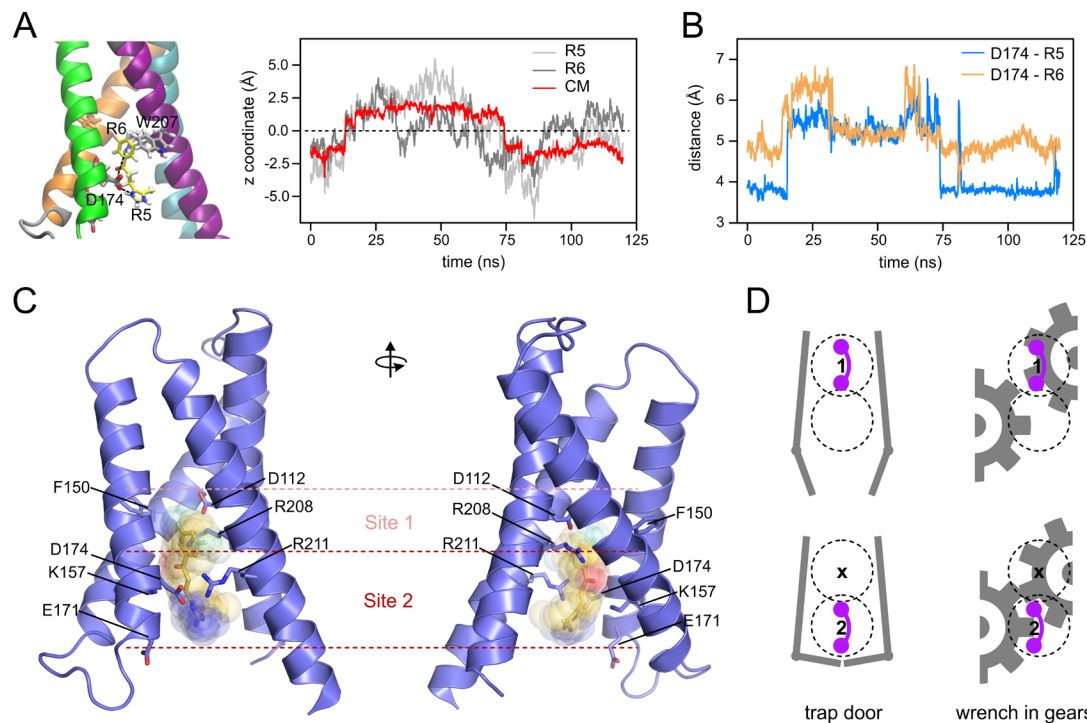


**Figure 5.6. Proposed HIF binding site in the closed channel and trapping mechanism.** **A)** Stability assessment of HIF within the binding site. The change in HIF's center of mass  $z$  coordinate is plotted as a function of time. Dashed line at  $z = 0 \text{ \AA}$  represents the average center of mass  $z$  position over the whole trajectory. The center of mass (CM) is evaluated for the entire ligand<sup>14</sup>, the five-membered ring alone (R5, light gray), and the six-membered ring alone (R6, dark gray). **B)** Distance measurements from the  $\gamma$ -carbon atom of D174 to HIF. The D174 to HIF contacts are measured from D174 to the nearest nitrogen atom of HIF (blue) and to the nearest carbon atom of the six-membered ring (orange). **C)** HIF bound to proposed site 2 in the closed VSD. The site contains an intracellular network of charged residues including D174, K157, E171, and R211. A representative snapshot is shown of the protein-ligand configuration from the last 40 ns of the MD trajectory. HIF is depicted as sticks, with transparent filled spheres portraying the region that HIF occupies over this portion of the trajectory. The location of site 1 (which includes D112 and F150) is shown here only for reference, as it is not accessible to the ligand in this state. HIF is shown bound to site 1 in the open VSD in Zhao et al., 2021a. **D)** MD simulations of HIF bound to the closed VSD do not support a “trap door” mechanism for trapping (left), as no steric or electrostatic barriers separate the ligand from the exit of the intracellular vestibule. In the simulations, HIF fits inside a pocket formed by side chains of VSD helices within the intracellular vestibule. It is proposed that these side chains act as gear teeth in a “wrench in gears” trapping mechanism (right).

Overall, the HIF fluorinated ring dwelt in the deepest part of the vestibule, while the 2-aminoimidazole ring (R5) engaged in hydrogen bonding with the network of charged residues in proximity of D174. The distance between R5 and D174 showed some fluctuations during the simulation (Fig. 6B). The transient changes in distance ( $\sim 2 \text{ \AA}$ ) suggest that multiple interactions with the electrostatic network of the vestibule contribute to the stability of HIF binding. Fig.

6C shows the ligand surrounded by a cloud representing the poses assumed during the last part of the trajectory of Fig. 6A. The results of the simulation confirm that the proposed location of binding site 2 is compatible with the structural model of the closed VSD based on the 3WKV crystal structure. In 3WKV, the Hv1 region comprising the inner ends of S2 and S3 is replaced with the corresponding part of CiVSP<sup>12</sup>. The difference in sequence between Hv1 and CiVSP in that region is not expected to change substantially the electrostatic network within the VSD since all the charged residues are either identical or with similar charge (E153, K157, E171, and D174 in Hv1 correspond to D164, R168, E183, and D186 in CiVSP, respectively).

#### 5.4 Discussion

The complex kinetics of HIF-mediated Hv1 inhibition is well explained by model S and model E with a trapped state slowly accessible from the closed conformation. We have previously found evidence of an intracellular gate in the Hv1 VSD that regulates 2GBI accessibility to its binding site<sup>21</sup>. 2GBI binding can only occur when the gate is open, and the gate cannot close until the inhibitor has left the binding site. HIF accessibility to site 1 is assumed to be similarly regulated. Both kinetic models imply that HIF cannot remain bound to site 1 when the gate closes (Fig. 2A-B and Fig. S8A-B). However, the two models differ in the way this is accomplished. In model S, ligand rearrangement and gate closure occur simultaneously. As result, the ligand leaves site 1 and migrates to site 2 as soon as the gate closes. In model E, the ligand is free to engage either site 1 or 2 in the open conformation but the gate can close only when the ligand is in site 2.

HIF binds slowly to the closed state in both models to account for the slow component of channel inhibition. Unbinding occurs slowly as well, to account for the slow recovery from inhibition. The faster unbinding from the open state (either from B, or from B1 and I2)

provides an explanation for the acceleration of the recovery from inhibition observed at high RDT<sub>off</sub>. The tight fit of the HIF molecule within the narrow intracellular vestibule (Fig. 6C) may be the reason for the relatively high energy barriers that the ligand needs to cross to get in and out of site 2 when the gate is closed.

The T  $\rightarrow$  B transition in model S, and the T2  $\rightarrow$  I2 transition in model E are significantly slower than the corresponding gating transition in the absence of the inhibitor (C  $\rightarrow$  O), suggesting that the gating process is hindered when the ligand interacts with the VSD. The idea that an arginine mimic bound to the Hv1 VSD can affect S4 movement is in agreement with recent measurements of gating currents from the VSD of Hv1 from *C. intestinalis*<sup>34</sup>. To enable the measurements, proton conduction was inhibited by placing an arginine at position N264 (corresponding to N214 in human Hv1). The presence of that arginine was proposed to also hinder the movement of S4, causing a discrepancy between the gating charge measured during activation and deactivation<sup>34</sup>.

While model S was able to replicate most aspects of HIF-mediated inhibition examined here, the fact that site 1 and site 2 are rendered mutually exclusive by the opening transition represents a limitation for applications involving HIF analogs like HIFEN. The Hill coefficient of the concentration dependence of inhibition for this compound is significantly higher than 1 ( $h = 1.50 \pm 0.11$ , Zhao et al., 2021) suggesting the involvement of at least two cooperating binding sites. The finding that the monomeric and dimeric versions of the channel display similar Hill coefficients<sup>23</sup> suggests that the cooperative binding sites for HIFEN are on the same subunit. In model E, site 1 and site 2 are not mutually exclusive in the open state. As a result, this model could be further developed to allow the two sites to be occupied simultaneously, thus providing a framework for intrasubunit cooperativity of ligand binding. Model S and model E were used here to simulate the reduction in Hv1 G<sub>max</sub> induced by HIF. But the ligand also affects the channel G-V curve, shifting it to more positive potentials (Fig.

S5A). Our kinetic models cannot simulate the G-V shift with the current parameters because the  $T \rightleftharpoons B$  and  $T2 \rightleftharpoons I2$  transitions were set to have the same voltage dependence of the  $C \rightleftharpoons O$  transition (see Methods). Future simulations of HIF-mediated inhibition as a function of membrane potential will require  $k_{TB}$  or  $k_{T2I2}$  to have a voltage dependence distinct from  $k_{CO}$ , and  $k_{BT}$  or  $k_{I2T2}$  to have a voltage dependence distinct from  $k_{OC}$ . Another aspect of the mechanism of inhibition that warrants further investigation concerns the nature of the I2 state. If the ligand can stay bound to site 2 in the open VSD, as implied by model E, what is the consequence on proton conduction? We assumed here that I2 is a non-conducting state like B1. However, site 2 is located in a wider portion of the intracellular vestibule compared to site 1. Therefore, in the open channel, the ligand may not be as efficient at blocking the proton current when bound to site 2 as it is when bound to site 1. This possibility could be further explored if ligands interacting with only site 2 are identified.

The high energy barriers ( $\approx 20$  kcal/mol at RT) that HIF is required to cross in and out of site 2 suggest some sort of trapping process. The atomistic simulations of HIF docked to the closed Hv1 VSD reveal important molecular details about this process. The simplest way HIF could be trapped in the intracellular vestibule is by a "trap door" mechanism. A cytoplasmic gate could close behind the ligand, thus obstructing the way out of site 2 (Fig. 6D). However, the entrance of the vestibule in the structural model of the Hv1 VSD is too wide to hinder HIF exit from the vestibule, making the "trap door" mechanism difficult to justify. On the other hand, during the simulation HIF remains confined inside a pocket formed by side chains from various VSD helices which act as teeth of interlocking gears. This finding suggests that the ligand could become trapped via a "wrench in gears" mechanism (Fig. 6D). If the degree of interlocking were to decrease in the open state, the energy barriers holding HIF in site 2 would be lowered, leaving the ligand free to move to site 1.

In recent years, there has been a renewed interest in the development of peptide ligands and small-molecules targeting the VSDs of voltage-gated sodium, potassium, and calcium channels for applications ranging from pain relief to antiarrhythmics<sup>24,42-46</sup>. The binding sites for the majority of these compounds are located on the extracellular portion of the VSD<sup>47-49</sup>.

However, the recent discovery of a cell-penetrating peptide toxin capable of interacting with the intracellular domain of a TRP channel<sup>50</sup> as well as the development of novel nanobodies<sup>51</sup>, open the possibility of targeting the intracellular side of VSDs not only with small molecules but also with larger peptide ligands. Here, we find that HIF interacts with the Hv1 VSD from the intracellular side. The deep region containing site 1 is accessible to ligands like 2GBI and HIF only in the proton-conducting state (up state). It is unlikely that the corresponding region of non-conducting VSDs could be accessible to similar ligands. The packing between helices at the center of those VSDs is expected to be too tight. On the other hand, the shallower site 2 is slowly accessible in non-conducting state(s) (S4 down), raising the prospect that other VSDs could harbor similar intracellular binding sites with slow accessibility. The presence of charged residues that are highly conserved among different channels at site 2, supports this idea (Fig. S9). The tight fitting of site 2 around the HIF molecule shows how the VSD intracellular vestibule can provide specificity of binding to VSD-targeting ligands, a desirable feature for further drug development.

Previous studies found evidence for an allosteric coupling between the Hv1 extracellular binding sites for Zn<sup>2+</sup> and the peptide toxin AGAP/W38F and the electrostatic network located in the channel intracellular vestibule<sup>52,53</sup>. The proposed mechanism of Hv1 inhibition by these two ligands involves rearrangements of the electrostatic network as a result of ligand binding to the opposite side of the VSD. Here we show that HIF compounds inhibit Hv1 by a direct interaction with the electrostatic network. Taken together, these findings

highlight the importance of the VSD intracellular vestibule as a hotpot for both direct and indirect pharmacological targeting.

## 5.5 Supplementary Information

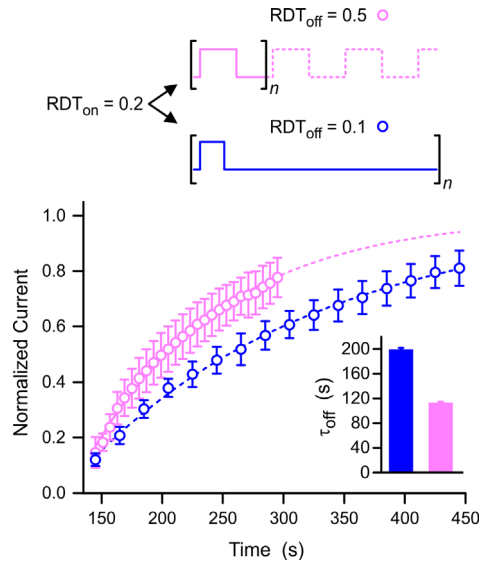


**Figure S5.1. Effect of depolarization frequency on recovery from HIF-mediated inhibition.** Time courses of recovery from inhibition of Hv1 WT measured with the two indicated voltage protocols ( $V_d = +120$  mV,  $V_r = -40$  mV). In both cases,  $100 \mu\text{M}$  HIF was perfused into the bath until current inhibition reached  $\sim 90\%$ . The current was monitored using a protocol with  $RDT_{on} = 0.2$  ( $t_d = 3$  s,  $t_r = 12$  s). The inhibitor was then washed out and the recovery from inhibition monitored under a protocol with  $RDT_{off} = 0.5$  ( $t_d = t_r = 3$  s), or under a protocol with  $RDT_{off} = 0.1$  ( $t_d = 2$  s,  $t_r = 18$  s). Points are averages from 6 independent measurements; error bars are SEM. Time courses were fitted with a single exponential function. Time constants from fits are shown in bar graph ( $\pm$ SE). The current recovers faster when the relative time spent in the open state is longer ( $RDT_{off} = 0.5$ , pink).

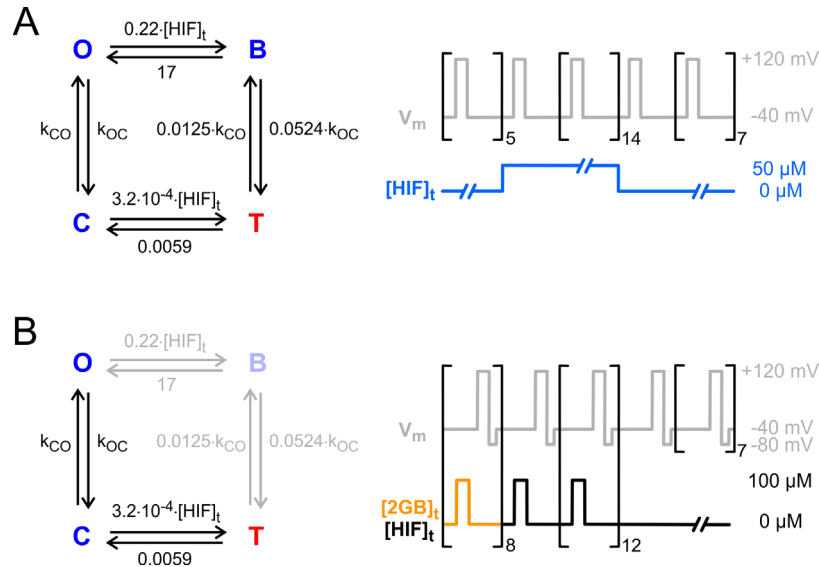


**Figure S5.2. Kinetic modeling of HIF-mediated Hv1 inhibition.** Kinetic constants for transitions  $C \rightarrow T$  and  $O \rightarrow B$  are in  $\mu M^{-1} s^{-1}$ ; for the other transitions, they are in  $s^{-1}$ . **A)** Parameters and protocols used to generate the time-course of inhibition and current traces in Fig. 2C.  $[HIF]_t = 50 \mu M$  for both the  $C \rightarrow T$  and  $O \rightarrow B$  transitions when the inhibitor is continuously perfused in the bath (sweeps 6-20). **B)** Parameters and protocols used to generate the time-course of inhibition in Fig. 2F. 2GBI or HIF are perfused into the bath only when the channel is closed. When the inhibitor is present,  $[HIF]_t = 100 \mu M$  for the  $C \rightarrow T$  transition and  $[HIF]_t = 0 \mu M$  for the  $O \rightarrow B$  transition. 2GBI was present in the first 8 sweeps, HIF was present in sweeps 9-21. Sweep length was 15 s in both (A) and (B) with a depolarization step of 3 s. The duration of the inhibitor application in (B) was 10% longer than the nominal value (3 s) to account for the non-instantaneous changes in inhibitor concentration attainable experimentally.  $k_{CO}$  was  $0.884 s^{-1}$  at +120 mV, and  $2.27 \cdot 10^{-4} s^{-1}$  at -40 mV.  $k_{OC}$  was  $0.0465 s^{-1}$  at +120 mV, and  $2.27 s^{-1}$  at -40 mV. To simulate accelerated channel closure at -80 mV in protocol (B), the value of  $k_{OC}$  was set to  $10.2 s^{-1}$  during the hyperpolarization step while  $k_{CO}$  was kept at  $2.27 \cdot 10^{-4} s^{-1}$ . The transitions connecting the T and B states had the same voltage dependence as the transitions connecting the C and O states, but they were slowed down by the indicated factors. Current was calculated as  $I = G_{max} \cdot O \cdot V_m$ , with  $G_{max} = 8.33 pA/mV$ .

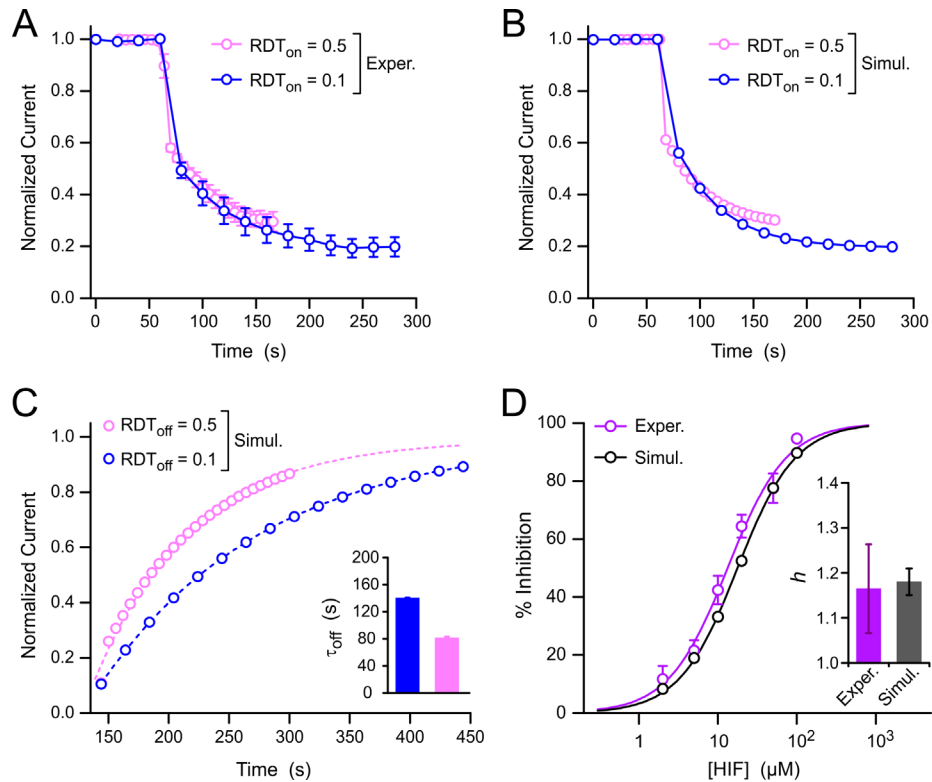


**Figure S5.3. Comparisons between experimental and simulated data. A-B)** Experimental and simulated time courses of HIF-mediated inhibition of Hv1 WT as a function of  $RDT_{on}$ . Experimental data are the same as in Fig. 1B. The recovery from inhibition was omitted for clarity.  $\tau_{slow}$  values as a function of  $RDT_{on}$  are reported in Fig. 1C;  $\tau_{slow, RDT=0.1}/\tau_{slow, RDT=0.5} = 1.15 \pm 0.20$ . Time courses of inhibition reported in (B) were generated with the 4-state model of Fig. S2A. The simulated data were then fitted with a double exponential function providing  $\tau_{slow, RDT=0.1}/\tau_{slow, RDT=0.5} = 1.03 \pm 0.05$ . Hence,  $\tau_{slow}$  is only weakly affected by differences in  $RDT_{on}$  in both experiments and simulations. **C)** Simulated time courses of recovery from inhibition of Hv1 WT as a function of  $RDT_{off}$ . Conditions and protocols were as in Fig. S1. Time courses were fitted with a single exponential function. Time constants from fits are shown in bar graph ( $\pm SE$ ). Simulated currents recover faster when the relative depolarization time increases, as observed experimentally (Fig. S1). **D)** Concentration dependence of HIF-mediated Hv1 inhibition simulated with the 4-state model of Fig. S2A (black), compared to the experimental concentration dependence from Zhao et al. 2021 (purple). Each experimental data point represents the mean of 3 to 5 independent measurements  $\pm SD$ . Simulated and experimental data points were fitted with the Hill equation. The resulting Hill coefficients ( $h$ ) are compared in the bar graph. Error bars are SE. Simulated  $IC_{50}$  was  $17.7 \pm 0.4 \mu M$ . Experimental  $IC_{50}$  was  $13.3 \pm 1.0 \mu M$  (Zhao et al., 2021).

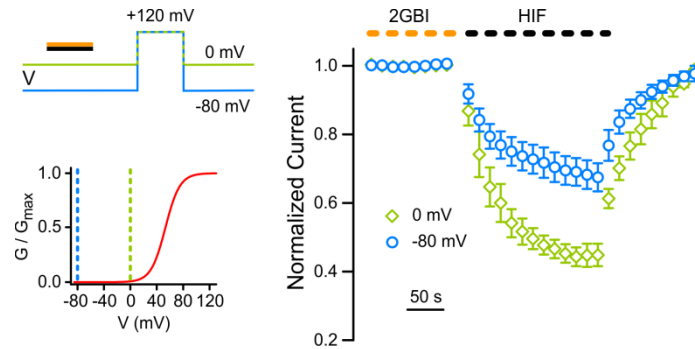


**Figure S5.4. Effects of voltage on HIF apparent binding to closed state.** Time courses of Hv1 inhibition by 2GBI and HIF and recovery from inhibition. 100  $\mu$ M 2GBI (yellow) or HIF (black) were transiently perfused when holding the membrane at 0 mV (green) or -80 mV (blue). The channel is expected to be in a deeper resting state at -80 mV than at 0 mV; see G-V curve<sup>14</sup> in inset. Current was measured with a depolarization step at +120 mV delivered after the inhibitor was removed from the solution. 2GBI failed to produce any inhibition, consistent with its inability to bind the channel in the closed state. HIF produced inhibition at both voltages, and the extent of inhibition was larger at 0 mV compared to -80 mV. Points are averages from at least 5 independent measurements, error bars are SEM.

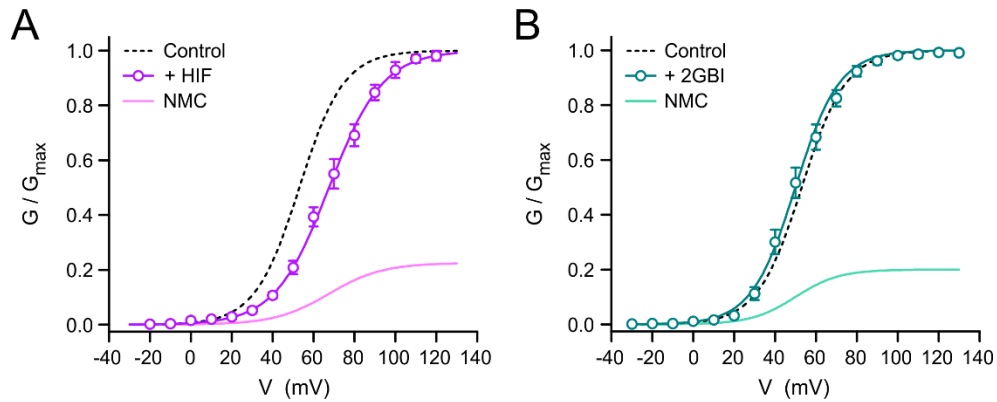


**Figure S5.5. Effect of HIF on the conductance vs voltage relationship of Hv1 WT.** **A)** G-V curves for Hv1 WT in the presence of 50  $\mu$ M HIF (circles) and in the absence of the inhibitor (dashed line). Points are averages from at least 5 independent measurements  $\pm$  SEM ( $V_{1/2} = 68 \pm 2$  mV, slope =  $13 \pm 1$  with HIF;  $V_{1/2} = 53 \pm 3$  mV, slope =  $11 \pm 1$  without HIF). NMC is the G-V in the presence of the inhibitor normalized to the control maximal conductance (no inhibitor). **B)** G-V curves for Hv1 WT in the presence of 200  $\mu$ M 2GBI (circles) and in the absence of the inhibitor (dashed line). NMC is the G-V in the presence of the inhibitor normalized to the control maximal conductance (no inhibitor). Data for 2GBI are from Hong et al. 2013 and reported here for comparison. All G-Vs were measured at  $pH_i = pH_o = 6.0$ . The concentrations of HIF and 2GBI were chosen based on their ability to reduce  $G_{max}$  to a similar extent.

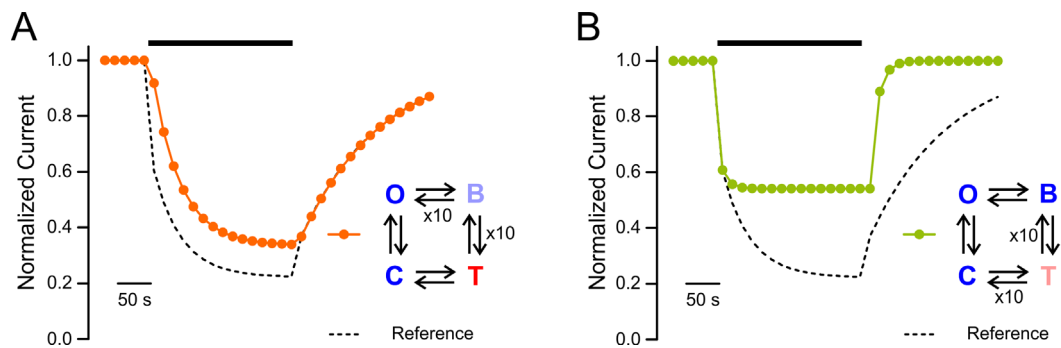


**Figure S5.6. Simulations of the time-course of HIF-mediated inhibition of Hv1 channels with destabilized B or T states.** Simulations were performed with the model S shown in Fig. 2. Rate constants were as in Fig. S2A (Reference), with the exception of the indicated transitions. **A)** Destabilization of the B state was simulated by a 10-fold acceleration of HIF unbinding from the B state ( $10 \times k_{OB}$ ) and a 10-fold acceleration of the  $B \rightarrow T$  transition ( $10 \times k_{BT}$ ). The result is the disappearance of the fast component of the time-course of inhibition ( $\tau_{fast}$  cannot be precisely derived from the double exponential fit). **B)** Destabilization of the T state was simulated by a 10-fold acceleration of HIF unbinding from the T state ( $10 \times k_{CT}$ ) and a 10-fold acceleration of the  $T \rightarrow B$  transition ( $10 \times k_{TB}$ ). The result is the disappearance of the slow component of the time-course of inhibition ( $\tau_{slow}$  cannot be precisely derived from the double exponential fit).

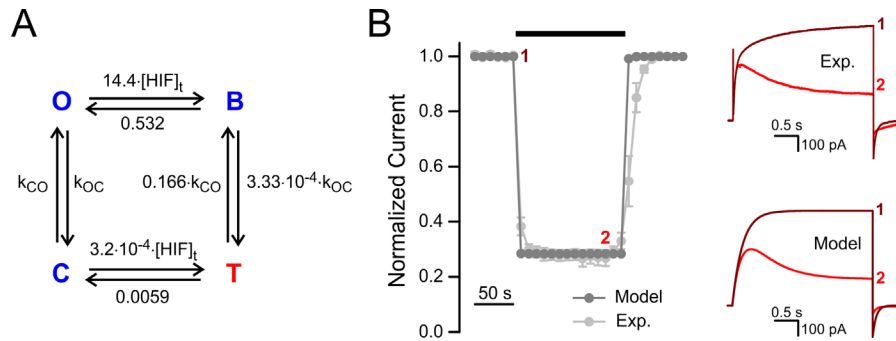


**Figure S5.7. Simulations of the time-course of HIF-mediated inhibition of Hv1 F150A.** **A)** Parameters used to simulate inhibition of Hv1 F150A by 0.1  $\mu\text{M}$  HIF. Kinetic constants for the  $\text{C} \rightarrow \text{T}$  and  $\text{O} \rightarrow \text{B}$  transitions are in  $\mu\text{M}^{-1}\text{s}^{-1}$ . They are in  $\text{s}^{-1}$  for the other transitions. F150A causes faster channel gating compared to Hv1 WT (Hong et al. 2013). Accordingly,  $k_{\text{CO}}$  was  $4.42 \text{ s}^{-1}$ , at +120 mV and  $2.27 \times 10^{-4} \text{ s}^{-1}$  at -40 mV;  $k_{\text{OC}}$  was  $0.233 \text{ s}^{-1}$ , at +120 mV and  $13.6 \text{ s}^{-1}$  at -40 mV. **B)** Comparison between simulated (dark gray) and experimental time-course of inhibition (light gray). Current traces on the right correspond to the indicated points, before (1) or after (2) perfusion of HIF. In the presence of the inhibitor, the current first increases upon depolarization and then decreases. The biphasic shape is expected for open channel block. The reason why this behavior is observed in the mutant channel but not in the WT is discussed in Hong et al. 2013. Current was calculated as  $I = G_{\text{max}} \cdot O \cdot V_m$ , with  $G_{\text{max}} = 5.46 \text{ pA/mV}$ .

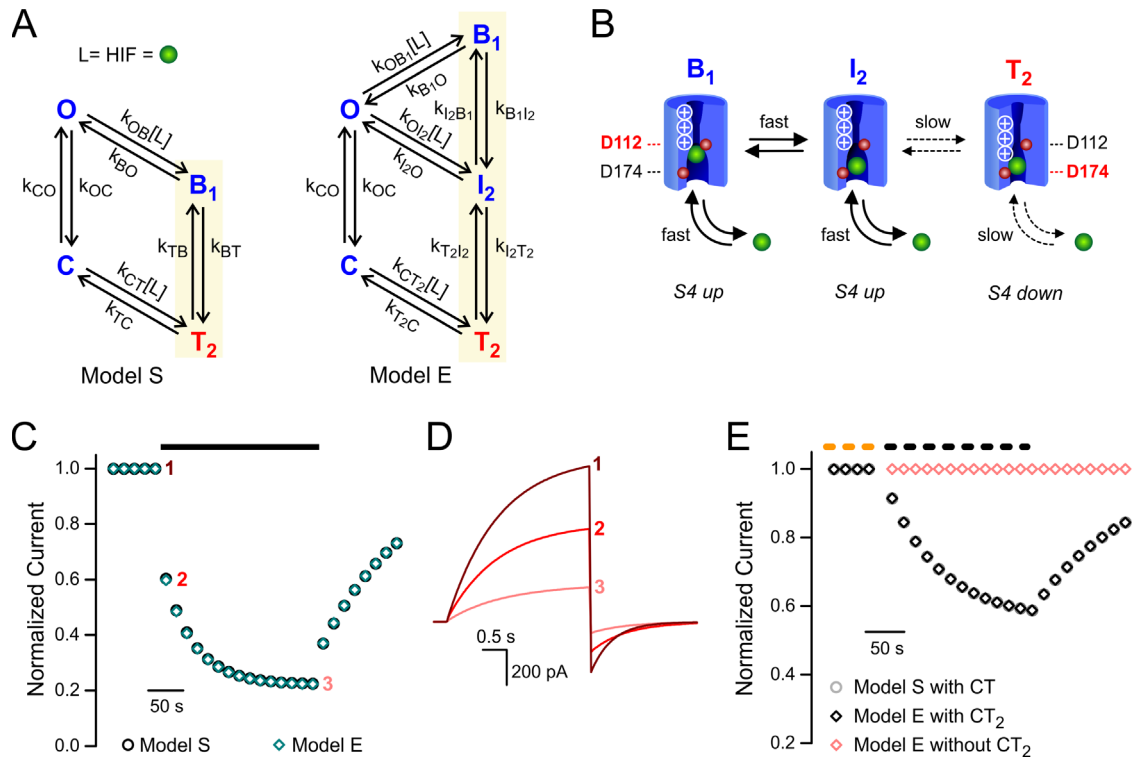


**Figure S5.8. Extended model E compared to model S.** **A)** Kinetic schemes of model S and model E highlighting the expansion of the  $B_1 \leftrightarrow T_2$  transition (same as  $B \leftrightarrow T$  in Fig. 2 and Fig. S2) to the  $B_1 \leftrightarrow I_2 \leftrightarrow T_2$  transitions. Rate constants  $k_{CO}$  and  $k_{OC}$  are the same in the two models (as in Fig. S2A). have the same values as  $k_{TC}$  and  $k_{CT}$  of model S, respectively. The other parameters for model E are:  $k_{OB1} = 0.19 \mu\text{M}^{-1}\text{s}^{-1}$ ,  $k_{B1O} = 19 \text{ s}^{-1}$ ,  $k_{OI2} = 0.10 \mu\text{M}^{-1}\text{s}^{-1}$ ,  $k_{I2O} = 30.9 \text{ s}^{-1}$ ,  $k_{B1I2} = 10 \text{ s}^{-1}$ ,  $k_{I2B1} = 30.9 \text{ s}^{-1}$ ,  $k_{CT2} = 3.2 \cdot 10^{-4} \mu\text{M}^{-1}\text{s}^{-1}$ ,  $k_{T2C} = 0.0059 \text{ s}^{-1}$ ,  $k_{I2T2} = 0.21 \cdot k_{OC}$ , and  $k_{T2I2} = 0.0125 \cdot k_{CO}$ . **B)** Schematics of  $B_1$ ,  $I_2$ , and  $T_2$ . The first two states correspond to an open VSD conformation, the third to a closed VSD conformation. When the VSD is open (S4 up), HIF is assumed to have access to both site 1 and 2 and to be able to quickly move from one site to the other ( $B_1 \leftrightarrow I_2$  transition). When the VSD is closed (S4 down), HIF is assumed to have access to site 2 only. VSD activation is slowed down by the interaction with HIF in both models. **C)** Time courses of HIF-mediated Hv1 inhibition and recovery simulated with model E and model S. Black bar indicates the presence of  $50 \mu\text{M}$  HIF in the bath compartment. **D)** Current traces generated by model E ( $G_{\text{max}}$  as in Fig. S2) at the time points indicated in (C). **E)** Time courses of channel inhibition under pulsed delivery of HIF (protocol in Fig. 5.2E) simulated by model E and model S. Yellow and black dashed lines indicate recurring transient exposure to  $100 \mu\text{M}$  2GBI or HIF, respectively. Black and light-red diamonds indicate normalized current predicted in the presence and absence of the  $C \leftrightarrow T_2$  transition, respectively.

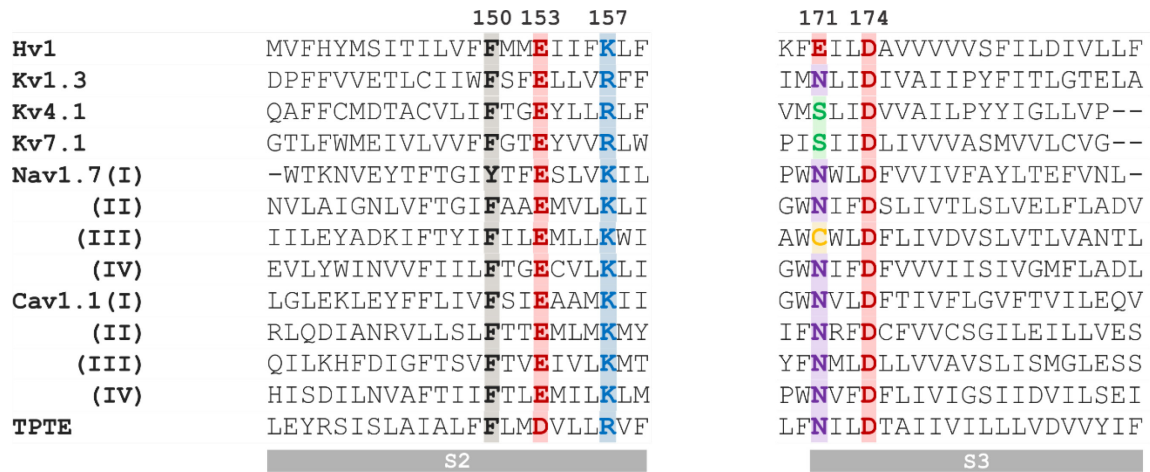


**Figure S5.9. Sequence alignment of S2 and S3 segments of representative human VSD-containing proteins.** Included in the comparison are three different potassium channels (Kv1.3/KCNA3, Kv4.1/KCND1, Kv7.1/KCNQ1), the four domains (I-IV) of the sodium channel Nav1.7/SCN9A and calcium channel Cav1.1/CACNA1S, and the VSD of TPTE, a human homologue of the CiVSP phosphatase. Highlighted are positions corresponding to F150 and residues contributing to the intracellular electrostatic network in the VSD intracellular vestibule. VSD ligands that bind in proximity of the conserved D174 could alter its interactions with other elements of the network including the positively charged residues in S4.

## 5.6 References

1. DeCoursey, T.E. Voltage-gated proton channels: molecular biology, physiology, and pathophysiology of the H(V) family. *Physiol Rev* **93**, 599-652 (2013).
2. Lishko, P.V. Contraception: Search for an Ideal Unisex Mechanism by Targeting Ion Channels. *Trends Biochem Sci* **41**, 816-818 (2016).
3. Ramsey, I.S., Moran, M.M., Chong, J.A. & Clapham, D.E. A voltage-gated proton-selective channel lacking the pore domain. *Nature* **440**, 1213-6 (2006).
4. Sasaki, M., Takagi, M. & Okamura, Y. A voltage sensor-domain protein is a voltage-gated proton channel. *Science* **312**, 589-92 (2006).
5. Koch, H.P. et al. Multimeric nature of voltage-gated proton channels. *Proc Natl Acad Sci U S A* **105**, 9111-6 (2008).
6. Lee, S.Y., Letts, J.A. & Mackinnon, R. Dimeric subunit stoichiometry of the human voltage-dependent proton channel Hv1. *Proc Natl Acad Sci U S A* **105**, 7692-5 (2008).
7. Tombola, F., Ulbrich, M.H. & Isacoff, E.Y. The voltage-gated proton channel Hv1 has two pores, each controlled by one voltage sensor. *Neuron* **58**, 546-56 (2008).
8. Gonzalez, C., Koch, H.P., Drum, B.M. & Larsson, H.P. Strong cooperativity between subunits in voltage-gated proton channels. *Nat Struct Mol Biol* **17**, 51-6 (2010).
9. Musset, B. et al. Zinc inhibition of monomeric and dimeric proton channels suggests cooperative gating. *J Physiol* **588**, 1435-49 (2010).
10. Tombola, F., Ulbrich, M.H., Kohout, S.C. & Isacoff, E.Y. The opening of the two pores of the Hv1 voltage-gated proton channel is tuned by cooperativity. *Nat Struct Mol Biol* **17**, 44-50 (2010).
11. Bayrhuber, M. et al. Nuclear Magnetic Resonance Solution Structure and Functional Behavior of the Human Proton Channel. *Biochemistry* **58**, 4017-4027 (2019).
12. Takeshita, K. et al. X-ray crystal structure of voltage-gated proton channel. *Nat Struct Mol Biol* **21**, 352-7 (2014).
13. Pupo, A. & Gonzalez Leon, C. In pursuit of an inhibitory drug for the proton channel. *Proc Natl Acad Sci U S A* **111**, 9673-4 (2014).
14. Seredenina, T., Demaurex, N. & Krause, K.H. Voltage-Gated Proton Channels as Novel Drug Targets: From NADPH Oxidase Regulation to Sperm Biology. *Antioxid Redox Signal* **23**, 490-513 (2015).
15. Cherny, V.V. & DeCoursey, T.E. pH-dependent inhibition of voltage-gated H(+) currents in rat alveolar epithelial cells by Zn(2+) and other divalent cations. *J Gen Physiol* **114**, 819-38 (1999).
16. DeCoursey, T.E. & Cherny, V.V. Potential, pH, and arachidonate gate hydrogen ion currents in human neutrophils. *Biophys J* **65**, 1590-8 (1993).
17. Hille, B. *Ion Channels of Excitable Membranes* (Sinauer Associates Inc., Sunderland, 2001).
18. Chamberlin, A. et al. Hydrophobic plug functions as a gate in voltage-gated proton channels. *Proc Natl Acad Sci U S A* **111**, E273-82 (2014).
19. Geragotelis, A.D. et al. Voltage-dependent structural models of the human Hv1 proton channel from long-timescale molecular dynamics simulations. *Proc Natl Acad Sci U S A* **117**, 13490-13498 (2020).
20. Gianti, E., Delemotte, L., Klein, M.L. & Carnevale, V. On the role of water density fluctuations in the inhibition of a proton channel. *Proc Natl Acad Sci U S A* **113**, E8359-E8368 (2016).
21. Hong, L., Pathak, M.M., Kim, I.H., Ta, D. & Tombola, F. Voltage-sensing domain of

- voltage-gated proton channel Hv1 shares mechanism of block with pore domains. *Neuron* **77**, 274-87 (2013).
22. Hong, L., Kim, I.H. & Tombola, F. Molecular determinants of Hv1 proton channel inhibition by guanidine derivatives. *Proc Natl Acad Sci U S A* **111**, 9971-6 (2014).
  23. Zhao, C. et al. Development of HIFs: arginine-mimic inhibitors of Hv1 with improved VSD-ligand interactions. *Co-submitted to J. Gen. Physiol.* (2020a).
  24. Ahuja, S. et al. Structural basis of Nav1.7 inhibition by an isoform-selective small-molecule antagonist. *Science* **350**, aac5464 (2015).
  25. Macey, R.O., G.; Zahnley, T. Berkeley Madonna User's Guide available from: <http://www.berkeleymadonna.com>. (2009).
  26. Trott, O. & Olson, A.J. AutoDock Vina: improving the speed and accuracy of docking with a new scoring function, efficient optimization, and multithreading. *J Comput Chem* **31**, 455-61 (2010).
  27. Phillips, J.C. et al. Scalable molecular dynamics with NAMD. *J Comput Chem* **26**, 1781-802 (2005).
  28. Klauda, J.B. et al. Update of the CHARMM all-atom additive force field for lipids: validation on six lipid types. *Journal of Physical Chemistry B* **114**, 7830-7843 (2010).
  29. MacKerell, A.D. et al. All-atom empirical potential for molecular modeling and dynamics studies of proteins. *Journal of Physical Chemistry B* **102**, 3586-3616 (1998).
  30. Jorgensen, W.L., Chandrasekhar, J., Madura, J.D., Impey, R.W. & Klein, M.L. Comparison of Simple Potential Functions for Simulating Liquid Water. *Journal of Chemical Physics* **79**, 926-935 (1983).
  31. Essmann, U. et al. A Smooth Particle Mesh Ewald Method. *Journal of Chemical Physics* **103**, 8577-8593 (1995).
  32. Feller, S.E., Zhang, Y.H., Pastor, R.W. & Brooks, B.R. Constant-Pressure Molecular-Dynamics Simulation - the Langevin Piston Method. *Journal of Chemical Physics* **103**, 4613-4621 (1995).
  33. Martyna, G.J., Tobias, D.J. & Klein, M.L. Constant-Pressure Molecular-Dynamics Algorithms. *Journal of Chemical Physics* **101**, 4177-4189 (1994).
  34. Carmona, E.M. et al. Gating charge displacement in a monomeric voltage-gated proton (Hv1) channel. *Proc Natl Acad Sci U S A* **115**, 9240-9245 (2018).
  35. DeCoursey, T.E. & Cherny, V.V. Voltage-activated hydrogen ion currents. *J Membr Biol* **141**, 203-23 (1994).
  36. Villalba-Galea, C.A. Hv1 proton channel opening is preceded by a voltage-independent transition. *Biophys J* **107**, 1564-72 (2014).
  37. Hong, L., Singh, V., Wulff, H. & Tombola, F. Interrogation of the intersubunit interface of the open Hv1 proton channel with a probe of allosteric coupling. *Sci Rep* **5**, 14077 (2015).
  38. Berger, T.K. & Isacoff, E.Y. The pore of the voltage-gated proton channel. *Neuron* **72**, 991-1000 (2011).
  39. Musset, B. et al. Aspartate 112 is the selectivity filter of the human voltage-gated proton channel. *Nature* **480**, 273-7 (2011).
  40. Ramsey, I.S. et al. An aqueous H<sup>+</sup> permeation pathway in the voltage-gated proton channel Hv1. *Nat Struct Mol Biol* **17**, 869-75 (2010).
  41. Randolph, A.L., Mokrab, Y., Bennett, A.L., Sansom, M.S. & Ramsey, I.S. Proton currents constrain structural models of voltage sensor activation. *Elife* **5**(2016).
  42. Liin, S.I., Larsson, J.E., Barro-Soria, R., Bentzen, B.H. & Larsson, H.P. Fatty acid analogue N-arachidonoyl taurine restores function of IKs channels with diverse long QT mutations. *Elife* **5**(2016).
  43. Liin, S.I. et al. Polyunsaturated fatty acid analogs act antiarrhythmically on the

- cardiac IKs channel. *Proc Natl Acad Sci U S A* **112**, 5714-9 (2015).
44. Ottosson, N.E. et al. Resin-acid derivatives as potent electrostatic openers of voltage-gated K channels and suppressors of neuronal excitability. *Sci Rep* **5**, 13278 (2015).
  45. Shen, H., Liu, D., Wu, K., Lei, J. & Yan, N. Structures of human Nav1.7 channel in complex with auxiliary subunits and animal toxins. *Science* **363**, 1303-1308 (2019).
  46. Xu, H. et al. Structural Basis of Nav1.7 Inhibition by a Gating-Modifier Spider Toxin. *Cell* **176**, 702-715 e14 (2019).
  47. Ahern, C.A., Payandeh, J., Bosmans, F. & Chanda, B. The hitchhiker's guide to the voltage-gated sodium channel galaxy. *J Gen Physiol* **147**, 1-24 (2016).
  48. Bosmans, F., Martin-Eauclaire, M.F. & Swartz, K.J. Deconstructing voltage sensor function and pharmacology in sodium channels. *Nature* **456**, 202-8 (2008).
  49. Wulff, H., Christophersen, P., Colussi, P., Chandy, K.G. & Yarov-Yarovoy, V. Antibodies and venom peptides: new modalities for ion channels. *Nat Rev Drug Discov* **18**, 339-357 (2019).
  50. Lin King, J.V. et al. A Cell-Penetrating Scorpion Toxin Enables Mode-Specific Modulation of TRPA1 and Pain. *Cell* **178**, 1362-1374 e16 (2019).
  51. Ingram, J.R., Schmidt, F.I. & Ploegh, H.L. Exploiting Nanobodies' Singular Traits. *Annu Rev Immunol* **36**, 695-715 (2018).
  52. De La Rosa, V., Bennett, A.L. & Ramsey, I.S. Coupling between an electrostatic network and the Zn(2+) binding site modulates Hv1 activation. *J Gen Physiol* **150**, 863-881 (2018).
  53. Tang, D. et al. Scorpion toxin inhibits the voltage-gated proton channel using a Zn(2+) -like long-range conformational coupling mechanism. *Br J Pharmacol* (2020).

## Chapter 6: Overview and Future Directions

### 6.1 Overview

The voltage-gated proton channel Hv1 is a member of the VGIC family. It is a dimer consisting of two VSDs, each carrying its own proton conduction pathway<sup>1-3</sup>, and lacking the PD found in other VGICs. Hv1 plays significant roles in the human immune system (e.g., respiratory burst in phagocytes)<sup>4</sup>, and reproductive system<sup>5</sup> (e.g., sperm motility and capacitation). Hv1 overexpression or excessive activity are associated with a wide variety of cancers<sup>6-8</sup> (e.g., breast cancer, colorectal cancer, B cell lymphoma). In the brain, Hv1 is highly expressed in the microglia<sup>9</sup>, and its activity has been implicated in several CNS diseases<sup>10-12</sup> (e.g., ischemic stroke, traumatic brain injury, spinal cord injury), and particularly in the recovery post-injury. Understanding how Hv1 works at the molecular level, as well as how its activity can be pharmacologically modulated could lead to new or improved treatments for a variety of pathological conditions. My thesis work focuses on two directions: 1) investigation of the biophysical properties of evolutionarily distant Hv1 homologs to dissect structure-function relationships; 2) Rational design and characterization of next-generation small molecule inhibitors targeting Hv1.

Chapter 2 of the thesis describes the identification of Hv1 channels in *fungi*: the first description of proton channels from this kingdom. I found that fungal Hv1s have distinctive biophysical properties (e.g. voltage range of activation, pH sensitivity, pharmacology, etc.)<sup>13</sup>. Hv1 homologs are present in fungi species from all five major phyla, and comparative sequence analysis and chimeragenesis between different fungal Hv1s led to the discovery that intra- and extracellular peripheral regions of these membrane proteins play critical roles in modulating channel activation.

In chapter 3, I report the first characterization of Hv1 homologs from plant species. Potential

Hv1 channels were previously identified in plants through BLAST searches by other groups (e.g., a homolog from the spreading earth moss *P. patens*<sup>14</sup>). However, it was unclear whether and how these predicted proteins could function as proton channels. Our collaborator Dr. De Angeli initially found an Hv1 homolog in *Arabidopsis thaliana*, a widely used plant model organism, and asked us to verify that the putative protein is indeed a proton channel. When expressed in *Xenopus* oocytes, AtHv1 failed to produce measurable proton currents. Assuming that the protein may not be targeted to the plasma membrane, Dr. De Angeli investigated its subcellular localization in *A. thaliana*. He found that GFP-tagged AtHv1 localizes to the plasma membrane of root hair cells and elongated root cells. *Xenopus* oocytes are the preferred heterologous expression system for plant ion channels and transporters, but mistargeting sometimes occurs even in this system. We asked whether other plant Hv1 homologs had a similar behavior. Through BLAST search, I identified several other Hv1 homologs in angiosperm, gymnosperm, and more primitive vascular plants. When representative channels from gymnosperm (PtHv1) and moss (SmHv1) were expressed in *Xenopus* oocytes, they produced robust proton currents with characteristics similar to those of other Hv1 channels. On the other hand, the proton channel from *Theobroma cacao*, an angiosperm like *A. thaliana*, failed to produce any current. Further examination led to the discovery that the angiosperm Hv1 channels (AtHv1 and TcHv1) are properly targeted to the plasma membrane in the heterologous system but they require membrane stretch for activation. I defined these channels as “mechanically primed” rather than “mechanically gated” because their opening still requires membrane depolarization, but the electrical stimulus is effective only if the channels have been pre-exposed to the mechanical stimulus. Mechanical priming might be a consequence of environmental adaptation, such as responding to turgor pressure or other abiotic stresses for growth and development.

Chapter 4 and 5 discuss our progress in developing the next-generation Hv1 inhibitors named HIFs, based on our understanding of how first-generation inhibitors, such as 2GBI, work at the

molecular level<sup>15,16</sup>. We studied the mechanism of Hv1 inhibition by guanidine derivatives combining electrophysiology, classic mutagenesis, and site-specific incorporation of unnatural amino acids (fluorinated phenylalanines)<sup>17,18</sup>. From the study, we concluded that there is an intrinsic vulnerability in the structure of the 2GBI scaffold that limits further improvements<sup>19</sup>. The scaffold of HIF compounds was designed to eliminate this vulnerability. In the new inhibitors, the aminoimidazole ring and the aromatic group are separated by extended linkers. My data show that, in the modified scaffold, substituents can be introduced in the aromatic group without interfering with the binding of the aminoimidazole ring<sup>19</sup>. Some of the HIF compounds inhibited Hv1 more potently than 2GBI and other guanidine derivatives, suggesting that the new scaffold could be further optimized to produce better Hv1 inhibitors.

In contrast to other Hv1 ligands that produce fast channel inhibition and recovery from inhibition, HIF inhibits Hv1 with both a fast and a slow component, and the recovery from inhibition occurs over an extended period of time. In chapter 5, I investigate the channel-ligand interactions that account for the complex kinetics of binding and unbinding. I found evidence of two HIF binding sites within the channel VSD: one site located in the deepest region of the intracellular vestibule (Fig 5.6, site 1), where 2GBI also binds, and an additional site (Fig 5.6, site 2) located in a shallower region of the vestibule. I propose that the binding and unbinding from site 2 is responsible for the slow modality of inhibition and recovery from inhibition<sup>20</sup>. The proposed mechanism of inhibition is supported by kinetic modeling, molecular docking, and atomistic MD simulations.

## 6.2 Future directions

### *Unsolved mysteries about Hv1 channels from fungi and plants*

We made interesting discoveries about the role of peripheral regions of fungal Hv1 in

modulating the voltage sensitivity and kinetics of activation<sup>13</sup>, but the physiological roles of these channels remain largely unknown. The great diversity between fungi species is well documented, and so is the fungi ability to adapt to environments with widely fluctuating pHs. This adaptability is critical for their growth and development. In this context, one could ask why some fungal Hv1 channels mediate both proton influx and efflux while other seems to be obligatory proton extruders? Do the channels have different roles in the pH regulation network in different species? What are the consequences of these differences on downstream events? We showed that while being slightly different from each other in terms of Zn<sup>2+</sup> sensitivity, fungal Hv1s are much less sensitive to this inhibitor than their animal homologs. This is interesting from the perspective of fungal pathogenesis and related anti-fungal treatment strategies. In the mammalian system, the level of trace elements like zinc and copper are tightly regulated and used as nutritional immunity against other pathogens<sup>21</sup>. Pathogenic fungi, on the other hand, possess great metal tolerance with robust assimilation and detoxification mechanisms<sup>22</sup>. Fungal infections are difficult to treat due to the limited number of effective drugs and quick development of drug resistance. If proton transport by Hv1 in fungi were to be proven critical for their growth and survival, the channel could be potentially a great molecular target for treating fungal infections. The need for metal tolerance in fungi may require transmembrane receptors such as Hv1 to be insensitive to Zn<sup>2+</sup>, however, other small molecules could be found that preferentially inhibit fungal Hv1s compared to the human counterpart. Understanding the structural differences between fungal Hv1s that make them differentially sensitive to known inhibitors, such as 2GBI and ClGBI, could facilitate the development of new anti-fungal treatments.

One of the most obvious unsolved problems from our plant Hv1 study is that the structural determinants responsible for the mechanically primed gating observed in Hv1s from angiosperm have not been identified. I tackled the problem using the same strategy used in the fungal Hv1s

study. I generated chimeras between AtHv1 (most mechanosensitive) and PsHv1 (least mechanosensitive) by swapping regions characterized by widely divergent sequences. Because the S1-S2 loop has a strong effect on gating in fungal Hv1s, I first tried swapping the S1-S2 loop in the plant channels. Neither PsHv1 with the S1-S2 loop of AtHv1 or the inverse chimera showed any apparent change in mechanosensitivity compared to the corresponding parent proteins. Exchanging the intracellular domains (PsHv1 with N- and C termini of AtHv1 and inverse chimera) also did not result in any difference.

After excluding the intra- and extracellular regions of the two plant channels as determinants for mechanically primed gating I turned to the transmembrane region. In addition to the distinctively different signature motif found in S4 (S·R·R·E in angiosperm but N·R·R·H in gymnosperm and others), I also noticed that the position in S2 equivalent to E153 in human Hv1, carried either a positively charged residue (K), in angiosperm, or a non-charged residue (N), in gymnosperm and other species. Therefore, I assembled chimeras in which the S4 segment and the additional residue in S2 were swapped between PsHv1 and AtHv1, and named the constructs PsHv1-S4N and AtHv1-S4K, respectively. Interestingly, I found that PsHv1-S4K acquired the mechanosensitivity of AtHv1, as it required mechanical priming prior to depolarization for activation (Fig.6.1). The inverse chimera AtHv1-S4N on the other hand, did not produce measurable currents with or without mechanical stimulation. This could be due to reduced channel density at the plasma membrane, or to a loss of function produced by the swapping. The issue could be further investigated by comparing the surface expression of the different proteins. Another important thing to do is to revert the charge in S2 in both PsHv1-S4K and AtHv1-S4N mutants and see if that additional residue is required for the change in mechanosensitivity.

Other interesting perspectives from biophysics would be finding other possible forms of

stimulation to activate the channel. Mammalian Hv1 are strongly temperature sensitive<sup>4</sup> and it would be interesting to compare whether AtHv1 and TcHv1 are similarly or even more temperature sensitive. Other stimuli such as anesthetics and unsaturated fatty acids have been shown to potentiate other channels such as TREK-1<sup>23</sup>, Piezo1<sup>24</sup> and several types of VGICs<sup>25</sup>. Mammalian Hv1s are no exception, as several studies demonstrated that arachidonic acid (AA) and anandamide (AEA) enhance the activity of mouse Hv1<sup>26</sup> and human Hv1<sup>5</sup> by facilitating the activation kinetics and left shifting the G-Vs. In electrophysiological measurements from inside-out patches, applications of phospholipase A<sub>2</sub>, which generates AA from phospholipids, results in similar effects as direct application of AA<sup>26</sup>. Therefore, it is reasonable to think other polyunsaturated fatty acids or hydrophobic molecules such as anesthetics could induce similar enhancement in the plant Hv1 channels, particularly the ones that require mechanical priming for activation.

In the future, it will be important to determine the physiological role of plant proton channels, and whether the exceptional mechanosensitivity of angiosperm Hv1s is a physiological requirement (i.e., regulation of turgor pressure is known to be critical for plant growth and development, polarization of the cells, as well as handling abiotic stresses). Taken together, the biophysical characterization of Hv1 channels from different plant species broadens our understanding of the network of molecules involved in pH regulation and provides us with the tools to answer many more interesting questions.

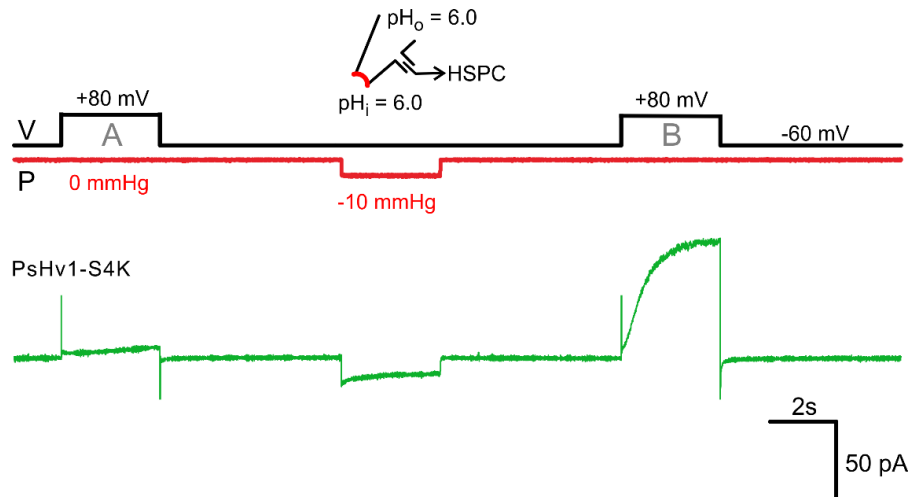


**Figure 6.1. Chimera PsHv1-S4K displays mechanosensitivity similar to AtHv1, and requires mechanical priming prior to depolarization for activation.** Examples of proton currents elicited by membrane depolarization for PsHv1-S4K before (pulse A) and after mechanical stimulus (pulse B). Change in membrane tension was induced via negative pressure applied to the patch pipette. The mechanical stimulus was delivered at resting membrane potential to inside-out patch. Corresponding voltage (black) and pressure (red) protocols are displayed above the current trace. The PsHv1-S4K chimera contains the S4 transmembrane segment plus a residue in S2 (N to K substitution) from AtHv1.

### ***Next steps on Hv1 Pharmacology***

Now that we have HIF compounds that inhibit Hv1 at lower concentrations than 2GBI, and are membrane permeant, albeit slowly, the most relevant questions to ask are: can HIF be used *ex vivo* and *in vivo*? Does HIF-mediated inhibition of proton currents lead to downstream physiological consequences such as a reduction in ROS production in phagocytes and a slowdown in cancer metastasis?

We tested HIF as well as other guanidine derivatives (2GBI and ClGBI) in fresh human neutrophils obtained from healthy individuals to test their abilities to block ROS production (Fig. 6.2) using a bioluminescence assay. Fresh neutrophils were extracted from blood containing anticoagulant Na-heparin, processed by centrifugation with Ficoll-Paque addition. Upon separation, pellet containing neutrophils from the lower layer were then lysed, and further purified through centrifugation, then finally plated into a 96-well plate together with media containing luminol. Control compounds and Hv1 inhibitors were added to the wells at various concentrations

followed by an incubation. PMA (phorbol myristate acetate) was finally added to the wells to elicit ROS production (through its activation of protein kinase C). Right after that, the plate was set into a plate reader for the detection of luminescence. We found HIF started to block ROS generation in human neutrophils at 5 $\mu$ M, and 20 $\mu$ M, and caused complete inhibition at 100 $\mu$ M (Fig. 6.2A, C). Surprisingly, guanidine derivatives 2GBI and ClGBI did not block ROS production (Figs. 6.2D and 6.2E, respectively), instead, they elicited a slight increase in ROS production compared to the control without any inhibitor (Fig. 6.2D orange circles). GBOZ (1-(1,3-benzoxazol-2-yl)guanidine) is a negative control for 2GBI with one of the nitrogens of the five membered ring replaced by an oxygen. We had previously found that GBOZ does not inhibit Hv1 significantly. Compared to PMA-stimulated neutrophils, GBOZ also triggered a slight increase in ROS production (Fig. 6.2F). However, the effect of GBOZ was smaller than the corresponding effects of 2GBI and ClGBI.

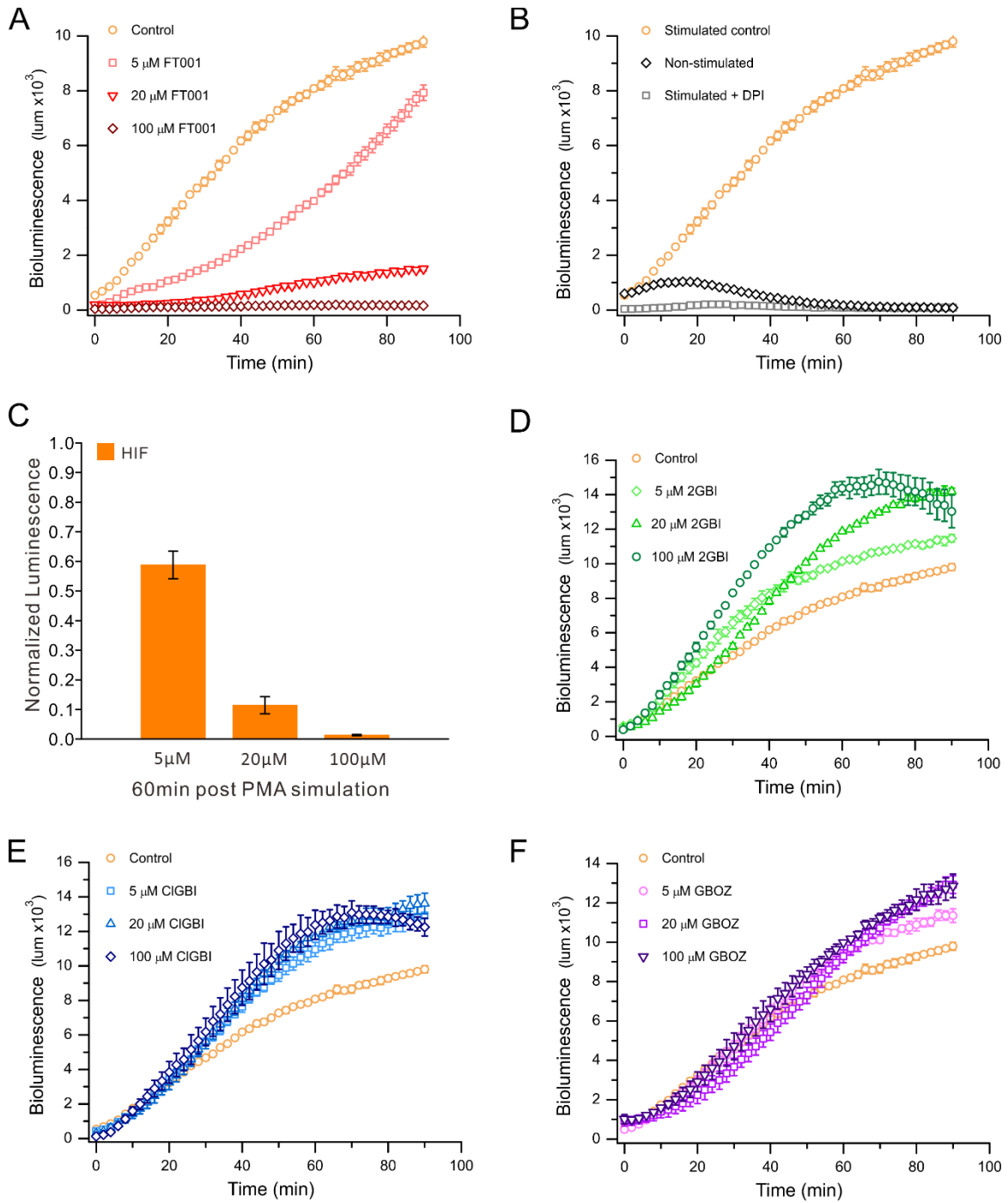


**Figure 6.2. PMA-induced ROS production in human neutrophils is potently inhibited by HIF.** **A)** HIF inhibits ROS produced by fresh human neutrophils upon PMA stimulation starting at 5 $\mu\text{M}$  (pink) and is more inhibited at 20 $\mu\text{M}$  (red). ROS production is completely prevented with HIF at 100 $\mu\text{M}$  (dark red). Reference in orange is ROS production by PMA-stimulated neutrophils without addition of inhibitor. **B)** ROS production by neutrophils under the following control conditions: PMA-stimulated (orange), non-stimulated (black), PMA-stimulated neutrophils with addition of diphenyleiodonium chloride (DPI) in grey. **C)** ROS inhibition in neutrophils by HIF at 5 $\mu\text{M}$ , 20 $\mu\text{M}$  and 100 $\mu\text{M}$  at 60 minutes after PMA stimulation. **D-F)** ROS inhibition in human neutrophils by **(D)** 2GBI, **(E)** ClGBI and **(F)** GBOZ at 5 $\mu\text{M}$ , 20 $\mu\text{M}$  and 100 $\mu\text{M}$ , respectively. Same control as **(A)** in orange is included. N=3, error bars are SEM.

While it is exciting that HIF effectively inhibits ROS production by human neutrophils at micromolar concentrations, and can do so after being added to the extracellular solution, it would be important to clarify why both 2GBI and ClGBI fail to inhibit ROS production. Earlier work from our group showed that native proton currents from several cell types (e.g., monocyte/macrophage cells RAW264.7 and THP-1 and microglial BV-2 cells<sup>15</sup>) are inhibited by ClGBI, so at least some inhibition of ROS production should be expected. There are several possible explanations for the negative result: 1) the luminescence that is detected is from luminol reacting with hydrogen peroxide, however physiologically relevant ROS species other than H<sub>2</sub>O<sub>2</sub> may be inhibited instead. 2) the guanidine derivatives may have off-target effects that lead to increased luminescence and mask the reduction of ROS caused by Hv1 inhibition. 3) Both ClGBI and 2GBI bind Hv1 only in the open conformation. If under oxidative burst conditions the channel opened only briefly, the compounds may not have the chance to block proton efflux and therefore ROS production. Future studies are required to test these hypotheses.

Another important issue that needs further investigation is the selectivity of HIF and its derivatives. Do these compounds affect other ion channels (e.g. hERG, Nav1.5, KCNQ1, etc.) in the concentration range required to block Hv1? One way to reduce off-target liability is to increase the affinity for the target (e.g., produce HIF derivatives with nanomolar IC50s). Another way is to rationally modify specific moieties within the inhibitor molecule to prevent cross-reaction with other channels.

### ***Physiological role of Hv1 in breast cancer***

While a handful of studies have demonstrated a correlation between overexpression of Hv1 and greater metastatic potential in various types of cancers<sup>6-8</sup>, the Hv1's role in cancer metastasis remains unclear. Whether ROS mediates the pro-metastatic properties of Hv1 is also unclear.

We reasoned that our improved HIF compounds could be used to shed light on the cellular events associated with H<sub>v</sub>1 hyperactivity. We took breast cancer as an example, and used the MDA-MB-231 cell line, which is extensively used as *in vitro* model for triple negative breast cancer, to test whether any of the HIF candidates can slow down the cell proliferation and migration in the wound healing assay. We employ the live imaging system IncuCyte together with a wound making module (WoundMaker, IncuCyte), which allows us to make consistent scratches across all wells of a 96-well plate. With IncuCyte, we can continuously observe the wound recovery in time-lapse mode. This is a powerful and versatile platform to test various conditions and drugs. In a pilot study, 100 $\mu$ M HIF produced a small decrease in the rate of cell migration (Fig. 6.3C, 6.4 grey triangles), however there was considerable variability in the results indicating that further experiments are required for proper quantification of the effect. On the other hand, the HIF derivative HIFPH demonstrated much higher potency and reduced breast cancer cell migration quite dramatically (Fig. 6.3D, 6.4 maroon squares). The migration rate can be further quantified as wound confluency and relative wound density (Fig. 6.4) using IncuCyte analysis software. The analysis tool puts a mask on the initial image with a fresh wound, and based on the determined wound area, it calculates changes in proliferation rate in later time points by computing the relative wound density (RWD) defined as:

$$\%RWD(t) = 100 \times \frac{(w(t)-w(0))}{(c(t)-c(0))}$$

Where  $w(t)$  is the density of the wound region at time  $t$ , and  $c(t)$  is the density of the cell region at time  $t$ .

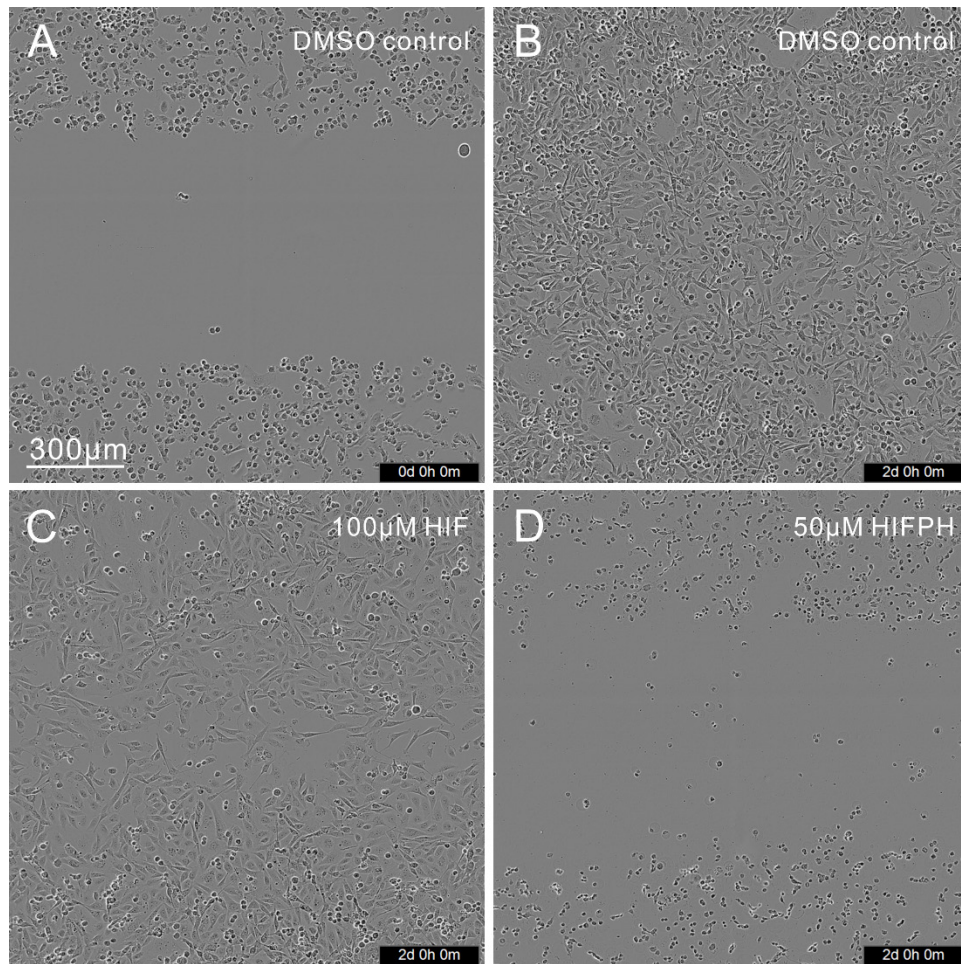


**Figure 6.3. Selective HIF compounds slow down the proliferation and migration of the MDA-MB-231 breast cancer cells. A)** Representative image from the control (0.1% DMSO) MDA-MB-231 cells at time 0, right after the wound was created. **B)** Representative image from the control (0.1% DMSO) MDA-MB-231 cells after 2 days. **C-D)** Same as B, but with addition of 100µM HIF (C), or 50µM HIFPH (D), another HIF derivative. Each culture condition was plated with 25,000 cells and cells were grown overnight prior to the experiment.

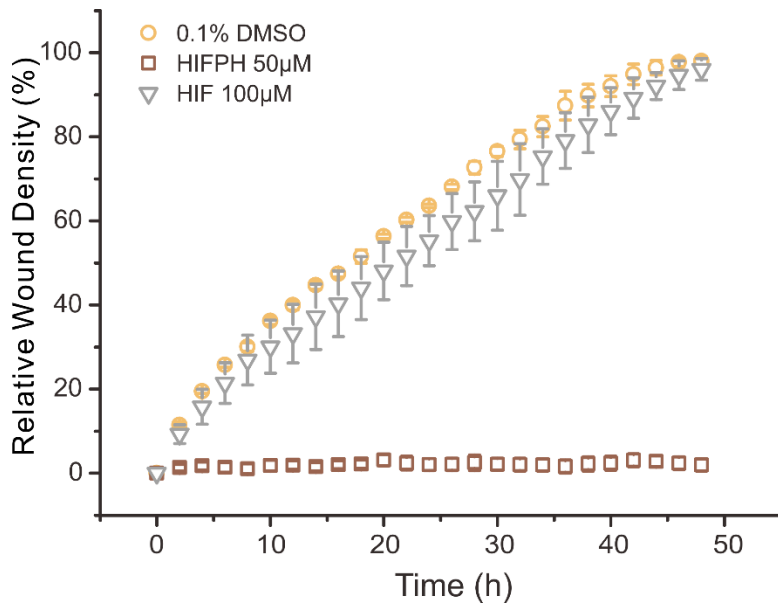


**Figure 6.4. Relative wound density (%) over 48 hours post wound scratching from MDA-MB-231 breast cancer cells with 50µM HIFPH (maroon), or 100µM HIF, referenced to control condition with 0.1% DMSO.** Relative wound density is calculated from images such as Fig.6.3. N=3 for all conditions, except N=2 for 100µM HIF.

In parallel to Hv1 inhibition with HIFs, we also seek other strategies to understand its physiological role in breast cancer. Previously, different groups generated Hv1 knockout cells or animals using different approaches<sup>27-29</sup>, however there is lack of consistency and sometimes different groups found contradictory results.

Our lab took advantage of the CRISPR technology<sup>30,31</sup>, which is highly efficient in modifying both genomic region as well as making point mutations. Full Hv1 knockout clones of the breast cancer MDA-MB-231 cells and their controls with same/similar number of passages were generated by GenOway. We reasoned that a complete deletion of the Hv1 protein would be different from having a non-conducting channel, e.g., the protein is still present at the cell membrane which might still allow for interactions with other proteins and relay second messengers. We originally wanted to introduce mutation N214R on both alleles to block proton conduction, however it was not possible to obtain biallelic modification, possibly because the resulting cells were too unhealthy. So, we limited our analysis to heterozygous cells in which only one copy of the gene

is mutated. For now, we choose to focus on comparing WT and the KO cells. When cultured in dish, we noticed the knockout (KD) cells seemed to grow slower (Fig. 6.5B) and appeared to have less density compared to the WT clone (Fig. 6.5A) plated at the same time. However, further evidence is needed to support this observation. We plan to investigate whether Hv1 KO cells present different properties in migration and invasion with the wound healing assay. If indeed there is a significant difference, we can apply a transwell assay to differentiate migration from proliferation.

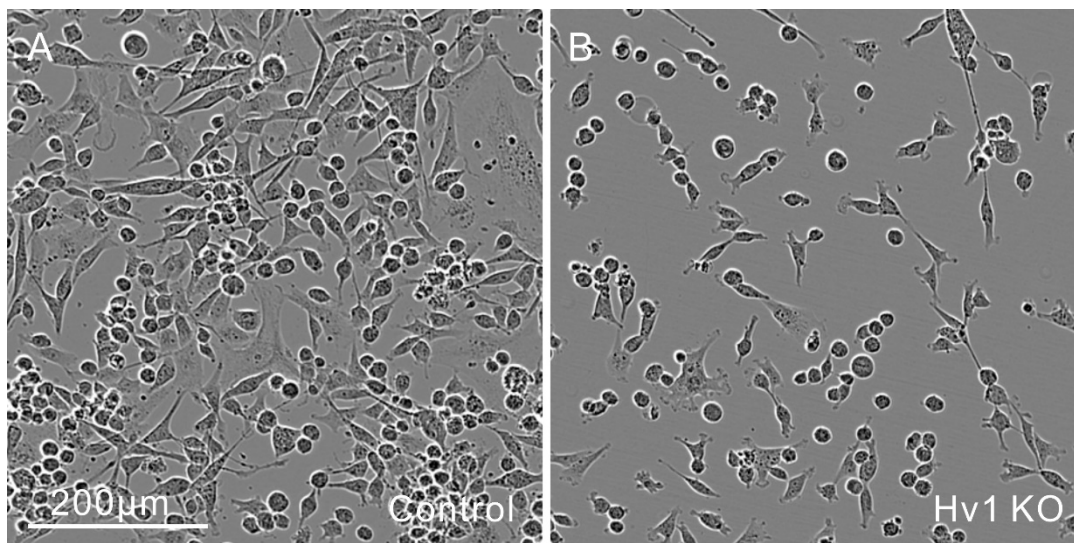


**Figure 6.5. Representative brightfield images of MDA-MB-231 breast cancer cells. A) Control breast cancer cells. B) Hv1 KO cells display lower density despite being plated at the same density as the control cells at the beginning.**

One of the most informative way to understand Hv1's role in breast cancer pathology is through a complete profiling. Therefore, we conducted RNA-seq for all of the clones, including Hv1 KO, control as well as N214R single allelic knockin breast cancer cells. We plan to compare the KO with control to identify any differentially expressed genes, and this might provide us with insights into candidates that can be placed up- or downstream of Hv1 activation, as well as new candidate genes to target.

### 6.3 References

1. Koch, H.P. et al. Multimeric nature of voltage-gated proton channels. *Proc Natl Acad Sci U S A* **105**, 9111-6 (2008).
2. Tombola, F., Ulbrich, M.H. & Isacoff, E.Y. The voltage-gated proton channel Hv1 has two pores, each controlled by one voltage sensor. *Neuron* **58**, 546-56 (2008).
3. Lee, S.Y., Letts, J.A. & Mackinnon, R. Dimeric subunit stoichiometry of the human voltage-dependent proton channel Hv1. *Proc Natl Acad Sci U S A* **105**, 7692-5 (2008).
4. DeCoursey, T.E. Voltage-gated proton channels: molecular biology, physiology, and pathophysiology of the H(V) family. *Physiol. Rev.* **93**, 599-652 (2013).
5. Lishko, P.V., Botchkina, I.L., Fedorenko, A. & Kirichok, Y. Acid extrusion from human spermatozoa is mediated by flagellar voltage-gated proton channel. *Cell* **140**, 327-37 (2010).
6. Wang, Y., Li, S.J., Wu, X., Che, Y. & Li, Q. Clinicopathological and biological significance of human voltage-gated proton channel Hv1 protein overexpression in breast cancer. *J. Biol. Chem.* **287**, 13877-88 (2012).
7. Wang, Y., Wu, X., Li, Q., Zhang, S. & Li, S.J. Human voltage-gated proton channel hv1: a new potential biomarker for diagnosis and prognosis of colorectal cancer. *PLoS One* **8**, e70550 (2013).
8. Hondares, E. et al. Enhanced activation of an amino-terminally truncated isoform of the voltage-gated proton channel HVCN1 enriched in malignant B cells. *Proc Natl Acad Sci U S A* **111**, 18078-83 (2014).
9. Wu, L.J. Voltage-gated proton channel HV1 in microglia. *Neuroscientist* **20**, 599-609 (2014).
10. Wu, L.J. et al. The voltage-gated proton channel Hv1 enhances brain damage from ischemic stroke. *Nat. Neurosci.* **15**, 565-73 (2012).
11. Ritzel, R.M. et al. Proton extrusion during oxidative burst in microglia exacerbates pathological acidosis following traumatic brain injury. *Glia* **69**, 746-764 (2021).
12. Murugan, M. et al. The voltage-gated proton channel Hv1 contributes to neuronal injury and motor deficits in a mouse model of spinal cord injury. *Molecular brain* **13**, 143 (2020).
13. Zhao, C. & Tombola, F. Voltage-gated proton channels from fungi highlight role of peripheral regions in channel activation. *Commun Biol* **4**, 261 (2021).
14. Taylor, A.R., Chrachri, A., Wheeler, G., Goddard, H. & Brownlee, C. A voltage-gated H<sup>+</sup> channel underlying pH homeostasis in calcifying coccolithophores. *PLoS Biol.* **9**, e1001085 (2011).
15. Hong, L., Kim, I.H. & Tombola, F. Molecular determinants of Hv1 proton channel inhibition by guanidine derivatives. *Proc Natl Acad Sci U S A* **111**, 9971-6 (2014).
16. Lim, V.T. et al. Insights on small molecule binding to the Hv1 proton channel from free energy calculations with molecular dynamics simulations. *Sci Rep* **10**, 13587 (2020).
17. Pless, S.A. & Ahern, C.A. Unnatural amino acids as probes of ligand-receptor interactions and their conformational consequences. *Annu. Rev. Pharmacol. Toxicol.* **53**, 211-29 (2013).
18. Van Arnem, E.B. & Dougherty, D.A. Functional probes of drug-receptor interactions implicated by structural studies: Cys-loop receptors provide a fertile testing ground. *J. Med. Chem.* **57**, 6289-300 (2014).
19. Zhao, C. et al. Development of HIFs: arginine-mimic inhibitors of Hv1 with improved VSD-ligand interactions. *Co-submitted to J. Gen. Physiol.* (2021a).

20. Zhao, C. et al. Hv1 inhibition by HIF reveals a new druggable pocket in the voltage-sensing domain. *Co-submitted to J. Gen. Physiol.* (2021b).
21. Hennigar, S.R. & McClung, J.P. Nutritional Immunity: Starving Pathogens of Trace Minerals. *American journal of lifestyle medicine* **10**, 170-173 (2016).
22. Ballou, E.R. & Wilson, D. The roles of zinc and copper sensing in fungal pathogenesis. *Curr. Opin. Microbiol.* **32**, 128-134 (2016).
23. Pavel, M.A., Petersen, E.N., Wang, H., Lerner, R.A. & Hansen, S.B. Studies on the mechanism of general anesthesia. *Proc Natl Acad Sci U S A* **117**, 13757-13766 (2020).
24. Romero, L.O. et al. Dietary fatty acids fine-tune Piezo1 mechanical response. *Nature communications* **10**, 1200 (2019).
25. Elinder, F. & Liin, S.I. Actions and Mechanisms of Polyunsaturated Fatty Acids on Voltage-Gated Ion Channels. *Frontiers in physiology* **8**, 43 (2017).
26. Kawanabe, A. & Okamura, Y. Effects of unsaturated fatty acids on the kinetics of voltage-gated proton channels heterologously expressed in cultured cells. *J Physiol* **594**, 595-610 (2016).
27. Ramsey, I.S., Ruchti, E., Kaczmarek, J.S. & Clapham, D.E. Hv1 proton channels are required for high-level NADPH oxidase-dependent superoxide production during the phagocyte respiratory burst. *Proc Natl Acad Sci U S A* **106**, 7642-7 (2009).
28. Okochi, Y., Sasaki, M., Iwasaki, H. & Okamura, Y. Voltage-gated proton channel is expressed on phagosomes. *Biochem. Biophys. Res. Commun.* **382**, 274-9 (2009).
29. Bare, D.J., Cherny, V.V., DeCoursey, T.E., Abukhdeir, A.M. & Morgan, D. Expression and function of voltage gated proton channels (Hv1) in MDA-MB-231 cells. *PLoS One* **15**, e0227522 (2020).
30. Zhang, F. Development of CRISPR-Cas systems for genome editing and beyond. *Q. Rev. Biophys.* **52**, e6 (2019).
31. Jiang, F. & Doudna, J.A. CRISPR-Cas9 Structures and Mechanisms. *Annual Review of Biophysics* **46**, 505-529 (2017).